

**ELECTROLYTIC SYNTHESIS OF NICKEL
BASED ALLOYS AND THEIR
CHARACTERIZATION**

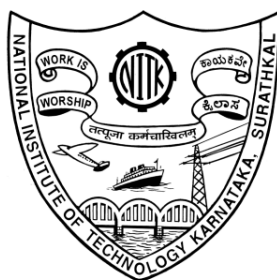
Thesis

Submitted in partial fulfillment of the requirements for the degree of

DOCTOR OF PHILOSOPHY

by

SANDHYA S



DEPARTMENT OF CHEMISTRY

NATIONAL INSTITUTE OF TECHNOLOGY KARNATAKA,

SURATHKAL, MANGALORE - 575025

January, 2018

DECLARATION

I hereby *declare* that the Research Thesis entitled “**Electrolytic synthesis of nickel based alloys and their characterization**” which is being submitted to the National Institute of Technology Karnataka, Surathkal in partial fulfillment of the requirements for the award of the Degree of **Doctor of Philosophy** in Chemistry is a *bonafide report of the research work carried out by me*. The material contained in this Research Thesis has not been submitted to any University or Institution for the award of any degree.

Sandhya S
Reg. No. 135018CY13F04
Department of Chemistry

Place: NITK, Surathkal
Date: 08-01-2018

CERTIFICATE

This is to *certify* that the Research Thesis entitled “**Electrolytic synthesis of nickel based alloys and their characterization**” submitted by **Sandhya S (Reg. No. 135018CY13F04)** as the record of the research work carried out by her is *accepted as the Research Thesis submission* in partial fulfillment of the requirements for the award of degree of **Doctor of Philosophy**.

Prof. A. Chitharanjan Hegde
Research Guide

Chairman - DRPC

ACKNOWLEDGEMENT

I would like to express my sincere gratitude to my academic advisor Prof. A. Chitharanjan Hegde, Dept. of Chemistry, NITK, Surathkal, for the continuous support of my Ph.D. research work, for his patience, motivation, and immense knowledge. His guidance helped me in all the time of my research and writing of this thesis. I could not have imagined having a better advisor and mentor for my Ph.D. work.

Besides my advisor, I would like to thank the Research Progress Assessment Committee members, Prof. A. Nityananda Shetty, Dept. of Chemistry and Prof. Dwarakish G. S., Dept. of Applied Mechanics and Hydraulics for their insightful comments and encouragement, but also for their interest in my work, which incited me to widen my research from various perspectives.

A very special gratitude goes out to National Institute of Technology Karnataka, Surathkal for providing the Institute fellowship and financial support necessary for the completion of my doctoral work.

I am extremely grateful to all teaching and non-teaching staff, Dept. of Chemistry, NITK, Surathkal their kind co-operation, immense support, and good wishes.

My sincere thanks also go to Prof. D. Krishna Bhat, Head, Dept. of Chemistry and Prof. Kasturi. V. Bangera Dept. of Physics who gave me access to their laboratory and research facilities. Without their precious support, it would not be possible to conduct this research.

Every result described in this thesis was accomplished with the help and support of fellow labmates. I gained a lot from their vast chemistry knowledge and scientific curiosity. Dr. Yathish Ullal, Dr. Vaishaka Rao, Dr. Liju Elias, Ms. Akshatha R. Shetty and Mr. Mohamed Jaffer Sadiq M, I wholeheartedly thank them for the stimulating discussions, unfailing support and assistance, it was great sharing the laboratory with them during last four years.

I would like to convey my grateful appreciation to Department of Metallurgical and Materials Engineering and Department of Physics NITK, Manipal Institute of

Technology, Manipal, Indian Institute of Science, Bengaluru, for allowing me to avail the instrumentation facility whenever required.

It would be remiss if I did not thank Mrs. Shamila Nandini, who deserves credit for providing paramount assistance with administrative tasks, reminding us of impending deadlines, and keeping our work running smoothly.

Finally, I would like to acknowledge my friends who supported me during my time here. I thank them for their friendship, love, unyielding support and much-needed laughter.

Last but not the least, I would like to thank my family for being my strength and greatest support throughout my Ph.D. work and my life in general.

Above all, I humbly thank God Almighty, who showered the choicest of his blessing to complete this endeavor.

Thank you.

Sandhya S

ABSTRACT

This thesis titled, *Electrolytic synthesis of nickel based alloys and their characterization* details a comprehensive approach for improving the corrosion resistance and electrocatalytic activity of Ni–M (where M = Sn and Mo) alloys through an inexpensive, yet advanced electrodeposition method. The coating properties have been improved by regulating the mass transfer process at cathode film, parallel to the process of deposition. The modulation in the mass transfer was affected by pulsing the current density (c.d.), magnetic field intensity (B) and ultrasonic power density (p.d.). The thesis comprises the optimization of two new binary alkaline baths, namely Sn–Ni and Ni–Mo using direct current (DC) for highest performance of corrosion resistance and electrocatalytic activity for hydrogen evolution reaction (HER) and oxygen evolution reaction (OER). The corrosion behaviors were evaluated in 5% NaCl solution using potentiodynamic polarization and electrochemical impedance spectroscopy (EIS) methods. Experimental results revealed that corrosion resistance of multilayer Sn–Ni alloy coatings developed by pulsing ultrasound p.d. is many folds better than its monolayer counterpart. The kinetic parameters for HER and OER were determined by cyclic voltammetry (CV) and chronopotentiometry (CP) methods in 1.0 M KOH medium. The electrocatalytic activity of magneto-electrodeposited Ni–Mo alloy coatings were improved, due to changed limiting c.d. (i_L) of more readily deposit-able metal, explained by the hydrodynamic effect. Effect of addition of reduced graphene oxide (rGO) into the alloy matrix and the anodic dissolution of the as-deposited coating as a tool to enhance the electrocatalytic activity of Ni–M alloys has also been examined. The changed property of alloy coatings was found to bear a close relationship with their composition, phase structure, surface morphology and roughness, confirmed by EDX, XRD, SEM and AFM analyses, respectively. The experimental data are compared, and results are discussed with Tables and Figures, a note for future work is mentioned at the end.

Keywords: *Sn–Ni alloy, Ni–Mo alloy, corrosion study, magneto-electrodeposition, sono-electrodeposition, electrocatalysis*

CONTENTS

CHAPTER 1	1
INTRODUCTION	1
1.1 ELECTROPLATING TECHNOLOGY	1
1.2 ALLOY DEPOSITION	2
1.3 ORIGIN OF ELECTROPLATING	3
1.4 PRINCIPLE OF ELECTROPLATING	4
1.4.1 Faraday’s Laws of Electrolysis	6
1.5 MODERN METHODS OF ELECTRODEPOSITION	7
1.5.1 Composition Modulated Multilayer Coatings	8
1.5.2 Magneto-electrodeposition	9
1.5.3 Sono-electrodeposition	12
1.6 WATER ELECTROLYSIS	13
1.6.1 Hydrogen Evolution Reaction	15
1.6.2 Oxygen Evolution Reaction	16
1.7 ELECTROCHEMICAL POLARIZATION	17
1.7.1 Activation Polarization	18
1.7.2 Concentration Polarization	20
1.7.3 Ohmic Polarization	22
1.8 CORROSION	23
1.8.1 Corrosion Protection	23
1.8.2 Electrochemical Corrosion Processes	24
1.9 CORROSION EVALUATION TECHNIQUES	25
1.9.1 Potentiodynamic Polarization Method	26
1.9.2 Electrochemical Impedance Spectroscopy Method	28

CHAPTER 2	33
LITERATURE REVIEW	33
2.1 INTRODUCTION	33
2.2 LITERATURE SURVEY	34
2.2.1 Sn–Ni Alloy	34
2.2.2 Ni–Mo Alloy	37
2.2.3 Magneto-electrodeposition of Ni-Based Binary Alloys	39
2.2.4 Sono-electrodeposition	41
2.2.5 Electrocatalytic Property of Ni-based (where M = Sn and Mo) Alloys	43
2.3 SCOPE AND OBJECTIVES	45
2.3.1 Scope	45
2.3.2 Objectives	48
CHAPTER 3	49
RESEARCH METHODOLOGY	49
3.1 INTRODUCTION	49
3.2 MATERIALS AND METHODS	50
3.2.1 Chemicals Used	50
3.2.2 Surface Cleaning	51
3.2.3 Purification of Electrolytes	52
3.2.4 Optimization of the Electrolyte Baths	52
3.2.4.1 Hull cell	52
3.3 ELECTRODEPOSITION OF MONOLAYER AND MULTILAYER ALLOY COATINGS	55

3.3.1	Development of Monolayer Alloy Coatings by Magneto-electrodeposition Method.....	56
3.3.2	Development of Monolayer and Multilayer Alloy Coatings by Sono-electrodeposition Method.....	57
3.4	ELECTROCHEMICAL MEASUREMENTS.....	58
3.4.1	Corrosion Study.....	58
3.4.2	Electrocatalytic Study.....	60
3.5	CHARACTERIZATION OF THE COATINGS.....	61
3.6	THICKNESS AND HARDNESS OF THE COATINGS.....	62
CHAPTER 4	65
	MAGNETO-ELECTRODEPOSITION OF Sn–Ni ALLOY COATING FOR BETTER CORROSION PROTECTION.....	65
4.1	INTRODUCTION.....	65
4.2	OPTIMIZATION OF Sn-Ni ALLOY BATH.....	66
4.2.1	Compositional Analysis.....	67
4.2.2	Effect of Current Density on Thickness, Composition, and Hardness of the Deposit.....	68
4.2.3	Surface Morphology.....	69
4.2.4	X-Ray Diffraction Study.....	70
4.2.5	Corrosion Study.....	71
4.3	MAGNETO-ELECTRODEPOSITION OF Sn–Ni ALLOY COATINGS.....	74
4.3.1	Surface Morphology.....	75
4.3.2	XRD Analysis.....	76
4.3.3	Corrosion Behaviour of MED Sn–Ni Alloy Coatings.....	78
4.4	DISCUSSION.....	82
4.5	CONCLUSIONS.....	86

CHAPTER 5	87
SONOELECTRODEPOSITION OF Sn–Ni ALLOY COATINGS FOR BETTER CORROSION PROTECTION	87
5.1 INTRODUCTION	87
5.2 DEVELOPMENT OF MONOLAYER Sn–Ni ALLOY COATING BY SONO-ELECTRODEPOSITION	88
5.2.1 Corrosion Study of SED Sn–Ni alloy Coatings	90
5.2.1.1 Potentiodynamic polarization study	90
5.2.1.2 Electrochemical impedance study	91
5.2.2 X-ray Diffraction Study	93
5.2.3 SEM Study of SED Sn–Ni Alloy Coatings	94
5.3 DEVELOPMENT OF SED MULTILAYER Sn–Ni ALLOY COATINGS	95
5.3.1 Corrosion Study	96
5.3.1.1 Polarization study	96
5.3.1.2 Electrochemical impedance spectroscopy study	98
5.3.2 Comparison of SED Monolayer and Multilayer Sn–Ni Alloy Coatings	100
5.3.3 SEM Study of SED Multilayer Sn–Ni Alloy Coating	101
5.4 CORROSION MECHANISM IN MONOLAYER AND MULTILAYER Sn–Ni ALLOY COATING	102
5.5 CONCLUSIONS	103
CHAPTER 6	105
ELECTROCATALYTIC STUDY OF ELECTRODEPOSITED Sn–Ni ALLOY COATINGS	105
6.1 INTRODUCTION	105

6.2	EXPERIMENTAL METHODS.....	106
6.2.1	Preparation of Sn–Ni Alloy Test Electrodes	106
6.2.2	Experimental Set Up	107
6.2.3	Development of Microporous Sn–Ni Alloy Coating	108
6.3	RESULTS AND DISCUSSION.....	108
6.3.1	Composition, Hardness and Thickness Analysis	109
6.3.2	Surface Morphology	109
6.3.3	X-ray Diffraction Study	110
6.3.4	Corrosion Stability	111
6.3.5	Electrocatalytic Study	114
6.3.5.1	Electrocatalysis for HER	115
	a) <i>Cyclic voltammetry study</i>	115
	b) <i>Chronopotentiometry study</i>	117
6.3.5.2	Electrocatalysis for OER	118
	a) <i>Cyclic voltammetry</i>	118
	b) <i>Chronopotentiometry</i>	119
6.3.6	Electrochemical Dissolution Treatment	120
6.3.7	Effect of Electrode Composition on Electrocatalytic Activity	124
6.3.8	Mechanism of HER and OER	125
6.4	CONCLUSIONS.....	127
CHAPTER 7		129
ELECTRODEPOSITION OF Ni–Mo ALLOY COATINGS AND ITS		
ELECTROCATALYTIC ACTIVITY FOR WATER SPLITTING REACTION..		129
7.1	INTRODUCTION.....	129
7.2	ELECTRODEPOSITION OF Ni–Mo ALLOY COATINGS	130
7.3	RESULTS AND DISCUSSION.....	131
7.3.1	SEM Analysis	131

7.3.2	AFM Study	132
7.3.3	EDX Analysis	133
7.3.4	XRD Study	134
7.3.5	Potentiodynamic Polarization Study	135
7.3.6	Electrocatalytic Study	137
7.3.6.1	Electrocatalytic behavior for HER	137
	a) <i>Cyclic voltammetry study</i>	137
	b) <i>Chronopotentiometry study</i>	139
7.3.6.2	Electrocatalytic behavior for OER	140
	a) <i>Cyclic voltammetry study</i>	140
	b) <i>Chronopotentiometry study</i>	142
7.4	MECHANISM OF WATER SPLITTING REACTION	143
7.2	CONCLUSIONS.....	144
CHAPTER 8		147
EFFECT OF INDUCED MAGNETIC FIELD ON ELECTRODEPOSITION OF Ni–Mo ALLOY COATINGS AND ITS ELECTROCATALYTIC ACTIVITY FOR HER.....		147
8.1	INTRODUCTION	147
8.2	MAGNETO–ELECTRODEPOSITION OF Ni–Mo ALLOY COATINGS	148
8.3	RESULTS AND DISCUSSION.....	149
8.3.1	Surface and Compositional Analysis	149
8.3.2	XRD Study	151
8.3.3	Potentiodynamic Polarization Study	152
8.3.4	Hydrogen Evolution Reaction on MED Ni–Mo Alloy	154
	8.3.4.1 <i>Cyclic voltammetry study</i>	154
	8.3.4.2 <i>Chronopotentiometry study</i>	156

8.4	DISCUSSION.....	157
8.5	MECHANISM FOR HER.....	159
8.6	CONCLUSIONS.....	159
CHAPTER 9.....		161
EFFECT OF rGO ON ELECTROCATALYTIC ACTIVITY OF HYDROGEN EVOLUTION REACTION ON Ni–Mo ALLOY COATINGS.....		161
9.1	INTRODUCTION.....	161
9.2	MATERIALS AND METHODS.....	162
9.2.1	Synthesis of Reduced Graphene Oxide (rGO).....	162
9.2.2	Electrodeposition of Ni–Mo–rGO Composite Coatings.....	162
9.3	RESULTS AND DISCUSSION.....	163
9.3.1	SEM Analysis.....	163
9.3.2	EDX Analysis.....	164
9.3.3	XPS Analysis.....	166
9.3.4	XRD Study.....	167
9.3.5	Potentiodynamic Polarization Study.....	169
9.3.6	Cyclic Voltammetry.....	172
9.3.7	Chronopotentiometry.....	174
9.3.8	Mechanism for HER.....	176
9.4	CONCLUSIONS.....	177
CHAPTER 10.....		179
SUMMARY AND CONCLUSIONS.....		179
10.1	SUMMARY.....	179
10.1.1	Corrosion Performance of Binary Alloys.....	180
10.1.2	Electrocatalytic Performance of Binary Alloys.....	183
10.2	CONCLUSIONS.....	185

10.3 SCOPE FOR THE FUTURE WORK	187
REFERENCES.....	189
RESEARCH PUBLICATIONS.....	215
BIODATA.....	217

List of Figures

Figure 1.1	Basic components of DC electroplating.....	4
Figure 1.2	Illustration of a fundamental cathodic electrodeposition process for a single constituent metal salt dissolved in an aqueous electrolyte (Ray 2015)	6
Figure 1.3	Representation of a typical CMMA coating.....	9
Figure 1.4	Hydrodynamic flow on electrode surface due to the applied magnetic field (B), where: a) B is parallel to the movement of ions, b) B is perpendicular to the direction of ions, and c) the primary MHD flow causes the vortex at spots of high c.d. leading to micro-MHD convection (Monzon and Coey 2014)	11
Figure 1.5	Effect of ultrasound on liquid medium showing: a) Acoustic streaming: a typical flow pattern induced by sonic horn, b) Cavitation collapse at an electrode surface and c) Cavitation bubble collapse in bulk solution (Banks and Compton 2003)	13
Figure 1.6	Diagrammatic representation of Butler-Volmer equation.....	20
Figure 1.7	Concentration of H^+ in solution near a surface controlled by concentration polarization.....	21
Figure 1.8	Cathodic concentration polarization: (a) plotted vs. reaction rate or current density, and (b) effect of solution conditions.....	21
Figure 1.9	Schematic representation showing the positioning of Luggin's tube to overcome iR drop in aqueous solution.....	22
Figure 1.10	Schematic representation of a basic corrosion process.....	25
Figure 1.11	Three electrode set up commonly used for corrosion study.....	26
Figure 1.12	Potentiodynamic polarization behavior showing Tafel plot.....	27
Figure 1.13	Variation of impedance with frequency of circuit elements C, L and R.....	30
Figure 1.14	Representative Nyquist plot showing frequency dependent impedance response.....	30

Figure 3.1	Top view of the Hull cell displaying the position of anode and cathode.....	53
Figure 3.2	Typical representation of a) Hull cell ruler corresponding to different cell current, and b) identification of c.d. corresponding to the different distance from HCD point.....	54
Figure 3.3	Experimental setup used for deposition of binary alloy using DC power analyzer (N6705A, Agilent Technology, USA)	56
Figure 3.4	Experimental setup used for magnetic field induced codeposition (magneto-electrodeposition) using DC Power source (Aplab, LD3205) and Electromagnet (Polytronics, Model: EM 100)	57
Figure 3.5	Experimental setup used for deposition of monolayer and multilayer alloy coating, under different conditions of sonication at constant c.d. using DC Power source (Aplab, LD3205) and Ultrasound generator (SONIC Vibra-Cell™ VC 750)	58
Figure 3.6	Experimental setup used for studying the corrosion behavior of electroplated alloy coatings.....	59
Figure 3.7	Experimental set-up used for electrodeposition of Ni–M alloy coatings on pre-polished copper surface using DC power analyzer (N6705A, Agilent Technology, USA)	60
Figure 3.8	Experimental setup used for quantitative measurement of H ₂ and O ₂ evolved on test electrode during water splitting reaction.....	61
Figure 4.1	EDX spectrum showing relative peaks of Sn and Ni in Sn–Ni alloy deposited at 1.0 A dm ⁻²	68
Figure 4.2	Effect of c.d. on Ni content and hardness of Sn–Ni coatings.....	69
Figure 4.3	SEM images of Sn–Ni alloy coating deposited at a) 1.0 A dm ⁻² , b) 2.0 A dm ⁻² , c) 3.0 A dm ⁻² and d) 4.0 A dm ⁻²	70
Figure 4.4	XRD peaks of Sn–Ni alloy coatings deposited at different c.d.'s.....	71
Figure 4.5	Potentiodynamic polarization curves of Sn–Ni coatings developed at different c.d.'s.....	72
Figure 4.6	Nyquist plots of Sn–Ni alloy coatings deposited at different c.d.'s	73

Figure 4.7	Schematic setup used for deposition of Sn–Ni alloy under the influence of magnetic field, where N and S represent North and South Pole of an Electromagnet	75
Figure 4.8	SEM images of MED Sn–Ni alloy coatings deposited at different conditions of B (perpendicular orientation), where (a), (b), (c) and (d) = 0.1 T, 0.2 T, 0.3 T and 0.4 T, respectively (all are at optimal c.d. = 1.0 A dm ⁻²)	76
Figure 4.9	XRD patterns of MED Sn–Ni alloy coatings deposited at optimal c.d. under different conditions of B (specified on each XRD plot), applied (a) parallel, and (b) perpendicular to the direction of movement of ions.....	77
Figure 4.10	Tafel plots of MED Sn–Ni alloy coatings under different conditions of applied B (perpendicular), developed from the optimal bath.....	80
Figure 4.11	Nyquist plots of MED Sn–Ni alloy coating at different conditions of applied B (perpendicular) deposited from the optimal bath.....	81
Figure 4.12	Relative response of Nyquist plots (a), and Tafel plots (b), of Sn–Ni alloy coatings, deposited under different optimal conditions of mass transfer, i.e. natural convection (ED) and forced convection (MED), both in parallel and perpendicular)	82
Figure 4.13	Schematic representation showing: (a) Decrease of cathode film thickness under B at definite c.d. and [Sn ⁺²], (b) Increase of i_L due to induction of B without increasing [Sn ⁺²] in the bath (Here, B represents magnetic field intensity applied perpendicular to the direction of movement of metal ions)	84
Figure 4.14	Variation in wt.% of Sn at different c.d.'s under different conditions of B : (a) ED coatings, $B = 0$ T, (b) and (c) MED coating at $B = 0.2$ T parallel and perpendicular, respectively.....	85
Figure 5.1	Process assembly used for SED of Sn–Ni alloy coating.....	89
Figure 5.2	Schematic representation of driving forces used for development of Sn–Ni alloy coatings from same optimized bath along with deposit patterns on top right: a) DC or constant current for ED Sn–Ni alloy, b) DC and	

	ultrasonic field for SED Sn–Ni alloy (both monolayer), and c) DC and pulsed ultrasound field for multilayer Sn–Ni alloy.....	89
Figure 5.3	Potentiodynamic polarization behaviors of SED Sn–Ni alloy coatings developed from the optimal bath under different conditions of ultrasound p.d.....	90
Figure 5.4	EIS of SED Sn–Ni alloy coatings developed from optimal bath under varying conditions of ultrasound p.d.	92
Figure 5.5	XRD peaks showing a change of crystallographic orientations of Sn–Ni alloy coatings deposited at different ultrasound p.d., in relation to its ED coatings, i.e. at 0 W cm^{-2} , deposited from the same bath at same c.d. = 1.0 A dm^{-2}	93
Figure 5.6	SEM micrographs of SED Sn–Ni alloy coatings developed under different conditions of ultrasound p.d.'s: a) 0 W cm^{-2} , b) 0.6 W cm^{-2} , c) 0.9 W cm^{-2} and d) 1.2 W cm^{-2} , deposited from the same bath at same c.d. = 1.0 A dm^{-2}	94
Figure 5.7	Potentiodynamic polarization behavior of SED multilayer Sn–Ni coatings, with a different number of layers developed from the same optimal bath at optimal c.d.	97
Figure 5.8	EIS response of SED multilayer Sn–Ni alloy coatings, with a different number of layers, developed from the same optimal bath at optimal c.d.....	99
Figure 5.9	Comparison of corrosion performance of monolayer (with and without sonication effect) and SED multilayer Sn–Ni alloy coatings through a) Nyquist plots and b) potentiodynamic polarization curves (developed under optimal conditions, from the same bath for same duration).....	100
Figure 5.10	SEM cross-sectional view of SED multilayer Sn–Ni coating, represented as $(\text{Sn-Ni})_{30/30/10}$ displaying 10 layers, having alternatively different composition	101
Figure 5.11	Schematic diagram representing the increased corrosion protection of SED multilayer Sn–Ni alloy coatings compared to its monolayer coating: a) Corrosion medium spreads laterally at the interface between	

	layers and reduces the corrosion, and b) Corrosion medium attacks directly to reach the substrate faster in monolayer coating.....	102
Figure 6.1	Customized glass cell used for electrodeposition of binary Ni–M alloy coatings on the cross-sectional surface area of a copper rod.....	107
Figure 6.2	Three electrode tubular glass cell assembly used for quantitative measurement of H ₂ and O ₂ formed on the surface of a Ni–M alloy coatings, used as electrode material for water splitting reactions of HER and OER.....	108
Figure 6.3	SEM images of Sn–Ni alloy coatings deposited from the optimized bath at different c.d.'s: a) 1.0 A dm ⁻² , b) 2.0 A dm ⁻² , c) 3.0 A dm ⁻² and d) 4.0 A dm ⁻²	110
Figure 6.4	XRD patterns of Sn–Ni alloy coatings deposited on a copper substrate at different c.d.'s, using the optimal bath.....	111
Figure 6.5	Potentiodynamic polarization behavior of Sn–Ni coatings deposited on copper at different c.d.'s, using the optimal bath.....	112
Figure 6.6	CV curves demonstrating increase of cathodic peak current densities (<i>i_{pc}</i>) with deposition c.d.'s, for HER on the surface of as-deposited Sn–Ni alloy coatings.....	115
Figure 6.7	CP curves of as-deposited Sn–Ni alloys, deposited at different c.d.'s under impressed cathodic current of –300 mA cm ⁻² for HER. The volume of H ₂ evolved in 300 s on each electrode are shown in the inset.....	117
Figure 6.8	CV curves for OER on as-deposited Sn–Ni alloy coatings deposited at different c.d.'s showing their anodic peak current density (<i>i_{pa}</i>).....	118
Figure 6.9	Chronopotentiograms of as-deposited Sn–Ni alloys for OER, at different deposition c.d.'s under impressed anodic current of +300 mA cm ⁻² . The volume of O ₂ evolved in 300 s on each test electrode is shown in the inset.....	120
Figure 6.10	SEM images of Sn–Ni alloy coatings deposited at optimal c.d. of 4.0 A dm ⁻² : a) as-deposited surface, and b) after anodic dissolution showing micro-porous structure.....	121

Figure 6.11	AFM images of Sn–Ni alloy coatings at optimal c.d. of 4.0 A dm ⁻² : a) as-deposited surface, and b) after anodic dissolution.....	122
Figure 6.12	Electrocatalytic response of as-deposited and anodically treated Sn–Ni alloy coatings, deposited at optimal c.d. (4.0 A dm ⁻²), through a) CV study, and b) CP study (with volume of H ₂ liberated in the inset)	123
Figure 6.13	Schematic diagram showing the mechanism of HER (a) and OER (b) on the surface of Sn–Ni alloy coatings having definite composition, used as cathode and anode respectively in 1.0 M KOH solution.....	126
Figure 7.1	SEM images of Ni–Mo alloy deposited from optimal bath at a) 1.0 A dm ⁻² , b) 2.0 A dm ⁻² , c) 3.0 A dm ⁻² and d) 4.0 A dm ⁻²	131
Figure 7.2	3D AFM images of Ni–Mo alloy coatings deposited at a) 1.0 A dm ⁻² , and b) 4.0 A dm ⁻²	132
Figure 7.3	EDX spectrum of Ni–Mo alloy coating, deposited at 1.0 A dm ⁻² showing the relative peaks corresponding to its Ni and Mo content.....	133
Figure 7.4	XRD patterns of Ni–Mo alloy coatings deposited at different c.d.'s from the optimal bath.....	134
Figure 7.5	Potentiodynamic polarization curves of Ni–Mo deposits, developed at different c.d. using optimal bath.....	135
Figure 7.6	Cyclic voltammograms of Ni–Mo alloy deposits developed at different c.d.'s with their cathodic peak current density, <i>i</i> _{pc} for HER.....	138
Figure 7.7	Chronopotentiograms of Ni–Mo deposits, developed at different c.d.'s under impressed cathodic current of –300 mA cm ⁻² (volume of H ₂ evolved in 300 s on each test electrodes are shown in the inset)	139
Figure 7.8	CV curves of Ni–Mo alloy coatings deposited at different c.d.'s demonstrating their anodic peak current density <i>i</i> _{pa} for OER, and their redox couples are shown in the inset.....	141
Figure 7.9	Chronopotentiograms of Ni–Mo deposits developed at different c.d.'s under impressed anodic current of +300 mA cm ⁻² (volumes of O ₂ evolved in 300 s on each test electrodes are shown in the inset)	143
Figure 8.1	Schematic of the experimental setup used for development of MED Ni–Mo alloy coatings.....	149

Figure 8.2	SEM micrographs of MED Ni–Mo alloy deposited under different conditions of magnetic field intensity: a) $B = 0$ T, b) $B = 0.1$ T, c) $B = 0.2$ T, d) $B = 0.3$ T and e) $B = 0.4$ T (applied perpendicular to the flow of metal ions)	150
Figure 8.3	XRD patterns of Ni–Mo alloy coatings deposited at different magnetic field intensity, in comparison with ED coating (deposited at $B = 0$ T)	151
Figure 8.4	Potentiodynamic polarization behavior of MED Ni–Mo alloy coatings, deposited under varying magnetic field intensity B , using the same bath at same c.d.	152
Figure 8.5	CV curves of MED Ni–Mo alloy coatings, showing the increase in cathodic peak current density (i_{pc}) with magnetic field intensity for HER.....	155
Figure 8.6	CP curves of MED Ni–Mo alloy coatings in comparison with ED Ni–Mo alloy coating under impressed cathode c.d. of -300 mA cm^{-2} with the volume of H_2 evolved in 300 s on each test electrodes are shown in the inset.....	156
Figure 8.7	Diagrammatic representation showing decrease in the thickness of EDL from δ_0 to δ_D , due to the effect of induced magnetic field (Ebadi et al. 2010)	157
Figure 9.1	SEM images of Ni–Mo–rGO composite coatings deposited from optimal bath at (a) 1.0 A dm^{-2} (b) 4.0 A dm^{-2} displaying irregularly shaped graphene layers embedded in Ni–Mo alloy matrix; (c) and (d) are magnified images showing layers of graphene and encapsulated alloy nodules on the graphene network.....	164
Figure 9.2	EDX spectrum of the composite coating developed at 1.0 A dm^{-2} showing the peaks for Ni, Mo, and C.....	165
Figure 9.3	Survey spectrum (a) and high-resolution spectrum of Ni 2p (b), Mo 3d (c) and C 1s (d) of Ni–Mo–rGO and Ni–Mo coatings.....	166
Figure 9.4	XRD patterns of Ni–Mo–rGO composite coatings deposited at different c.d.'s	167

Figure 9.5	XRD patterns of Ni–Mo alloy and Ni–Mo–rGO composite coatings deposited at 4.0 A dm^{-2} , along with the XRD pattern of rGO shown in the inset.....	168
Figure 9.6	Potentiodynamic polarization curves of Ni–Mo–rGO composite coatings deposited at different c.d.'s	169
Figure 9.7	Comparison of Tafel curves of Ni–Mo alloy and Ni–Mo–rGO composite coatings developed at same c.d.	170
Figure 9.8	Cyclic voltammograms of Ni–Mo–rGO coatings deposited at different c.d.'s showing their cathodic peak current density, i_{pc} for HER.....	173
Figure 9.9	Comparison of CV curves for HER on the surface of Ni–Mo alloy and Ni–Mo–rGO composite coatings deposited at same c.d. (1.0 A dm^{-2})	174
Figure 9.10	Chronopotentiograms of Ni–Mo–rGO composite coatings, deposited at different c.d.'s under impressed cathodic current of -300 mA cm^{-2} with the volume of H_2 evolved in 300 s on each test electrodes are shown in the inset.....	175
Figure 9.11	CP curves at -300 mA cm^{-2} recorded for Ni–Mo alloy and Ni–Mo–rGO composite coatings developed at 1.0 A dm^{-2} . The inset chart shows the volume of H_2 liberated in 300 s on each of the electrodes.....	176
Figure 10.1	Histogram showing the corrosion rates of Sn–Ni and Ni–Mo alloy coatings, deposited under different conditions of electrodeposition (from the respective baths given in Table 10.1)	182
Figure 10.2	Histogram showing the electrocatalytic activity of Sn–Ni and Ni–Mo alloy coatings, expressed in terms of their cathodic peak current density (i_{pc}) developed through different mode of electrodeposition, from their respective bath for the same duration of time	184

List of Tables

Table 3.1	List of common chemicals used in the present research work.....	50
Table 3.2	Composition of the electro-cleaning bath used for cleaning the substrate.....	51
Table 4.1	Composition and operating parameters of optimized Sn–Ni alloy bath.....	67
Table 4.2	Coating characteristics of monolayer Sn–Ni alloy coating developed at different c.d.'s	72
Table 4.3	Effect of applied magnetic field intensity, B on deposit characters of Sn–Ni alloy electrodeposited from optimal bath at 298 K.....	79
Table 5.1	Corrosion data of SED Sn–Ni alloy coatings developed at different conditions of ultrasound p.d., at constant c.d. of 1.0 A dm^{-2} , from the optimal bath.....	91
Table 5.2	Corrosion data for SED multilayer Sn–Ni alloy coatings having a different number of layers, deposited from same bath keeping other parameters constant, like c.d. = 1.0 A dm^{-2} , ultrasound p.d. = 0.9 W cm^{-2}	98
Table 6.1	Composition, hardness, thickness and electrochemical corrosion parameters of Sn–Ni alloy coatings deposited on copper, at different c.d. from the optimal bath.....	113
Table 6.2	Electrocatalytic kinetic parameters for HER and OER, determined on as-deposited Sn–Ni alloy coatings, deposited on copper from the optimal bath.....	113
Table 6.3	Electrochemical parameters for HER of as-deposited Sn–Ni coatings developed at different c.d.'s from the optimal bath.....	116
Table 6.4	Electrochemical parameters for OER on as-deposited Sn–Ni alloy coatings developed at different c.d.'s from the optimal bath.....	119
Table 6.5	AFM parameters of Sn–Ni alloy coatings deposited at 4.0 A dm^{-2} before and after electrochemical dissolution.....	122
Table 6.6	Electrocatalytic parameters of CV and CP study for HER in 1.0 M KOH on Sn–Ni alloy, deposited at 4.0 A dm^{-2} under different conditions.....	124

Table 7.1	Composition and deposition conditions of the optimized Ni–Mo bath..	130
Table 7.2	Corrosion data, like E_{corr} , i_{corr} and CR of Ni–Mo alloy, electrodeposited at different c.d., from the optimal bath.....	136
Table 7.3	Kinetic parameters for HER and OER on Ni–Mo electrode in 1.0 M KOH solution, obtained from the potentiodynamic polarization curves.....	137
Table 7.4	HER parameters of Ni–Mo alloy deposits, developed at different c.d.’s from the optimal bath.....	138
Table 7.5	Electrode kinetic parameters of OER on the surface of Ni–Mo alloy coatings electrodeposited at different c.d.’s from the optimal bath.....	142
Table 8.1	Corrosion data of MED Ni–Mo alloy coatings deposited at the different intensity of applied magnetic field B , using the same bath at same c.d...	153
Table 8.2	Electrocatalytic kinetic parameters for HER on MED Ni–Mo coatings, deposited at different magnetic field intensity B , using the same bath at same c.d.	154
Table 8.3	Electrocatalytic parameters for HER on MED Ni–Mo coatings developed at different magnetic field strength B , from the same optimal bath at same c.d.	155
Table 9.1	Composition and deposition conditions of the optimized Ni–Mo–rGO bath.....	163
Table 9.2	Elemental composition of Ni–Mo–rGO coatings deposited at different c.d.’s from the optimal bath.....	165
Table 9.3	Scherrer’s equation parameters of Ni–Mo and Ni–Mo–rGO composite coatings.....	169
Table 9.4	Corrosion parameters like E_{corr} , i_{corr} and CR’s of Ni–Mo–rGO composite coatings deposited at different c.d.’s, using same optimal bath.....	170
Table 9.5	Kinetic parameters obtained from the cathodic polarization curves for HER on Ni–Mo–rGO composite coatings developed at different c.d.’s	171
Table 9.6	Comparison of Tafel slope (β_c) exchange current density (i_o) and cathodic overpotential (η_c) of Ni–Mo alloy and Ni–Mo–rGO composite coatings deposited at 1.0 A dm ⁻² and 4.0 A dm ⁻²	172

Table 9.7	HER parameters of Ni–Mo–rGO coatings developed at different c.d.’s from the optimal bath.....	173
Table 10.1	Composition and operating parameters of binary alloy baths for deposition of uniform alloy coating.....	180
Table 10.2	Comparative account of CR’s and other deposit characters of conventional electrodeposited monolayer Ni–M alloy coatings, developed from their optimal baths (given in Table 10.1)	181

A. LIST OF ABBREVIATIONS

AC	Alternate current
AFM	Atomic force microscopy
c.d.	Current density
CMMA	Composition modulated multilayer alloy
CP	Chronopotentiometry
CR	Corrosion rate
CV	Cyclic voltammetry
CVD	Chemical vapor deposition
DBT	Dual bath technique
DC	Direct current
ED	Conventional electrodeposition
EDL	Electrical double layer
EDXA	Energy dispersive X-ray analysis
EIS	Electrochemical impedance spectroscopy
HER	Hydrogen evolution reaction
MED	Magneto-electrodeposition
MHD	Magneto-hydrodynamic
MS	Mild steel
OCP	Open circuit potential
OER	Oxygen evolution reaction
p.d.	Power density
PVD	Physical vapor deposition
rGO	Reduced graphene oxide
SBT	Single bath technique
SCE	Saturated calomel electrode
SED	Sono-electrodeposition
SEM	Scanning electron microscopy
wt. %	Weight percentage
XPS	X-ray photoelectron spectroscopy
XRD	X-ray diffraction

B. List of Symbols

$A\text{ cm}^{-2}$	Ampere per centimeter square
$A\text{ dm}^{-2}$	Ampere per decimeter square
B	Magnetic field intensity
C_{dl}	Capacitance double layer
E^0	Standard electrode potential
E_{corr}	Corrosion potential
F_L	Lorentz force
i_{corr}	Corrosion current density
i_o	Exchange current density
i_{pa}	Anodic peak current density
i_{pc}	Cathodic peak current density
mA	Milliampere
mV	Millivolts
R_a	Mean roughness
R_{ct}	Charge transfer resistance
R_o	Pore resistance
R_P	Polarization resistance
R_q	Root mean square roughness
R_s	Solution resistance
β_a	Anodic Tafel slope
β_c	Cathodic Tafel slope
δ	Diffusion layer thickness
η_a	Anodic overpotential
η_c	Cathodic overpotential

CHAPTER 1

CHAPTER 1

INTRODUCTION

This chapter gives an overview of basic concepts of electroplating technology and various advanced methods of electrodeposition for enhanced alloy properties. It also gives a brief introduction to corrosion and corrosion measurement techniques, with a detailed account on water splitting application.

A wide range of metallic objects which we use in our day-to-day life, in most cases have a limited lifetime due to environmental effects and operating conditions. There are usually mechanical interactions between components in contact with one another, or there will be chemical or electrochemical reaction with the environment. In the worst case, this can lead to a catastrophic breakdown, hazardous both for humans and the environment. The surface of any material or component, because of its atomic structure is more vulnerable to various types of attack, and it could be mechanical, chemical, electrochemical or thermal, in nature. The effects may be present individually or in combination. They may arise as a tension, or as an impact or perhaps intermittently. Hence, one can protect the surface from environmental attack by application of organic, inorganic or metallic coatings, which extends the life of not just the surface, but the entire component or equipment. In this regard, *Metal Finishing* is a term embracing the surface treatment in which a metallic coating is formed from an aqueous solution or a molten salt by means of an electrochemical reaction. The properties of such coatings are determined by the deposition process as well as pre-treatment and post-treatments involved (Kanani 2006).

1.1 ELECTROPLATING TECHNOLOGY

Basically, electroplating technology is based on the phenomenon of electro-crystallization, controlled by the rate of mass transfer of metal ions towards the cathode. The process of electrodeposition relies on electrical currents to coat the material on a substrate, called cathode with positive cations transferred from the positively charged electrode (anode), or a bath. On applying the electric charge, oxidation takes place at the anode to produce metal ions, which is then reduced as metal atom on the cathode. All electroplating processes are governed quantitatively by Faraday's laws, with

allowance for side effects, which most frequently consist in the release of hydrogen along with the metal on the surface of the article being coated. Qualitatively, these processes are controlled by the type and composition of the electrolyte and by the mode of electrolysis, i.e. current density as well as temperature and the intensity of mixing. Electroplating can be defined as a treatment that modifies the surface of a metal or non-metal, without changing its bulk properties, in order to increase the specific properties including corrosion resistance. Strong adherence of the coating can be ensured by proper preparation of the surface of the base metal, which involves the complete removal of oxides and grease impurities by pickling or degreasing.

One of the common purposes of electroplating is to improve the corrosion resistance and wear resistance of friction surfaces to the finished or semi-finished articles. It is used for both protective and decorative finishing of surfaces (chromium or nickel plating, or plating with precious metals). Compared to many methods of applying coatings used since ancient time, electroplating has a number of advantages, particularly when only a very thin coating is required (Lowenheim 1974).

1.2 ALLOY DEPOSITION

It is well stated that properties of alloy deposits are superior to those of single-metal electroplates, and are widely described in the literature (Brenner 1963). In other words, it is recognized that more often than not, alloy deposition provides properties not obtained by employing electrodeposition of single metals. It is further asserted that relative to the single-component metals involved, alloy deposits can have different properties in certain composition ranges. They can be denser, harder, more corrosion resistant, more protective of the underlying base metal, tougher and stronger, more wear resistant, superior with respect to magnetic properties, more suitable for subsequent electroplate overlays and conversion chemical treatment, and superior in antifriction applications (Paunovic and Schlesinger 2006). Alloy plating technology is of a particular interest as the current trend in engineering and technology, supports the replacement of individual metals by their alloys, which usually feature a wider spectrum of properties. In fact, alloy plating is technically a more complicated process as compared to the deposition of individual metals, as it requires a more stringent control

of the composition of electrolyte, deposition conditions as well as closer monitoring of those parameters.

Electrodeposited alloys find a wide range of applications in electronics, surface finishing industries, and automobile industries. A large number of binary and ternary alloys have been plated from aqueous solutions, for microfabrication or surface coating (Kanani 2006). The compositions of electrodeposited alloys are governed by the kinetics of the partial electrode reactions, and it can be modeled in terms of mixed potential theory, commonly used in corrosion science (Landolt 2002). The ultimate goal of research in the electroplating technology is to investigate how to produce plated films with desirable properties, like mechanical, physical, and chemical which meet particular applications (Watanabe 2004).

1.3 ORIGIN OF ELECTROPLATING

Several key inventions have taken place before the discovery of electroplating, which played an important role in its development. As early as 1800, Alessandro Volta invented the voltaic pile, a row of voltaic cells that create an electric current, the first electric battery. Relying on Volta's voltaic pile as a main source of electricity, the Italian chemist Luigi Brugnatelli invented electroplating in 1805. His early attempts in electroplating evolved until he successfully plated a thin layer of gold onto silver coins. Despite the publication of his findings in the *Belgian Journal of Physics and Chemistry*, his research was not taken seriously due to Napoleon Bonaparte and the French Academy of Sciences. It wasn't until similar research surfaced almost forty years later, that process began to change. Faraday discovered electromagnetic induction in 1831 and Pixii used the commutator in 1832 to produce a direct current generator, but it was not until about 1870 that several independent inventors used electromagnetic field coils to generate the heavy currents needed for electrolysis. Large scale electroplating enterprises were established by the latter part of the 19th century. Aqueous solutions have always been by far the most important electrolytes. There have been many investigations of non-aqueous solutions or ionic melts, and Davy deposited the alkali metals from the latter in 1807 (Gabe et al. 1994).

Although electroplating is patented by the Elkingtons, it stretched quickly and successfully across Europe, and process remained relatively unchanged until the 1940s,

when a surge in the electronics industry led to the replacement of traditional cyanide solutions with safer acid baths, at least on the commercial level. The 1970s saw the development of safer water disposal regulations and continual hardware upgrades, which streamlined the process by enabling faster and more efficient electroplating. Today, electroplating technology has developed in both evolutionary and revolutionary ways and made it possible to electroplate a wide range of materials, including platinum and osmium.

1.4 PRINCIPLE OF ELECTROPLATING

Electroplating is generally carried out in a specially designed electrolytic bath, containing the desired metals ions, suspended in a solution. The solution of plating bath serves as a conductive medium and utilizes the DC (direct current). The material that is to be plated is submerged into the plating bath, and a low voltage DC is applied to the bath. The material to be plated acts as a negatively charged cathode, and the coating metal as positively charged anode, which completes the DC circuit. Electrodes are carefully positioned at the ends of the plating tank, as shown schematically in Figure 1.1.

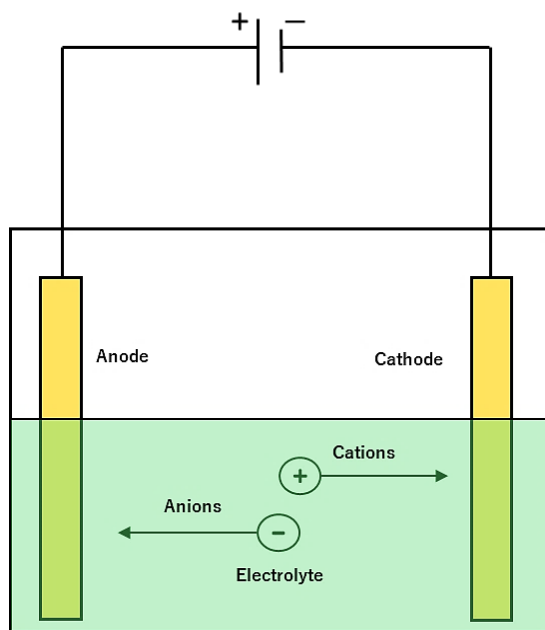


Figure 1.1 – Basic components of DC electroplating

Electrodes are connected to a DC power source, to drive the process of deposition. As electrical current flows (from positive to negative) in the circuit, the cations formed at anode flow through electrolyte towards negatively charged cathode; and anions from

the electrolyte solution move towards the cathode. This movement causes the metal ions in the bath to migrate towards extra electrons located at the cathode's surface. Thus, due to induced DC, metal ions are taken out of solution and are deposited as a thin layer of metal atoms onto the surface of the cathode. When the overall reaction is controlled solely by the rate at which the electroactive species (including metal ions) reach the surface, the current is said to be mass transport limited. Mass transport process in electrolyte solution occurs in three different modes (Wang 2000):

- *Diffusion* – the spontaneous movement of the metal ions under the influence of concentration gradient, taking place to minimize the concentration differences.
- *Convection* – transport of ions towards electrode by a gross physical movement; such fluid flow occurs with stirring or flow of the solution and with rotation or vibration of the electrode (i.e., forced convection) or due to density gradients (i.e., natural convection);
- *Migration* – movement of charged particles under the influence of an electric field.

Generally, in an electrode, the inner layer (region closest to the electrode), known as the *inner Helmholtz plane*, contains solvent molecules and specifically adsorbed ions. The next layer, *the outer Helmholtz plane*, reflects the imaginary plane passing through the center of solvated ions at their closest approach to the surface, as shown in Figure 1.2. The solvated ions are non-specifically adsorbed and are attracted to the surface by long-range Coulomb forces. The discharge of adsorbed ions to form adsorbed atoms takes place within the *Electrolyte double layer* called the *Helmholtz double layer*, which forms spontaneously at the metal-solution interface. Although the metal ions lose most of their charge in this process, the residual charge remains on it, and are adsorbed as atoms. During electrodeposition, metal ions are discharged as metal atoms at *Electrical Double Layer* (EDL), or cathode film through the process of nucleation, followed by its crystal growth. Nucleation results from diffusion controlled migration of the adsorbed atoms on the surface. The growth process begins once the nuclei have reached a critical size, and this process is called electro-crystallization (Schwarzacher 2006). Thus, the property of any electrodeposit, in terms of its

composition, phase structure, and surface morphology depends on the rate of electrocrystallization taking place at cathode film, which is determined by the rate of mass transfer of metal ions towards the cathode. Hence, it may be summarized that the property of any electrodeposit can be altered by modulating the mass transport process towards the cathode.

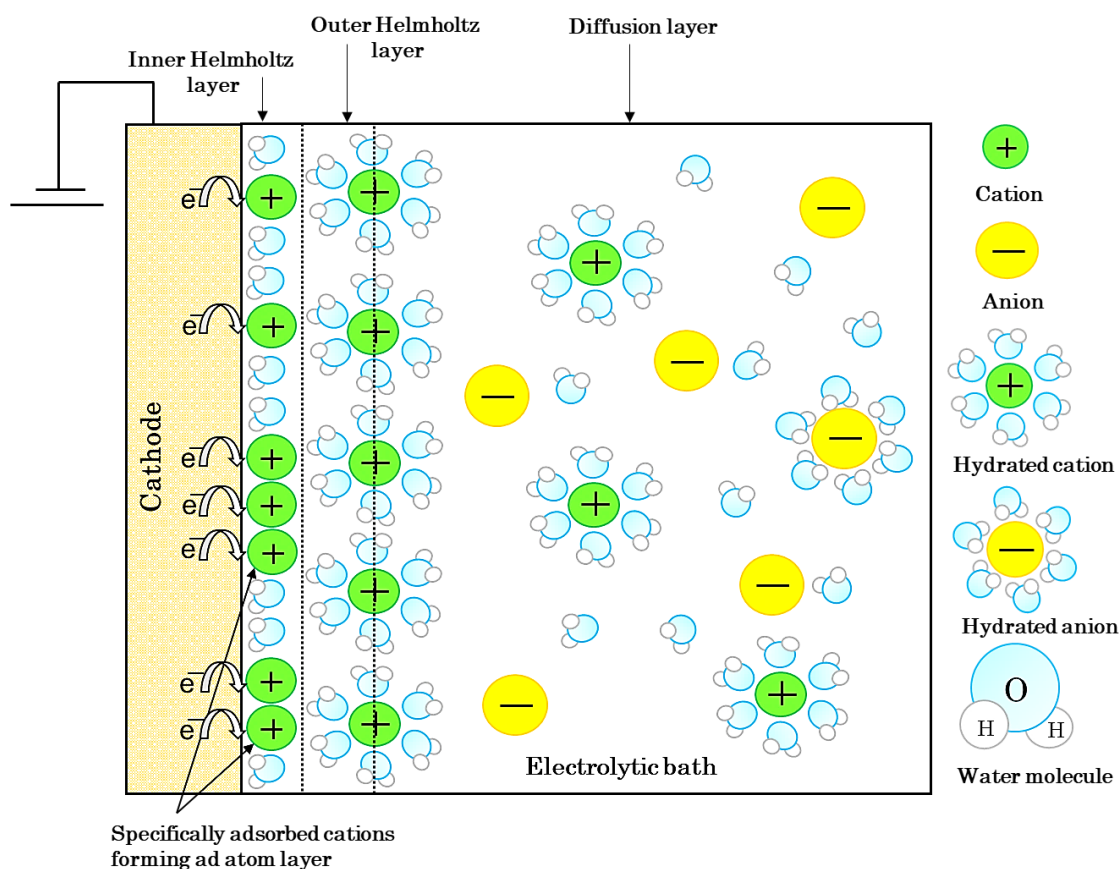


Figure 1.2 – Illustration of a fundamental cathodic electrodeposition process for a single constituent metal salt dissolved in an aqueous electrolyte (Ray 2015)

1.4.1 Faraday's Laws of Electrolysis

All processes of electrodeposition are governed by the most fundamental laws of electrochemistry, called Faraday's laws of electrolysis. According to which, the extent of deposition or dissolution of a metal/alloy is determined by the quantity of electricity passed, and its equivalent mass. The two laws of electrolysis can be summarized as below (Kelly et al. 2002).

First Law of Electrolysis

The mass, m of a metal/alloy discharged at an electrode by electrolysis is directly proportional to the amount of electrical charge passed through the electrode.

$$m = ZQ \text{ or } m = ZIt \quad (1.1)$$

where Q = electric charge in coulombs, I = current in amperes, t = time in seconds, m = mass of the product discharged at the electrode in grams, Z = electrochemical equivalent.

Second Law of Electrolysis

If the same amount of electrical charge is passed through several electrodes, the mass, m of the substances discharged at the electrodes are directly proportional to their equivalent masses.

$$\frac{m_1}{m_2} = \frac{Z_1}{Z_2} \quad (1.2)$$

1.5 MODERN METHODS OF ELECTRODEPOSITION

Electrodeposition is a well-known surface coating technique in which coating property can be tuned by altering the size and shape of the microcrystals. A common method to manipulate crystal size is to employ a growth medium, having certain additives which can preferentially adsorb on specific crystallographic planes. Therefore, the property of any electrodeposit, of a metal/alloy can be modified by changing the mass transport process of metal ions towards the cathode. This can be coupled with periodic modulation of such mass transport process. Modern methods of electrodeposition enabled the development of metals and alloys in multilayers for better properties. The improved property of multilayer coatings is attributed to increased interfacial surface area. Thus, development of modern multilayer alloy coating and its improved material property are attributed by the following facts, respectively:

- Periodic modulation in mass transport process at cathode film brings a periodic modulation in the composition of the coatings deposited.
- Materials' property can be increased substantially by increasing its surface area, through layering.

The increase of the surface area leads to an increase of material property, which is the basis of nanotechnology. The composition of alloy coatings can be changed by bringing modulation in the mass transport process, which can be affected by alerting periodically any of the following parameters during deposition. They are:

- Cathode current density – leads to coatings in multilayers
- Magnetic field intensity – leads to magneto-electrodeposition
- Sonication (agitation) – leads to sono-electrodeposition

1.5.1 Composition Modulated Multilayer Coatings

The concept of composition modulated multilayer coatings (CMMCs) has now created a high level of interest in surface engineering (Kanani 2006). This subject area is one that abounds with terminology, with the coating systems produced often being described as composition modulated alloy (CMMA) coatings, multilayer coatings or just layered coatings (Wilcox 2003). The concept of CMMA coating is relatively new and is gaining interest amongst researchers because these layered coatings possess improved properties, such as increased strength, microhardness, wear and corrosion resistance, electrical and magnetic properties. Here, the term multilayer is taken to mean a sequence of alloys of same metals, but of different composition deposited alternately one above the other till required thickness is reached. This multilayer alloy coatings can be electrodeposited from the same bath having both metal ions by periodic modulation of the cathodic current density (c.d.) between two set values; and such deposition allows the growth of coatings, having a periodic modulation in their composition. They can be individual pure metals or two different compositions of the same alloy. The individual layer thicknesses are often on the nanometre scale, this, therefore, limits the deposition for all type of coatings. In reality, there are probably only three main methods of multilayer coating which have been widely utilized. They are chemical vapor deposition (CVD), physical vapor deposition (PVD) and electrodeposition. Clearly, each of the three processes has its own advantages and disadvantages but most researchers tend to use electrodeposition method as it is the most simple and flexible of the three. Figure 1.3 illustrates a typical CMMA system where Alloy A and Alloy B, are different in composition.

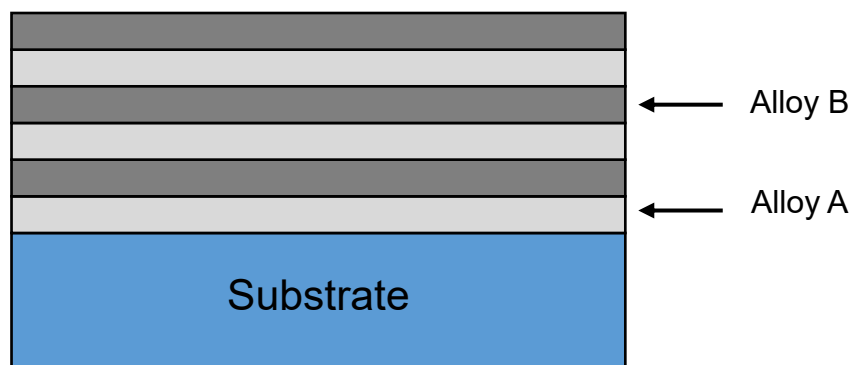


Figure 1.3 – Representation of a typical CMMA coating

Under electrodeposition method, CMMA coatings can be obtained by using either a single-bath technique (SBT), where deposition takes place in a plating solution containing ions of the alloy components, or a double-bath technique (DBT), where deposition is carried out from separate plating baths by using manual/automated transfer of the substrate from one bath to another. Both techniques are known to have their own advantages and disadvantages. Generally, in SBT the metal ions required to form both deposit layers are contained in a single electrolyte, and alloy deposition is achieved by modulating alternately the mass transport process at EDL (Cohen et al. 1983, Yahalom 1987, Haseeb et al. 1994). Even though substantial success has been achieved in SBT, the selection of constituents is limited because their deposition potentials must be sufficiently different to allow a separate electrodeposition of each layer. Difficulties can also be encountered in the deposition of very thin layers due to very short relaxation time for the redistribution of solutes in the diffusion double layer (Thangaraj et al. 2009).

1.5.2 Magneto-electrodeposition

Mass transport of ions towards electrode surface can be controlled through diffusion, ionic migration, and convection (natural and forced). Natural convection depends on the geometric configuration of the working electrode and forced convection can be generated by various means, like stirring, rotating disc or by inducing the magnetic field during deposition. The process of deposition of a metal/alloy by electric current in the presence of applied magnetic field is known as *magneto-electrolysis* or *magneto-electrodeposition*. When magnetic field is applied to the cathode surface, there is an

increase in rate of transport of ions to the electrode surface, thus increasing the mass transport current of the electrode reaction, explained by *magneto-hydrodynamic* (MHD) effect (Ebadi et al. 2010), induced by maximal Lorentz force generated in the hydrodynamic layer as shown in Figure 1.4.

When a magnetic field is applied to an electrolytic bath, the total force acting on a moving charged particle, like electron or an ion is given by the relation,

$$F_L = q(E + v \times B) \quad (1.3)$$

Where, F_L is the Lorentz force, q the charge of an ion, E the electric field strength, v the velocity of the ions and B , the magnetic field intensity. The Lorentz force is vector product of current density, i and magnetic field intensity, B .

$$\vec{F}_L = \vec{i} \times B \quad (1.4)$$

The Lorentz force, in reality, induces the convection flow of the electrolyte near the electrode surface, depending on the direction of applied magnetic field (parallel or perpendicular), with respect to the direction of movement of the ions. When a magnetic field is applied parallel to the plane of the cathode, i.e. perpendicular to the direction of flow of ions the Lorentz force exerted is found to be its maximum. The magnetic field applied to charge carriers in the electrolyte solution induces a convective flow. This increase in the rate of mass transport was attributed to the formation of a hydrodynamic boundary layer at the electrode surface due to the tangential velocity induced by the field that actually decreases the diffusion layer thickness and increases the flux of the species. Thus, magnetically induced convection reduces the thickness of Nernst diffusion layer (or EDL) and thereby enhancing the limiting current density (i_L) (Hinds et al. 2001).

The benefits of large-scale convection can be more effectively achieved by mechanical agitation as well. The combined effect of magnetic field and local current density (i) is responsible for changing the flow patterns on a scale that would be otherwise unattainable. The effect is observed to be more at sharply localized spots of high current density, due to high micro-MHD effect (Figure 1.4 (c)). As c.d. is inevitably non-uniform at the edge of an electrode, there is normally an MHD flow around the rim when a magnetic field is perpendicular to the electrode surface

(Figure 1.4 (b)). Furthermore, uneven growth at the cathode during electrodeposition produces a locally non-uniform current distribution, giving rise to secondary micro-MHD vortices around growing asperities that protrude into the diffusion layer, as illustrated in Figure 1.4 (c).

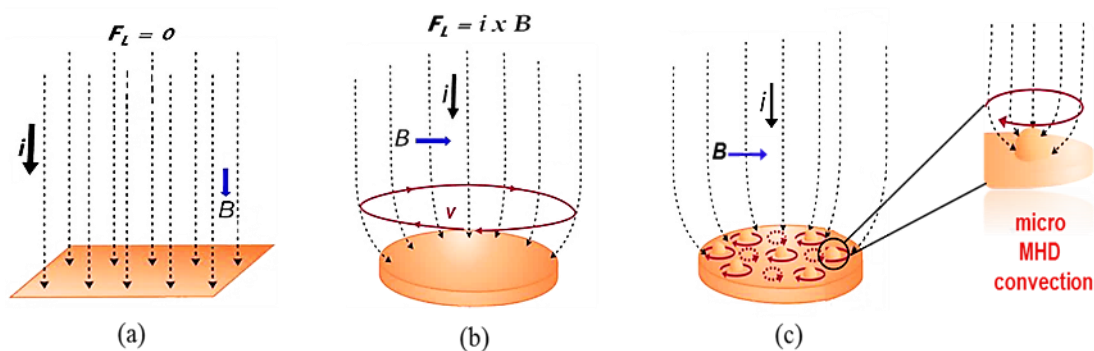


Figure 1.4 – Hydrodynamic flow on electrode surface due to the applied magnetic field (B), where: a) B is parallel to the movement of ions, b) B is perpendicular to the direction of ions, and c) the primary MHD flow causes the vortex at spots of high c.d. leading to micro-MHD convection (Monzon and Coey 2014)

Hydrogen bubble formation and its release during the process of electrodeposition, due to electrolysis of water is strongly influenced by magnetically-induced flow. Gas bubbles occlude the electrode surface, deforming the local current density. At electrodes where the average current distribution is uniform, generally, the bubbles released are smaller when a magnetic field is present. This is beneficial during electrodeposition, as the films produced are devoid of defects, due to hydrogen evolution. Even when the field is parallel to the direction of ion flow and MHD is negligible, there are still micro-MHD flows arising from the deformation of the current distribution by the spherical bubbles, which induce hydrodynamic drag forces that sweep the bubbles away from the electrode surface, thereby impeding their growth. Besides enhancing the deposition rate via, the MHD effect, there are many studies which show the influence of magnetic fields on the morphology, texture, roughness and dendritic character of electrodeposits (Monzon and Coey 2014).

1.5.3 Sono-electrodeposition

The part of the sonic spectrum which ranges from about 20 kHz to 10 MHz is called ultrasound, and it can be subdivided into three main regions: power ultrasound (20–100 kHz), high-frequency power ultrasound (100 kHz–1.0 MHz) and diagnostic ultrasound (1.0–10 MHz) (Peters 1996). When power ultrasound is applied to a liquid electrolyte, a number of well-known effects occur that can influence an electrochemical process. In particular, micro-jetting or microstreaming can improve the mass transport, thereby thinning of diffusion layers and generate localized heating. Such benefits can be used to enhance two widely used electrochemical metallization processes, namely, electroplating and electroless plating. Power ultrasound enhances chemical and physical changes in a liquid medium through the generation and subsequent destruction of cavitation bubbles. Like any sound waves, ultrasound is propagated via a series of compression and refraction waves induced in the molecules of the medium through which it passes. At sufficiently high-power density, the rarefaction cycle may exceed the attractive forces of the molecules in the liquid, and cavitation bubbles will form. These cavities when the collapse in succeeding compression cycles, which generates the energy for chemical and mechanical effects. This is a remarkable phenomenon induced throughout the liquid at ultrasonic frequencies, i.e. 20 kHz or above (Mason and Cordemans 1996). The variety of induced effects on electrochemistry processes by ultrasound waves can be attributed to the generation, growth, and collapse of microbubbles in the electrolyte. All these phenomena lead to the decreasing of the diffusion layer thickness and can improve the overall mass transport, increasing reaction rates, indeed of cleaning and degassing of the electrode surface (Sáez and Mason 2009).

Two forms of cavitation are known: stable and transient. Stable cavitation means that the bubbles oscillate about their equilibrium position over several refraction-compression cycles, while in transient cavitation, the bubbles grow over one (sometimes two or three) acoustic cycle to double their initial size and finally collapse violently. Thus, created motion in the ions due to cavitation force causes the ions to move towards the cathode surface. The schematic representation of a typical flow pattern induced by a sonic horn, cavitation collapse at an electrode and in bulk solution

is given in Figure 1.5 (a), (b) and (c) respectively. Cavitation at the solid-liquid interface occurs more readily than in bulk solution, where crevices and active sites exist and vapor bubbles forms readily. When transient cavitation occurs near a solid surface such as an electrode, collapse becomes non-spherical driving a high-speed liquid jet into the surface in the perpendicular direction (see Figure 1.5 (b)) (Banks and Compton 2003). At the same time, if ultrasound intensity is higher than that of threshold intensity, collapsed bubble will generate shock waves and microstreaming. As a result, the thickness of diffusion layer decreases with increased mass transport reaction rates. Thus, in general when ultrasound is applied to liquid media, a range of processes occur which can create unusual physical and chemical conditions; these include acoustic streaming, turbulent convection, microstreaming in the presence of oscillating bubbles and cavitation, as shown in Figure 1.5.

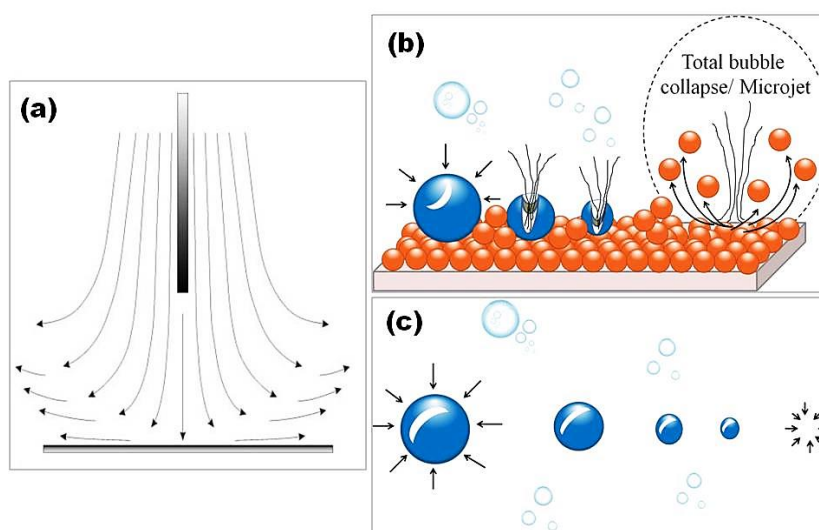


Figure 1.5 – Effect of ultrasound on liquid medium showing: a) Acoustic streaming: a typical flow pattern induced by sonic horn, b) Cavitation collapse at an electrode surface and c) Cavitation bubble collapse in bulk solution (Banks and Compton 2003)

1.6 WATER ELECTROLYSIS

With ever increasing energy costs owing to the dwindling availability of petroleum resources, concerns with global warming and climate change blamed on man-made carbon dioxide (CO₂) emissions associated with use of fossil fuels, hydrogen has in recent years become very popular for a number of reasons: *i*) it is perceived as a clean fuel, emits almost nothing other than water at the point of use; *ii*) it can be produced

using any energy sources, with renewable energy being most attractive; *iii*) it works with fuel cells and together, they may serve as one of the solutions to the sustainable energy source in so-called “hydrogen economy” (Zhang and Zeng 2010).

There are many processes that produce hydrogen, one such process being fossil fuel reforming, mainly from methane, however, it will lead to substantial environmental pollution. On the other hand, hydrogen production by the electrolysis of an aqueous solution could use only renewable energy throughout the process, making it economically and environmentally attractive.

Electrolytic water splitting was the first electrochemical process to be performed. It is the decomposition of water (H_2O) into oxygen (O_2) and hydrogen gas (H_2) due to an electric current being passed through the water. Historically, the first experiment on water electrolysis was attributed to Nicholson and Carlisle, who in 1800 using the newly invented Volta’s pile, observed the formation of gaseous products in the laboratory (Trasatti 1999). Despite such an early observation, the production of hydrogen by water electrolysis on an industrial scale dates back only to the beginning of the 1900s, with the increasing need for large amounts of hydrogen for ammonia synthesis. At that time, water electrolysis was the most economic among the chemical processes able to produce hydrogen with purity close to that necessary for the catalytic synthesis of ammonia. Reasons were the low cost of hydroelectric power and the flexibility of the process itself that allowed the use of seasonal peaks of electric power. Actually, the electrolytic method was largely applied until the mid-1900s, when the rising costs of electric power and the abundant availability of hydrogen from natural hydrocarbons confined the use of electrolytic hydrogen to cases where the purity of hydrogen is a necessary requirement, such as in the pharmaceutical industry, hydrogenation in the food industry and so on.

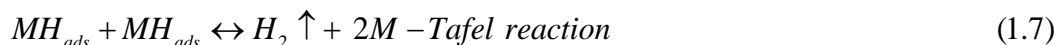
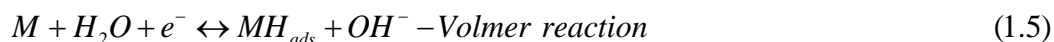
In the 1970s, a first serious energy crisis related to a sharp increase in the cost of fossil fuels led to a revival of interest in water electrolysis. This time the interest was focused on hydrogen as an energy vector that could possibly replace fossil fuels in the world economy. The aim was two folded, one is to become relatively independent of the influence of an oil market and the second one is to reduce the environmental impact of the use of fossil fuels whose combustion is responsible for the production of

‘greenhouse’ gases, such as CO₂ and NO_x, and of polluting compounds such as SO₂ (acid rain). In that scenario, the idea of a “hydrogen economy” was put forward, where hydrogen is the engine of the world producing electric power in fuel cells and replacing oil as a fuel in internal combustion engines (Marbán and Valdés-Solís 2007). However, the use of electric cars and of electrolytic hydrogen entails the consumption of large amounts of electricity to recharge batteries and to feed electrolyzers. The solution of this circle necessarily lies in the use of clean, renewable energy sources that also avoid the risk of exhaustion implicit in the use of fossil fuels. The water splitting reaction is considered to have two half-cell reactions, and they are hydrogen evolution reaction (HER) and oxygen evolution reaction (OER), both of which are essential for the overall efficiency of water splitting. It has been demonstrated that electrochemical water splitting can be completed both in acidic and alkaline media. But unfortunately, the acid electrolyzers are hindered due to lack of efficient and low-cost counter electrode catalysts in acidic electrolytes (Liu et al. 2017).

1.6.1 Hydrogen Evolution Reaction

Hydrogen is considered as the cleanest and most promising candidate to replace carbon-based fuels. However, the practical widespread application of water electrolysis is limited by its high-energy consumption. The energy consumption can be reduced by using more active electrode for HER. Platinum (Pt) and its alloys have a higher electrocatalytic activity for HER. However, issues related to their high cost and scarcity severely limits their usage. Hence, it motivated many researchers to find alternative Pt-free electrode systems (Zhang et al. 2017). In this regard, many efficient and inexpensive non-precious HER catalysts have been developed. The non-platinum-active metals such as Fe, Ni, or Co as well as their alloys and composites have received great attention as electrocatalysts for the HER.

HER in alkaline solution has received considerable attention in the application fields, such as hydrogen production, chlorine, and alkali production and electrochemical CO₂ reduction (Abbas et al. 2017). The HER mechanism in alkaline solution proceeds via three-step reaction mechanism (Tasić et al. 2013):



Where M represents the electrode material and MH_{ads} represents the hydrogen adsorbed on the electrode surface. The Volmer reaction is a primary reaction for HER, which produces adsorbed H atoms (H_{ads}) on the electrode surface by the discharge of H_2O . Subsequently, the adsorbed H_{ads} may react with H_2O in solution (Heyrovsky reaction) or other adsorbed H_{ads} on the electrode (Tafel reaction) to release H_2 , depending on the type of electrodes (Zhang et al. 2017). The overall reaction proceeds via two possible reaction pathways, Volmer-Heyrovsky and Volmer-Tafel.

1.6.2 Oxygen Evolution Reaction

The electrocatalytic oxygen evolution reaction (OER) at the anode often couples with electron or photoelectron CO_2 reduction and, H_2 evolution reactions at the cathode but limits the performance of the entire system because of the sluggish OER kinetics, insufficient reaction sites, or low stability of precious metal catalysts. OER is a demanding step that includes four proton-coupled electron transfers and oxygen–oxygen bond formation, so it is kinetically not favored and requires a catalyst to expedite the reaction (Kanan and Nocera 2008, Koper 2011). To date, RuO_2 is considered the most active catalyst for OER, but its high cost and low abundance has prevented its large-scale application as an OER catalyst (Lee et al. 2012). Thus, active, stable, and affordable OER catalysts are highly sought after.

OER is a reaction of generating molecular oxygen through several proton/electron-coupled processes. In acidic conditions, the reaction operates through oxidation of two water molecules (H_2O) into four protons (H^+) and one oxygen molecule (O_2) by losing a total of four electrons (Conway and Liu 1990). In basic conditions, oxidation of hydroxyl groups (OH^-) takes the lead and transforms into H_2O molecules and an O_2 molecule with the same four electrons involved (Birss et al. 1986).



The overvoltage of the OER has been identified as the greatest source of energy loss in water electrolysis, which can be alleviated by designing more efficient electrodes. In addition, during electrolysis operation, the anode can suffer corrosion processes resulting in higher overpotentials. This overpotential is directly related to the potential difference, necessary to drive the system at a given current density and therefore it has a tremendous impact on the cost of the hydrogen production (Pérez-Alonso et al. 2014). It is recognized that although nickel has OER overpotential higher than RuO₂ or IrO₂, nickel-based electrodes are relatively inexpensive and display excellent corrosion resistance in aqueous alkaline media, and thus offer an attractive compromise solution. That said, the OER electrocatalytic performance of metallic Ni in alkaline solution diminishes markedly with time. In view of the aforementioned considerations, extensive research focussed on the development of OER electrocatalysts that display a combination of the desired characteristics of long-term physical and chemical stability, satisfactorily low reaction overpotential and viable cost. (Lyons and Brandon 2008). Recent works have shown the advantage of using Ni-based alloys with transition metals (like Mo, Cu, Fe, V and Pt) due to the high adsorption ability of Ni atoms and also to the fact that the introduction of a transition metal alters significantly the electronic properties of the system (Pérez-Alonso et al. 2014).

1.7 ELECTROCHEMICAL POLARIZATION

Electrochemical polarization (usually referred as polarization) is the change in electrode potential due to the flow of a current. There are three types of polarization (Mc Cafferty 2010), they are:

- 1) Activation polarization.
- 2) Concentration polarization
- 3) Ohmic polarization

The degree of polarization is measured by the quantity, called *overvoltage* (over potential), η is given by the following equation:

$$\eta = E - E_0 \quad (1.10)$$

where E is the electrode potential for some condition of current flow and E_0 is the

electrode potential for zero current flow, also called as open-circuit potential (OCP) or rest potential.

1.7.1 Activation Polarization

When some step in the half cell reaction controls the rate of charge flow, the reaction is said to be under activation or charge transfer control, and activation polarization results. Hydrogen evolution on a metal surface occurs, in three major steps.



First H^+ reacts with an electron from the metal to form an adsorbed hydrogen atom, H_{ads} , at the surface.



Two of these adsorbed atoms must react in the second step to form the hydrogen molecule,



A third step requires sufficient molecules to combine and nucleate a hydrogen bubble on the surface. Any one of the above steps can control the rate of reaction and cause activation polarization. The relationship between activation polarization or overpotential η , and the rate of the reaction in terms of anodic and cathodic current density, abbreviated, respectively as i_a and i_c is given by,

$$\eta_a = \beta_a \log \frac{i_a}{i_o} \quad (1.14)$$

for anodic polarization, and

$$\eta_c = \beta_c \log \frac{i_c}{i_o} \quad (1.15)$$

for cathodic polarization.

Here, β_a and β_c are Tafel constants for anodic and cathodic reaction, respectively, and i_o is the exchange current density, corresponding to OCP, or overvoltage equal to zero. It is corresponding to the half-cell electrode potential E_{H^+/H_2} , is established, where reaction is at equilibrium. The rate of discharge of H^+ (forward) exactly balances the rate of ionization of H_2 (reverse). The presence of overpotential suggests the presence

of energy barriers (activation energies) ΔG_f^* and ΔG_r^* corresponding to forward and reverse reaction, is given by,

$$\Delta G_f^* - \Delta G_r^* = \Delta G_{H^+/H_2} = -nF e_{H^+/H_2} \quad (1.16)$$

On further substitution, one will arrive at the most celebrated equation of electrochemistry known as Butler-Volmer equation.

Butler-Volmer equation

The Butler-Volmer equation is one of the most fundamental relationships in electrochemical kinetics. It describes how the electrical current on an electrode depends on the electrode potential, considering that both cathodic and anodic reaction occurs on the same electrode. Butler-Volmer dependence of the electrode current (i) on activation polarization overpotential (η), where $\eta = (E - E_{equ})$ is given by relation,

$$i = i_c - i_a = i_o \left\{ \exp\left(\frac{\alpha_a n F}{RT} (E - E_{equ})\right)_f - \exp\left(-\frac{\alpha_c n F}{RT} (E - E_{equ})\right)_r \right\} \quad (1.17)$$

where E and E_{equ} are the electrode potentials (volts) under conditions of non-equilibrium and equilibrium, respectively. i_a and i_c are cathodic and anodic current density, i_o exchange current density, T is the absolute temperature in Kelvin, n is a number of electrons involved in the electrode reaction, F is Faraday constant, R is universal gas constant. α_c is cathodic charge transfer coefficient, and α_a is anodic charge transfer coefficient (both are dimensionless quantity). The diagrammatic representation of Butler-Volmer equation is as shown in Figure 1.6.

This form of Butler-Volmer equation is valid when the electrode reaction is controlled by electrical charge transfer at the electrode, not by the mass transfer to or from the electrode surface, from or to the bulk electrolyte. Nevertheless, the utility of the Butler-Volmer equation in electrochemistry is very wide, and it is often considered to be central in the *phenomenological electrode kinetics*.

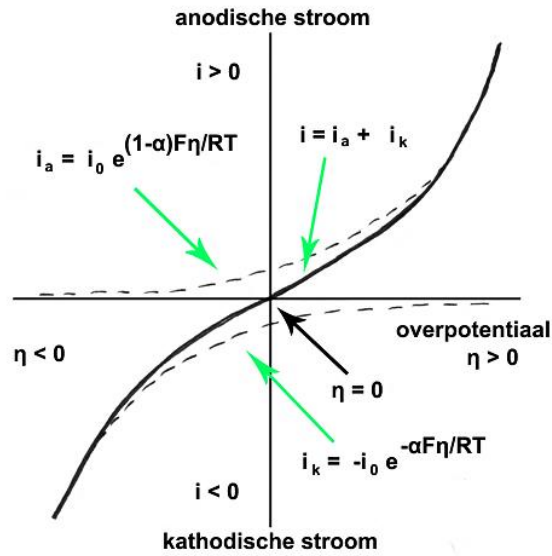


Figure 1.6 – Diagrammatic representation of Butler-Volmer equation

1.7.2 Concentration Polarization

At high rates of cathodic reaction, cathodic reduction rates deplete the adjacent solution for dissolved species being reduced. The concentration profile of H^+ ions (in place of M^{+n} ions) is shown schematically in Figure 1.7. Here, C_B is the H^+ concentration of the uniform bulk solution, and δ is the thickness of the concentration gradient in solution. The half-cell electrode potential (HCE) E_{H^+/H_2}^0 of the depleted surface is given by the Nernst equation as the function of H^+ concentration.

$$E_{H^+/H_2} = E_{H^+/H_2}^0 + \frac{2.303RT}{nF} \log \frac{[H^+]^2}{H_2} \quad (1.18)$$

It is apparent that the HCE potential E decreases as H^+ is depleted at the surface. This decrease in concentration amounts to the concentration polarization (η_{conc}) and is given by equation 1.19, as a function of current density (Jones 1996).

$$\eta_{conc} = \frac{2.303RT}{nF} \log \left[1 - \frac{i_c}{i_L} \right] \quad (1.19)$$

The plot of above equation, in Figure 1.8 (a) shows that η_{conc} is low until a limiting current density, i_L is approached. Limiting current density is the measure of maximum reaction rate that cannot be exceeded because of a limited diffusion rate of H^+ ions in solution. The limiting current density i_L is given by relation,

$$i_L = \frac{nFDC_B}{\delta} \quad (1.20)$$

Where D is diffusion coefficient of the reacting species, (it may be H^+ ions or any other species). δ is the diffusion layer thickness, C_B is the concentration of the electroactive (limiting) species in the bulk of the electrolyte. Hence, it may be noted that i_L increases with the increase of bulk concentration (C_B), D and high solution agitation, but decreases with δ , as shown in Figure 1.8 (b).

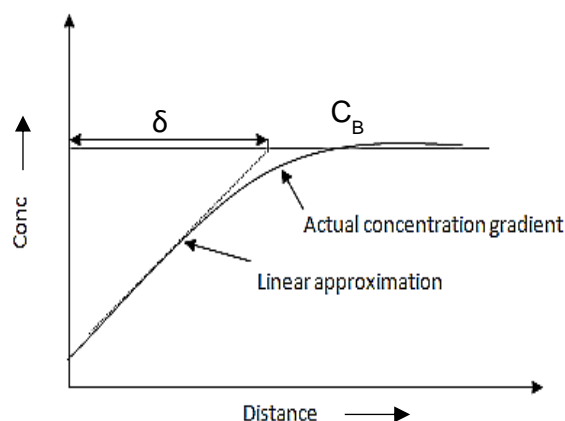


Figure 1.7 – Concentration of H^+ in solution near a surface controlled by concentration polarization

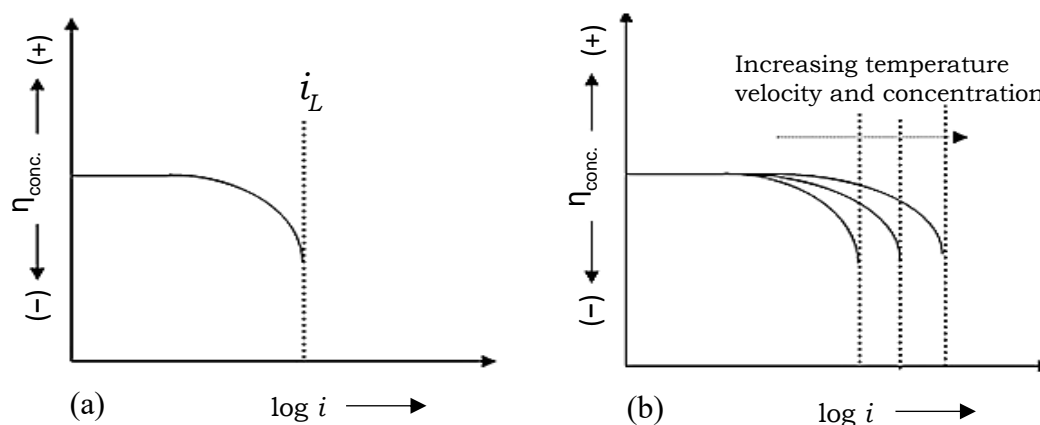


Figure 1.8 – Cathodic concentration polarization: (a) plotted vs. reaction rate or current density, and (b) effect of solution conditions

The concentration polarization for anodic oxidation, i.e. for corrosion, can usually be ignored due to an unlimited supply of metal atoms at the interface. Some concentration polarization of the anodic reaction is possible at very high corrosion rates or during intentional anodic dissolution by impressed currents (e.g. electrochemical

machining or electrorefining), when rates are limited by transport of soluble oxidation products away from the surface.

1.7.3 Ohmic Polarization

Ohmic polarization results from the pure resistance of elements along the current path within the solution. To minimize error due to such circuit elements, called iR drops, Luggin-Haber capillary tube is generally used. This method alleviates the problem of keeping the reference electrode directly at the electrode-electrolyte interface. The Luggin's tube, generally used in all electrochemical work is shown in Figure 1.9. The Luggin capillary and salt bridge connecting the cell and the reference electrode do not carry the polarizing current, and it serves the purpose of reducing the ohmic resistance gradient through the electrolyte between the working electrode and auxiliary/counter electrode. Ohmic polarization is observed either in the region of ionic conductivity, where current is transported by the movement of ions through the electrolyte from the anode to cathode or in the electronic conductivity region. The term iR solution is usually negligible for high-conductivity solutions, such as most aqueous solutions, but can be a problem for low-conductivity solutions, such as organic media, and for some soils. If the iR drop is due to the existence of a surface film on a metal, such as an oxide, hydroxide, oxyhydroxide or salt film, then they are usually understood to be the part of system and the electrode potential is considered to be that for the total system: metal/film/solution (Mc Cafferty 2010).

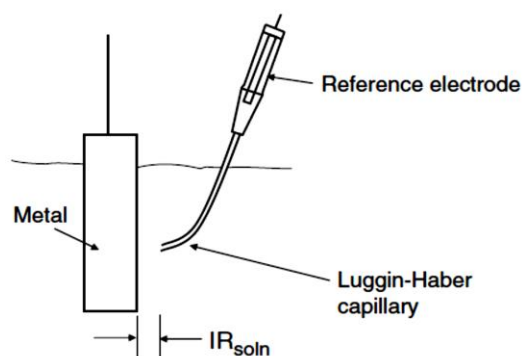


Figure 1.9 – Schematic representation showing the positioning of Luggin's tube to overcome iR drop in aqueous solution

1.8 CORROSION

Corrosion is defined as the gradual deterioration of metals/alloys due to chemical or electrochemical attack by the environment. Up to the 1960s, the term corrosion was restricted only to metals and their alloys and it did not incorporate ceramics, polymers, composites, and semiconductors in its regime. The term corrosion now encompasses all types of natural and man-made materials including biomaterials and nanomaterials, and it is not confined to metals and alloys alone. The environments are liquids or gases, although under special circumstances certain solid-solid reactions might be included as corrosion. Corrosion study is of utmost importance when it comes to electroplated coatings as it gives us valuable information about the thickness, corrosion susceptibility, time duration of coating resistance to atmospheric factors, and overall benefit of the coating in the protection of underlying metal.

Corrosion processes, which include oxidation and reduction reactions, mainly occur at the interface between the metal and the environment. Both structure and properties of metal, as well as the characteristics of the environment, affect the corrosion process. The rate of corrosion depends on the electrochemical susceptibility of a given metal, its chemical composition, homogeneity, and surface topography. It also depends on the type and chemical composition of the environment, the concentration of aggressive agents, temperature and the type of corrosion products themselves. In reality, electrochemical corrosion process is accompanied by mass transport and flow of electric charge through the metal medium interface (Trzaska 2012).

1.8.1 Corrosion Protection

The recognition that one might protect a surface of any object from environmental attack (by application of an organic, inorganic or metallic coating) to extend the life of not just the surface, but the entire component or equipment, was one of the major advancements in the history of coating technology. The implications of allowing the use of fewer materials or less expensive materials, coupled with associated energy savings have the most profound economic consequences, which contributed to the huge economic significances in surface engineering (Kanani 2006). Corrosion protection of over-ground and underground structures by protective coatings is one of the most

proven methods. Other methods include cathodic protection, environmental modification, material selection and design. In contrast to the behavior of rust on steel, the formation of an oxide affords protection against corrosion. If the resistivity of the electrolyte is increased and the electron flux is retarded, the rate of corrosion is decreased. By applying coatings of high resistivities, such as epoxies, vinyl, chlorinated rubbers, etc. the flow of electric current to the metal surface is impeded. Also, higher the thickness of coating higher would be the electrical resistance of the coating. A much higher resistance to the current flow would, therefore, be offered. Thus, increasing the electrical resistance of metals by coating offers an excellent method of corrosion prevention. Another method to prevent corrosion is by the use of inhibitors. An alternative method is to use a metal more anodic than iron, such as zinc. This is done by using zinc-rich paints. The zinc metal prevents the corrosion of iron by releasing electrons into the iron surface. Thus, the coating is an effective method to control corrosion. Any protective coatings are supposed to have the following characteristics for good corrosion resistance (Ahmad 2006):

- high degree of adhesion to the substrate
- minimum discontinuity (porosity) in the coating
- high resistance to the flow of electrons
- sufficient thickness (greater the thickness, more the resistance)
- low diffusion rate for ions such as Cl^- and for H_2O .

1.8.2 Electrochemical Corrosion Processes

In the simplest case, the corrosion reaction is the transfer of metal atoms from the solid to the solution where they exist as ions (i.e., $\text{M} \rightarrow \text{M}^{n+} + n\text{e}^-$). Because there is a loss of electrons from the metal atom in this transfer, the metal has undergone oxidation. The oxidation is sustained by the consumption of the electrons by another reaction, generalized in this case as $\text{X}^{x+} + x\text{e}^- \rightarrow \text{X}$. The corrosion process is schematically shown in Figure 1.10. The oxidation occurs at a site on the metal surface referred to as the anodic reaction site, it is the location of the loss of metal by corrosion. The electrons are picked up at a cathodic reaction site. These sites together make up a *corrosion cell* (Stansbury and Buchanan 2000), having a flow of corrosion current.

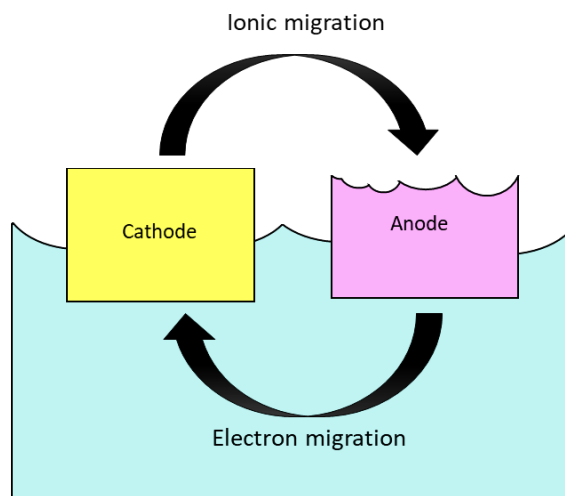


Figure 1.10 – Schematic representation of a basic corrosion process

Oxidation and reduction processes are accompanied by the flow of electric charge through the interface of metal-medium. In metals, the charge carriers are electrons while in the corrosive environment, charge flow is due to ions. Thus, an active assessment of electrochemical corrosion processes can be achieved by assessing the electrical charge transfer process (Trzaska 2012). Though corrosion is an anodic process, the total corrosion becomes possible only after the cathodic reaction. The anodic reaction is very simple with the formation of metal ions from metal atoms. However, cathodic reaction is very complex with several possible reactions, depending upon the reducible species present in the environment.

1.9 CORROSION EVALUATION TECHNIQUES

Any process measured in electroanalytical chemistry occurs at the surface of the electrode. Therefore, electrochemical measurements reflect an inherently surface process rather than a solution process. Hence, the surface, distance of the analyte from the surface, the rate at which the analyte reaches the surface and interactions of the analyte with the surface will affect the measurement. At present, there are many methods for determination of corrosion rates of metals/alloys, such as gravimetric-based mass loss, quartz crystal microbalance based mass loss, electrochemical, electrical resistance and solution analysis. The polarization measurement methods, based on electrochemical concepts, enables determination of instantaneous reaction rates at electrode/solution interface, such as the exchange current density (i_0) in the case

of an electrode equilibrium and the corrosion current density (i_{corr}) in the case of a corrosion system, from a single experiment. All other methods require multiple measurements over time to provide information on the corrosion rate (Badea et al. 2010).

The corrosion processes of metallic materials mainly use following methods:

- Potentiodynamic polarization method
- Electrochemical impedance spectroscopy method

The basis of potentiodynamic polarization technique is the stimulation of the corrosion system by a potential, whose value varies linearly in time and the recording of the instantaneous value of current flowing in the system. The electrochemical impedance spectroscopy consists of a perturbation of the steady state corrosion by applying the sinusoidal alternating potential signal of small amplitude (± 10 mV) but in a wide range of frequencies; and the automatic recording of current intensity responses of the system. Investigations of corrosion by those methods, based on a change in the relationship between potential and current were implemented in the three-electrode system (Trzaska 2012). The schematic setup for corrosion study is shown in Figure 1.11

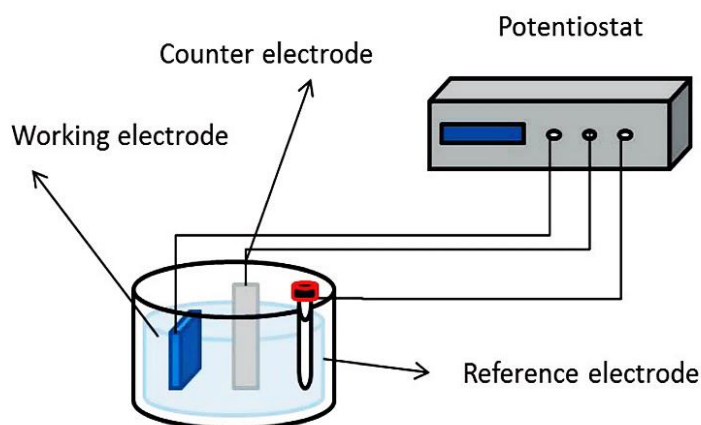


Figure 1.11 – Three electrode set up commonly used for corrosion study

1.9.1 Potentiodynamic Polarization Method

In any of electrochemical corrosion oxidation processes, i.e. the anodic processes, as well as the reduction i.e. cathodic processes occur on the surface of the metal. In the measurement system, these processes occur simultaneously during the polarization for each of the applied potential values but at different speeds. The resultant speed of the

processes constituting a sub-inflicted response to the potential changing at prescribed rate is recorded by the measurement system in the form of instantaneous current values. The characteristic current density as a function of the potential, i.e. $i=f(E)$ obtained is called potentiodynamic polarization curves. Potentiodynamic polarization method was applied to a wide range of potential changes to characterize the current-potential relationship in corrosion systems under investigation. The corrosion current density, i_{corr} and corrosion potential, E_{corr} of tested metallic materials were further determined based on extrapolation of tangents to the curves of the cathodic and anodic polarization zones (Jones 1996, Trzaska 2012).

At the high potential region where the rate of a single partial corrosion reaction predominates, the graphical representation in coordinates $E\text{-log}i$, for reactions under pure activation control give straight lines (so called Tafel lines), as in Figure 1.12. At potentials, well away from the corrosion potential, the applied c.d. reflects the kinetics of only one of the corrosion reactions (Badea et al. 2010). Figure 1.12 shows a typical Tafel plot for the measurement of corrosion rate (CR).

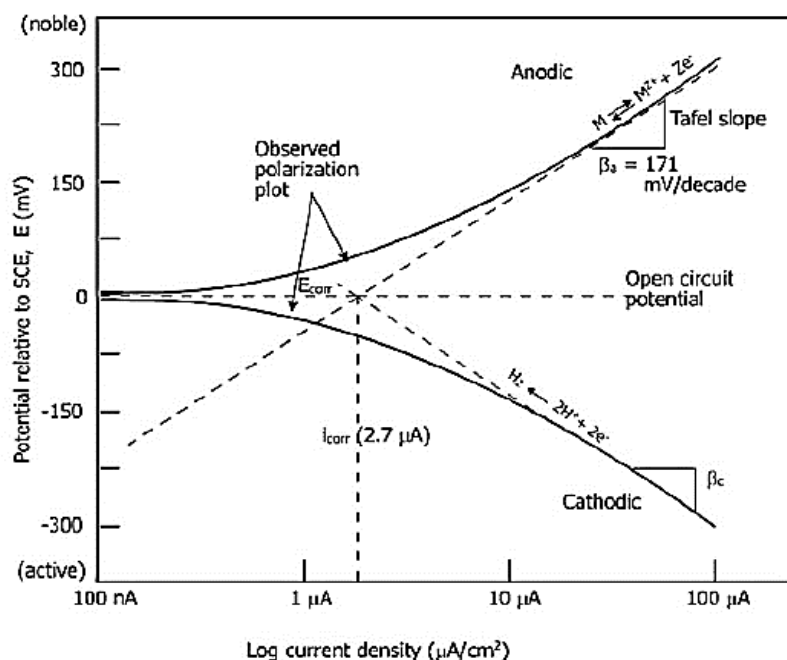


Figure 1.12 – Potentiodynamic polarization behavior showing Tafel plot

The slope of the oxidation reaction that represents metal becoming soluble metal ion is linear. When applied potential, $E \gg E_{\text{corr}}$ it obtains Tafel slope of anodic

reaction, represented by β_a . The curve shows that for an active metal, as the electrode potential is made more positive or as the solution becomes more oxidizing, the metal dissolution increases. The cathodic branch of the polarization curve is the solid line at more negative potential than the OCP; a cathodic current to the metal specimen is measured. The slope of the linear portion of the polarization curve is the cathodic Tafel slope, represented by β_c i.e. when $E \ll E_{\text{corr}}$. As the potential is made more negative, the rate of the reduction reaction increases. The both Tafel lines intersect in the point of coordinates $(E_{\text{corr}}, i_{\text{corr}})$ that makes possible the estimation of the i_{corr} by the extrapolation of the Tafel slopes with E_{corr} . At E_{corr} , the rate of hydrogen evolution is equal to the rate of metal dissolution, and this point corresponds to the CR of the system in terms of c.d. (Fontana 1987).

This method offers the following significant advantages:

1. Under ideal conditions, the accuracy of the Tafel extrapolation method is equal or greater than conventional weight loss methods.
2. With this technique, it is possible to measure extremely low corrosion rates (CR's), and it can be used for continuous monitoring the CR of a system.
3. Tafel Plots can provide a direct measure of the i_{corr} , which can be related to CR.
4. The rapid determination of CR's with Tafel Plots can be advantageous for such studies as inhibitors evaluation and alloy comparisons.

1.9.2 Electrochemical Impedance Spectroscopy Method

Electrochemical Impedance Spectroscopy (EIS) or AC impedance methods have seen a tremendous increase in popularity in recent years. Initially applied to the determination of the double-layer capacitance and in AC polarography, they are now applied to the characterization of electrode processes and complex interfaces. EIS study involves the system's response to the application of a periodic small amplitude AC signal. These measurements are carried out at over a wide spectrum of AC frequency, and hence the name *impedance spectroscopy* was later adopted. Analysis of the system response contains information about the interface, its structure and reactions taking place there (Lasia 2014). The EIS technique works in the frequency domain and is based on the concept that an interface can be seen as a combination of passive electrical circuit elements, i.e., resistance, capacitance, and inductance. When an alternating current is

applied to these elements, the resulting current is obtained using Ohm's law (Montemor 2003). The usefulness of impedance spectroscopy lies in the ability to distinguish the dielectric and electric properties of individual contributions of components under investigation. EIS is a non-destructive technique and so can provide time-dependent quantitative and time-dependent information about the electrode processes and complex interfaces (Cesiulis et al. 2016). EIS is usually measured by applying an AC potential to an electrochemical cell and then measuring the current through the cell. If there is a sinusoidal potential excitation, the response to this potential is an AC current signal. This current signal can be analyzed as a sum of sinusoidal functions (a Fourier series). The excitation potential or AC voltage can be expressed as a function of time, given by:

$$E_t = E_o \sin(\omega t) \quad (1.21)$$

where, E_t = potential at time t

E_o = the amplitude of the voltage

ω = the radial frequency

The relationship between radial frequency ω (radians s^{-1}) and frequency f (hertz) is:

$$\omega = 2\pi f \quad (1.22)$$

The response to the AC voltage is given by:

$$I_t = I_o \sin(\omega t + \phi) \quad (1.23)$$

where, I_t = response current

I_o = the amplitude of the current

ϕ = the phase shift

For AC current, the ohm's law is represented as given below:

$$Z = \frac{E_t}{I_t} = \frac{E_o \sin(\omega t)}{I_o \sin(\omega t + \phi)} = Z_0 \frac{\sin(\omega t)}{\sin(\omega t + \phi)} \quad (1.24)$$

Here, impedance (Z) is the AC analog of DC resistance. For applied AC, the behavior of the pure resistor is same as DC. But in the case of circuit elements like capacitor and inductor, the current phase leads and lags by 90° respectively. This leads to capacitive reactance and inductive reactance.

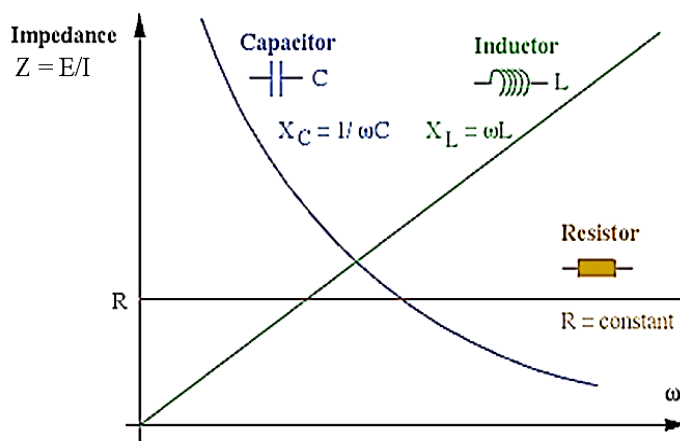


Figure 1.13 – Variation of impedance with frequency of circuit elements C , L and R

The Nyquist plot, shown in Figure 1.14 is a representation of the impedance in the form of complex number over a range of frequency. Each point represents the magnitude and direction of the impedance vector at a particular frequency.

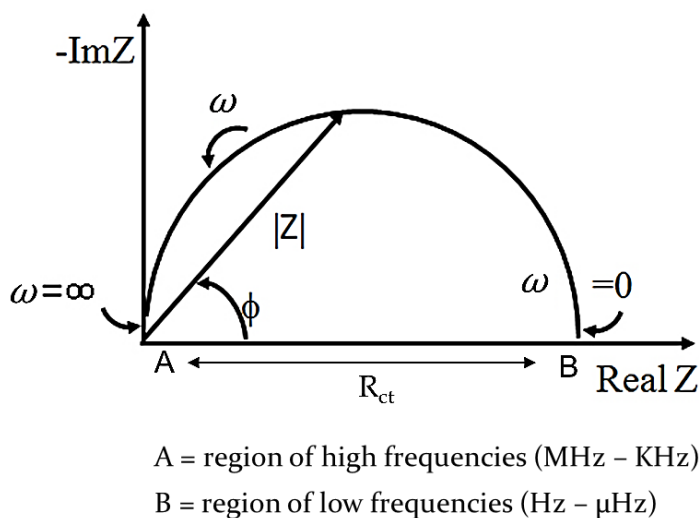


Figure 1.14 – Representative Nyquist plot showing frequency dependent impedance response

A diagram is a complex plane of Cartesian coordinates, where the abscissa is the real part (resistive terms) and the ordinate is the imaginary part (capacitive or inductive terms). Nyquist plots have the advantage that activation-controlled processes with distinct time constants show up as unique impedance arcs and the shape of the curve provides insight into the possible mechanism or governing phenomena (Ribeiro and Abrantes 2016). The diameter of the extrapolated semicircle in the Nyquist diagram

represents the charge transfer resistance, R_{ct} , which is equivalent to the polarization resistance (R_p). Thus, the larger the diameter of the semicircle the higher the resistance, R_p , and lower the CR.

Impedance data, represented on the Cartesian plane under a wide range of frequencies (from 100 kHz to 10 mHz, but more commonly from 10 kHz to 0.1 mHz) generate typical configurations according to the predominant electrochemical mechanisms present. In simple terms, it is possible to identify three frequency bands, in which different processes have an impedance response (Aguilar et al. 1990, Ribeiro and Abrantes 2016)

- High frequencies (MHz-kHz): the electrolyte gives a response. The capacitances are on the order of pF/cm². Greater than one-time constant may appear due to the moisture content of the material and the different constituents of the solid phase.
- Medium frequencies (kHz-Hz): the faradaic give a response. Typical capacitances are of the order of μF/cm². Greater than one-time constant may be noted when there is localized corrosion. Certain materials produce a flattening of the semicircle in the Nyquist diagrams.
- Low frequencies (Hz-μHz): redox reactions may occur, depending on the potential. The measured capacitances are in the order of mF/cm². Diffusion phenomena may appear through the passive layer.

Main advantages of EIS analyses are as follows:

- 1) It provides information regarding the corrosion kinetics.
- 2) It is an accurate and reproducible technique suitable for highly resistive environments.
- 3) It provides data about the electrochemical control mechanism, indicating whether the corrosion follows activation, concentration or diffusion controlled polarization.
- 4) It is a non-destructive and non-invasive technique because the signals applied are of small amplitude, so the E_{corr} is not changed.
- 5) It allows for monitoring of the evolution of the passive or active state over time.

CHAPTER 2

CHAPTER 2

LITERATURE REVIEW

This chapter covers a review of the literature on the properties of certain Ni-based alloy coatings developed through conventional electrodeposition method and their various applications. It also sheds a light on the effect of magnetic field and ultrasound on structure and properties of electroplated alloys. This is followed by scope and objectives of the thesis, given at the end.

2.1 INTRODUCTION

Electroplating technology really took off with the development of effective electrolytes for silver and gold deposition around 1840. This became the basis of an extraordinarily successful decorative plating industry. However, the electrolytes were extremely toxic as they incorporated cyanide; and the search for better, safer substitutes continued. Finding environmentally friendly alternatives to established electrodeposition processes is still an important general challenge. Parallel to the development of new processes, considerable effort has been devoted to gaining the fundamental understanding of electrodeposition. Electrodeposition is a key method for making the materials used in computer chips and magnetic data storage systems etc. Every day it helps lower the cost and improves the performance of our information society. However, electrodeposition is also emerging as a uniquely capable method for making materials and structures needed for a nanotechnology and nanobiotechnology-based future. It also provides some unique opportunities for directly writing materials onto a surface without going through the photoresist masking steps that are used in conventional electrochemical microfabrication. Electrodeposition has three main attributes that make it so well suited for nano-, bio- and micro-technologies (Schwarzacher 2006).

- It can be used to grow functional material through complex 3D masks.
- It can be performed near room temperature from water-based electrolytes.
- It can be scaled down to the deposition of a few atoms, or up to large dimensions.

2.2 LITERATURE SURVEY

Electrodeposition is a versatile technique for producing nanocrystalline materials. The synthesis of nanostructured materials by electrodeposition has seen advances from a laboratory scale phenomenon to one of practical industrial relevance. Electrodeposited nickel coatings are used in a wide range of applications to enhance mechanical properties, corrosion, and wear resistance of the coated components. Nickel deposition has been widely studied, and much work has been devoted to the mechanism of the deposition process. The properties and structures of the electrodeposits are closely related to the electrolyte composition and electroplating parameters. In order to improve the performance of nickel coatings, different approaches have been applied. Alloying with other elements, structural refinement using additives (grain size reduction), and deposition of composite coatings by dispersing reinforcing particles inside the Ni matrix are commonly used structural modification techniques.

The purpose of deposition of alloy coatings is to attain the properties which cannot be obtained with pure metal alone (Bakhit and Akbari 2013). In this regard, Ni-M (where M = Sn and Mo) alloys are used for a wide variety of applications, including aircraft gas turbines, steam turbine power plants, medical applications, nuclear power systems, and the chemical and petrochemical industries. Its mechanical properties can be varied by altering the electrolyte composition and operating parameters. It can also be varied by incorporating other metallic elements and ceramic particles/fibres within the electrodeposited nickel matrix. The applications of such deposits fall basically into three main categories: decorative, functional and electroforming (Schlesinger and Paunovic 2000).

2.2.1 Sn–Ni Alloy

The process of plating metals and alloys are widely used in different technologies due to their unique corrosion and wear resistance (Narayanan and Seshadri 2004), hardness, lubricity, uniformity of deposit regardless of geometries, solderability bond-ability and nonmagnetic properties (Ramalho and Miranda 2005). Sn–based alloy is used today in a large variety, especially for corrosion-resistance of metal materials (Huttunen-Saarivirta and Tiainen 2005, Wang et al. 1999) and for the purpose of heat-resistance and weldability (Kong et al. 2009).

Sn–Ni alloy is a homogeneous intermetallic phase, and the one electrodeposited from the fluoride-containing electrolyte possesses interesting and valuable properties. Sn–Ni alloy is hard, very resistant to corrosion, and can be used as a protective coating for different metals. The corrosion resistance, attractive appearance, and low-cost properties are the basis for its engineering applications. This alloy is used in the electronics industry, as etching resists for the fabricating printed circuit boards (Wilson 1972). The corrosion stability of Sn–Ni alloy has been attributed to the presence stable, protective, a self-limiting film of a glassy nickel polystannate on the alloy surface (Clarke et al. 1971).

Sn–Ni alloys were first deposited by Monk and Ellingham, who were interested in determining the extent at which the hardness and abrasion resistance of Sn coatings could be improved by the presence of small amounts of nickel. The basis for the present commercially successful plating process was the work of Parkinson, which was published in 1951. In his bath, Sn is present as a stannous fluoride complex ion. His work detailed the process data, describing a process capable of electroplating a deposit of Ni and Sn with the composition of approximately 65/35 wt.% corresponding to a one-to-one atomic ratio of Ni/Sn, referred to as NiSn alloy (Brenner 1963). Because of the corrosive and toxic nature of fluoride in fluoride baths, pyrophosphate baths have been developed which operate at lower temperatures, and near neutral pH. Bright deposits of Sn–Ni alloy have been successfully obtained from pyrophosphate baths. The composition of the alloy obtained from this bath does not vary with changes in pyrophosphate concentration, but variation in the content of individual metals, Sn or Ni, changes the composition of the alloy. The pH values below 7.5 or above 8.5 were found to be undesirable (Jiménez et al. 2008).

Refaey et al. (2006) have studied the effect of the addition of Ni (34%) to the Sn metal to form Sn–Ni alloy film with a higher resistance, compared to Sn metal alone. These results indicate the effect of aggressive anions on the general and pitting corrosion, which may be negligible compared to that of the base metals (Ni, Sn) in 0.5 M NaCl solutions. The observed corrosion resistance of Sn–Ni alloy is due to the formation of a thin passive film from Sn and Ni oxides. They finally concluded that the corrosion resistance of Sn–Ni alloy suggests that it can be used in a different application

in aqueous NaCl medium. Subramanian et al. (2006) conducted the corrosion protection performance of Sn–Ni alloy on mild steel and the results were assessed using salt-water immersion and electrochemical corrosion tests. They found a sharp decrease in i_{corr} and high charge transfer resistance (R_{ct}), indicating the improved corrosion resistant behavior of the deposited Sn–Ni alloy. Kong et al. (2009) prepared electroless Sn–Ni alloy without activation pre-treatment. Sn–Ni alloy exhibited a compact, and low porosity surface compared to irregularly nodular concave or convex surface of Sn or Ni. Meanwhile, the Sn–Ni alloy exhibited a good anticorrosion ability in 3.5% NaCl solution than those of electroless plated Ni and Sn. Ni–Sn alloy coatings was also deposited from choline chloride–ethylene glycol (ILEG) ionic liquids by Anicai and co-workers. These coatings were characterized by a good adherence and uniformity, with a very bright appearance. XRD analysis has also revealed the formation of an alloy deposit with a nanocrystalline structure. Ni–Sn alloys coatings formed in choline chloride-based ionic liquids showed a good corrosion performance, materialized in polarization resistances of about 80 k Ω . After 336 h of continuous immersion in chloride containing an aggressive medium, the exposed specimens did not exhibit any major surface modification and no pits have been evidenced (Anicai et al. 2013). Numerical analysis demonstrated by Hoffman et al. (2016) showed a range of overpotential that can continuously vary the deposit composition, and that a low concentration of the more noble element in the plating bath is the key to achieve a large variance in deposit composition. SEM images demonstrated that surface morphology was relatively independent of the ratio of Ni²⁺ and Sn²⁺ concentrations in the plating bath, while higher c.d.'s resulted in substantial nodular growth or cracking.

Over the last decade researchers have come up with different methods to develop Sn–Ni alloy instead of tradition electrodeposition, for instance, Dhanapal and co-workers successfully synthesized Ni–Sn alloy by using borohydride assisted chemical reduction method. The composition of an individual constituent in the alloy was measured, in which Sn composition is found to be high when compared to the initial composition. The morphology of the samples observed from FESEM analysis points the morphology changes from the foam like nature to fine spherical like nature as the percentage of Sn increases (Dhanapal et al. 2016). Georgiou et al. (2016) showed that

Ni-20 wt.% Sn can be deposited by supersonic spraying, as dense coatings with a thickness of 80 μm . In addition, a very limited number of cracks or flaws was observed either at the interface between the sprayed coatings and the substrate or between sprayed splashes within the coating. These supersonic-sprayed Ni-20 wt.% Sn coatings consist of a nanostructured Ni matrix, dispersed Ni_3Sn and metastable NiSn intermetallic phases.

2.2.2 Ni–Mo Alloy

Functional coatings containing molybdenum are characterized by high hardness, high wear resistance, high thermal and corrosion resistance, and good electrocatalytic properties for HER. They also offer an important alternative to hard chromium coatings, as chromates are known to be highly toxic and carcinogenic (Brooman 2000). Ni–Mo coatings can be applied as protective materials, e.g. in the automotive and aviation industries for various parts of machines operating at elevated temperatures and aggressive environments; as well as electrodes for HER and fuel cells (Clark et al. 1997, Hu and Weng 2000). The corrosion behavior appears to depend on both parameters: molybdenum content and grain size, which controls the grain boundary volume fraction. When the Mo content is increased, the intrinsic corrosion resistance tends to increase, but the grain size is reduced and hence the fraction of inter-crystalline regions increases drastically, which has an opposite effect. The best corrosion resistance is obtained for alloys with 15–30 wt.% Mo. Larger molybdenum contents induce cracking of the films leading to non-protective coatings. For lower molybdenum content, films with the smaller grain size have the best corrosion resistance (Chassaing et al. 2004).

Ni–Mo alloys can be prepared using several methods. Metallurgical methods are not very convenient because of easy oxidation at the crystallization step and high melting temperature of molybdenum. To prepare the molybdenum alloys, other advanced processing methods such as powder metallurgy and mechanical alloying (Oleszak et al. 1999, Kedzierzawski et al. 2001), spark plasma sintering (De la Torre et al. 2000), laser cladding (Goswami et al. 2003) and electrodeposition are used. Mechanical alloying offers an opportunity to prepare alloys of various structural and chemical factors that are important for their final catalytic properties. For the electrodeposition of the amorphous molybdenum alloys with the iron-group metals the

citrate–ammonia baths are used in most of the cases (Podlaha et al. 1996, Stepanova et al. 2000, Sanches et al. 2004). However, if the content of Mo does not exceed 12-13 at. %, the deposits obtained in the citrate ammonia bath consist of just one crystallographic phase, i.e. the solid solution of Mo in nickel (Stepanova et al. 2000). Then the structure of the alloy is polycrystalline. When the content of Mo increases up to 18 at. %, the initial indications of the formation of the amorphous/nanostructured phase arise. The alloys become really amorphous/nanostructured when the content of Mo exceeds 22-25 at.%. The electrodeposition of such a high-molybdenum-content alloys from the citrate–ammonia solution is possible, however, the very-high-molybdenum-content alloys (63 or 38 at.% of Mo), independently of the alloy deposition rate, exhibit cracks, and small pits which diminish their practical importance (Donten et al. 2005). Pulse plating has proved to be an important technology for improving the properties of deposits. It can also produce alloy compositions and microstructures which are not obtainable with DC plating techniques (Kelly et al. 2001, Nakanishi et al. 2001). Compared to DC plating, pulse current techniques offer several advantages such as the availability of additional process parameters which can be varied independently and the possibility of achieving higher instantaneous c.d.'s (Cheh 1971, Viswanathan et al. 1978, Chin 1983). Although molybdenum cannot be separately deposited in aqueous solutions, it can be co-discharged with an iron-group metal, in the presence of appropriate complexing agents (Chassaing et al. 2004). In electrodeposition method, the initial size of the nuclei can be controlled through the applied overpotential, which leads to dense, non-porous materials, avoiding further compaction.

From a theoretical point of view, electrodeposition of Ni–Mo alloy comes under so-called induced co-deposition mechanism (Brenner 1963). The induced co-deposition of molybdenum with nickel, cobalt or iron has been investigated by Marlot et al. (2002) using direct current plating. A reaction model was proposed to explain the co-deposition mechanism. It involves an adsorbed Ni–Mo intermediate, the formation of which requires the presence of nickel ionic species at the electrode surface. Molybdenum deposition proceeds through the mixed reaction intermediate while nickel deposition takes place by the usual two steps mechanism. Depending on relative concentrations, mass transport of either molybdate or nickel may limit the deposition

rate of molybdenum and therefore, control the alloy composition. The model was found to correctly predict the influence of the electrode rotation rate and the imposed potential on the current efficiency and the alloy composition. In the last decade, nanocrystalline materials have been developed, due to their exceptional mechanical, magnetic and other properties. Several methods have been proposed for their preparation such as melt spinning, ball milling and gas condensation (Suryanarayana 1995). Since the pioneering work by Erb et al. (1993), investigations on nanocrystalline materials produced by electrodeposition methods have considerably increased.

2.2.3 Magneto-electrodeposition of Ni-Based Binary Alloys

The electrochemical reactions effected by electric current in the presence of an imposed magnetic field are called *magneto-electrodeposition* (MED). Basically, MED covers four major specific aspects of electric/magnetic field interactions. They are: *i*) magnetic field effect on electrolyte properties, *ii*) electrolytic mass transport, *iii*) electrode kinetics and *iv*) deposit (cathodic) quality. In most electrochemical processes, as in electrodeposition or electro-dissolution in the diffusion-controlled regime, mass transfer is limited by the near-wall hydrodynamics of the bath which controls the thickness of the diffusive boundary layer of the electroactive species. Among all the possibilities to act on that system are the adaptation of the cell geometry and a judicious choice of the governing parameters (species concentration, flow velocity, flow configuration etc.). These possibilities are limited, the necessity to increase both productivity and quality sometimes appear as contradictory objectives. Therefore, the interest of an external parameter which allows dealing with the two types of the problem seems evident. A superimposed magnetic field on the existing electric field could be a solution. Hence this magnetically assisted mass transfer is viewed as a relatively new and promising branch of electrochemical science. The current understanding of the influence of a magnetic field on electrochemical phenomena is far from being complete.

The MED is found to enhance the surface smoothness of the electrodeposit (Shannon et al. 1997, Shannon et al. 1999). Devos et al. (1998) reported that a magnetic field could change the surface morphology and the preferred orientation of the nickel grain due to an increase of the diffusion flux of specific inhibiting species. Ganesh et al. (2005) have observed the grain refinement, even up to 1.0 T during electrodeposition

of Ni- from sulphamate bath at a constant c.d. (1.0 mA cm^{-2}). It was further observed that the magnetic convections increased the mass transfer rate and reduced the concentration polarization. Koza et al. (2008) studied the effect of the constant magnetic field with magnetic induction value ranging from 0 to 1.0 T in various configurations in relation to the electrode surface. They observed that constant magnetic field applied increased the limiting current density (i_L) and the deposition rate. This was explained by MHD effect induced by the maximal Lorentz force generated in the hydrodynamic layer. Coey and Hinds (2001) confirmed that induced magnetic field increased significantly the rate of electrodeposition of copper, and studied increased transport of cationic mass, of both diamagnetic (Ag^+ , Zn^{2+} , Bi^{3+}) and paramagnetic (Cu^{2+} , Ni^{2+}) ions. O'Reilly et al. (2001) found that under a magnetic field, an increase in i_L occurred, caused by the decrease of diffusion layer thickness (δ). Ragsdale et al. (1998, 1999) showed microscopic images confirming MHD flow in the electrolyte, demonstrating that the flow is more intense when the direction of B is parallel to the working electrode surface than it is perpendicular. Chiba et al. (1986) using XRD analysis concluded that the magnetic field could modify the crystal growth orientations in relation to the easy magnetization axis and this effect is more dominant at low c.d.'s where the magnetic field effect dominates over that of the electric field.

Rao et al. (2013) reported that the Zn–Ni coatings developed under optimal magnetic field (perpendicular) are about 55 times more corrosion resistant than the one under natural convection. The surface morphology and corrosion performance of the coatings are related to the orientation of the coatings, depending on the direction of applied magnetic field. The results obtained in the study of Zieliński et al. (2015), indicated that the use of constant magnetic field resulted in changes of Co–W–Cu alloy deposition kinetics, chemical composition, and surface morphology. The force induced MHD effects in solutions, which caused electrolyte movement. Consequently, the Nernst diffusion layer (δ_D) was reduced and a new Navier-Stokes hydrodynamic layer (δ_H), determining the velocity of electroactive ions flow towards the working electrode, appeared. They finally concluded that the presence of the magnetic field during plating leads to substantial increase of corrosion resistance; and a decrease of roughness and thickness of the coating. Magneto-electrodeposited coatings deposited under constant

magnetic field were found to be more homogeneous and smooth than those obtained without it.

It has been shown by Aaboubi and Msellak (2017) that during the electrodeposition of ternary CoNiMo alloys, the application of external homogeneous magnetic field parallel to electrode surface induces some modifications of film composition, morphology, stationary and dynamic electrochemical responses. The quantitative chemical analysis of alloys showed an increase of Co content and decrease of Ni content when a magnetic field is applied during electrodeposition process. Moreover, the phase structure of CoNiMo coatings did not change by increasing the intensity of magnetic field; and typical amorphous structure is obtained in both cases. Electrochemical investigations (polarization curves and EIS diagrams) clearly highlight the role of the induced Lorentz force convection. Stronger the magnetic field intensity, greater the hydrodynamic regime being controlled. They concluded that CoNiMo films of smooth and compact surface could be obtained under magnetic field as a result of induced MHD convection.

2.2.4 Sono-electrodeposition

Over the last few years, a large number of chemists and engineers working in synthesis and material processing have developed a varied interest in applications of ultrasound frequency in industries. Ever since the pioneering works of Walker and Walker (1973) who first described the beneficial effect of ultrasound in plating, many works have reported finer grains, reduced porosity and increased brightness (Prasad et al. 1993). The effect of ultrasound on structure and properties of electrodeposited Ni coatings were reported as the grains of the coatings were refined by the ultrasonic effect. The reason is explained as the cavitation effect, creating a strong shock pressure (Banks and Compton 2003). Electroless copper coatings (Touyeras et al. 2005) exhibit a better adhesion for substrates and a reduction in internal stress in the presence of high-frequency ultrasound. The same authors also studied the effect of high-frequency ultrasound (300, 500 and 800 kHz) on the electrodeposition of nickel and found that grain size varied as a function of the ultrasonic power for each frequency. Kobayasi et al. (2000) explored low-frequency ultrasound (28–100 kHz) on nickel electrodeposition from a Watts bath and discovered an improvement in charge transfer reaction and

crystal orientation. Tudela et al. (2005) observed systematically the effect of ultrasonic power on the characteristic of thin nickel coatings. They observed a modification in deposit orientation, different from that expected only from agitation of the solution. The ultrasonic energy activates the surface of the electrode and destroys the normal growth of grains, which makes the grains to form the new smaller nucleus and nuclear proliferations, thus the rate of nucleation is increased. When the rate of nucleation exceeds the rate of growth, the grains will become refined (Wu et al. 2010). It was shown that ultrasonic irradiation can significantly change the morphological and structural properties of Zn and Zn–TiO₂ electrodeposits. By combining ultrasonic irradiation and high-speed deposition, compact and homogeneous Zn–TiO₂ layers with enhanced particle incorporation, better particle distribution in the matrix as well as improved hardness were obtained (Camargo et al. 2016). The main advantage observed with ultrasonic agitation was a significant increase in the plating rate. When ultrasonic agitation was employed to NiB coating, by Bonin et al. (2017) its thickness was found to be increased by over 50%. This is an important finding since industry demands higher plating speeds, reduced production times and enhanced material properties. The results from the study of Bonin and co-workers suggest that the use of ultrasound to agitate electroless NiB solutions has the potential to fulfill these requirements.

Use of ultrasound during silver coating elaboration, irrespective of hydrodynamic conditions kept otherwise constant made it possible to modify significantly the microstructures and morphology of deposits without relying on chemical additives. The way ultrasound work is certainly related to major heterogeneities in the cavitation collapse mechanism, with highly disturbed zones as well as stiller zones. Also, for an average level of agitation, there is a decrease in the number of nucleation points that promotes the growth of large crystalline structures. In all cases, agitation is always beneficial to widen the c.d. range favorable for structural modifications without the risk of coating deterioration due to burning. Moreover, at the same level of agitation, use of ultrasound offers more advantages because it ensures harder and less structured deposits in increased c.d. range (Nevers et al. 2017).

2.2.5 Electrocatalytic Property of Ni-based (where M = Sn and Mo) Alloys

To solve the energy and environmental problems related to the excessive use of fossil fuels, humankind needs to develop sustainable energy resources, such as solar, wind, and tide, to generate electricity (Tachibana et al. 2012). As electricity has limitations in delivery and storage, we have to convert electricity into alternative energy forms. Hydrogen gas has long been considered as an ideal energy carrier due to its cleanness and recyclability, high energy density, feasibility in transportation, storage and high energy conversion efficiency in fuel cells (Winter and Ralph 2014). Electrochemical splitting of water to produce hydrogen and oxygen with sustainable energy input (i.e., the wind and solar) may be an integral part of future energy storage and conversion strategies, and could potentially meet the large-scale energy needs for the future (Turner 2004, Gray 2009). However, the sluggish reaction kinetics for such an electrolytic water splitting process requires high overpotentials to drive the two half reactions, including the HER and OER at practical rates, leading to a much larger operating cell voltage of 1.8-2.0 V than the minimum value of 1.23 V in theory for practical overall water splitting (Zeng and Zhang 2010). Hydrogen production by electrolysis consumes high energy and this is also one of the reasons for ranking behind fossil fuel as an energy source in large-scale commercial applications (Mahale and Ingle 2017). To promote the overall water splitting, efficient electrocatalysts are necessary to decrease the reaction overpotentials, thus making the splitting process more energy-saving (Walter et al. 2010). A typical water electrolysis cell consists of a cathode for HER, and an anode for the OER. Many noble metal-based (Lee et al. 2012), noble metal-free (Zou and Zhang 2015) or even metal-free (Zhao et al. 2013, Tian et. al 2014, Chen et al. 2015) complexes and materials have been widely studied for electrocatalytic HER and OER. Currently, the best electrocatalysts for the HER (Pt-based electrodes) and OER (Ru- or Ir-based complexes) are still precious metal based materials, which are precluded from large-scale use for their reserve scarcity and high price. Thus, the development of highly efficient electrocatalytic materials based on earth-abundant elements as a substitute for this noble metal based catalysts for overall water splitting is eagerly desired (Gao et al. 2017).

In order to satisfy technical, economical, and environmental criteria, and achieve cheap hydrogen production, it is necessary to investigate appropriate *i*) media and *ii*)

electrodes for water electrolysis, since electrolysis being an electrode reaction and its operating voltage depends on the overpotential for the cathodic and anodic reactions and internal resistance of the cell (Rosalbino et al. 2005). Because of the importance of HER in both fundamental and technological electrochemistry, the aim of many papers dealing with this reaction is to understand the principles of its kinetics, mechanism; and how to improve its electrocatalytic behaviors. The improvement consisted in targeting several fields of interest such as the intrinsic nature of the reaction (Okido et al. 1993), electrode composition (Raj and Vasu 1990, Chen et al. 1991, Los et al. 1993), surface morphology (Choquette et al. 1990, Tanaka et al. 1999), structural, chemical and electronic properties (Ezaki et al. 1993, Jaksic 1994), physicochemical and electrochemical activation treatment (Spriano et al. 1994, Dabo et al. 1998). Two properties play an important role in selecting catalytically active materials for the HER. Firstly, the actual electrocatalytic effect of the material which is directly dependent on the voltage used to operate the electrolyzer at significant c.d.'s and secondly, its long-term stability. Thus, from an electrochemical point of view, the problem to be tackled in order to decrease the cost of electrolytic hydrogen is the reduction of overpotential, which can be achieved by choosing a highly catalytically active electrode material, or by increasing the active surface area of the electrode (Rosalbino et al. 2007). The electrochemical stability and the corrosion behavior of the electrode materials for long operation time are important for their practical applications. (Solmaz and Kardaş 2009). Therefore, alkaline solutions are highly preferred media because of fewer corrosion effects allowing a wider range of choice of electrode materials, although the strong caustic environments have their own limitations (Shervedani and Madram 2008).

According to the theory of electrocatalysis, the electrocatalytic activity depends on the heat of adsorption of the intermediate on the electrode surface, defined by the well-known '*volcano*' curve, where poor catalysts are located on the extreme left-hand side, strong catalysts are located on the extreme right-hand side and moderate catalysts are placed around the apex of the curve (Parsons 1958). It is clear that besides the precious metals, there is practically no way to find the new materials among pure metals, which would possess high catalytic activity for the HER. So, the alloying of two (or more) metals has long appeared as the most straightforward approach to achieve

electrocatalytic activity for the HER (Xu et al. 2016). The Brewer–Engel theory (Brewer and Beck 1963) predicts that for alloys and intermetallic compounds, a maximum in bond strength and stability is expected when metals of the left half of the transition series, having empty or half-filled vacant d-orbitals, are alloyed with metals of the right half of the transition series having internally paired d-electrons. Also, a synergistic effect in the hydrogen evolving activity of these materials is expected.

Several electrodeposited transition metals (like Ni, Co, Fe, Mo, and Mn), their mutual alloys and few of their composites have been used as electrodes for electrolysis of water, and they offered several advantages over other precious metals. Electrodeposition is a simple and less expensive approach to the development of many binary/ternary alloys, they can experiment for Ni–M (where M = Sn and Mo) alloy coatings. Moreover, electrodeposition being an atomistic deposition process, the property of the coatings can be controlled closely by regulating the deposition parameters and bath composition. Another advantage is that electrodeposited materials do not require any post-preparation treatment before using as electrocatalysts for intended reaction to occur (Hwang et al. 2011). Navarro-Flores and co-workers have studied the electrocatalytic activity of Ni, Ni–Mo, Ni–W and Ni–Fe for HER reaction in acidic medium. The experimental results showed the increased HER activity of the alloy coatings while demonstrating the advantages of alloying of Ni with Fe, Mo, and W (Navarro-Flores et al. 2005). Song and co-workers developed Ni–Fe–C composite electrodes electrolytically for HER in seawater and studied the relation of grain size to the carbon content in the electrode, consequent to HER efficiency (Song and Meng 2010).

2.3 SCOPE AND OBJECTIVES

2.3.1 Scope

Generally, electrodeposited coatings consisting of metal-based alloys and compounds have been extensively used as protective and/or functional materials in a wide variety of industrial areas. For protection applications, coatings with desired composition and structure can be used to enhance the surface properties such as the wear resistance, corrosion resistance and the high-temperature oxidation resistance of the substrates. On the other hand, for functional applications, coatings with attractive physical and

chemical properties (e.g., ferromagnetic, optical and catalytic properties) have attracted great interest. To date, a large number of technologies, such as the CVD, PVD, plasma spray, hot dipping and electrochemical deposition, have been developed to prepare coatings. Among these methods, the electrochemical deposition method has received a great attention due to its distinct advantages. Various parameters of the coatings, such as the composition, structure, and thickness can be controlled through rationally selecting the electrodeposition conditions such as the composition of the electrolytes, electrodeposition current/potential, its mode (like constant or varied current/potential), and the modulation in metal ions supply (Gu et al. 2017). Electroplated nickel layers are characterized by good corrosion resistance and electrochemical activity towards processes of cathodic hydrogen evolution and anodic oxygen evolution. They are used as protective coatings, as well for the protection of base metals against the aggressive environment. In order to improve the usable properties of nickel alloy coatings, the coatings were co-deposited from baths containing other metals. Such a procedure led to the production of coatings with a composite structure and was characterized by special properties such as good catalytic activity, good corrosion resistance, heightened hardness or resistance to high temperatures (Serek and Budniok 2003).

Superimposition of external parameters, like the *magnetic field* and *ultrasound frequency*, offers many possibilities to influence the electrodeposition process and therefore to control the deposit properties. Hence in the proposed project, the benefit of *magneto-electrodeposition* and *sono-electrodeposition* in the development of monolayer and multilayer coatings of Ni-based alloys have been exploited. It is also intended to demonstrate how the mass transport rates can significantly alter the electrolytic processes when the *magnetic field* and *ultrasound frequency* are superimposed externally during the process of electroplating. The advent of these two techniques in maximizing the deposit character is studied and discussed.

The literature review confirmed the fact that fuel cell technology is going to be the key element in the future clean energy market. Even though they are now ready for large-scale commercialization, further cost reduction and quality advancement are of high concern to make them available for everyone at a low price. Enormous reports are available in the literature pertaining to the development of many mutual alloys of

transition metals, as efficient electrode materials for HER to be used in fuel cell applications. But most of the method which is employed for the production of hydrogen in large scale belongs to noble metals, and are quite expensive. Hence it was found that electrochemical method is the best way to produce hydrogen gas because this method has been found to be cheap, efficient and technically simple. This method is also found to be highly eco-friendly and results in zero-emission of any greenhouse gas.

Thus, an extensive literature review on electrodeposition and characterization of Ni-based alloys revealed that these materials exhibit good corrosion protection and electrocatalytic activity. In pursuit of efficient corrosion resistant coatings and good electrode materials, few binary alloy coatings of transition metals have been tried and tested. Thus, the present study is devoted to the development of few new coating materials, for better corrosion protection and good catalytic behavior, using the advantage of the pulsed electric field, magnetic field and ultrasound field, applied parallel to the process of deposition. In this regard, two Ni-based alloys, namely Sn–Ni and Ni–Mo, have been selected to have an extensive study on their production and properties (like corrosion and electrocatalytic behavior) through electrochemical methods. To begin with two new electrolytic baths (alkaline) of Sn–Ni, and Ni–Mo alloys have been developed. The composition and operating parameters of these baths are optimized to maximize the appearance and corrosion properties of alloy coatings (monolayer), using constant current, or DC. Later, by using two basic principles of development of nano-coatings, they are developed in multilayers to achieve their increased properties. The guiding principles adopted for the development of high-performance Ni–M alloy coatings in the present thesis are:

- 1) Periodic modulation in mass transport process at cathode brings a periodic modulation in the composition of the coatings.
- 2) Property of any materials (or coatings) can be increased substantially by increasing the surface area. i.e., by multilayer coating.

Accordingly, the corrosion resistance of monolayer (homogenous) Ni–M alloy coatings were tried to increase further by inducing a magnetic field and ultrasound field effects, parallel to the process of deposition. In addition, they are developed in multilayers by modulating the power density (p.d.) at constant current.

2.3.2 Objectives

The experimental work exemplified in the thesis is guided by the following objectives:

1. To optimize the alkaline electrolytic baths for electrodeposition of Sn–Ni and Ni–Mo alloy coatings onto to the surface of the substrate.
2. To characterize the electrodeposited Sn–Ni and Ni–Mo alloy coatings using EDX, SEM, AFM and XRD techniques; and to understand the influence of deposition current density (c.d.) on the properties of the coatings.
3. To study the effect of the magnetic field (B), in terms of both intensity and direction on the surface morphology, crystallographic orientation, and hence corrosion behavior and electrocatalytic property of alloy coatings.
4. To study the effect of ultrasound power density (p.d.) on the process of electrodeposition of alloys, and to optimize their conditions for the development of monolayer and their multilayer coatings for peak performance against corrosion.
5. To evaluate the electrocatalytic property of both Ni–Mo and Sn–Ni alloy deposit in 1.0 M KOH using electrochemical techniques, like cyclic voltammetry (CV) and chronopotentiometry (CP).
6. To enhance the electrocatalytic performance of electrode materials by modifying their structural properties using techniques like electrochemical anodic dissolution treatment and composite coating for the electrolysis of water.
7. To figure out the most suitable mode of mass transport for the production of the most efficient Ni–M alloy coatings studied, in terms of their corrosion and electrocatalytic performance.

CHAPTER 3

CHAPTER 3

RESEARCH METHODOLOGY

This chapter details the materials used and the methodology employed for the development of Ni–M alloys. It gives a description of the experimental setup used for electrodeposition of different alloy coatings, using DC power source (for monolayer), magneto-electrodeposition (MED) and sono-electrodeposition (SED). Experimental procedure for characterization such as corrosion resistance and electrocatalytic behaviors of different alloy coatings are also given in detail.

3.1 INTRODUCTION

Electroplating or electrodeposition is used to change the surface properties of a material by adding a metal coating through the action of electric current. The article to be coated receives a negative charge and is immersed into a solution that contains a salt of the metal to be deposited. The chemical and physical nature of a metallic surface has a very marked effect upon the quality of any electroplated metal that may be used to protect it. In the preparation of almost all metals for decorative plating, one of the most important consideration is the pre-plating sequence i.e., the cleaning process. It is so important in electroplating that the successful adhesion of surface coating depends on removing contaminants and films from the substrate. This is so because the appearance, adhesion, and acceptance of the finished article depend primarily on a sound foundation for the final finish, which is achieved only with an active and clean substrate. In general, it may be noted that production of protective, decorative or functional metal deposits of high quality is dependent upon the proper and thorough pre-treatment of the surface of the base metal. Hence, the surface of the substrate to be coated has to be cleaned properly prior to electroplating using proper procedure. Similarly, the material having been plated has to be rinsed and need to be subjected to further finishing operations.

3.2 MATERIALS AND METHODS

3.2.1 Chemicals Used

All chemicals used in the present study are of analytical grade, prepared using double distilled water. The chemicals used with their molecular formula and their makers are listed in Table 3.1. Mild steel (MS) plates (0.063% C, 0.23% Mn, 0.03% S, 0.011% P, 99.6% Fe) and commercial grade copper plates were used as cathodes, respectively for corrosion study and water splitting applications throughout the research work presented in the thesis.

Table 3.1 – List of common chemicals used in the present research work

Chemicals	Molecular formula	Makers
Nickel chloride	$\text{NiCl}_2 \cdot 6\text{H}_2\text{O}$	Merck, India
Tin chloride	$\text{SnCl}_2 \cdot 2\text{H}_2\text{O}$	Merck, India
Nickel sulphate	$\text{NiSO}_4 \cdot 6\text{H}_2\text{O}$	Merck, India
Sodium molybdate	Na_2MoO_4	Merck, India
Tri-Sodium citrate	$\text{Na}_3\text{C}_6\text{H}_5\text{O}_7$	Merck, India
Potassium pyrophosphate	$\text{K}_4\text{P}_2\text{O}_7$	Merck, India
Potassium hydroxide	KOH	Merck, India
Gelatin	$\text{C}_{102}\text{H}_{151}\text{N}_{31}$	Nice Chemicals, India
Sodium chloride	NaCl	Nice Chemicals, India
Sodium hydroxide	NaOH	Nice Chemicals, India
Nitric acid	HNO_3	Nice Chemicals, India
Ammonium hydroxide	NH_4OH	Nice Chemicals, India
Trichloroethylene	C_2HCl_3	Nice Chemicals, India

The primary additive, namely gelatin was dissolved in hot water (being insoluble in cold water) and added to the bath to impart a lustrous appearance to the coating. Potassium pyrophosphate is used as a complexing agent and trisodium citrate as a conducting salt as well as a complexing agent in the electrolyte bath. All depositions have been carried out under identical conditions of pre-treatment, and common electrochemical methods were employed for evaluating their corrosion behavior and electrocatalytic activity in 5% NaCl solution and 1.0 M KOH solution, respectively.

3.2.2 Surface Cleaning

Effective surface cleaning is achieved through a combination of chemical reaction, solvent dissolution, and mechanical action. The substrate of various sizes ($10.0 \times 5.0 \text{ cm}^2$, $5.0 \times 5.0 \text{ cm}^2$, and $3.0 \times 3.0 \text{ cm}^2$) are pre-treated by mechanical polishing, using emery coated mops of gradually decreasing grit size. The mirror polished specimens were degreased with trichloroethylene. Then the plates were electro-cleaned cathodically for 2 min and then anodically for 30 s using the bath given in Table 3.2. Later, the polished plates were pickled in 1:1 mixture of 0.5 M HNO_3 and 0.5 M H_2SO_4 for 10 s, to render the surface active for deposition. Finally, they are washed and rinsed thoroughly several times with distilled water and immediately taken for deposition.

Table 3.2 – Composition of the electro-cleaning bath used for cleaning the substrate

Sodium hydroxide	35 g L ⁻¹
Sodium carbonate	25 g L ⁻¹
Sodium lauryl sulphate	1.0 g L ⁻¹
Temperature	30 – 80°C
Current density	6.0 A dm ⁻²
Duration	2 min cathodically followed by 30 s anodically

3.2.3 Purification of Electrolytes

Certain impurities in electrolytes cause great difficulty during the electroplating process, in some cases due to the impurity itself the deposit produced will be impure of less value, tampering the property of the metal or alloy plated. To ensure the uniform deposition, the electrolytes are prepared in the following order: for both Sn–Ni, and Ni–Mo baths first, the complexing agents, potassium pyrophosphate/tri-sodium citrate was dissolved in desired quantity of distilled water. To this bath, required quantity of Nickel chloride/Nickel sulphate is added followed by Tin chloride/Sodium molybdate. Once the salts are dissolved, known amount of gelatin is added to the prepared bath, stirred until it becomes homogenous. Once all the ingredients are added, the solution is made up to its final volume. The solution was filtered after preparation, using filter paper (Whatmann-40) to remove the suspended impurities. The pH of plating bath was adjusted to the required value, using dilute NH_4OH or $\text{HCl}/\text{H}_2\text{SO}_4$, monitored using digital pH Meter (Systronics, μ pH system-362).

3.2.4 Optimization of the Electrolyte Baths

The limiting conditions, in terms of composition and operating parameters of electrolytic baths, have been carried out, using standard Hull cell method by passing 1.0 A cell current for the duration of 5 min (Pardhasaradhy 1987). The Hull cell is a specially designed cell, made up of PVC material generally used for fixing the limiting conditions of the bath for the development of good coatings.

3.2.4.1 Hull cell

The Hull cell is basically a trapezoidal container that holds 267 mL of solution in a depth of 48 mm of the cell. It is named after Richard Hull, who introduced his invention to the industry in 1939. The Hull cell is a miniature plating unit designed to produce cathode deposits on a panel that correlates the characteristics of the plating unit being evaluated. Interpretation of the ‘as plated’ cathode panel gives rapid information about brightness levels, irregular plate deposits, uniformity of deposits, coverage, throwing power, impurities, and plating bath chemistry. It is among the most useful tools available to the plating chemist for control of plating baths. It is an indispensable

adjunct to standard analytical methods, enabling the skilled operator to determine and control the effects of addition agents, impurities and purification treatments on the plating electrolyte, many of which can be determined by no other method. Practically every plating solution can be controlled or evaluated to varying degrees by the use of the Hull Cell. The cell is designed so that the cathode is at a pre-defined angle to the anode as shown in Figure 3.1, to produce a range of c.d.'s. As a result, when a current is applied across the anode and cathode, the resulting c.d. will vary along the length of the cathode. At the points close to the anode, the c.d. is high, and it is called high current density (HCD) region, where the deposit may be burnt. But at the points far away from the anode, the c.d. is low, and it is called low current density (LCD) region, where no deposition is likely to take place. Hence the c.d. is distributed on the inclined cathode from maximum to minimum, as shown in Figure 3.1. Thus, the Hull cell allows the determination of the *operating window*, within the c.d. the range over which acceptable deposition occurs.

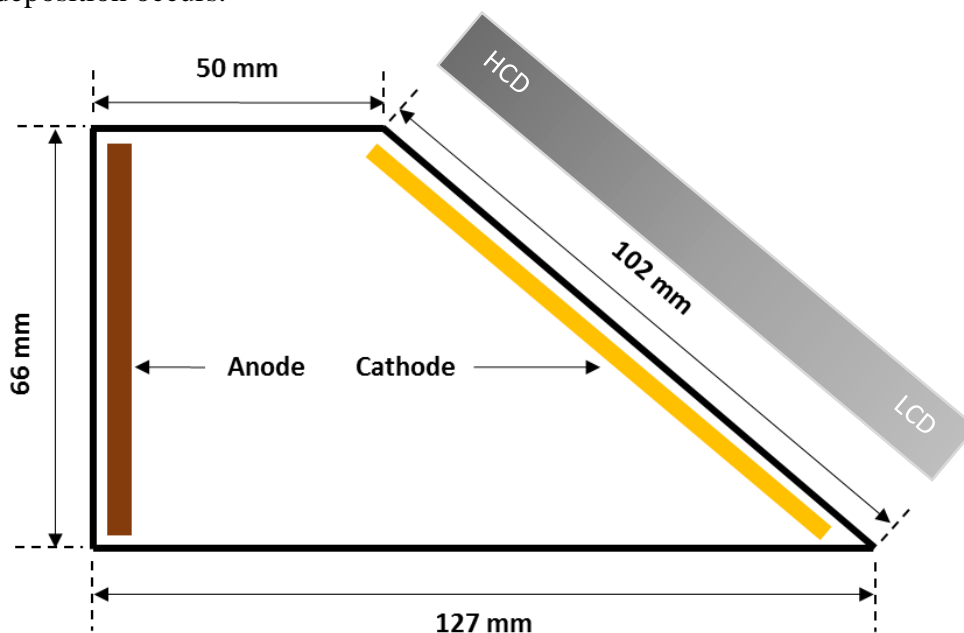


Figure 3.1 – Top view of the Hull cell displaying the position of anode and cathode

By taking required electrolytic solution, the deposition can be carried out on cathode at definite cell current, such as 1 A, 2 A or 3 A etc. The corresponding c.d.'s at

a definite distance from HCD end can be obtained from Hull cell ruler shown in Figure 3.2. The current variation along the length of the cathode is given by the formula:

$$i = I(5.1 - 5.24 \log X) \quad (3.1)$$

where,

i = Current density ($A \text{ dm}^{-2}$) at the given distance from the point of HCD on the cathode

I = Cell current used for the test (in ampere)

X = Distance from HCD end to the point where test is applicable

For Hull cell test assessment, the Hull cell ruler is overlaid upon the completed Hull cell panel as seen in Figure 3.2.

(a)

Current Applied	Current Density A/dm^2													
	Position on Hull Cell panel													
Amperes	a	b	c	d	e	f	g	h	i	j	k	l	m	n
1	5	4	3	2	1.5	1.25	1	0.75	0.5	0.4	0.3	0.2	0.1	0.05
2	10	8	6	4	3	2.5	2	1.5	1	0.8	0.6	0.4	0.2	0.1
3	15	12	9	6	4.5	3.75	3	2.25	1.5	1.2	0.9	0.6	0.3	0.15

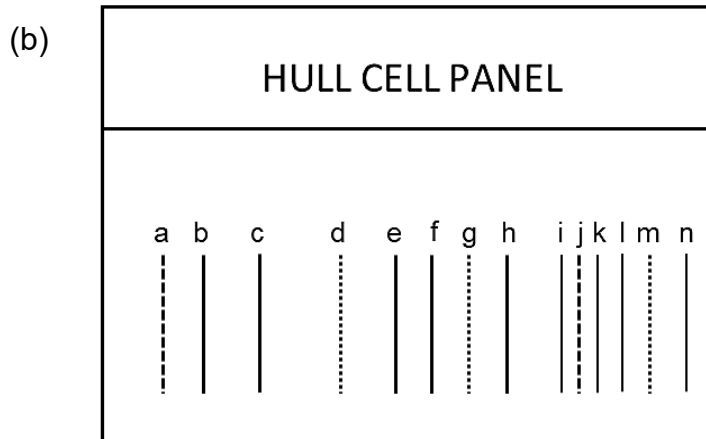


Figure 3.2 – Typical representation of a) Hull cell ruler corresponding to different cell current, and b) identification of c.d. corresponding to the different distance from HCD point

The grid of the Hull cell ruler provides a reference to evaluate the plating across a range of c.d.'s. The high c.d. is located on the left side of the panel (closest to the anode), while the low c.d. is located on the right side (furthest away from the anode). The range of c.d. flows from left to right. After reviewing the panel which has been overlaid upon the Hull cell ruler, evaluation of the panel will lead to theories regarding the desired action to improve the operation of the plating bath. Theories which the Hull cell test procedure can show are the effect of addition agents, the effect of contaminants and impurities and correspondingly, the success of purification on the working bath.

3.3 ELECTRODEPOSITION OF MONOLAYER AND MULTILAYER ALLOY COATINGS

Different modern electroplating techniques, like MED, SED and DC pulsed electrodeposition (multilayered) have been used to improve the material properties of Sn–Ni, and Ni–Mo alloy coating, especially their corrosion, and electrocatalytic properties. However, in all these techniques conventional DC is used as the driving force for electroplating, where metal ions are discharged as metal atoms at the expense of applied current. Therefore, all electroplating, under different conditions of mass transport are carried out using DC Power Analyzer (Agilent N6705A, USA, and Aplab, LD3205), as the power source. Hull cell is used for fixing the limiting conditions of electroplating of the baths, a 200 mL PVC cell was used for regular electroplating. The real experimental setup used for the electroplating is shown in Figure 3.3.

All electrolytic baths have been prepared from analytical grade reagents, using double distilled water. The optimal bath composition, working conditions for deposition of Ni–M (M = Sn, Mo) alloys was arrived by standard Hull cell method mentioned elsewhere. The bath composition and operating parameters (such as pH, temperature, and c.d.) have been optimized based on visual observation of the coatings on Hull cell panel. Pure nickel/tin panels, having the same active surface area as a cathode was used as the anode. All depositions were carried out on the active surface area ($7.5 \times 3.0 \text{ cm}^2$) for 10 min (600 s), solely for comparison purpose. After deposition,

the coated surfaces were rinsed with distilled water several times, dried in hot air and desiccated under vacuum till further testing.

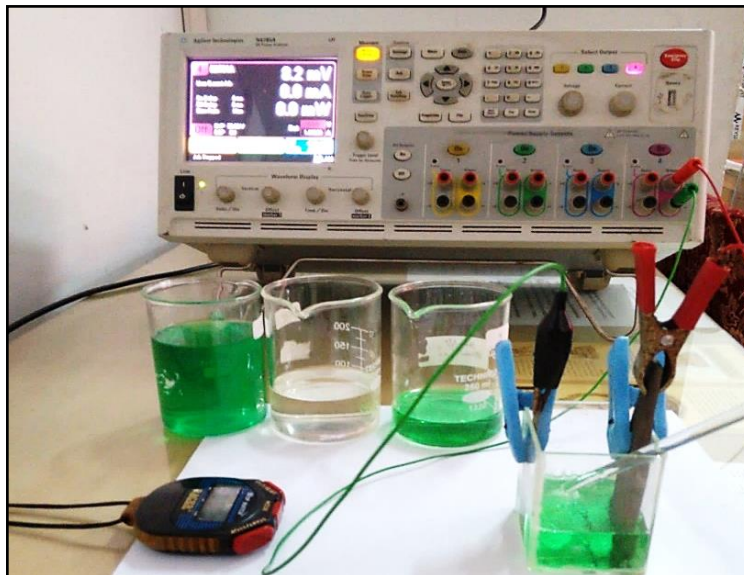


Figure 3.3 – Experimental setup used for deposition of binary alloy using DC power analyzer (N6705A, Agilent Technology, USA)

3.3.1 Development of Monolayer Alloy Coatings by Magneto-electrodeposition method

The magneto-electrodeposition (MED) of alloy coatings were accomplished at optimal c.d. in conjunction with the magnetic field of desired intensity (B), using DC power source (Aplab, LD3205), and Electromagnet (Polytronics, Model: EM 100), respectively. The full experimental set used for MED is shown in Figure 3.4. MED's were carried out under different conditions of both intensity (from 0.1 T to 0.4 T), and direction (parallel and perpendicular to the direction of flow of metal ions). The cell was kept in the space provided between the poles of an electromagnet. A constant distance was maintained between the cathode and anode. After deposition, the coated surfaces were rinsed with distilled water several times, dried in hot air and desiccated under vacuum until further testing.

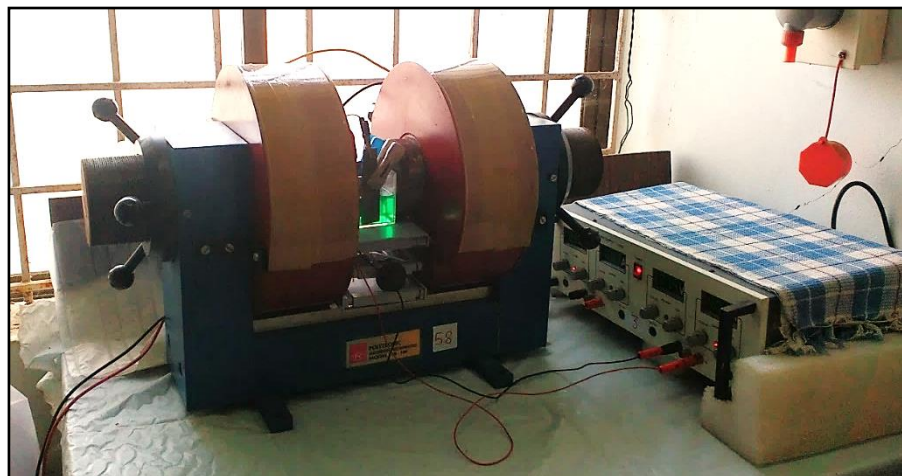


Figure 3.4 – Experimental setup used for magnetic field induced codeposition (magneto-electrodeposition) using DC Power source (Aplab, LD3205) and Electromagnet (Polytronics, Model: EM 100)

3.3.2 Development of Monolayer and Multilayer Alloy Coatings by Sono-electrodeposition Method

Ultrasound-induced electrodeposition, or simply sono-electrodeposition (SED) of both monolayer and multilayer alloy coatings were carried out by making use of an ultrasound generator (SONIC Vibra-Cell™ VC 750, 20 kHz, maximum power 750 W, sonotrode, a cylindrical rod with a 13 mm tip diameter) at different p.d. (W cm^{-2}), coupled with DC source. The ultrasonic horn was kept at a distance of 1.0 cm from the cathode during SED. The process assembly used for SED is shown in Figure 3.5. Multilayer Sn–Ni alloy coatings, having nano/micrometric layers of alloys (with alternately different compositions), were developed by turning the ultrasound generator ON (t_{ON}) and OFF (t_{OFF}) periodically during deposition. The periodic modulation in mass transfer, due to the turning ON and OFF of the sonicator, allowed the growth of coatings with a periodic change in their composition. In other words, periodic ON and OFF allowed the growth of the coatings in multilayers.



Figure 3.5 – Experimental setup used for deposition of monolayer and multilayer alloy coating, under different conditions of sonication at constant c.d. using DC Power source (Aplab, LD3205) and Ultrasound generator (SONIC Vibra-Cell™ VC 750)

3.4 ELECTROCHEMICAL MEASUREMENTS

3.4.1 Corrosion Study

All corrosion measurements were made using an electrochemical workstation (VersaSTAT3, Princeton Applied Research, USA) in a three-electrode configuration cell, using saturated calomel electrode (SCE) as a reference electrode and a platinum electrode as a counter electrode as shown in Figure 3.6. The corrosion tests were carried out, taking 1.0 cm^2 exposed surface area of the coatings in 5% NaCl solution (as representative of severe corrosion medium), maintained at 298 K, pH 6.0, prepared in distilled water. Both electrochemical methods, DC (Potentiodynamic polarization method) and AC (Electrochemical Impedance Spectroscopy) were used for evaluating the corrosion behaviors of coatings. Potentiodynamic polarization study was carried out by polarizing the test electrode with the application of a potential drift -250 mV cathodically, and $+250 \text{ mV}$ anodically relative to the OCP, at a scan rate of 1.0 mV s^{-1} . The potentiodynamic current-potential curves (Tafel plots) were simultaneously developed and extrapolated to study the corrosion behavior. Electrochemical impedance spectroscopy (EIS) study was made using an AC signal of 10 mV amplitude,

in the frequency range from 100 kHz to 10 mHz, and corresponding Nyquist plots were analyzed.

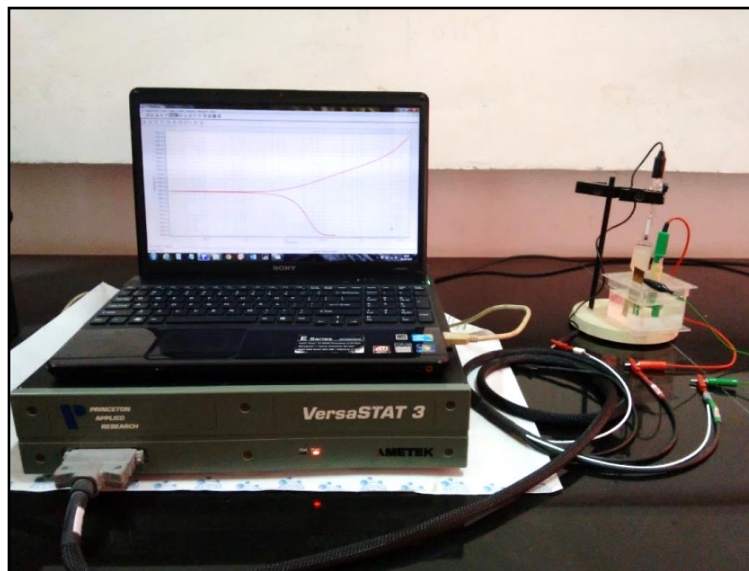


Figure 3.6 – Experimental setup used for studying the corrosion behavior of electroplated alloy coatings

The corrosion rates were expressed in mm y^{-1} , determined by the Tafel extrapolation method. From the Tafel plots, the polarization parameters, like corrosion potential (E_{corr}), corrosion current density (i_{corr}), corrosion rate (CR), anodic Tafel slope (β_a) and cathodic Tafel slope (β_c) were deduced. The corrosion rate was calculated using the following Eqn. (Fontana 1987):

$$CR(\text{mm y}^{-1}) = \frac{K \times i_{\text{corr}} \times E.W}{\rho} \quad (3.2)$$

where constant $K = 0.00327$ defines the unit of corrosion rate in mm y^{-1} , i_{corr} is the corrosion current density in $\mu\text{A cm}^{-2}$, ρ is the density of the corroding material in g cm^{-3} , $E.W$ is the equivalent weight of the alloy (g equiv^{-1}).

The equivalent weight of the alloy can be calculated using the Eqn. (3.3).

$$E.W = \frac{1}{\sum \left[\frac{n_i \times f_i}{W_i} \right]} \quad (3.3)$$

where f_i is the weight fraction of the i^{th} element in the alloy, W_i is the atomic weight of the i^{th} element in the alloy and n_i is the valence of the i^{th} element of the alloy (Fontana 1987).

3.4.2 Electrocatalytic Study

Electrocatalytic studies were carried out by coating the deposit on a cross-sectional area of a copper rod (having 1.0 cm^2 surface area), fitted into a customized glass cell, shown in Figure 3.7.

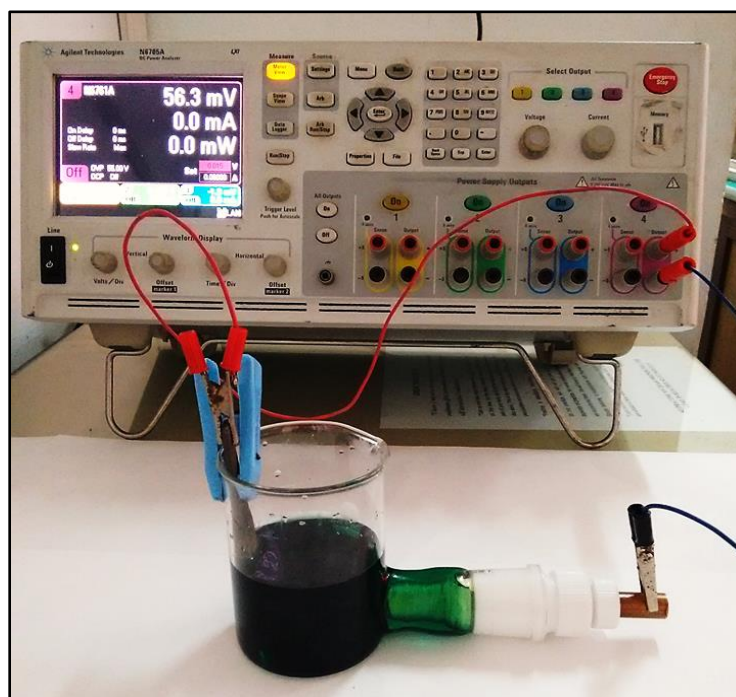


Figure 3.7 – Experimental set-up used for electrodeposition of Ni–M alloy coatings on pre-polished copper surface using DC power analyzer (N6705A, Agilent Technology, USA)

During deposition, anodes and cathodes were kept parallel to each other at 5 cm distance. Binary alloy coatings were deposited on copper plates and copper rods, keeping a 1.0 cm^2 active surface area. All electrodepositions were carried out galvanostatically for a constant duration of 600 s for comparison purpose. Same DC power analyzer (Agilent N6705A, USA) was used as the power source for electrodeposition. Electrochemical behaviors of deposits, in terms of HER and OER,

were evaluated by subjecting them to cyclic voltammetry (CV) and chronopotentiometry (CP) study in 1.0 M KOH medium, exposing 1.0 cm² surface area using electrochemical workstation (IVIUM VERTEX, Netherlands) in 1.0 M KOH as shown in Figure 3.8. Corrosion data were used to compare the stability of Ni–Mo alloy coatings in the working condition (alkaline medium), and β_c was used to determine the mechanistic pathway for HER onto the surface of the electrodeposit.

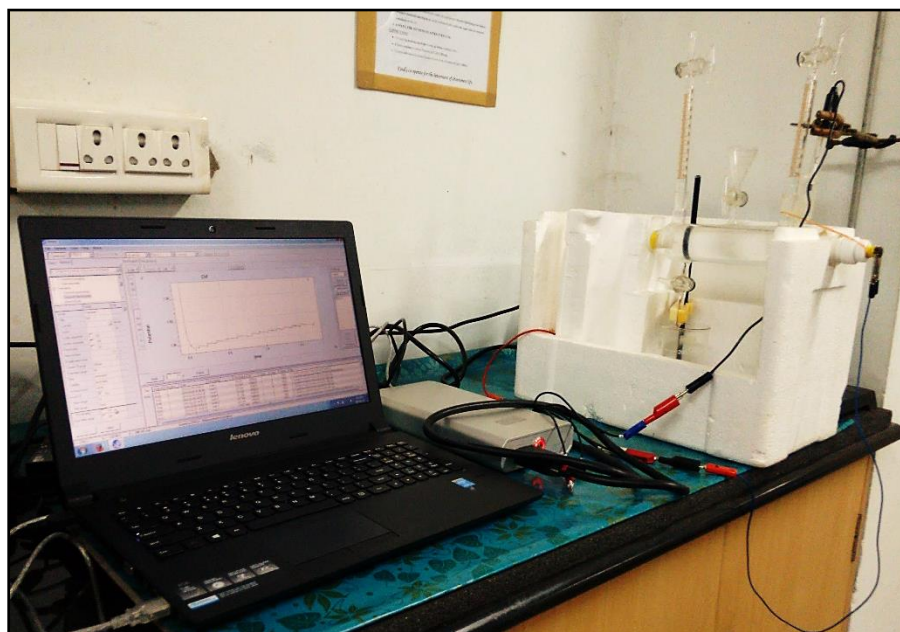


Figure 3.8 – Experimental setup used for quantitative measurement of H₂ and O₂ evolved on test electrode during water splitting reaction

3.5 CHARACTERIZATION OF THE COATINGS

Surface morphology of coatings was examined using scanning electron microscopy (SEM, EVO 18 from Carl Zeiss, Germany and SEM, Model JSM-6380 LA from JEOL, Japan). The change in the composition of coatings is studied by energy dispersive X-ray (EDX) analysis, interfaced with SEM. To average out the composition, each reading is taken from an average of the five readings, taken at five different locations. The phase structures of coatings for different conditions were analyzed by X-ray diffraction (XRD) study (Rigaku Miniflex 600), using Cu K α ($\lambda=1.5406$ Å) radiation, in continuous scan mode at a scan rate of 2° min⁻¹ to demonstrate the phases and their

crystallite size of the nanocrystalline coatings. The numerical procedures were facilitated by using the computer software PANalytical X'Pert Highscore Plus. All graphs were generated using Origin software version 8.2. The grain size of all electroplated Ni–Mo alloy coatings has been calculated using Scherrer Eqn. (Anicaia et al. 2013) given in Eqn. (3.4).

$$d = \frac{0.9\lambda}{\beta \cos \theta} \quad (3.4)$$

where d is crystallite size, λ is the wavelength of X-ray radiation, β is the full width at half height of symmetrical shape of the diffraction peak and θ is the Bragg's angle.

The AFM (atomic force microscope) measurements were carried out using an Innova SPM atomic force microscope. The alloy surfaces were imaged in tapping mode. An antimony doped silicon cantilever having a force constant in the range of 20–80 N m⁻¹ was used to analyze the alloy surface topography. The surface roughness of the membranes, expressed in terms of average roughness was measured. The chemical states of the elements in the as-synthesized samples were recorded by using X-ray photoelectron spectroscopy (XPS, Kratos XSAM800) using monochromatic Al-K α radiation. All measurements were performed after 10 min of argon ion sputtering to avoid the influence of oxidation by air and were referenced to the C (1s) line binding energy of 284.5 eV.

3.6 THICKNESS AND HARDNESS OF THE COATINGS

The thickness of electrodeposited coatings was calculated theoretically from Faraday's law using Eqn.,

$$t = \frac{E.W \times i \times CCE \times \Delta T}{d \times F} \quad (3.5)$$

t = thickness of the deposit, E = equivalent weight of deposit, i = c.d. at which deposition is carried out, CCE = cathode current efficiency, ΔT = time of deposition, d = density of deposit and F is the Faraday's constant (96,485C mol⁻¹).

Theoretically determined thickness value is further verified using Digital Thickness Tester (Coatmeasure Model M&C, AA Industries/Yuyutsu Instruments). While the Faradaic efficiency (FE) or CCE was calculated using the mass gained by the substrate, charge transferred and chemical composition of the deposit:

$$FE = \frac{\text{measured mass gain}}{\text{theoretical mass gain}} \times 100 = \frac{w \times F}{E.W \times I \times t} \times 100 = \frac{wF}{It} \sum \frac{c_i}{M_i} \times 100 \quad (3.6)$$

here, w = measured mass of the deposit (g), t = time of deposition (s), I = average applied c.d. (A), c_i = weight fraction of the element in the alloy deposit, n_i = number of electrons transferred per atom of each metal and M_i = atomic mass of that element.

The hardness of coatings was measured using Digital Micro Hardness Tester (CLEMEX). Averages of 10 hardness measurements were calculated as the hardness value.

CHAPTER 4

CHAPTER 4

MAGNETO-ELECTRODEPOSITION OF Sn–Ni ALLOY COATING FOR BETTER CORROSION PROTECTION

This chapter details the optimization of deposition conditions of a new Sn–Ni alloy bath, for the development of its coating for good corrosion resistance, and how it can be improved further using the principle of magneto-electrodeposition (MED). The first part reports the limiting conditions for deposition of Sn–Ni coatings by conventional electrodeposition (ED) method and their characterization, the second part details the significant increase in its corrosion resistance through MED approach; using the same bath, depositing at the same time.

4.1 INTRODUCTION

Sn–Ni coatings are of great interest in galvanotechnics, particularly due to its very bright appearance and corrosion resistance behaviour. The excellent frictional resistance, ability to retain an oil film on its surface and good throwing power compared to chrome plating made Sn–Ni alloy coating as the most industrially important. According to Brenner (1963), there have been many studies on Sn–Ni alloy deposition from fluoride, pyrophosphate and chloride solutions. In all these, the most important aspect of ED Sn–Ni alloy coatings is their bright appearance and good corrosion resistance. But good corrosion resistance of ED Sn–Ni coating is limited from further improvement due to its inherent single-phase homogeneous intermetallic compound formation, having equiatomic composition NiSn (35 wt.% Ni–65 wt.% Sn, 50 at.% Ni–50 at.% Sn) (Tan et al. 2013), and most importantly the precipitation of bath at high Sn content due to hydrolysis. Hence, any effort to increase the corrosion resistance of Sn–Ni coatings by manipulating the deposition conditions, like current density (c.d.), bath composition and even temperature were found to be practically difficult. However, from the literature, it is well known that the total electrochemical process can be greatly affected by applying the magnetic field, under governing principles of *magneto-hydrodynamic* (MHD) effect (Fahidy 1983). The magnetic field induces the movement

of the electrolyte by Lorentz force, and thereby increase/decrease the transport of electro-active molecules towards the electrode.

Keeping in view of the appealing appearance, and better corrosion resistance of Sn–Ni alloy coatings, a new pyrophosphate bath has been proposed for development of protective coatings on MS against corrosion. Thus, by taking the benefit of MHD effect, an effort was made to increase the corrosion resistance character of ED alloy coatings by MED method. The effect of inducing the magnetic field, in terms of both intensity and direction on corrosion behaviors have been studied. Emphasis has been given to explain how applied magnetic field can bring change in mass-transport process at the cathode. The change in surface morphology, composition and phase structure of the coatings, due to MED were analyzed using advanced instrumental techniques. Improved corrosion protection, due to different crystallographic orientation, attributed by the applied magnetic field has been identified, and results are discussed.

4.2 OPTIMIZATION OF Sn–Ni ALLOY BATH

Current density (c.d.) is the most important of all operating variables in electroplating, and no study of alloy deposition is complete without a comprehensive data on its variation. Moreover, the effect of c.d. is less consistent or predictable than that of the other operating variables, with respect to the change in the composition of the electrodeposited alloy. Hence, to begin with, a detailed study on the effect of c.d. on the composition of Sn–Ni alloy was undertaken, and their electrochemical corrosion behaviors were evaluated. A new potassium pyrophosphate ($K_4P_2O_7$) bath has been proposed for deposition of bright Sn–Ni alloy coatings on MS. $K_4P_2O_7$ and gelatin were used as a complexing agent and brightening agent, respectively. Gelatin was dissolved in hot water, being insoluble in cold water; and then added into the bath to impart homogeneity and brightness to the coating. The pH of the bath was adjusted to 8.6 using either dil. NaOH or HCl, and then filtered before each deposition. Bath composition and operating parameters were arrived after optimization and are given in Table 4.1.

Table 4.1 – Composition and operating parameters of optimized Sn–Ni alloy bath

Bath constituents	Amount (g L ⁻¹)	Operating parameters
SnCl ₂ . 2H ₂ O	22.6	Anode: pure Sn plate
NiCl ₂ . 6H ₂ O	33.7	Cathode: MS
K ₄ P ₂ O ₇	119	pH: 8.6
Gelatin	5.0	Temperature: 298 K
		Deposition time: 10 min
		Current density: 1.0 – 4.0 A dm ⁻²

It is appropriate to recall here that the standard electrode potentials (E°) of Sn and Ni are relatively close together: Sn, -0.14 V and Ni, -0.25 V, and has a difference of only about 0.1 V. In view of this proximity of E° values, one would expect alloys to be readily deposited from a mixed solution of the simple ions. Because of the high overvoltage of nickel deposition, this does not occur easily, and mainly tin deposits from solutions containing both of the metals as simple ions. But under the conditions of some complexing agents, the cathode potentials involved in the deposition of Sn–Ni alloys are of unusual interest and show the anomalous type of codeposition (Brenner 1963). These peculiarities are due to the cathode potentials involved in the deposition of the alloy and found that there exists a large displacement of the cathode potential curve of alloy deposition towards more noble potentials, with respect to the potentials of the parent metals. Hence, in the present pyrophosphate bath, it is essential to consider the fact that bath follows the anomalous type of codeposition with preferential deposition of more noble metal (Sn) compared to less noble metal (Ni). This is due to a large shift in cathode potential, caused by the complexation of metal ions in the bath.

4.2.1 Compositional Analysis

The composition of Sn–Ni coatings deposited at different c.d.'s from the same bath is investigated by EDX analysis and the corresponding EDX spectrum of Sn–Ni alloy deposited at 1.0 A dm⁻², having ~ 80.4 % Sn is shown in Figure 4.1. From the

composition analysis it is evident that wt.% of Sn is more than wt.% of Ni in the coatings, making Sn as the most readily deposit-able metal between two. High wt.% of Sn at low c.d. range indicates that the bath follows the anomalous type of codeposition (Brenner 1963). Further, it was found that the wt.% of Sn decreases with the increase of c.d. as shown in Figure 4.2.

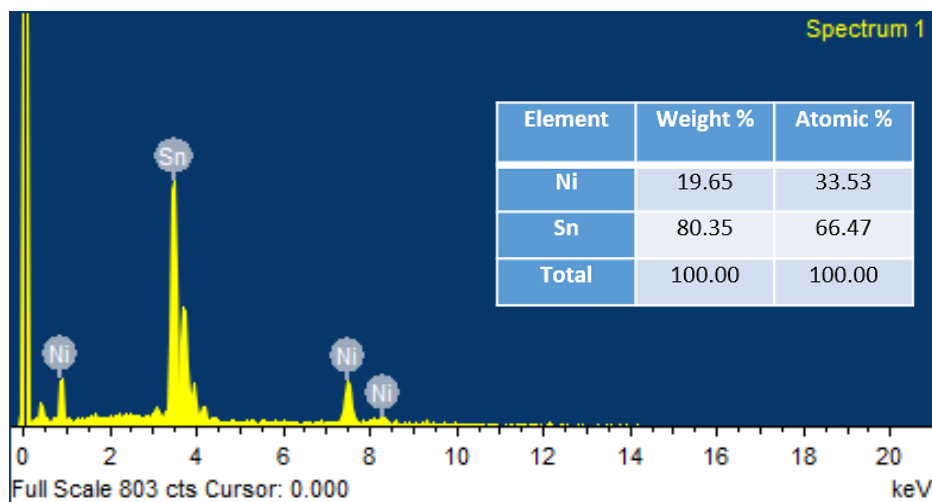


Figure 4.1 – EDX spectrum showing relative peaks of Sn and Ni in Sn–Ni alloy deposited at 1.0 A dm^{-2}

4.2.2 Effect of Current Density on Thickness, Composition, and Hardness of the Deposit

The applied c.d. has a great influence on the appearance, chemical composition, and physical properties of the deposited coatings. The coatings appeared bright when deposited at low c.d., but those deposited at higher c.d. were semi-bright, which is reflected in their CR values (Table 4.2). The thickness of Sn–Ni coatings, developed at different c.d. is shown in Table 4.2. The effect of c.d. on hardness and wt.% of Ni in the deposited coatings are shown in Figure 4.2. Hardness, along with wt.% of Ni is found to increase with c.d. This increase in hardness is due to increase in nickel content of the coatings when compared to tin.

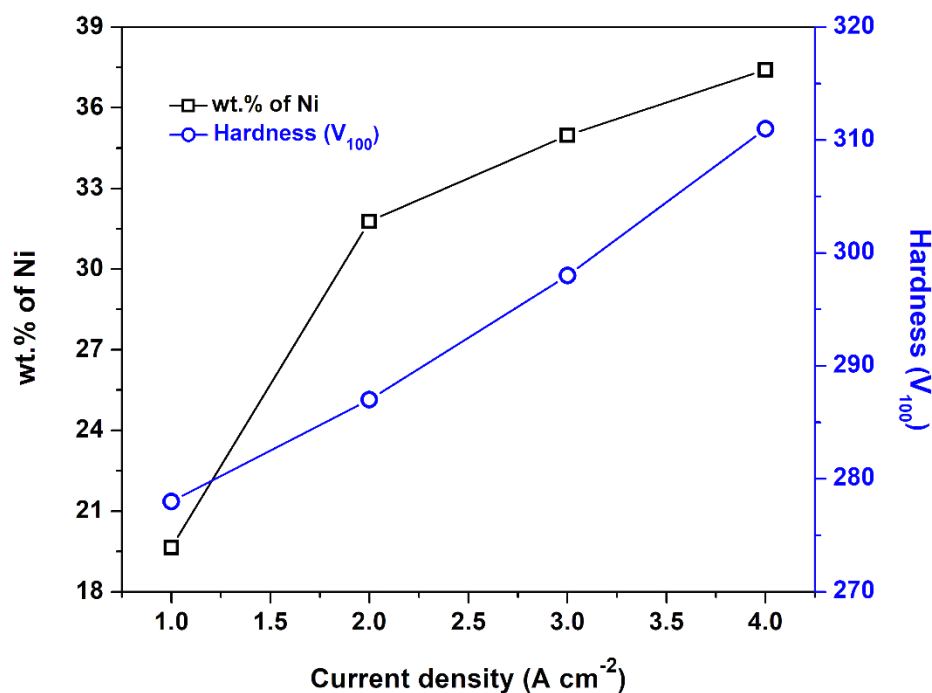


Figure 4.2 – Effect of c.d. on Ni content and hardness of Sn–Ni coatings

4.2.3 Surface Morphology

The SEM micrographs of Sn–Ni alloy coatings at different c.d.'s is shown in Figure 4.3. Surface morphology of the coatings was found to be changed drastically with c.d., as shown in Figure 4.3, from (a) through (d). Surface morphology of the coatings indicates that c.d. plays a significant role on crystal orientation of the deposit. All coatings are found to be characterized by nodules. The dimensions of nodules for samples corresponding to 1.0 and 2.0 A dm⁻² were found to be smaller than those corresponding to 3.0 and 4.0 A dm⁻². The coating corresponding to 1.0 A dm⁻² (Figure 4.3 (a)) is comparatively smooth; while those at higher deposition c.d., shown in Figure 4.3 (b), 4.3 (c) and 4.3 (d) are porous. Further, it should be noted that the both number and dimensions of pores were increased with c.d.'s. This progressive increase in the porosity with c.d. may be attributed to the formation of metal hydroxide at cathode film, due to an increase in pH caused by local alkylation (due to excessive hydrogen evolution during deposition). Experimental observation revealed that Sn–Ni alloy, deposited at 1.0 A dm⁻² is more bright, uniform and homogeneous, hence, responsible for better corrosion protection.

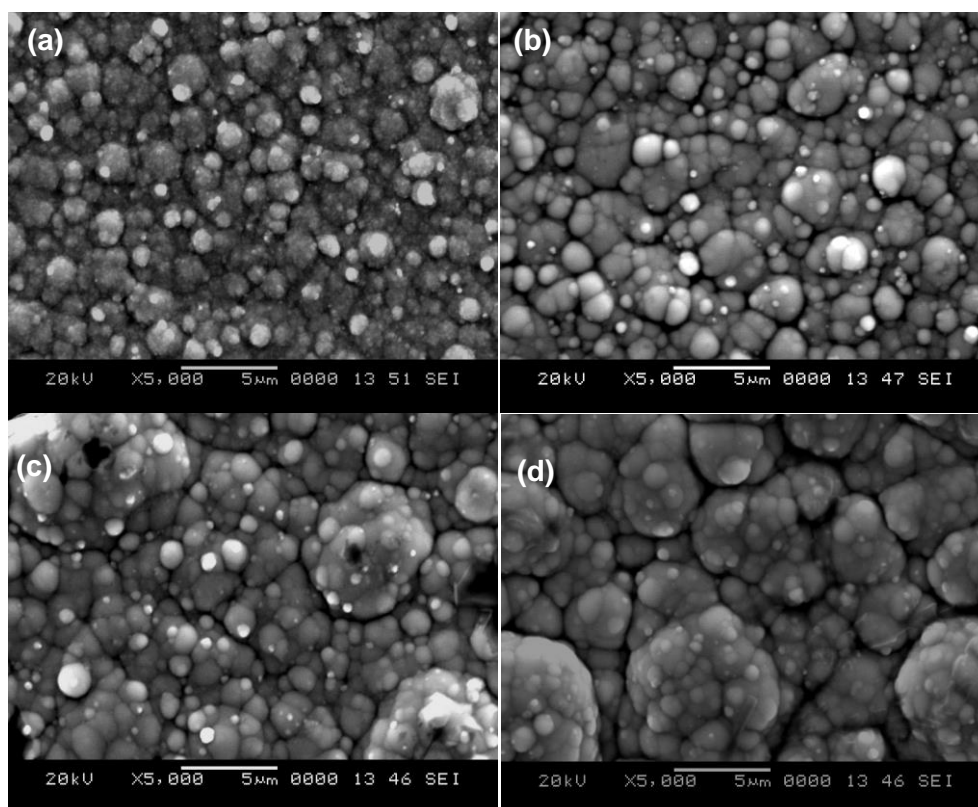


Figure 4.3 – SEM images of Sn–Ni alloy coating deposited at a) 1.0 A dm^{-2} , b) 2.0 A dm^{-2} , c) 3.0 A dm^{-2} and d) 4.0 A dm^{-2}

4.2.4 X-Ray Diffraction Study

The crystal structure of ED Sn–Ni alloys, under varying conditions of c.d.'s was studied by XRD analyses. The identification of the phases was obtained from the peak profiles of X-ray reflection, plotted as a function of 2θ . The XRD patterns of Sn–Ni alloys, deposited at different c.d.'s in the range of 1.0 to 4.0 A dm^{-2} is given in Figure 4.4. The two prominent peaks at the angle corresponding to 30.4° and 43.8° are due to Ni_3Sn_2 (101) and Ni_3Sn_2 (110) phase. There is a presence of Ni_3Sn_2 (201), (202), (211) and (300) phases at all c.d.'s but they are not well formed. The indexed phases were likely to be in good agreement with the standard pattern of Ni_3Sn_2 (JCPDS No. 00 007-0256). Further, almost same XRD peaks indicate that coatings deposited at different c.d.'s correspond to same phase composition, and are the results of stable Ni_3Sn_2 intermetallic compound formation in the deposit. An increase in intensity with c.d. was observed, with no change in diffraction angle. It may be explained by the limited diffusion current

for hydrogen evolution, which suppresses the anomalous codeposition (due to decreased local alkalinity) (Rao et al. 2014). This indicates that only the composition of coating changed with c.d., without any change in the phase structures.

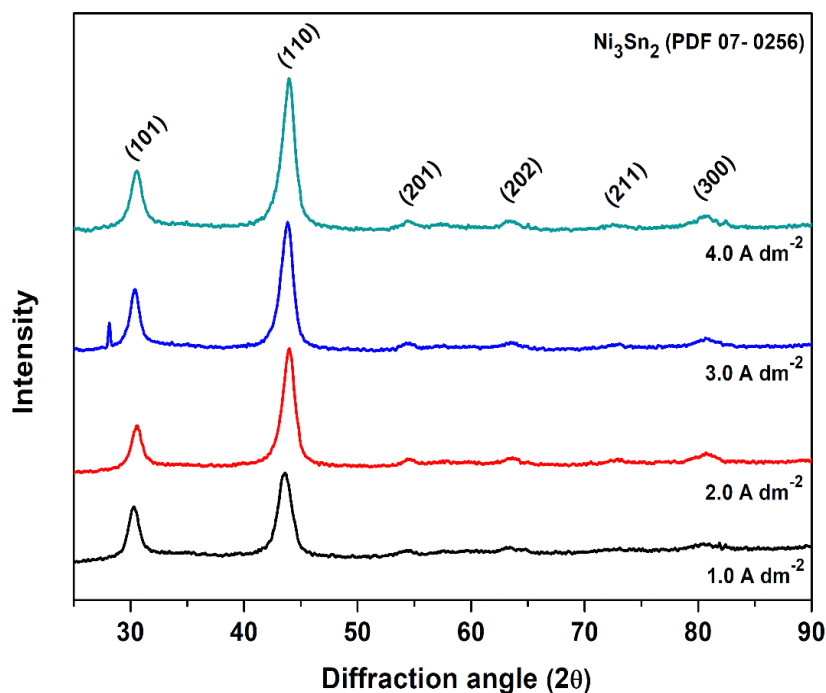


Figure 4.4 – XRD peaks of Sn–Ni alloy coatings deposited at different c.d.’s

4.2.5 Corrosion Study

The corrosion behavior of Sn–Ni coatings deposited at different c.d.’s was evaluated by subjecting them to polarization study (Jones 1996). Corrosion rates (CR’s) were calculated by Tafel extrapolation method, and corresponding plots are shown in Figure 4.5. The observed E_{corr} , i_{corr} and CR are reported in Table 4.2. The corrosion data revealed that optimized bath (Table 4.1) could produce the most bright, smooth, uniform Sn–Ni coatings at c.d. = 1.0 A dm^{-2} , showing minimum CR ($18.60 \times 10^{-2} \text{ mm y}^{-1}$), compared to those coatings produced at higher c.d.’s (Table 4.2). The improved corrosion resistance is attributed to the high Sn content of the alloy and also due to less porous surface of the coating, as the smooth surface provides fewer sites for localized corrosion attack.

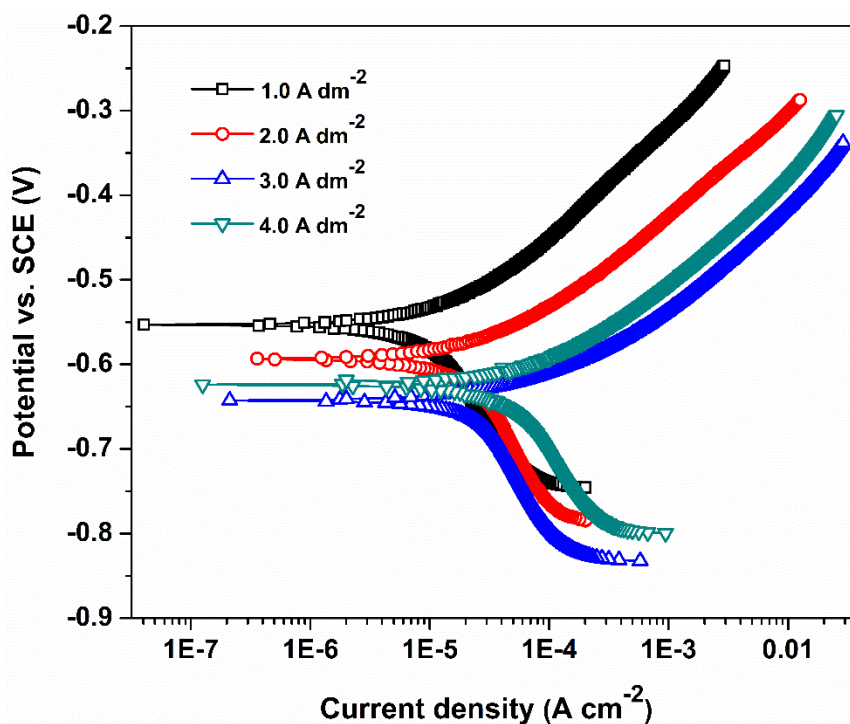


Figure 4.5 – Potentiodynamic polarization curves of Sn–Ni coatings developed at different c.d.'s

Table 4.2 – Coating characteristics of monolayer Sn–Ni alloy coating developed at different c.d.'s

c.d. (A dm ⁻²)	Thickness (μm)	$-E_{\text{corr}}$ (V vs. SCE)	i_{corr} ($\mu\text{A cm}^{-2}$)	CR ($\times 10^{-2}$) mm y ⁻¹)
1.0	8.2	0.553	9.761	18.60
2.0	9.5	0.593	20.78	39.59
3.0	11.0	0.642	23.89	45.52
4.0	12.6	0.623	28.40	54.12

The powerful and non-destructive EIS method has also been used to study the corrosion behavior of Sn–Ni alloy coatings. The plot of the imaginary impedance component (Z'') against the real impedance component (Z') at each excitation

frequency, called the Nyquist plot was used to study the corrosion behavior of Sn–Ni alloy coatings, and it is shown in Figure 4.6. The interception of frequency responses on the real axis of the Nyquist plot at higher frequencies is attributed to the electrolyte bulk resistance (R_s) and at lower frequencies to the polarization resistance or charge transfer resistance (R_{ct}) (Barsoukov and Macdonald 2005). The existence of single semicircle for all coating configuration showed that single charge transfer process is involved in the corrosion process (Ullal and Hegde 2014). The larger capacitive loop, observed at high-frequency limit indicates that the increased corrosion protection is attributed by decreased double layer capacitance (C_{dl}).

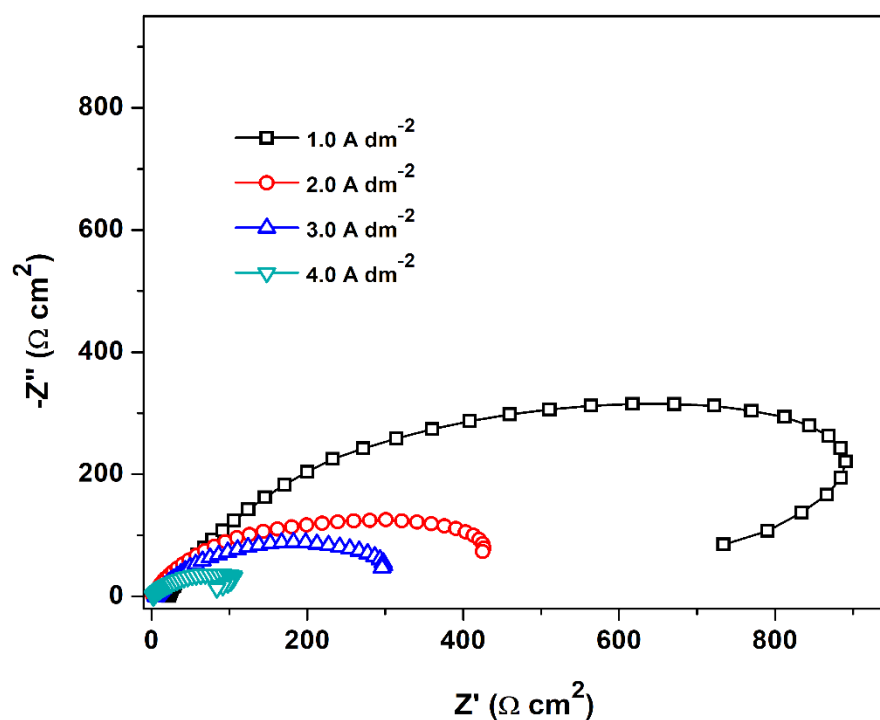


Figure 4.6 – Nyquist plots of Sn–Ni alloy coatings deposited at different c.d.'s

A decrease in the radius of a semicircle with c.d. indicated that CR bears a close relation with c.d. employed for its deposition. Further, the maximum diameter of the capacitive loop, corresponding to the optimal c.d. (1.0 A dm^{-2}) confirmed that the deposit is the most corrosion resistant. The anomalous flattening behavior of Nyquist plot is generally ascribed to the inhomogeneity of the metal surface arising from surface roughness, or interfacial phenomena occurring during deposition (Dobrzański et al. 2007).

4.3 MAGNETO-ELECTRODEPOSITION OF Sn–Ni ALLOY COATINGS

As stated earlier, the proposed bath could develop Sn–Ni coating at 1.0 A dm^{-2} , with high Sn content (about 80.4%) and exhibits the least CR, using the principle of *conventional electrodeposition* (ED). High Sn (more noble metal) content at low c.d. range gives an indication that Sn content in the deposit cannot be further increased by increasing c.d., as envisaged by Brenner (1963). Further, a decrease of Sn content at high c.d.'s, (after 2.0 A dm^{-2}) supports that limiting current density (i_L) for deposition of Sn is in the range of 1.0 A dm^{-2} . Therefore, under these conditions of experimental observation, there are two options to increase the Sn content, thereby increasing the corrosion resistance of the coatings. They are either to decrease the deposition c.d. (below 1.0 A dm^{-2}), or to increase the molar ratio of $[\text{Sn}^{+2}]/[\text{Ni}^{+2}]$ in the bath, i.e. by increasing $[\text{Sn}^{+2}]$ in the bath. Since $\text{SnCl}_2 \cdot 2\text{H}_2\text{O}$ starts precipitating at a high molar ratio of $[\text{Sn}^{+2}]/[\text{Ni}^{+2}]$ in the bath due to hydrolysis, no further decrease of CR is expected to be achieved. The c.d. below 1.0 A dm^{-2} is not suggested to use for the development of sound coating. Thus, these limitations (low i_L and precipitation of electrolyte) for the development of more corrosion resistant Sn–Ni alloy coating has been tried to resolve by taking the advent of *magneto-electrodeposition* (MED), and experimental results are discussed below.

The literature on MED reveals that magnetic field has a crucial role in mass transport process towards EDL, or cathode film (Hinds et al. 1998, Matsushima et al. 2008). Hence, by using the same electrolytic bath (Table 4.1), monolayer Sn–Ni alloy coatings has been accomplished on MS by MED approach. The coatings have been developed by applying the magnetic field (B), both in direction, parallel and perpendicular to the plane of the cathode. The experimental setup used for MED is shown schematically in Figure 4.7. A PVC cell of 200 mL capacity was kept in the gap between two electromagnets, and a constant distance was maintained between cathode and anode. The magnetic field was considered to be constant and uniform, and experiments were carried out under different conditions of magnetic field intensity (0.1 T–0.4 T). Accordingly, MED Sn–Ni alloy coatings have been deposited, and their corrosion behaviors were studied. Change in the composition, surface morphology and

crystallographic orientations of the coatings, due to the applied magnetic field have been observed, and results are discussed.

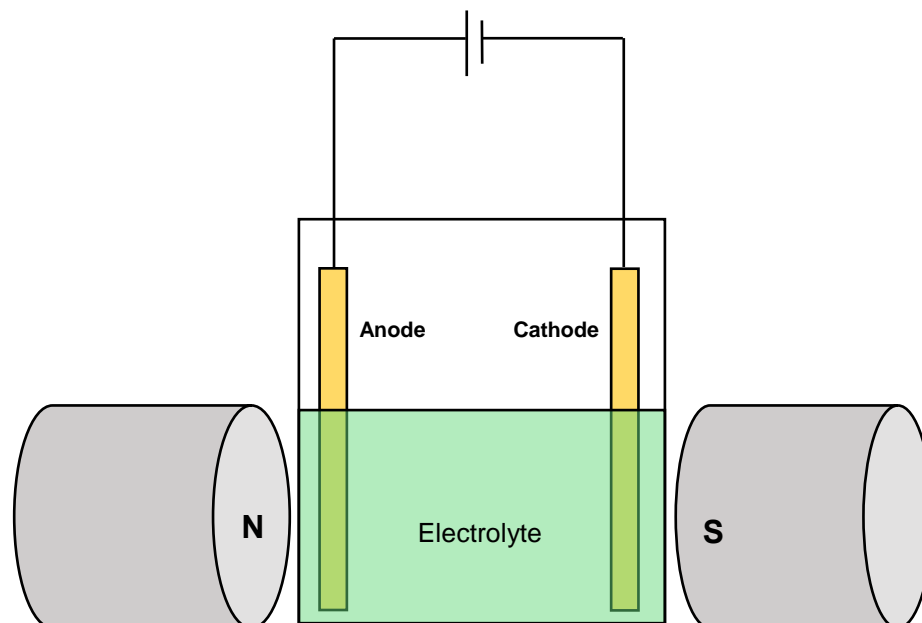


Figure 4.7 – Schematic setup used for deposition of Sn–Ni alloy under the influence of magnetic field, where N and S represent North and South Pole of an Electromagnet

4.3.1 Surface Morphology

The surface morphology of MED coatings, developed under different conditions of magnetic field intensity (B), have been examined under SEM. The surface morphology of MED coatings under perpendicular orientation varying from 0.1 to 0.4 T is shown in Figure 4.8. A clear difference in the surface morphology of ED and MED coatings was found as seen in Figures 4.3 and 4.8. It should be noted that MED coatings display more uniform coating compared to ED coatings (Figure 4.3), developed from the same bath, at same c.d. The enhancement in the compactness of MED coatings is due to the difference in the crystallographic orientation of atoms during electrodeposition, affected by the induced magnetic field as reported earlier by Matsushima et al. (2008).

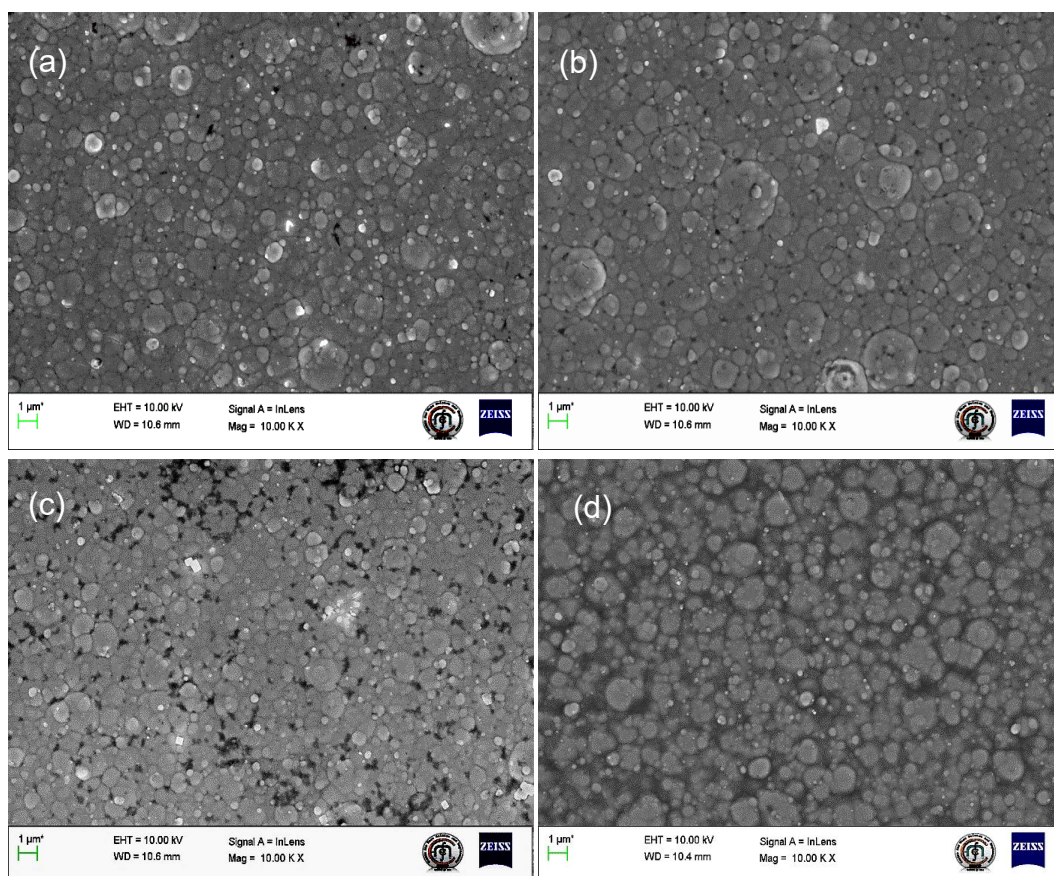


Figure 4.8 – SEM images of MED Sn–Ni alloy coatings deposited at different conditions of B (perpendicular orientation), where (a), (b), (c) and (d) = 0.1 T, 0.2 T, 0.3 T and 0.4 T, respectively (all are at optimal $c.d.$ = 1.0 A dm^{-2})

4.3.2 XRD Analysis

XRD patterns of coatings at different conditions of magnetic field intensity, applied parallel and perpendicular is shown in Figures 4.9 (a) and (b), respectively. The XRD peaks of Sn–Ni alloy coating, developed by ED method is represented as $(\text{Sn–Ni})_{B=0 \text{ T}}$ is shown as the reference in Figures 4.9 (a) and (b), for comparison purpose. A significant change in the phase structure of Sn–Ni alloy coatings were found, when the deposition was carried out under the conditions of induced magnetic field, as seen in Figure 4.9.

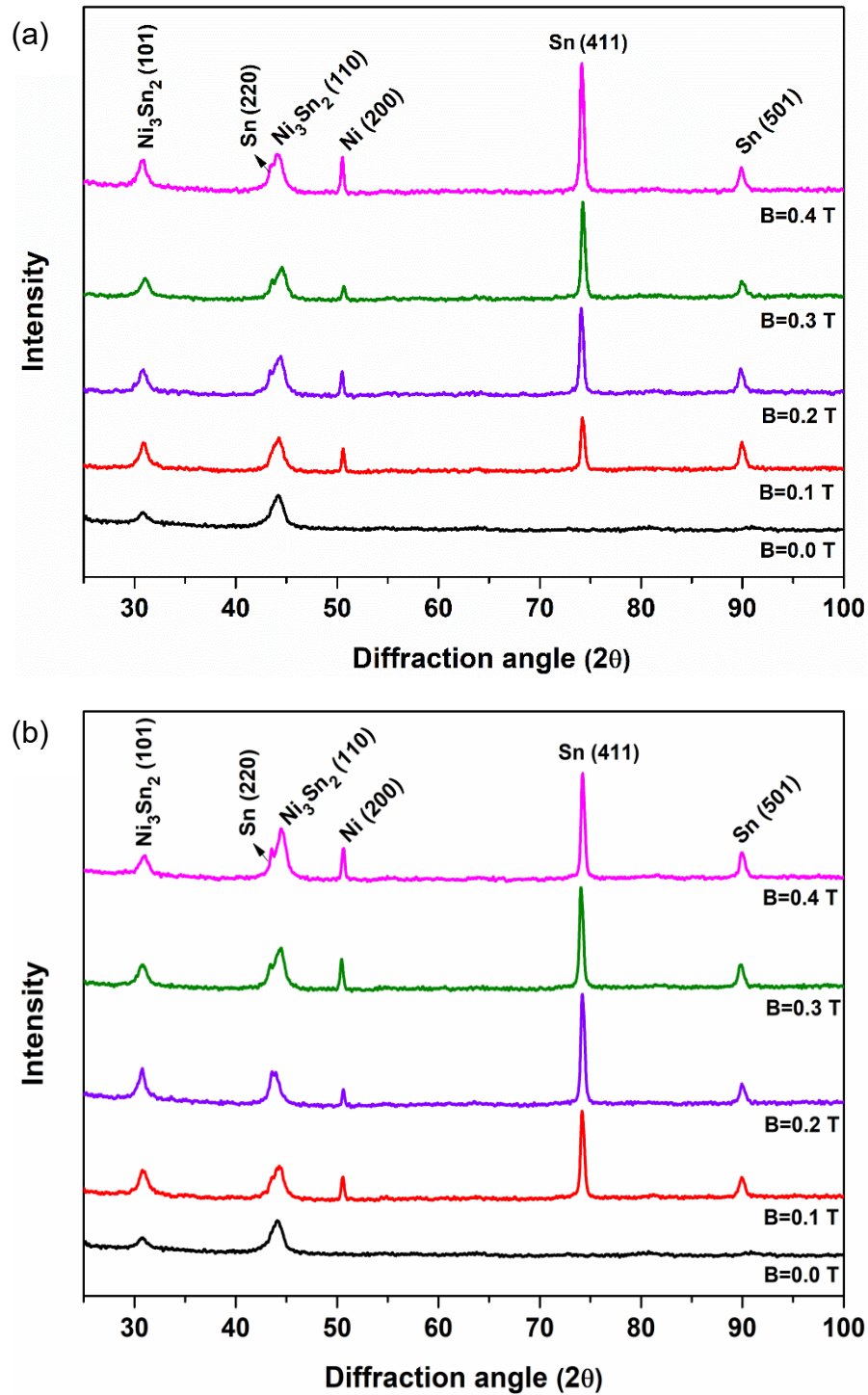


Figure 4.9 – XRD patterns of MED Sn–Ni alloy coatings deposited at optimal c.d. under different conditions of B (specified on each XRD plot), applied (a) parallel, and (b) perpendicular to the direction of movement of ions

The unique phase structures found in MED coatings, at $2\theta = 74.2^\circ$ and 89.8° corresponds to Sn phases, namely (411) and (501) (JCPDS No. 03-065-2631). There is also an appearance of cubic Ni (200) phase at 50.5° (JCPDS No. 00-001-1258) and tetragonal Sn (220) at 43.5° present on top of broad reflection Ni_3Sn_2 (110), arises due to applied magnetic field which does not correspond to any distinct phases in ED Sn–Ni coatings, i.e. corresponding to $B = 0$ T as seen in Figure 4.9 (a) and (b). The presence of pure Sn phases attributes to the increase in Sn content of the coatings developed under varying intensity of magnetic field, supported by wt.% of Sn data, given in Table 4.3. Therefore, a substantial decrease in CR of MED Sn–Ni coatings can be attributed to the new phases, which are otherwise not observed in ED coatings (developed under natural convection), from the same bath. Thus, from the XRD signature, it may be concluded that the preferential orientations of Sn (220), (411), and (501) phases which are favored to exist only in MED Sn–Ni alloy coatings are responsible for their improved corrosion protection, compared to ED coatings. The grain size of all electroplated Sn–Ni alloy coatings has been calculated using Scherrer equation (Eqn. (3.4)). On calculating the crystallite size, the average crystallite size was found to be in the range of 20 nm. Hence, it can be inferred that the MED Sn–Ni alloy coatings from the proposed bath is nanocrystalline in nature.

4.3.3 Corrosion Behaviour of MED Sn–Ni Alloy Coatings

MED Sn–Ni alloy coatings have been developed by keeping other parameters constant (c.d. = 1.0 A dm^{-2} and pH = 8.6), except magnetic field intensity. Different magnetic field intensity (from 0.1 to 0.4 T) was applied, both parallel and perpendicular to the direction of migration of ions, and corresponding corrosion data are reported in Table 4.3 in comparison with ED coatings. Sn–Ni alloy coatings deposited under natural convection and forced convection, i.e. ED and MED coatings are conveniently represented as $(\text{Sn–Ni})_{B=0 \text{ T}}$ and $(\text{Sn–Ni})_{B=0.1 \text{ T/perp, or para}}$, respectively, indicating the intensity and direction of the magnetic field used.

Table 4.3 – Effect of applied magnetic field intensity, B on deposit characters of Sn–Ni alloy electrodeposited from optimal bath at 298 K

Sn–Ni coating configuration	wt.% Sn	Thickness (μm)	$-E_{corr}$ (V vs. SCE)	i_{corr} ($\mu\text{A cm}^{-2}$)	CR ($\times 10^{-2}$ mm y^{-1})
(Sn–Ni) $_{B=0.1}$ T/para.	86.7	8.1	0.524	7.80	17.48
(Sn–Ni) $_{B=0.2}$ T/para.	90.2	7.8	0.510	5.09	11.41
(Sn–Ni) $_{B=0.3}$ T/para.	92.5	7.5	0.503	4.47	10.02
(Sn–Ni) $_{B=0.4}$ T/para.	89.5	7.3	0.508	6.80	15.24
(Sn–Ni) $_{B=0.1}$ T/perp.	87.5	7.7	0.580	1.25	2.76
(Sn–Ni) $_{B=0.2}$ T/perp.	94.2	7.2	0.496	0.96	2.18
(Sn–Ni) $_{B=0.3}$ T/perp.	90.7	6.4	0.538	2.48	5.64
(Sn–Ni) $_{B=0.4}$ T/perp.	89.4	5.5	0.517	6.67	15.18
(Sn–Ni) $_{B=0}$ T	80.4	8.2	0.553	9.76	18.60

From the corrosion data reported in Table 4.3, it can be observed that corrosion protection efficacy of MED coatings increased drastically, compared to the one developed under natural convection. At the same time, it is important to note that wt.% of Sn in the deposit has increased depending on both direction and intensity of magnetic field intensity, compared to that in ED coating (80.4%), and reported in Table 4.3. Here, the effect of perpendicular magnetic field intensity is more pronounced than the parallel one. This may be explained by increased Lorentz force (F), which is the vector product of current density (i) and magnetic field intensity (B), given by relation, $F = i \times B \sin\theta$ (Tacken and Janssen 1995). The potentiodynamic polarization behaviors of MED Sn–Ni alloy coatings, developed under different magnetic field intensity (applied in the perpendicular direction) is shown in Figure 4.10. From this data, it may be inferred that coatings having (Sn–Ni) $_{B=0.2}$ T/perp configuration showed the least CR (2.18×10^{-2} mm y^{-1}) when compared with all other coatings.

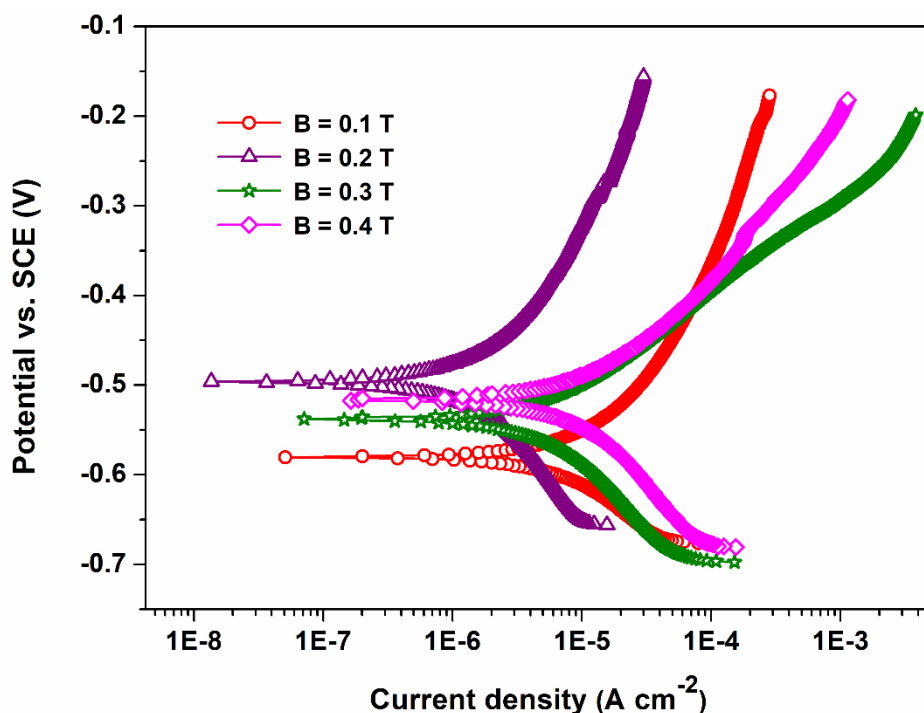


Figure 4.10 – Tafel plots of MED Sn–Ni alloy coatings under different conditions of applied B (perpendicular), developed from the optimal bath

The corrosion behaviors of Sn–Ni alloy coatings were evaluated more accurately by Nyquist plots, by drawing Z_{real} vs. Z_{img} components of impedance over a wide range of frequency. Figure 4.11 displays the Nyquist plots of MED Sn–Ni alloy coatings at different magnetic field intensity (only perpendicular). As seen, the solution resistance R_s is nearly same in all cases, since same solution and cell configurations are used for the study. All impedance plots, (Figure 4.11) are found to be in depressed semi-circular (incomplete) shape, and this type of anomalous flat semicircles are generally attributed to the inhomogeneity of the metal surface arising from surface roughness or interfacial phenomena. They are generally referred to frequency dispersion of interfacial impedance inherent of electrodeposited coatings. The single capacitive loop without kink on the entire frequency range, for all MED Sn–Ni coatings (Figure 4.11) indicates that only one charge transfer process having one-time constant ($\tau = RC$) is operative at the interface (Yuan et al. 2009). The highest corrosion resistance of $(\text{Sn–Ni})_{B=0.2 \text{ T/perp}}$, compared to other alloy coatings are evident from its large capacitive loop, shown in the inset of Figure 4.11, a similar observation was made by Rao and Hegde (2014).

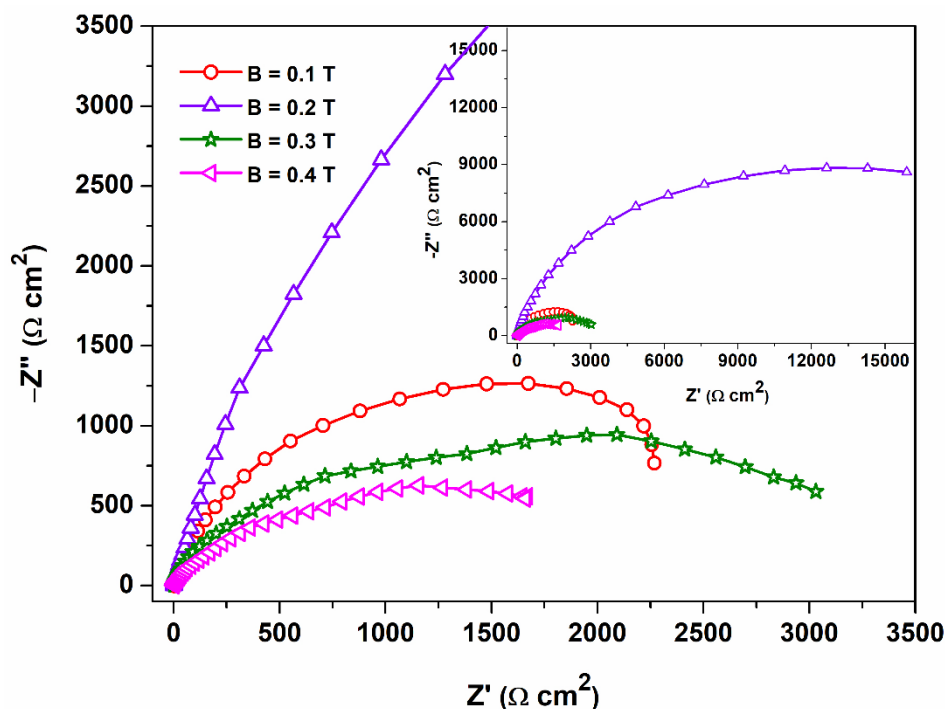


Figure 4.11 – Nyquist plots of MED Sn–Ni alloy coating at different conditions of applied B (perpendicular) deposited from the optimal bath

From the thickness data given in Tables 4.2 and 4.3, it may be noted that the thickness of Sn–Ni alloy coatings increases with increase in c.d., may be explained by Faraday’s law. However, in presence of magnetic field intensity, the thickness of coatings decreased with the increase in its intensity. This is due to the decrease in the thickness of diffusion layer caused by the increased tangential velocity of the ions. Further, it was observed that the decrease of coating thickness is more pronounced in the case of perpendicular magnetic field intensity as seen in Table 4.3 and are attributed to the MHD effect caused by Lorentz force (Rao et al. 2013, Zieliński et al. 2015). The less CR’s of MED coatings, compared to ED coatings (Tables 4.2 and 4.3) can also be interpreted in terms of decreased geometric surface area of the coatings instead of considering their true surface area, used for the calculation. Since ED coatings are more porous, they offer large surface area compared to MED coatings (Figures 4.2 and 4.6), and hence responsible for showing more corrosion current density (i_{corr}), therefore, more CR.

In Figure 4.12, the relative response of Nyquist and Tafel plots of MED Sn–Ni alloy coatings, deposited under different conditions of the magnetic field is shown. From the graph, it is evident that coating developed at $(\text{Sn–Ni})_{B=0.2 \text{ T/perp}}$ is superior in terms of their corrosion stability when compared to other coatings.

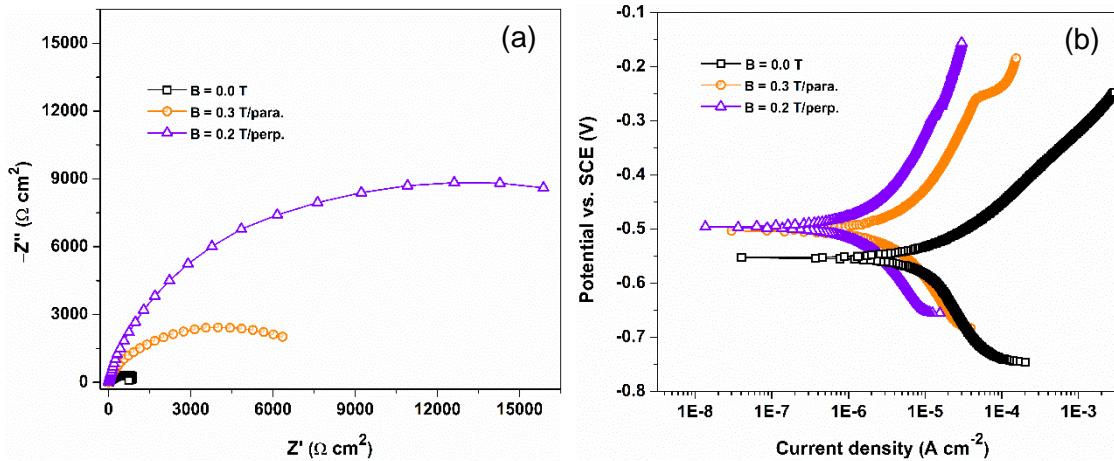


Figure 4.12 – Relative response of Nyquist plots (a), and Tafel plots (b), of Sn–Ni alloy coatings, deposited under different optimal conditions of mass transfer, i.e. natural convection (ED) and forced convection (MED), both in parallel and perpendicular

4.4 DISCUSSION

The novelty of present work is to improve the corrosion resistance of Sn–Ni coatings by increasing the wt.% of Sn in the deposit by inducing magnetic field during the deposition, and same has been accomplished. The observed increase of Sn content may be attributed to increased i_L for the deposition of Sn (more noble metal). The increase of i_L of Sn due to induced magnetic field is explained as follows: Generally, effects of plating variables on the composition of the deposit are determined by simple diffusion theory (Fahidy 1983). Limiting current density, i_L is the measure of maximum reaction rate that cannot be exceeded because of a limited diffusion rate of metal ions in solution. In the region of the limiting current, when electrode process is mass-transfer controlled, the value of i_L is given by Eqn. (4.1),

$$i_L = \frac{DnFC_B}{\delta} \quad (4.1)$$

where D is the diffusion coefficient of the reacting species, n is the valency of the metal

ion, F is the Faraday constant (96,500 Coulombs), C_B is the concentration of the ions in the bulk and δ is the thickness of the EDL. Hence, Sn content in the deposit can be increased by those processes which can increase the Sn^{+2} ions at the electrode interface.

It can be achieved by many means, like increasing the total metal content of bath, a decrease of deposition c.d., elevation of bath temperature and increased convection effect. In this regard, an increase of i_L for deposition of Sn by inducing the magnetic field is more practical, which can be best explained by the MHD effect. According to which the induced magnetic field intensity causes the concentration gradient of Sn^{+2} ions to increase drastically at cathode film by the combined effect of both hydrodynamics and Lorentz force (Fahidy 1983). Hence, induced magnetic field can increase the i_L by decreasing the diffusion layer thickness (δx) and is given by Eqn. (4.2).

$$i_L = DnF \left(\frac{\delta C_B}{\delta x} \right)_{x \rightarrow 0} \quad (4.2)$$

Here $(\delta C_B / \delta x)_{x \rightarrow 0}$ represents the concentration gradient of Sn^{+2} ions. Hence, as the thickness of diffusion layer decreases due to applied magnetic field, the value of i_L increases drastically. Change in the value of i_L due to induction of magnetic field is shown schematically in Figure 4.13, i.e. comparison of i_L for ED and MED coatings. Thus, as evident from Equations (4.1) and (4.2), it may be noted that thickness of cathode film decreased from δ_{ED} to δ_{MED} , as a mode of the coating is changed from ED to MED type. Further, an increase of i_L for deposition of Sn, due to the magnetic field is shown schematically in Figure 4.13 (b), supported by the Equation (4.2).

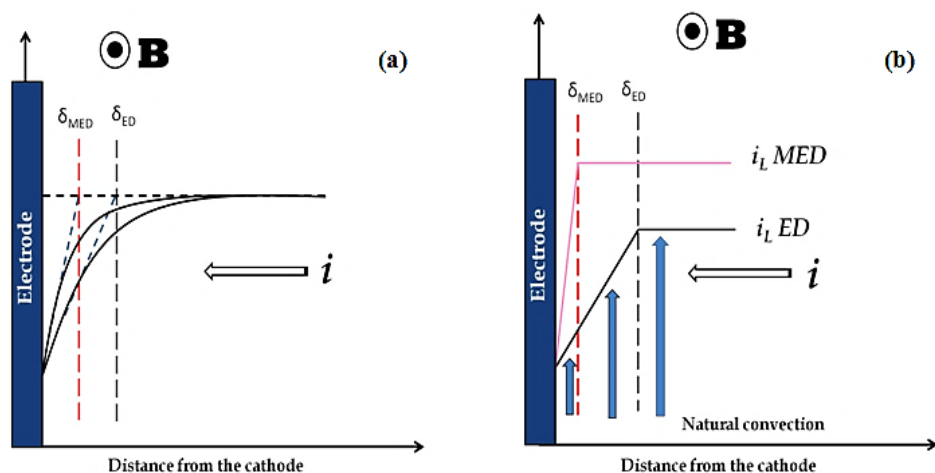


Figure 4.13 – Schematic representation showing: (a) Decrease of cathode film thickness under B at definite c.d. and $[Sn^{+2}]$, (b) Increase of i_L due to induction of B without increasing $[Sn^{+2}]$ in the bath (Here, B represents magnetic field intensity applied perpendicular to the direction of movement of metal ions)

Drastic decrease of Sn content at higher c.d. during ED indicates that i_L for Sn is around 1.0 A dm^{-2} (Figure 4.14). It is important to note that effect of magnetic field is relatively stronger only in the neighborhood of the limiting current plateau, envisaged by (Coey and Hinds 2001). Hence, selection of 1.0 A dm^{-2} , which is the i_L for deposition of Sn from the optimal bath (Figure 4.14), is very crucial to bring the effect of the magnetic field to the highest. The increase of i_L for deposition of Sn due to the magnetic field is further confirmed by plotting wt.% of Sn vs. c.d., under different conditions of magnetic field, as shown in Figure 4.14. An increase of i_L was observed (shown by arrow mark) when coatings were conducted under magnetic field effect, both in parallel and perpendicular direction. It may be noted that the effect is more pronounced in the case of perpendicular magnetic field direction, as convection effect is a vector product of current density (i) and magnetic field intensity (B) (Hinds et al. 1998). The reduced CR's of Sn–Ni alloy coatings affected by applied magnetic field is due to both increased i_L and Sn content in the alloy, supported by Figures 4.13 and 4.14, respectively.

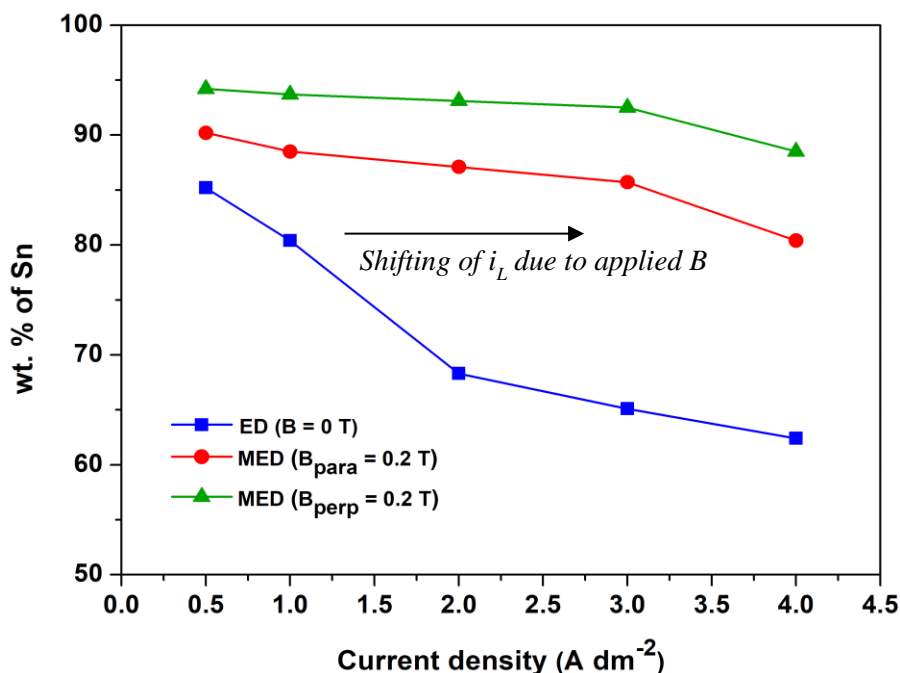


Figure 4.14 – Variation in wt.% of Sn at different c.d.'s under different conditions of B : (a) ED coatings, $B = 0$ T, (b) and (c) MED coating at $B = 0.2$ T parallel and perpendicular, respectively

The poor corrosion performance of Sn–Ni alloy coatings at higher c.d. may be attributed to increased porosity, due to the formation of larger globular nodules as seen in Figure 4.3 (c) and 4.3 (d). The increase in coating thickness with c.d. may be attributed to the formation of metal hydroxide film at the cathode, due to an increase in pH caused by local alkylation, caused by excessive hydrogen evolution and Faraday's law (Rao and Hegde 2014). The better corrosion protection of MED Sn–Ni coatings compared to ED Sn–Ni alloy coatings is also attributed to the surface morphology of the coatings. It may be seen that MED Sn–Ni coatings are more homogeneous and smooth compared to ED coatings as shown in Figures 4.3 and 4.8, respectively. The MED coatings are found to be smooth and less developed, compared to more rough and porous ED coatings. Hence, lowering in surface roughness reduces the access of oxidative reagents to active sites thereby making MED coating less susceptible to corrosion (Tacken and Janssen 1995). In addition, the thickness of MED coatings is found to be less compared to those of ED coatings. This is attributed to the

superimposition of an external magnetic field, both parallel and perpendicular direction, leading to an enhancement in the compactness of grain structures by allowing the crystal to grow with more regular sizes and geometrical shapes, which was also reported in the work of Brillas et al. (1999). The additional peaks of Sn (220), (411), and (501) corresponding to MED Sn–Ni coatings, observed in Figures 4.9 (a) and (b) are credited to the increased wt.% of Sn in the deposit. Furthermore, it is well known that the kinetics of Sn–Ni alloy deposition, in terms of their chemical composition, surface morphology and crystallographic orientations can be changed due to the applied magnetic field as proposed by Krause (2006).

4.5 CONCLUSIONS

The experimental work for optimization of deposition conditions for the development of ED and MED Sn–Ni alloy coatings, showing better corrosion resistance has made the following observations as conclusions:

1. Under optimal conditions, MED Sn–Ni alloy coatings exhibit almost 9 times better corrosion resistance compared to ED coatings, deposited from the same bath.
2. The MHD effect has induced the deposition of specific crystallographic texture, due to the formation of a new Sn (220), (411), (501) and Ni (200) phases.
3. Both roughness and thickness of Sn–Ni alloy coatings were found to be decreased under the condition of induced magnetic field, explained by the MHD effect.
4. The decrease in cathode film thickness, due to applied magnetic field is responsible for the development of coatings having more Sn content, i.e. by increasing its i_L .
5. The limitations, like low i_L and precipitation of electrolyte to develop more corrosion resistant coatings from the proposed bath, has been resolved by MED approach.

CHAPTER 5

CHAPTER 5**SONOELECTRODEPOSITION OF Sn–Ni ALLOY COATINGS FOR BETTER CORROSION PROTECTION**

Development of composition modulated multilayer alloy (CMMA) coatings of Sn–Ni, using the ultrasound effect is explained in this chapter. Modulation of the composition of individual layers has been affected by modulating the ultrasound power density (p.d.) periodically, parallel to the process of deposition. Sono-electrodeposition (SED) conditions, like cyclic power density (p.d.) and a number of layers have been optimized to maximize its corrosion resistance, compared to its monolayer coatings, developed through conventional electrodeposition (ED) method. The first part details the optimization conditions for SED of monolayer Sn–Ni alloy coating, the second part details the optimization conditions for the development of its multilayer coatings for better corrosion protection, by pulsing the sonication effect periodically.

5.1 INTRODUCTION

A new class of materials with alternate layers of metals/alloys, having a thickness of a few nanometers with ultrafine microstructure are known as composition-modulated multilayer alloys (CMMA) (Thangaraj et al. 2009). Actually, alloy coatings are developed in multilayers, from an electrolytic bath having ions of two or more metals by modulating alternately the mass transport process at EDL during deposition (Cohen et al. 1983, Yahalom and Zadok 1987, Haseeb et al. 1994). A well-trying method for development of multilayer alloy coatings through the SBT is by changing alternately the cathodic c.d., i.e. c.d. is made to change alternately between two values at regular time intervals, depending on the requirement of composition and thickness of alternate layers (Mason and Cordemans 1996, Sáez and Mason 2009). In this direction, there are several reports on the development of multilayer alloy coatings for improved corrosion protection of MS, instead of their monolayer, or monolithic alloy coating, developed using DC. Among them are the papers of our group (Yogeshha and Hegde 2010; 2011; Venkatakrisna and Hegde 2011; Pavithra and Hegde 2012; Ullal and Hegde 2014) focused on development of corrosion protective CMMA coatings of Zn–M (where M = Ni, Co and Fe) alloys by pulsing the c.d., in different patterns, namely square and

triangular shape. The coating configurations, in terms of pulsing c.d. and a number of layers, have been optimized to maximize their corrosion performance.

Though there are many reports in the literature on both ultrasound induced electrodeposition, of many metals/alloys and multilayer Zn-based alloy coatings for better corrosion protection (Rao and Hegde 2013, Rao et al. 2013), to the best of the authors knowledge development of multilayer alloy coatings using the ultrasound effect as a tool is not available. Hence to fill this knowledge gap, development of ultrasound assisted multilayer Sn–Ni alloy coating for better corrosion resistance has been tried. The corrosion performance of SED multilayer Sn–Ni alloy coatings were evaluated in relation to its monolayer (conventional) electrodeposits, developed with/without the use of the ultrasound frequency. The chapter goes in two sections, the first section details the optimization conditions for the development of SED monolayer Sn–Ni alloy coating, whilst the second section details the optimization conditions for the development of its multilayer coatings for better corrosion protection, using the ultrasound frequency.

5.2 DEVELOPMENT OF MONOLAYER Sn–Ni ALLOY COATING BY SONO-ELECTRODEPOSITION

The composition and conditions used for electrodeposition of Sn–Ni alloy coating, used in this study is given in Table 4.1. The electrolyte was freshly prepared from distilled water using analytical grade reagents. Polished MS plates with an exposed surface area of $7.5 \times 3.0 \text{ cm}^2$, used as a cathode; and anode used was pure nickel plate with the same exposed area. Electrodeposition of monolayer Sn–Ni alloy coating, both in presence and absence of the ultrasound frequency, have been carried out, and deposition conditions were optimized for maximum corrosion protection of the coatings. The electrodeposition was carried out using constant current or DC power source (Aplab, LD3205), and SED was carried out using an ultrasound generator (SONIC Vibra-Cell™ VC 750, 20 kHz, maximum power 750 W, having sonicator probe (electrode) of 13 mm tip diameter), coupled with DC power source. The ultrasonic horn was kept at a distance of 1.0 cm from the cathode during SED. The process assembly used for SED is shown in Figure 5.1.

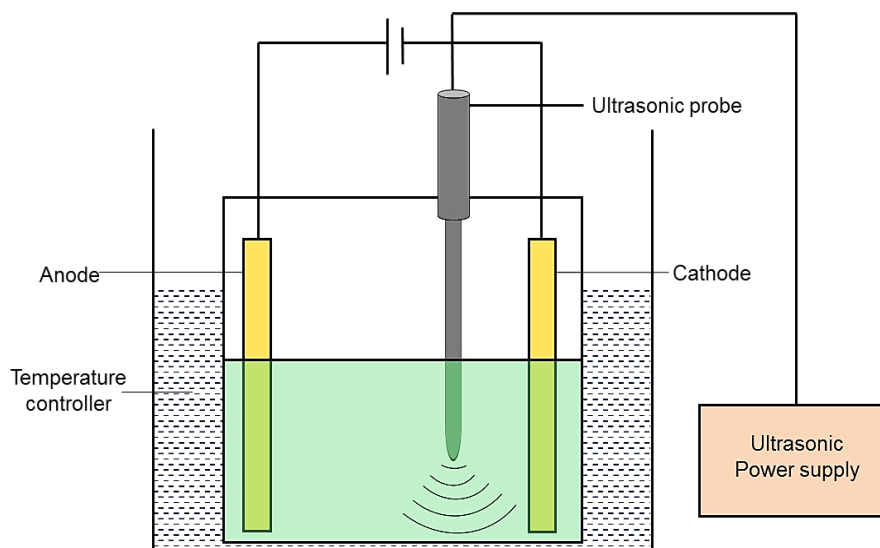


Figure 5.1 – Process assembly used for SED of Sn–Ni alloy coating

The power patterns used for development of monolayer Sn–Ni alloy coatings, using only DC is shown in Figure 5.2 (a), and both DC and ultrasound field, are shown in Figure 5.2 (b) and Figure 5.2 (c), respectively.

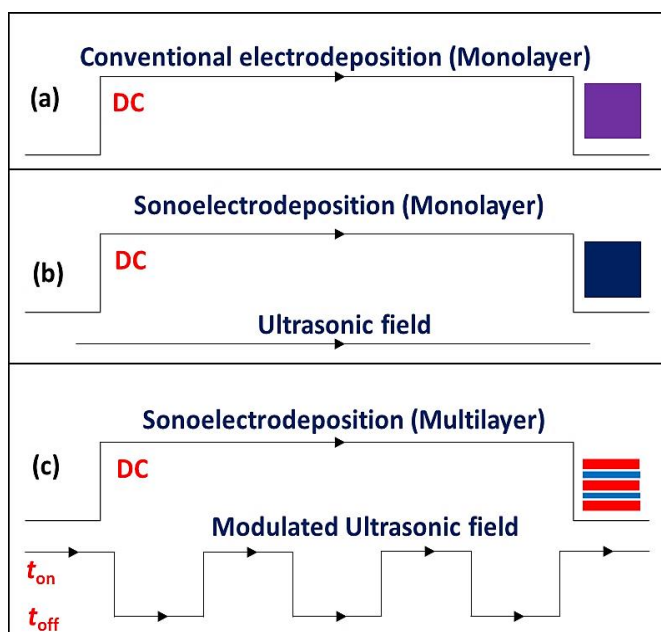


Figure 5.2 – Schematic representation of driving forces used for development of Sn–Ni alloy coatings from same optimized bath along with deposit patterns on top right: a) DC or constant current for ED Sn–Ni alloy, b) DC and ultrasonic field for SED Sn–Ni alloy (both monolayer), and c) DC and pulsed ultrasound field for multilayer Sn–Ni alloy

The experimental investigation in Chapter 4 revealed that using optimal Sn–Ni alloy bath (Table 4.1) at optimal c.d. = 1.0 A dm^{-2} , the bath was able to produce the coatings of least CR ($16.63 \times 10^{-2} \text{ mm y}^{-1}$), i.e. with no ultra-sonication effect. Hence, keeping this c.d. as constant, the corrosion protection of Sn–Ni alloy coatings were tried to enhance by SED method. Accordingly, monolayer SED Sn–Ni alloy coatings were deposited under different conditions of ultrasound p.d. i.e. at 0.6 , 0.9 and 1.2 W cm^{-2} , their corrosion performances were evaluated, and experimental results are described below.

5.2.1 Corrosion Study of SED Sn–Ni alloy Coatings

5.2.1.1 Potentiodynamic polarization study

The potentiodynamic polarization method was used to study the corrosion behavior of the SED Sn–Ni alloy coatings. Tafel plots of SED Sn–Ni alloy coatings, deposited at different ultrasound p.d. including the coating in the absence of ultrasound p.d. is shown in Figure 5.3.

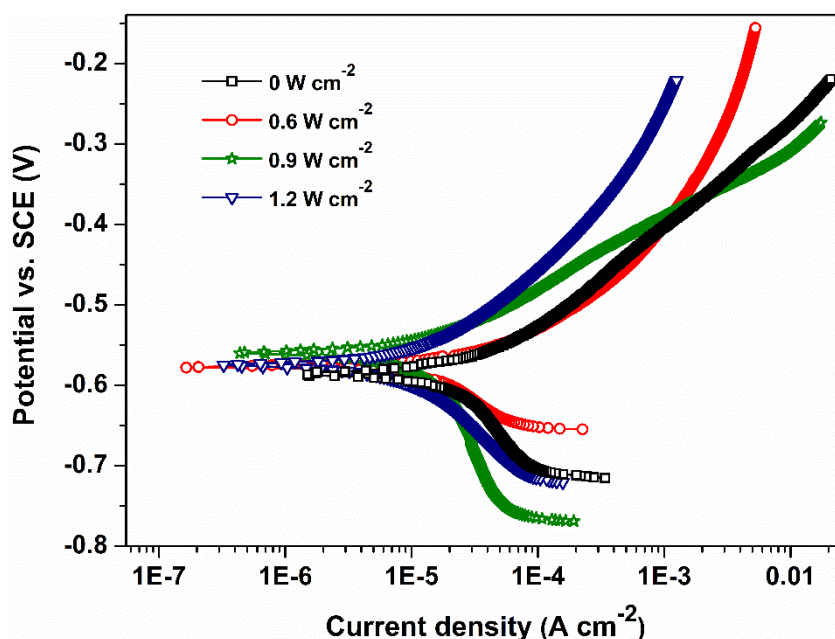


Figure 5.3 – Potentiodynamic polarization behaviors of SED Sn–Ni alloy coatings developed from the optimal bath under different conditions of ultrasound p.d.

Tafel extrapolation method was used to study the corrosion behavior of SED Sn–Ni alloy (monolayer) coatings, and corresponding CR's are reported in Table 5.1, along with the coating developed in the absence of ultrasound frequency. From the CR data,

it may be noted that SED Sn–Ni alloy coatings are more corrosion resistant compared to ED coating, i.e. at p.d. = 0 W cm⁻². Among the SED coatings, Sn–Ni alloy corresponding to 0.9 W cm⁻² is found to exhibit the least CR (7.81×10^{-2} mm y⁻¹). This may be attributed to the relatively compact structure of the coatings as seen in Figure 5.6. It should be noted that at high p.d. of 1.2 W cm⁻², the CR of Sn–Ni alloy coating started increasing. Hence, 0.9 W cm⁻² was taken as the optimal p.d. for SED.

Table 5.1 – Corrosion data of SED Sn–Ni alloy coatings developed at different conditions of ultrasound p.d., at constant c.d. of 1.0 A dm⁻², from the optimal bath

Ultrasound p.d. (W cm ⁻²)	t_{ON} (sec)	wt.% Ni	wt.% Sn	$-E_{corr}$ (V vs. SCE)	i_{corr} (μ A cm ⁻²)	CR ($\times 10^{-2}$ mm y ⁻¹)
0	300	60.9	39.1	0.587	10.74	16.6
0.6	300	43.5	56.5	0.576	5.36	9.3
0.9	300	42.2	57.8	0.559	4.47	7.8
1.2	300	41.4	58.6	0.576	4.74	8.2

5.2.1.2 Electrochemical impedance study

As EIS study considers the response of test specimen for small amplitude AC signals, it is considered as a non-destructive one. The most versatile tool is the Nyquist plots which commonly plot the data as imaginary impedance, Z'' verses real impedance Z' with the provision to distinguish the contribution of polarization resistance (R_p) and solution resistance (R_s) (Thangaraj et al. 2006). Hence, in the conformation of the corrosion response of monolayer SED Sn–Ni coatings, evidenced by Tafel extrapolation method, their EIS study have also been carried out and the corresponding graphs are shown in Figure 5.4. It may be noted that polarization resistance, R_p increases with increase in ultrasound p.d. and then decreased substantially on its further increase, i.e. at 1.2 W cm⁻², indicating its poor corrosion resistance as shown in Figure 5.4. The solution resistance (R_s) is nearly identical in all cases, as same bath chemistry and cell configuration were used for corrosion study.

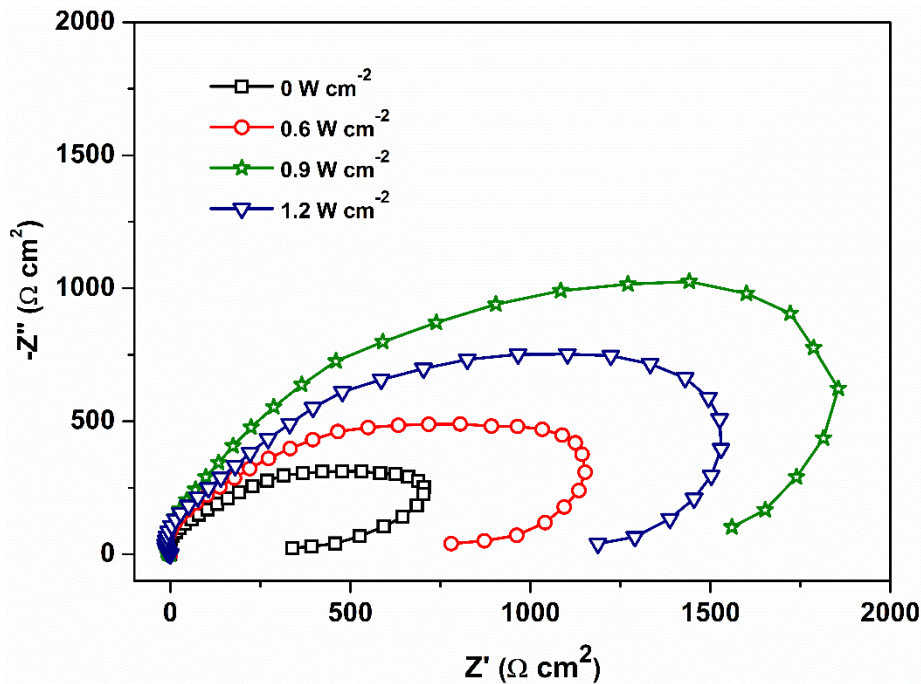


Figure 5.4 – EIS of SED Sn–Ni alloy coatings developed from optimal bath under varying conditions of ultrasound p.d.

Here, it is important to note from the data reported in Table 5.1 the wt.% of Sn in Sn–Ni alloy deposit has increased drastically when the deposition was carried out under the effect of ultrasound. This drastic increase in wt.% of Sn is due to thinning of EDL (Nernst's diffusion layer) to few microns thickness (Del Campo et al. 1999). The absolute value of EDL thickness is actually determined by the geometry of the sono-electrode and the ultrasonic p.d. The decrease of EDL thickness leads to an increase of i_L required for the electrochemical process taking place at the electrode-electrolyte interface and is described by the Eqn. 4.1 (Brett and Brett 1993).

The variation of the ultrasound intensity and the electrode-to-horn distance allow the diffusion layer thickness, δ to be reduced (Compton et al. 1997). Accordingly, the decreased thickness of EDL, due to ultrasound effect has increased the i_L for the deposition of more noble metal (Sn) in the deposit, since $E_{Ni}^0 = -0.25$ V and $E_{Sn}^0 = -0.14$ V, as discussed in Section 4.3. Thus, the applied ultrasound provides an increased mass transport regime in which electron transfer process has changed. Therefore, it may be inferred that ultrasound effect has decreased the CR by increasing the Sn content in the alloy, effected by increasing the i_L of less readily deposit-able metal, i.e. Sn; which

otherwise not possible due to the inherent limitation of the anomalous type of codeposition followed by the bath.

5.2.2 X-ray Diffraction Study

XRD patterns of SED Sn–Ni alloy coatings corresponding to different ultrasound p.d. (from 0 W cm^{-2} to 1.2 W cm^{-2}) is shown in Figure 5.5. It may be noted that the preferential orientations Ni_3Sn_2 (214), (413) and (242) phases are favoured to exist in coatings, developed both in the presence and absence of ultrasound frequency, but Ni_3Sn_2 (302) (JCPDS card No. 65-1315) and Ni_3Sn (201) (JCPDS card No. 35-1362) reflection which is nickel-rich phase cease to exist under ultrasound field.

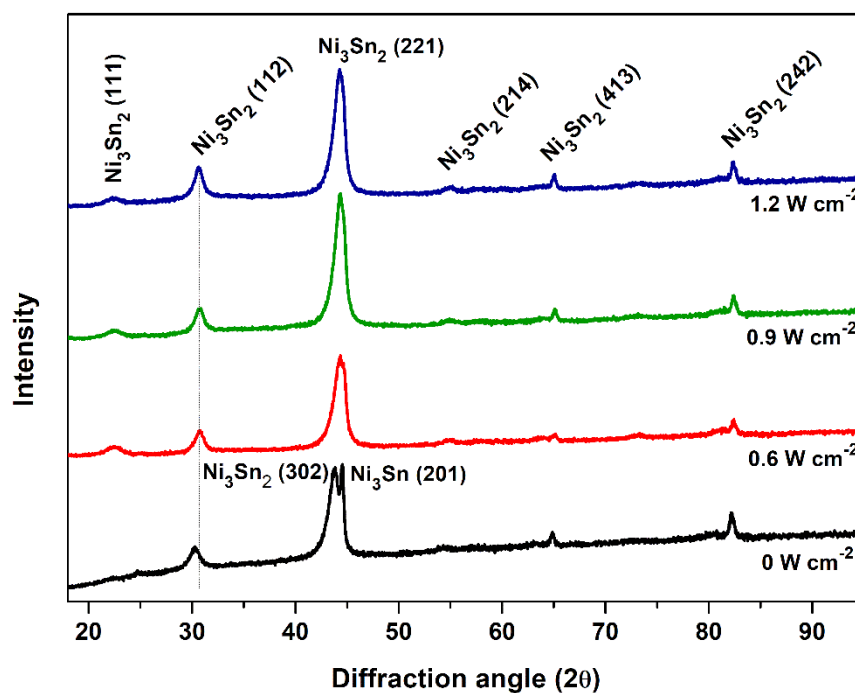


Figure 5.5 – XRD peaks showing a change of crystallographic orientations of Sn–Ni alloy coatings deposited at different ultrasound p.d., in relation to its ED coatings, i.e. at 0 W cm^{-2} , deposited from the same bath at same c.d. = 1.0 A dm^{-2}

There is also a formation of new peak Ni_3Sn_2 (221) due to applied ultrasound field, whose peak intensity was found to increase with an increase of p.d. The Ni_3Sn_2 (111) phase is found to be characteristic of ultrasound field, and it observed to be increased with p.d. as may be seen in Figure 5.5. Another interesting observation is that there is a shift in the peak of Ni_3Sn_2 (112) due to the effect of ultrasonication. When the ultrasound p.d. is applied, the wt.% of Sn in the alloy coatings is increased, which is

evident from the disappearance of the Ni_3Sn phase (a nickel-rich phase). Hence, it can be concluded that ultrasound p.d. plays a vital role in composition, and hence the phase structure of the coatings. The Sn–Ni alloy coatings were found to have an average grain size of 13.7 nm, calculated from the diffraction peak width, using Scherrer formula, given by Eqn. (3.4).

5.2.3 SEM Study of SED Sn–Ni Alloy Coatings

The surface morphology of Sn–Ni alloy coatings at differently applied ultrasound p.d. (at 0, 0.6, 0.9 and 1.2 W cm^{-2}) is shown in Figure 5.6. It may be noted that there are no significant changes in the surface morphology of the SED coatings, which is inherent of Sn–Ni deposit.

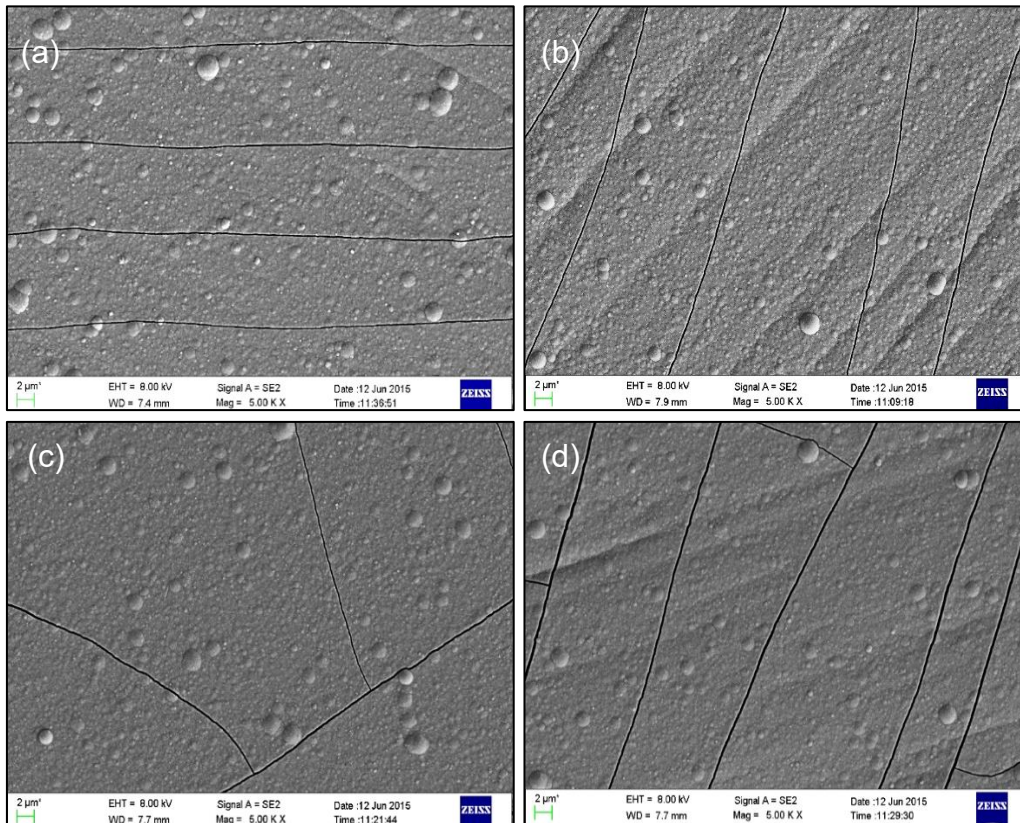


Figure 5.6 – SEM micrographs of SED Sn–Ni alloy coatings developed under different conditions of ultrasound p.d. 's: a) 0 W cm^{-2} , b) 0.6 W cm^{-2} , c) 0.9 W cm^{-2} and d) 1.2 W cm^{-2} , deposited from the same bath at same c.d. (1.0 A dm^{-2})

Another interesting observation is that Sn–Ni alloy coatings show characteristic microcracks on their surface as seen in Figure 5.6, which may be attributed to the hydrogen embrittlement as envisaged by Zhu et al. (2002). According to which during

alloy deposition, hydrogen gas remained adsorbed on the surface due to low hydrogen overvoltage of Sn. The adsorbed hydrogen leads to the development of strain in the deposit, which subsequently leads to the formation of microcracks on the surface. The corrosion protection and other physical properties of binary/ternary alloy coatings largely depend upon their phase composition. Hence any phase variation, affected by altering the deposition conditions, is of great value and is subjected to materials research (Ganesan et al. 2007).

Further, the experimental observation revealed that composition, phase structure and surface morphology of Sn–Ni alloy coatings largely depends on ultrasound p.d. used. Hence, corrosion resistance property of SED Sn–Ni alloy coating has been tried to increase further by multilayer approach, using the same bath. SED multilayer Sn–Ni alloy coatings have been developed by pulsing the ultrasound between p.d. 0.9 W cm^{-2} (optimal p.d.) and 0 W cm^{-2} (as t_{ON} and t_{OFF} , respectively), keeping other parameters constant, i.e. at the optimal condition of c.d. = 1.0 A dm^{-2} , and pH = 8.6. The experimental results are reported as below.

5.3 DEVELOPMENT OF SED MULTILAYER Sn–Ni ALLOY COATINGS

SED Multilayer Sn–Ni alloy coatings, having nano/micrometric layers of alloys (with alternately different compositions), were developed by turning the ultrasound generator ON (t_{ON}) and OFF (t_{OFF}) periodically, during the process of conventional deposition. The periodic modulation in mass transfer, due to the turning ON and OFF of the sonicator probe, allowed the growth of coatings with periodic modulation in their composition. In other words, periodic ON and OFF allowed the deposition to take place in multilayers. SED layered coatings has been accomplished by the combined effect of two driving forces: one is c.d., expressed in A dm^{-2} , and another one is ultrasonic p.d., expressed in W cm^{-2} . Here c.d. acts as the driving force for reduction of metal ions, and p.d. for modulating the mass transfer process at EDL. The driving forces employed for deposition of multilayer Sn–Ni alloy from the optimal bath (Table 4.1) under combined effect of both c.d. and p.d. is shown schematically in Figure 5.2 (c), along with the multi-layered deposit pattern on the right-hand side. The configuration of SED multilayer Sn–Ni coatings is conveniently represented as $(\text{Sn–Ni})_{1/2/n}$, where 1 and 2 indicate, respectively, ON time (t_{ON}) and OFF time (t_{OFF}) of sonication (in seconds),

and 'n' represents the number of layers formed during total deposition time (i.e. 300 seconds).

The properties of SED multilayer Sn–Ni alloy coatings, including their corrosion behavior can be increased substantially by increasing the number of layers (usually up to an optimal limit), without sacrificing the demarcation between each layer (Yogesha et al. 2011). Generally, corrosion behavior of multilayer Sn–Ni alloy coating depends upon a variety of factors, such as choice of electrolyte, bilayer numbers, and thickness of each layer (Ganesan et al. 2007). Keeping this in view, multilayer Sn–Ni alloy coatings (having a layered structure with alternate layers of an alloy of two different compositions) have been developed by pulsing p.d. with different degree of layering. This is accomplished by setting the sonicator to turn ON and OFF at regular time intervals. Accordingly, multilayer Sn–Ni alloy coatings having 10, 30, 75, 100, 150 and 300 layers have been developed by programming the sonicator to go ON and OFF, alternatively at 30, 10, 4, 3, 2 and 1 second interval, respectively, and their corrosion behaviours have been studied, and reported in Table 5.2. It should be noted that during periodic sonication, two layers of alloys of same metals but of different composition (57.8 and 39.1 wt.% Sn) were found to be formed alternatively as the sonicator probe go ON and OFF, evidenced by EDX data given in Table 5.1.

5.3.1 Corrosion Study

5.3.1.1 Polarization study

The potentiodynamic polarization behavior of SED multilayer Sn–Ni alloy coatings with different degrees of layering is shown in Figure 5.7. It may be observed that the corrosion resistance increased with the number of layers as evidenced by their corrosion data, reported in Table 5.2. The successive decrease of CR with the number of layers indicated that improved corrosion resistances are due to the layered coating, having a distinct interface between layers. It is important to note that CR's of multilayer coating decreased drastically with increase in the number of layers up to 150 layers, and then increased. i.e. multilayer coating having 150 layers, represented as (Sn-Ni)_{2/2/150} shows the least CR.

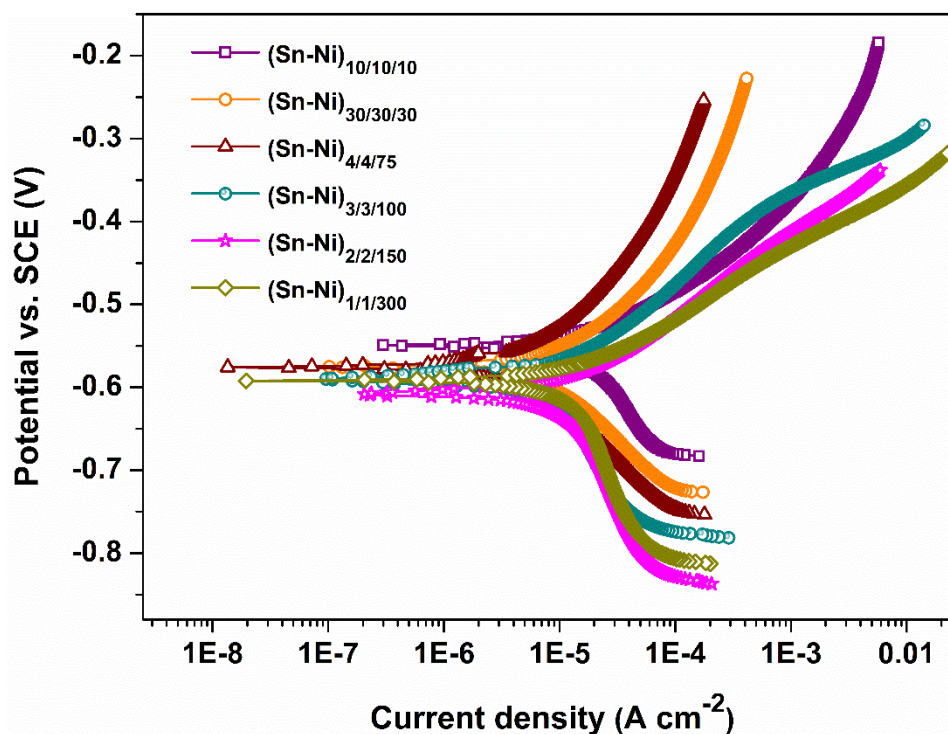


Figure 5.7 – Potentiodynamic polarization behavior of SED multilayer Sn–Ni coatings, with a different number of layers developed from the same optimal bath at optimal c.d.

However, an increase of CR at a high number of layers (300 layers) may be attributed to interlayer diffusion due to short relaxation time for metal ions, caused by rapidly changing ultrasound effect. This may be explained as follows: During SED, metal ions (Sn^{+2} and Ni^{+2} ions) from the bulk electrolyte diffuse towards the cathode and discharge as metal atoms, this process of mass transfer by diffusion is mainly controlled by the ultrasonic effect. As the number of layers increased, t_{ON} for metals to diffuse towards cathode is too small (1 s). Here, it should be noted that total time for deposition remains same (300 s). Thus, at a high degree of layering, there is no sufficient time for metal ions to relax (against diffusion under applied p.d.) and to deposit (Yogesh and Hegde 2010, 2011, Venkatakrishna et al. 2011, Pavitra and Hegde 2011). As a result, at a high degree of layering no modulation in the composition is likely to take place, and hence no improvement in corrosion resistance was found. Based on the corrosion data, $(\text{Sn-Ni})_{2/2/150}$ coating has been proposed as the optimal coating configuration, developed from the bath for highest protection against corrosion.

Table 5.2 – Corrosion data for SED multilayer Sn–Ni alloy coatings having a different number of layers, deposited from same bath keeping other parameters constant, like c.d. = 1.0 A dm⁻², ultrasound p.d. = 0.9 W cm⁻²

SED multilayer Sn–Ni alloy coating configuration	Total time taken for deposition, $t = 300$ s		No. of layers formed	$-E_{\text{corr}}$ (V vs. SCE)	i_{corr} $\mu\text{A cm}^{-2}$	CR ($\times 10^{-2}$ mm y ⁻¹)
	t_{on} (s)	t_{off} (s)				
(Sn–Ni) _{30/30/10}	30	30	10	0.610	3.544	6.18
(Sn–Ni) _{10/10/30}	10	10	30	0.589	3.113	5.43
(Sn–Ni) _{4/4/75}	4	4	75	0.575	2.384	4.16
(Sn–Ni) _{3/3/100}	3	3	100	0.591	1.622	2.83
(Sn–Ni) _{2/2/150}	2	2	150	0.610	1.128	1.97
(Sn–Ni) _{1/1/300}	1	1	300	0.591	2.621	4.57
<i>Monolayer Sn–Ni alloy</i>						
(Sn–Ni) _{1.0 A dm⁻²}	DC monolayer			0.587	10.749	16.63
(Sn–Ni) _{1.0 A dm⁻²/0.9 W cm⁻²}	SED monolayer			0.559	4.473	7.81

5.3.1.2 Electrochemical impedance spectroscopy study

In this technique, it is common to plot the data as imaginary impedance versus real impedance with provision to distinguish the contribution of polarization resistance (R_p) from the solution resistance (R_s). These plots are called Nyquist diagrams. Nyquist plots of MED Sn–Ni deposits with a different number of layers were studied, and are shown in Figure 5.8. The plots showed depressed semicircle in the studied frequency range (100 kHz to 10 mHz). In addition, the increase of axial radius of the semicircle with number layers was found. Impedance signals clearly indicated that the charge transfer resistance (R_{ct}) has increased progressively with a number of layers before it starts decreasing. i.e. at 300 layers. Thus, impedance response of (Sn–Ni)_{2/2/150}, is characterized by very high polarization resistance, R_p indicate that this coating configuration is more stable than other coatings, in compliance with Tafel plots shown in Figure 5.7.

An increase of capacitive loop radius with a number of layers, shown in Figure 5.8 demonstrated that corrosion rate of multilayer coatings decreases with increase in the number of layers (only up to 150), and then decreased. The electrochemical equivalent circuit corresponding to (Sn-Ni)_{2/2/150} has been simulated and is shown in the inset of Figure 5.8. Where R_s is solution resistance, R_o is pore resistance, R_{ct} is charge transfer resistance and Q is the capacitance of EDL. Here R_o refers to the resistance of ion conducting paths developed in the coating due to the presence of microcracks, or due to deformation of the coating at the topmost layer of the CMMA coating. These paths are physical pores filled with electrolyte, i.e. corrosion medium. Accordingly, a good agreement was found between experimental and simulated EIS response, corresponding to (Sn-Ni)_{2/2/150} coating. Hence it may be concluded that highest corrosion protection of (Sn-Ni)_{2/2/150} coating is mainly attributed to charge transfer resistance (R_{ct}).

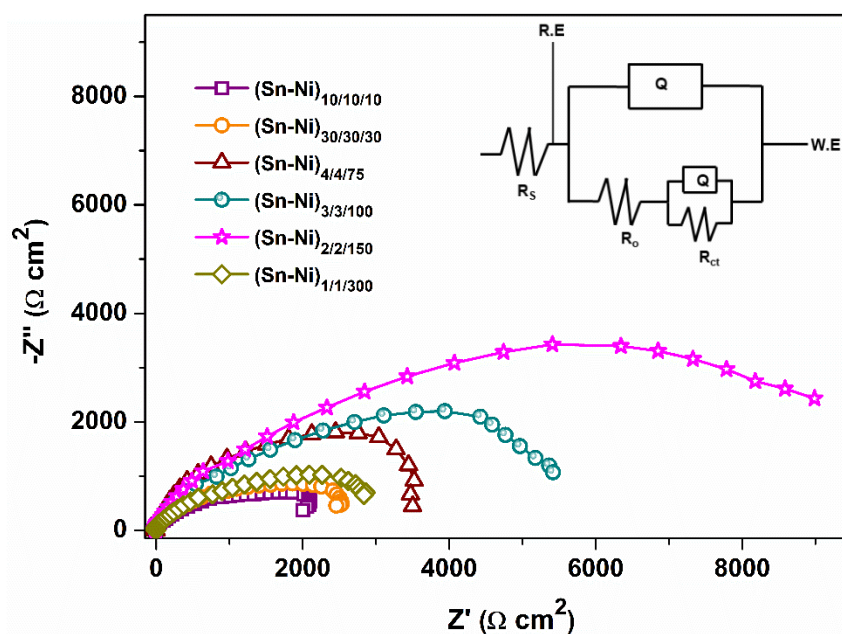


Figure 5.8 – EIS response of SED multilayer Sn–Ni alloy coatings, with a different number of layers, developed from the same optimal bath at optimal *c.d.*

It is important to note that though there are some pores or the cracks on the surface of the coatings, they do not affect the total performance of the coating when it is in multilayers. This is due to the fact that the corroding medium reaches the substrate (confirmed from the SEM cross-sectional analysis, shown Figure 5.10) only after passing several such layers of different composition, one after another. The extended

corrosion protections of multilayer alloy coatings, having pores/cracks are well explained by Elias and Hegde (2015).

5.3.2 Comparison of SED Monolayer and Multilayer Sn–Ni Alloy Coatings

The decrease of CR's, when the coating is changed from conventional monolayer to SED monolayer and multilayer coating is confirmed from the data, summarized in Table 5.2. The corrosion behavior of the monolayer (with and without sonication effect) and SED multilayer Sn–Ni alloy coatings (all are under optimal conditions) are shown comparatively, through Nyquist plots and potentiodynamic polarization curves in Figure 5.9 (a) and Figure 5.9 (b), respectively.

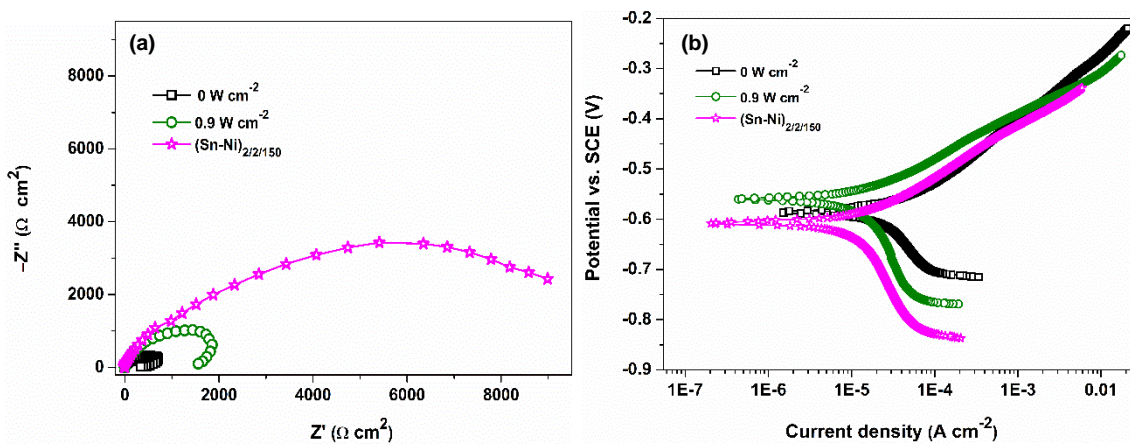


Figure 5.9 – Comparison of corrosion performance of monolayer (with and without sonication effect) and SED multilayer Sn–Ni alloy coatings through a) Nyquist plots and b) potentiodynamic polarization curves (developed under optimal conditions, from the same bath for same duration)

From the data given in Table 5.2, it may be noted that a drastic decrease of CR's was observed due to sonication effect, compared to its conventional alloy coating. Similarly, a drastic decrease of CR was found in the case of SED multilayer Sn–Ni alloy coatings. It is supported by Nyquist and Tafel plots shown in Figure 5.8. Thus, from corrosion data, it may be concluded that under optimal conditions, (Sn-Ni)_{2/2/150} coating is about 4 times more corrosion resistant ($\text{CR} = 1.97 \times 10^{-2} \text{ mm y}^{-1}$) than SED monolayer coating ($\text{CR} = 7.81 \times 10^{-2} \text{ mm y}^{-1}$); and 8.4 times more corrosion resistant than ED coating ($\text{CR} = 16.63 \times 10^{-2} \text{ mm y}^{-1}$), respectively.

5.3.3 SEM Study of SED Multilayer Sn–Ni Alloy Coating

The SEM image of cross-sectional view of SED multilayer Sn–Ni coating with 10 layers, having alternatively different composition (5 each), represented as $(\text{Sn-Ni})_{30/30/10}$ is shown in Figure 5.10. Clear demarcations on the cross section of the coating, evidence the formation of layered coatings, developed due to the periodic pulsing of p.d. during deposition. In other words, periodic modulation of ultrasound p.d. during deposition allowed the formation of layers with the interface, separating two layers of alloys of different composition. It may be further noted that in the total duration of 300 s coating of about $5\ \mu\text{m}$ (micron) thickness has developed on the substrate, as seen in Figure 5.10. Therefore, it may be concluded that the SED multilayer Sn–Ni coating under optimal condition, i.e. with $(\text{Sn-Ni})_{2/2/150}$ configuration, the average thickness of each layer is found to be in the range of 33 nm. Thus, improved corrosion protection of multilayer Sn–Ni alloy coating is due to nano/micrometric layering of alloys, affected due to the periodic pulsing of the sonicator probe.

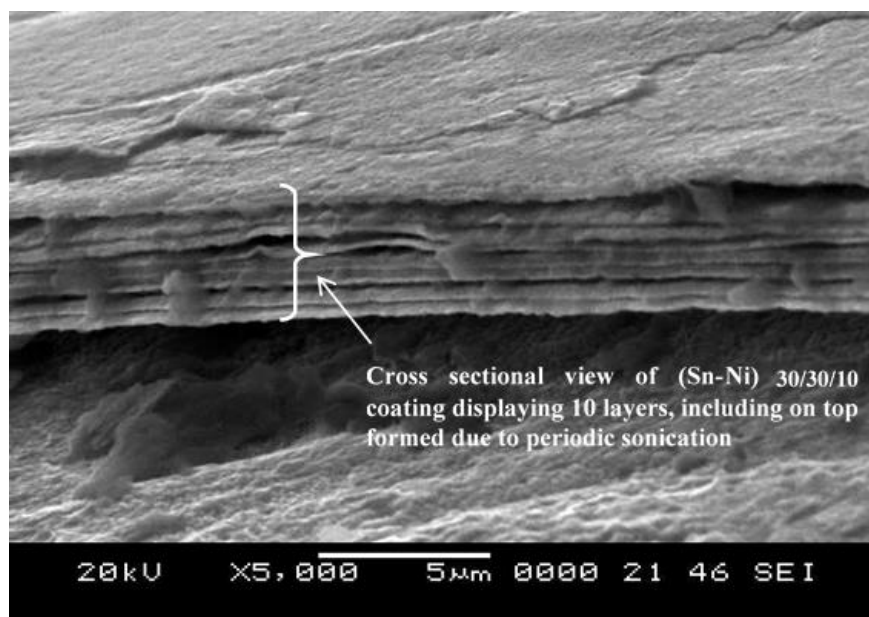


Figure 5.10 – SEM cross-sectional view of SED multilayer Sn–Ni coating, represented as $(\text{Sn-Ni})_{30/30/10}$ displaying 10 layers, having alternatively different composition

5.4 CORROSION MECHANISM IN MONOLAYER AND MULTILAYER Sn–Ni ALLOY COATING

The corrosion protection of the substrate (MS) by multilayer alloy coating in contrast to its monolayer alloy coating can be convincingly explained by a pictorial representation, shown in Figure 5.11. This mechanism is attributed by the selective dissolution of several number of layers with alternating compositions (Elias and Hegde 2015). In Figure 5.11, it should be noted that Sn–Ni multilayer coating is represented by 4 layers of alloys, where 2 layers of alloys have one composition (grey colour) which is alternated by 2 layers of alloys with a different composition (blue colour), of same thickness.

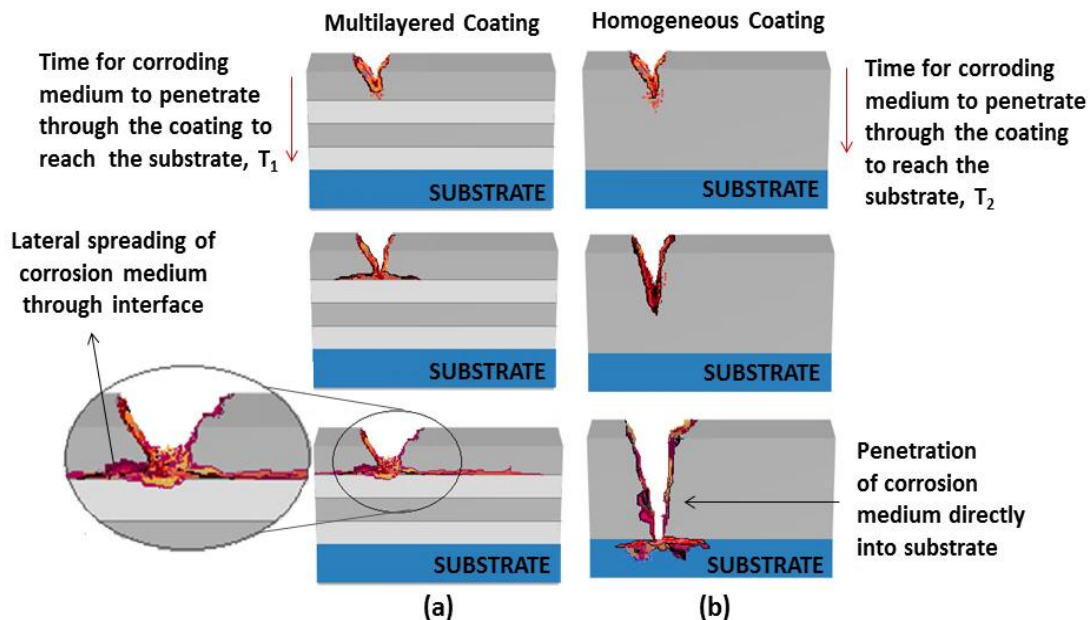


Figure 5.11 – Schematic diagram representing the increased corrosion protection of SED multilayer Sn–Ni alloy coatings compared to its monolayer coating: a) Corrosion medium spreads laterally at the interface between layers and reduces the corrosion, and b) Corrosion medium attacks directly to reach the substrate faster in monolayer coating

When layered alloy coating comes in contact with the corrosion medium, the top layer is exposed directly and gets corroded first. The layers present beneath are safe until the breakdown of the topmost layer occurs. As the corrosive agent penetrates the lower layers the corrosion product spreads laterally at the interface as shown in Figure

5.11 (a). Once that layer breaks down, the lower layer gets exposed to the corrosive medium and this process repeats layer after layer. Thus, if the number of layers is more, the corrosive agent takes a longer time to penetrate through the layers and then into the substrate. Hence, this process blocks or extends the path of the corrosive agent (Leisner et al. 1996, Venkatakrishna and Hegde 2010). In the case of monolayer (both ED and SED) Sn–Ni alloys, corrosion takes place continuously to reach the substrate directly as shown in Figure 5.11 (b). Thus, the observed decrease of CR with an increase of a number of layers may be attributed to increased number of layers, or interfaces separating alloys of different composition. Here, the word ‘interface’ is used in the sense of phase boundary separating alloys of different composition, but of the same metals. Therefore, as the number of layers increases, the total surface area of phase boundary (under given area of the coating) increases. This allows the corrosion medium to spread laterally more than to filter directly into the substrate, as in monolayer coating (Dobrzański et al. 2005, Elias et al. 2016). Thus, it may also be concluded from Figure 5.11 that the total time required for the corroding medium to reach the substrate by penetrating through the multilayer coating (T_1) is much greater than that through the monolayer coating (T_2), i.e. $T_1 \gg T_2$.

5.5 CONCLUSIONS

The SED multilayer Sn–Ni alloy coatings have been developed on MS by pulsing the ultrasound p.d. periodically at EDL, parallel to the process of deposition and the following conclusions are drawn.

1. Ultrasound effect decreases the CR of Sn–Ni alloy coatings by increasing the Sn content of the alloy, which otherwise is not possible due to the inherent limitation of the anomalous type of codeposition, followed by the bath.
2. Multilayer SED Sn–Ni alloy coatings, having layers in micrometric scale with alternately changing composition, were developed by turning the sonicator ON and OFF as required, keeping the c.d. constant.
3. Under optimal conditions, SED multilayer coating (Sn–Ni)_{2/2/150} is about 4 times more corrosion resistant ($CR = 1.97 \times 10^{-2} \text{ mm y}^{-1}$) than SED monolayer coating (Sn–Ni)_{1.0 A dm⁻²/0.9 W cm⁻²} ($CR = 7.81 \times 10^{-2} \text{ mm y}^{-1}$), and 8.4 times more

corrosion resistant than its ED coating (Sn–Ni)_{1.0 A dm⁻²} (CR = 16.63 × 10⁻² mm y⁻¹), respectively developed from the same bath for same time.

4. The improved corrosion protection of SED multilayer Sn–Ni alloy coating is due to nano/micrometric layering of alloys of different composition (57.8 and 39.1 wt.% Sn), affected due to periodic sonication.
5. Improved corrosion protection of SED multilayer Sn–Ni alloy coatings is attributed to the formation of more number of layers, changed phase structure and surface morphology, supported by EDX, XRD and SEM study.

CHAPTER 6

CHAPTER 6

ELECTROCATALYTIC STUDY OF ELECTRODEPOSITED Sn–Ni ALLOY COATINGS

This chapter explores the use of Sn–Ni alloy coating, electrodeposited on copper as an electrode material for water splitting applications of both hydrogen evolution reaction (HER) and oxygen evolution reaction (OER). The experimental investigation on the electrocatalytic behavior of as-deposited Sn–Ni alloy, developed at different c.d.'s, followed by its improvement via structural modification by electrochemical anodic dissolution is reported here.

6.1 INTRODUCTION

Development of advanced electrode materials and optimization of their structural design is considered to be very crucial to reduce the electrical consumption and improve their efficiency for water electrolysis (Marozzi and Chialvo 2001, Łosiewicz et al. 2004). Some Ni-based alloys, either binary (Solmaz and Kardaş 2009, Zeng and Zhang 2014) or ternary (Campillo et al. 2002, Maslovara et al. 2013) with high catalytic activities for HER have been successfully tested as efficient cathode materials. Of the different catalyst, one of the best material for the HER is Raney-Ni (Chen and Lasia 1991, Chade et al. 2013), as it is comparatively inexpensive and highly active, without a noble metal. In addition, some literature (Santos et al. 1992, Yamashita et al. 1993, Jović et al. 2012, Jović et al. 2013, Vijayakumar et al. 2013) have reported that the electrodeposited Ni–Sn alloys possess high catalytic properties for HER than Raney-Ni electrode. Yamashita et al. (1993) investigated the relationship between the catalytic activities for HER and reported that Ni–Sn alloy shows good chemical stability and service life in alkaline water electrolysis. Santos et al. (1992) also reported that the electroplated Ni–Sn alloys exhibit low overpotential for the HER in alkaline solution. The increase of electrode surface area is one of the effective means of improving the activity of electrodes. Porous electrodes are the center of interest in electrocatalysis, especially for gas evolution, consumption reactions, batteries and fuel cells. The

important increase in the real surface area obtained on such electrodes leads to high apparent electrochemical activities (Lasia 1998).

The purpose of this chapter is to study the electrocatalytic activity of Sn–Ni alloy coatings developed from the optimal bath (Table 4.1), under different conditions of c.d. and to improve it further by anodic dissolution, relying on the fact that increase of active surface area (by selective dissolution) can increase its electrocatalytic property. An effort was made to correlate the increased electrocatalytic activity of the coatings with their deposition c.d., chemical composition, morphology, and phase structure.

6.2 EXPERIMENTAL METHODS

6.2.1 Preparation of Sn–Ni Alloy Test Electrodes

The composition and operating parameters required to deposit a bright, smooth, and uniform Sn–Ni alloy coating is reported in Table 4.1. The electrocatalytic behavior of Sn–Ni alloy coatings was studied, by depositing it on a known surface area of copper, taken in the form of either plate or rod (both having same specifications), depending on the requirement. For compositional analysis, Sn–Ni alloy coatings were carried out on a known surface area (2.5 cm × 2.5 cm) of the copper plate in 200 mL capacity cubic cell (made of PVC material), by covering the remaining region of the plate with cellophane tape. All electrocatalytic studies were made by coating the deposit on a cross-sectional area of a copper rod (having 1.0 cm² surface area), fitted into a customized glass cell, as shown in Figure 6.1. Copper substrate was ground to the mirror finish, using grinding wheels of varying grade emery mops, and then degreased using trichloroethylene. It was then electro-cleaned and pickled in 0.5 M HNO₃ to activate the surface prior to deposition and then rinsed with distilled water. Copper substrate was used as the cathode in the electrochemical cell, and pure nickel plate of same exposed surface area as an anode; maintaining a distance of 5 cm from each other. Electrodepositions were carried out at different c.d.'s (1.0 – 4.0 A dm⁻²) for a constant duration (600 s) to compare their electrocatalytic performance. The coatings are then rinsed several times with distilled water, later dried in hot air, and then desiccated until further testing.

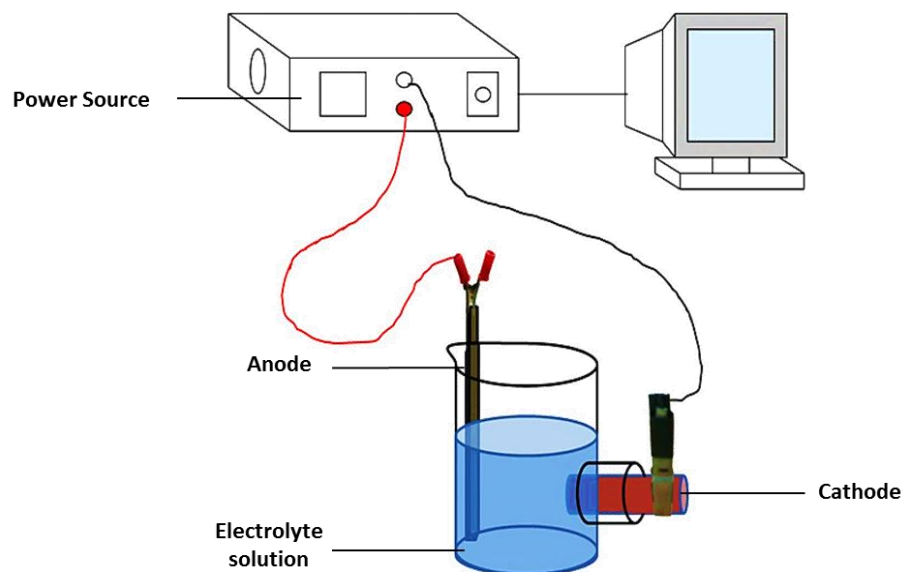


Figure 6.1 – Customized glass cell used for electrodeposition of binary Ni–M alloy coatings on the cross-sectional surface area of a copper rod

6.2.2 Experimental Set Up

Electrocatalytic study of Sn–Ni alloy has been carried out using a three-electrode tubular glass cell (customized), shown schematically in Figure 6.2. This experimental setup enabled the quantitative evaluation of the electrocatalytic behavior of Sn–Ni alloy deposited under different conditions of c.d.'s. The customized cell was designed to collect the liberated H_2 and O_2 gas, when the electrode is subjected to cathodic and anodic polarization, respectively. The platinum electrode of 1.0 cm^2 surface area is used as a counter electrode, placed at one end of the tube and as-deposited Sn–Ni alloy at another end, which serves as a test electrode. SCE is used as a reference electrode and its connection is established through Luggin's capillary with an Agar-KCl salt bridge to eliminate the error due to iR drop. The cell is fitted with graduated tubes (burette), which collects the volume of liberated gas (hydrogen and oxygen) by displacing the solution, whose volume could be easily read. This arrangement helps in evaluating the electrocatalytic efficiency of Sn–Ni alloy by measuring the amount of H_2 and O_2 generated practically, at cathode and anode respectively.

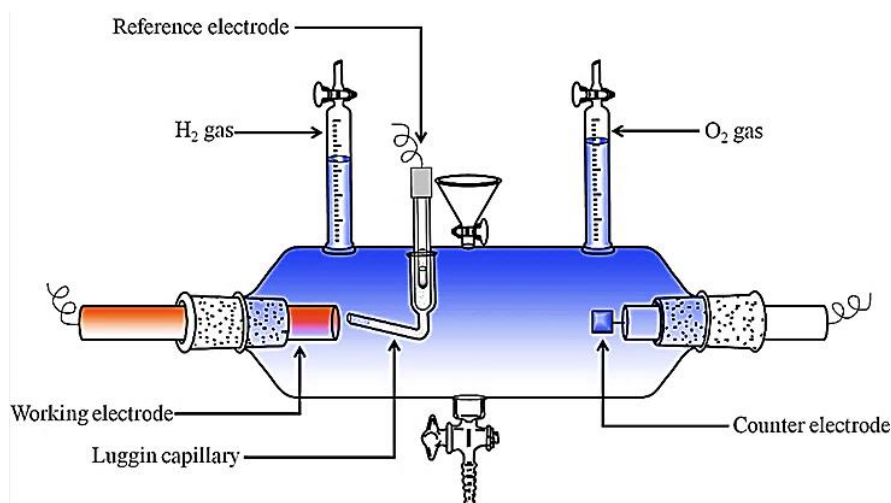


Figure 6.2 – Three electrode tubular glass cell assembly used for quantitative measurement of H_2 and O_2 formed on the surface of a Ni–M alloy coatings, used as electrode material for water splitting reactions of HER and OER

6.2.3 Development of Microporous Sn–Ni Alloy Coating

Microporous Sn–Ni alloy coating was prepared by electrochemical anodic dissolution of as-deposited Sn–Ni alloy. The electrochemical dissolution was carried out in 0.5 M HCl solution, using as-deposited Sn–Ni alloy as an anode, and a copper plate as a cathode to establish an electrochemical circuit. The current and the duration of electrochemical dissolution were optimized for peak performance of the coatings for HER, in the same 1.0 M KOH solution, on trial and error basis. A c.d. of 4.0 A dm^{-2} , for the duration of 5 min was found to be the optimal condition for imparting good micro-porosity to as-deposited Sn–Ni alloy coating, by selective dissolution, without destructing its microstructure.

6.3 RESULTS AND DISCUSSION

Sn–Ni alloy coatings, electrodeposited on a copper substrate at different c.d.'s was first characterized for their composition, hardness, thickness, phase structure, surface morphology, and corrosion resistance behaviors before testing them for water splitting application of HER and OER, and the experimental results of that investigation are detailed as follows.

6.3.1 Composition, Hardness and Thickness Analysis

Sn–Ni alloy coatings were electrodeposited galvanostatically on copper at different c.d.'s, and their composition, hardness, and thickness are reported in Table 6.1. It can be seen that the composition of all test specimens solely depends on the c.d. used for its deposition. The wt.% of Sn in the deposit is found to be always more than that in the bath, proving that Sn is more readily deposit-able metal in the bath. Furthermore, it was observed that the proposed bath is able to deposit coatings having about 80.4% Sn at low c.d. (1.0 A dm^{-2}), which was found to decrease at high c.d. (62.4%). The high wt.% of Sn at low c.d. range indicates that the bath follows the anomalous type of codeposition (Brenner 1963, Raj 1993).

The hardness of Sn–Ni alloy coatings increased with c.d. due to the increase of Ni content in the alloy, and its thickness obviously increased with c.d. as seen in Table 6.1. The increase of thickness with c.d. is attributed to increased deposition c.d. and porosity of the coatings.

6.3.2 Surface Morphology

Figures 6.3 (a) through (d) show in comparison, the morphology of various electrodeposited samples, examined under SEM. A variation in the surface morphology was observed as c.d. increased. The coating electrodeposited at 1.0 A dm^{-2} is found to be relatively compact and uniform as seen in Figure 6.3 (a) and as the c.d. increased, the coatings showed rough and cauliflower-like morphology, with a porous structure formed by aggregates of small grains. Coatings at higher c.d.'s also shows some microcracks on its surface. The roughness of Sn–Ni coatings obtained at higher c.d.'s was much more pronounced, as the nodules became well defined and separated as seen in Figures 6.3 (c) and (d). The rough morphology of the coatings obviously increases the real surface area of the deposit, and it is expected to be beneficial for HER. The progressive increase in the porosity with c.d. may be attributed to the formation of metal hydroxide at cathode film due to local alkylation (an increase of pH) caused by excess hydrogen evolution, during deposition.

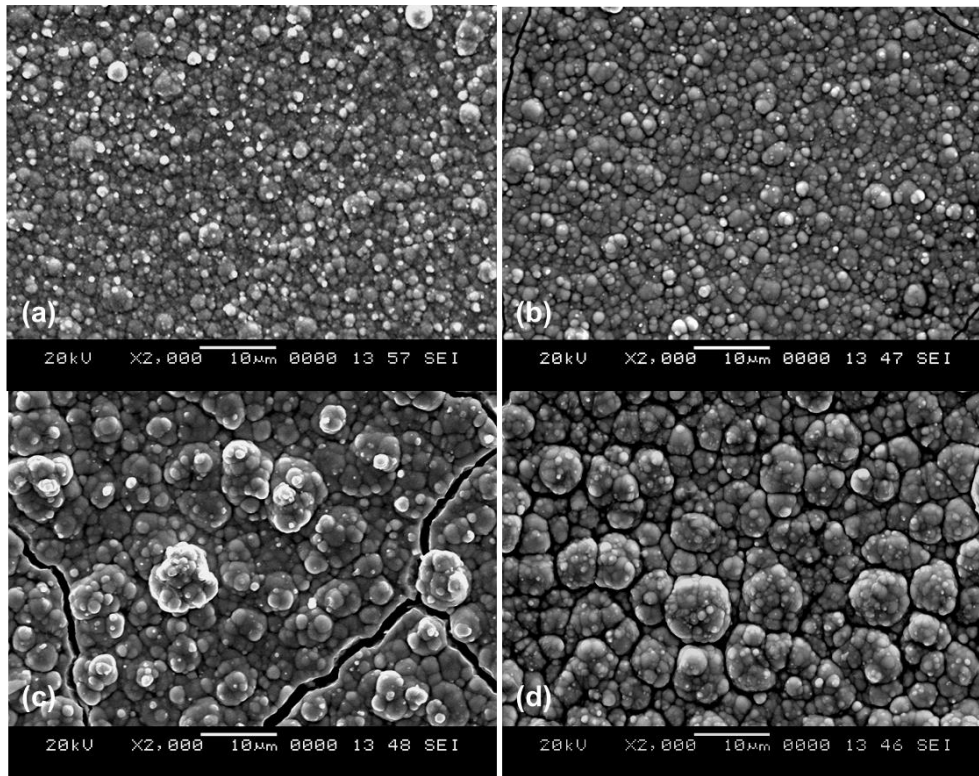


Figure 6.3 – SEM images of Sn–Ni alloy coatings deposited from the optimized bath at different c.d.'s: a) 1.0 A dm^{-2} , b) 2.0 A dm^{-2} , c) 3.0 A dm^{-2} and d) 4.0 A dm^{-2}

6.3.3 X-ray Diffraction Study

The phase structure and grain size of alloy coatings are analyzed using XRD technique. The XRD patterns of Sn–Ni alloy coatings, deposited at different c.d.'s from 1.0 to 4.0 A dm^{-2} is shown in Figure 6.4. As seen in Figure 6.4, the peaks at 2θ values of 30.5° , 44.1° , 50.2° , 77.7° and 89.6° correspond to characteristic peaks of Ni_3Sn_2 , which could be assigned to (101), (110), (200), (004) and (114) reflection, respectively. The hexagonal Ni_3Sn_2 (JCPDS No. 01-072-2561) peaks are consistent with the standard patterns, which were identified using JCPDS-PCDFWIN powder diffraction software package. Furthermore, the intensity of XRD peaks corresponding to Ni_3Sn_2 (200), Ni_3Sn_2 (004) and Ni_3Sn_2 (114) phases are found to be decreased with the increase in c.d. (from 1.0 to 4.0 A dm^{-2}). Therefore, it may be inferred that the c.d. has a profound influence on the phase structure of the alloy coatings. The average crystallite size of the

coatings was found to be 19 nm, calculated from full width half maximum (FWHM) for all the peaks using Eqn. (3.4).

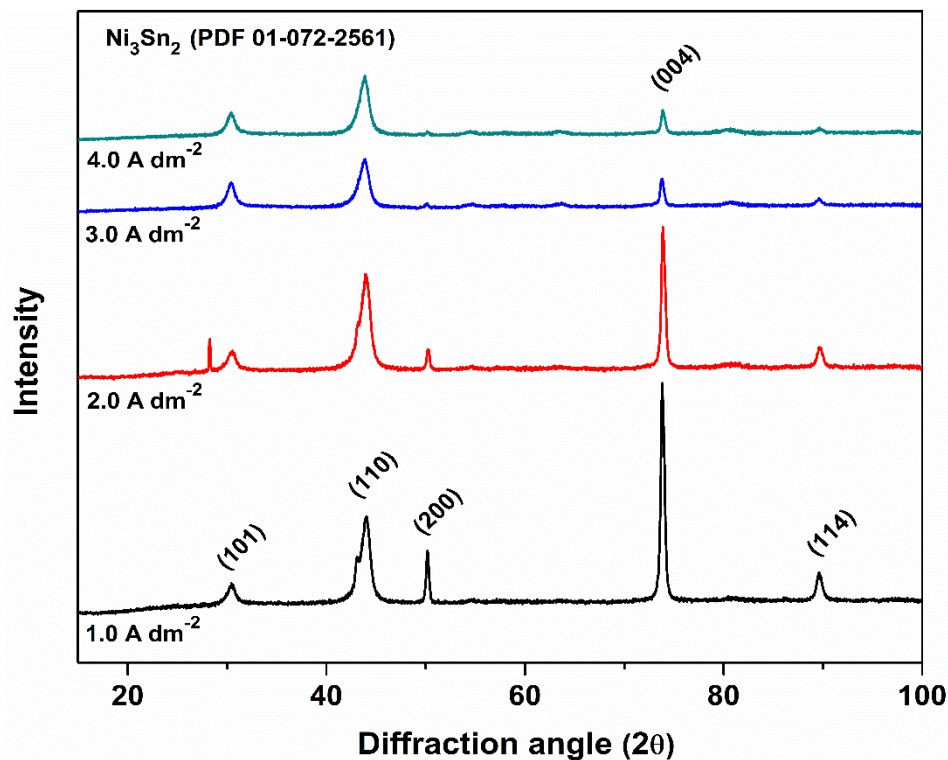


Figure 6.4 – XRD patterns of Sn–Ni alloy coatings deposited on a copper substrate at different c.d.'s, using the optimal bath

6.3.4 Corrosion Stability

To qualify the electroplated Sn–Ni alloy coatings to use as an electrode material for water splitting applications in 1.0 M KOH, they are subjected to a corrosion test in the same medium. The corrosion behavior of coatings deposited at different c.d.'s was evaluated by subjecting them to the potentiodynamic polarization study. The potentiodynamic polarization curves of Sn–Ni alloy coatings, deposited at different c.d.'s, are shown in Figure 6.5. Tafel extrapolation on such curves was used to determine the corrosion potential (E_{corr}), corrosion c.d. (i_{corr}), and corrosion rate (CR) (Venkatakrishna and Hegde 2010). The linear behavior, exclusively associated with the cathodic branch is assumed to represent the cathodic reaction of hydrogen evolution through reduction of water.

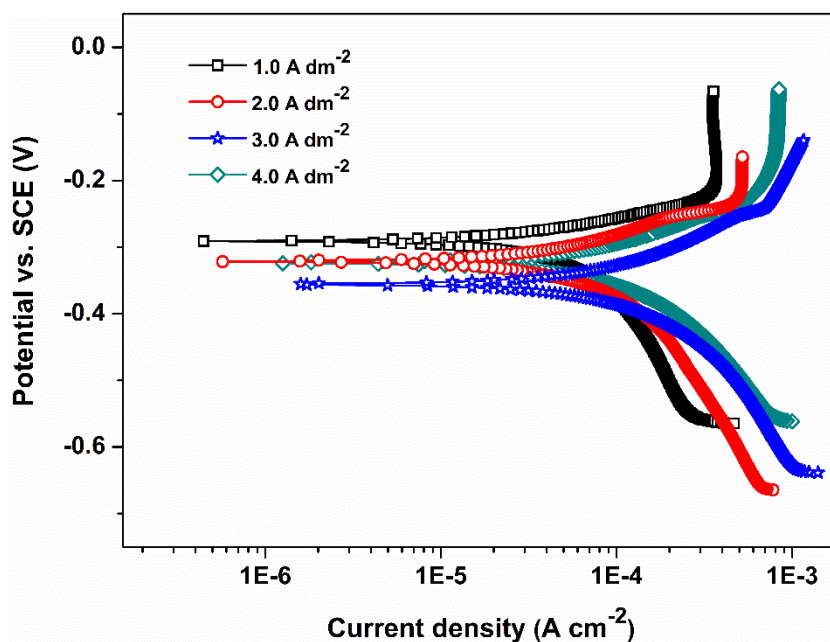


Figure 6.5 – Potentiodynamic polarization behavior of Sn–Ni coatings deposited on copper at different c.d.'s, using the optimal bath

The anodic branch, on the other hand, show inflection points characterized by two different slopes at potentials more positive than corrosion potential. This is called kinetic barrier effect, most probably due to deposition of corrosion product (in the form of a surface film) followed by its dissolution at increased anodic overvoltage (Dinodi and Shetty 2014). The corrosion data, like E_{corr} , i_{corr} , and CRs, are reported in Table 6.1. It may be noted from the corrosion data that Sn–Ni alloy coating at 1.0 A dm^{-2} (having about 80.4% Sn) shows the least CR, i.e. $66.40 \times 10^{-2} \text{ mm y}^{-1}$, while coatings at higher c.d.'s are more susceptible to corrosion. Furthermore, an increase of CRs at high c.d. indicates that corrosion stability decreases with Sn content, evidenced by the data in Table 6.1.

To investigate the electrocatalytic activity of as-deposited alloys, linear Tafel fit was performed at the cathodic and anodic region of the polarization curve. The kinetic parameters such as cathodic Tafel slope (β_c), exchange current density (i_0), cathodic overpotential (η_c) and anodic overpotential (η_a) were determined from the linear part of semi-logarithmic polarization plots, and are given in Table 6.2. From the data it clear

that β_c obtained directly from slopes of Tafel curves is found to be least for the electrode deposited at 4.0 A dm^{-2} , compared to coatings developed at lower c.d.'s, indicating its improved electrocatalytic performance for HER. Furthermore, Sn–Ni alloy at 4.0 A dm^{-2} exhibits the highest i_o further confirming its maximum efficiency for HER.

Table 6.1 – Composition, hardness, thickness and electrochemical corrosion parameters of Sn–Ni alloy coatings deposited on copper, at different c.d. from the optimal bath

Deposition c.d. (A dm^{-2})	wt.% Sn	Vicker Hardness (V_{100})	Thickness (μm)	$-E_{\text{corr}}$ (V vs. SCE)	i_{corr} ($\mu\text{A cm}^{-2}$)	CR ($\times 10^{-2}$) mm y^{-1})
1.0	80.4	148	8.8	0.290	31.94	66.40
2.0	68.3	161	10.6	0.321	42.51	80.10
3.0	65.1	172	12.1	0.355	51.07	93.93
4.0	62.4	193	13.4	0.323	53.31	96.12

Table 6.2 – Electrocatalytic kinetic parameters for HER and OER, determined on as-deposited Sn–Ni alloy coatings, deposited on copper from the optimal bath

Deposition c.d. (A dm^{-2})	$-\beta_c$ (mV dec^{-1})	i_o ($\mu\text{A cm}^{-2}$)	$-\eta_c$ (V vs. SCE)	η_a (V vs. SCE)
1.0	130.35	1.42	1.428	0.515
2.0	119.71	1.84	1.393	0.526
3.0	92.01	2.35	1.351	0.541
4.0	82.43	2.94	1.316	0.594

Generally, any good electrocatalyst for HER is required to have less applied η_c and high i_o to bring about the reaction more efficiently. Accordingly, from the Table 6.2, it

is clear that Sn–Ni alloy developed at 4.0 A dm^{-2} has the lowest η_c (-1.316 V) signifying its highest efficiency for HER. Similarly, it may be noted that Sn–Ni alloy developed at 1.0 A dm^{-2} show the lowest η_a (0.515 V), testifying its highest suitability for OER, compared to other coatings.

6.3.5 Electrocatalytic Study

The HER and OER on metal/metal-based materials continue to attract great attention among electrochemists. The steady-state equilibrium method is one of the simplest techniques for investigating the electrocatalytic activity in alkaline water electrolysis. In this direction, cyclic voltammetry (CV) and chronopotentiometry (CP) studies are considered to provide a wealth of information with a set of parameters which are useful for evaluation of electrode materials, as an electrocatalyst for water splitting applications. In CV study, the hydrogen desorption peak area is one of the main parameters among the electrode characteristics, and it depends on its active specific surface area. Larger the active specific surface area, higher is the amount of hydrogen produced during the reduction and adsorption on the electrode. Another important parameter characterizing cathodic materials is the discharge/onset potential of hydrogen determining the interception of the voltammetric curve tangent to the X-axis. It represents the electrocatalytic properties of the cathodic material to be used for water electrolysis, and thus, allowing the evaluation of energy consumption in hydrogen production (Lupi et al. 2009).

In CP, a constant current is applied between the auxiliary and working electrodes, and the variation of working electrode potential (measured with respect to the reference electrode, SCE) is monitored. When the controlled current is passed through a cell, between the auxiliary and working electrode initially its potential changes rapidly as charge builds up at the electrode-solution interface until the potential is reached, at which the electrolysis of an electroactive component of the solution on the surface of electrode begins (Herraiz-Cardona et al. 2011). Hence, Sn–Ni alloy coatings electrodeposited at different c.d.'s from the proposed bath were tested for electrocatalytic activity for HER and OER in 1.0 M KOH , and the experimental results are reported as follows.

6.3.5.1 Electrocatalysis for HER

a) Cyclic voltammetry study

The water splitting ability of Sn–Ni alloy coatings, deposited at 1.0 to 4.0 A dm⁻² for HER has been evaluated by CV study. To begin with, the electrocatalytic activity of Sn–Ni alloy coating deposited at 1.0 A dm⁻² was studied in the potential range of 0.0 V to –1.6 V at a scan rate of 50 mV s⁻¹ for 50 cycles. The scan rate (50 mV s⁻¹) was selected, among different scan rates tried based on the best one showing clear peaks. It was observed that the initial cycles showed larger cathodic peak current density (i_{pc}) that eventually decreased with an increase in the number of cycles. After about 30 cycles, the i_{pc} was found to be constant, and CV curves were observed to retrace the path of the previous cycle. This situation is corresponding to a condition where the rate of adsorption of the H atom on the surface for formation of H₂ gas is equal to the rate of desorption of H₂ gas (Thomas and Henze 2001). The CV curves for HER of as-deposited Sn–Ni alloy coatings, deposited at higher c.d.'s is shown collectively in Figure 6.6, and corresponding electrochemical parameters are given in Table 6.3.

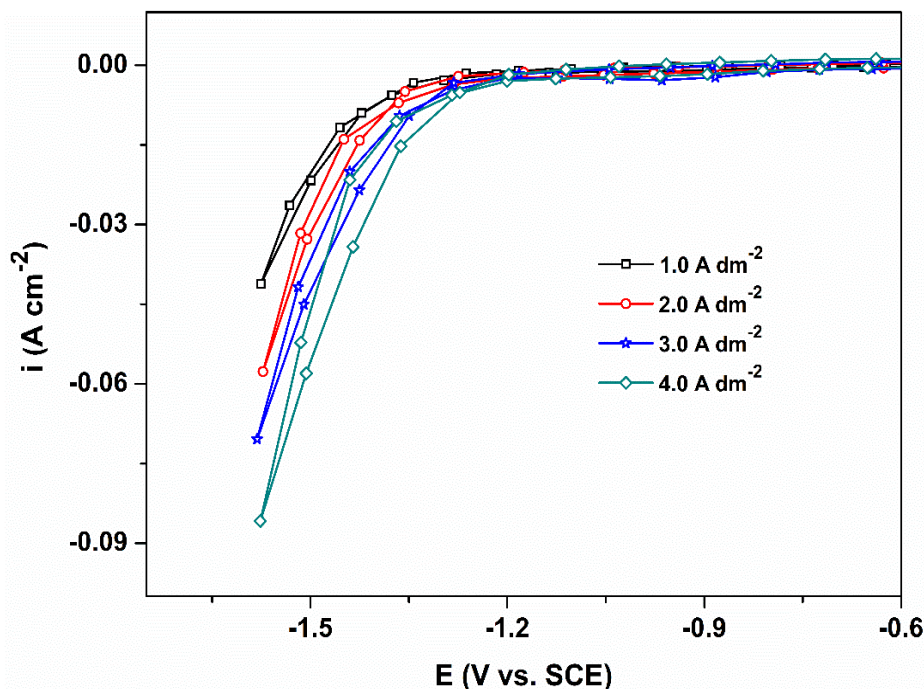


Figure 6.6 – CV curves demonstrating increase of cathodic peak current densities (i_{pc}) with deposition c.d.'s, for HER on the surface of as-deposited Sn–Ni alloy coatings

From Figure 6.6, it may be noted that as-deposited Sn–Ni alloy coating formed at 4.0 A dm^{-2} exhibits the highest i_{pc} (-0.086 A cm^{-2}), compared with all other coatings. The highest i_{pc} values recorded at 4.0 A dm^{-2} may be attributed to more Ni content (37.6 wt.%) of the alloy compared to other coatings, deposited from the same bath. Furthermore, it may be noted that the onset potential for H_2 evolution decreased as their deposition c.d. increased, suggesting that more Ni content of alloy (deposited at high c.d.) are more congenial for HER. Thus, the electrocatalytic behavior of as-deposited Sn–Ni alloy deposits were found to have a close relationship with the c.d. employed, as it is a deciding parameter for surface morphology, composition, and phase structure of the deposits.

Table 6.3 – Electrochemical parameters for HER of as-deposited Sn–Ni coatings developed at different c.d.’s from the optimal bath

Deposition c.d. (A dm^{-2})	Cathodic peak c.d. (i_{pc}) (A cm^{-2})	Onset potential HER (V vs. SCE)	Volume of H_2 evolved 300 s (cm^3)
1.0	-0.041	-1.34	10.5
2.0	-0.057	-1.30	10.8
3.0	-0.070	-1.28	11.1
4.0	-0.086	-1.26	11.4

An experimental study by Herraiz-Cardona et al. (2011) revealed that the intrinsic catalytic activity of Ni-based electrodeposits for HER is mainly due to the catalytic property of nickel (low hydrogen overpotential) and its counterpart (Sn having high hydrogen adsorption ability). Hence, it may be concluded that the highest i_{pc} value recorded by Sn–Ni coating at 4.0 A dm^{-2} is attributed to the synergistic effect of both Ni (37.6 wt.%) and Sn (62.4 wt.%) content in the deposit (Lupi et al. 2009).

b) Chronopotentiometry study

The CP study on as-deposited Sn–Ni alloy coatings, at different c.d. (1.0 to 4.0 A dm^{-2}), was made by applying a constant current of -300 mA cm^{-2} for a duration of 1800 s . The electrocatalytic activity of each as-deposited Sn–Ni alloy developed at different c.d.'s was evaluated by measuring the amount of H_2 liberated. The volume of H_2 gas evolved due to electrolysis was measured quantitatively using a specially designed glass setup (Figure 6.2). The nature of chronopotentiogram obtained for each sample is shown in Figure 6.7, and volume of hydrogen gas liberated for the initial 300 s is given in the inset. Experimental results showed that Sn–Ni alloy deposited at 4.0 A dm^{-2} liberate the maximum amount of H_2 , compared to other coatings deposited at lower c.d.'s. This supports the fact that as-deposited Sn–Ni alloy at 4.0 A dm^{-2} is electrocatalytically more active for HER.

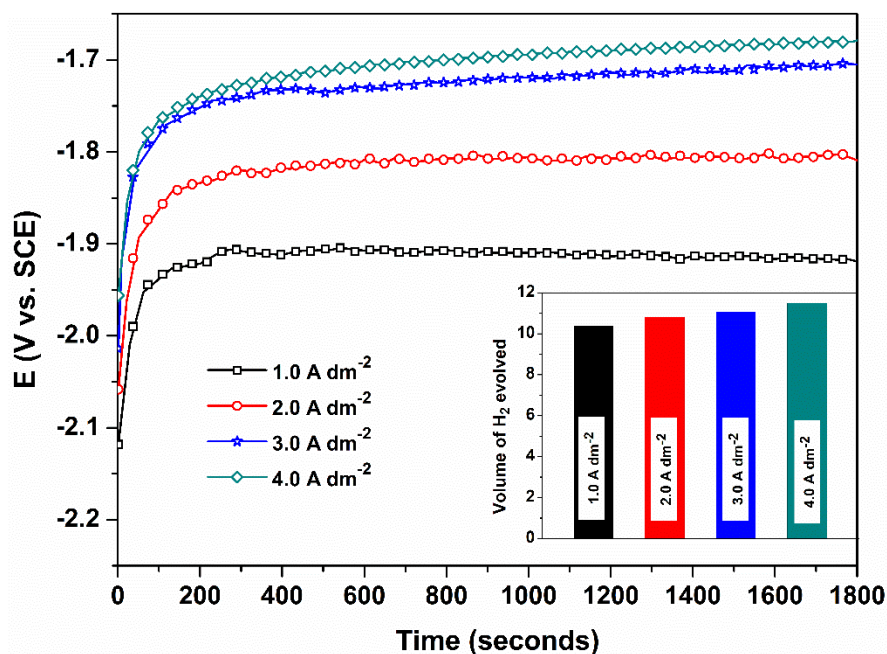


Figure 6.7 – CP curves of as-deposited Sn–Ni alloys, deposited at different c.d.'s under impressed cathodic current of -300 mA cm^{-2} for HER. The volume of H_2 evolved in 300 s on each electrode are shown in the inset

Furthermore, an initial sharp increase of potential soon after the initiation of electrolysis was observed in all cases, followed by a steady-state potential response. This can be explained by the progressive depletion of the electrolyzed species at the

surface of the test (working) electrode, where reduction of H^+ ions from the solution takes place to liberate H_2 gas, and eventually reaches a state of equilibrium between H^+ ions and H_2 (Thomas and Henze 2001, Ullal and Hegde 2014). The electrolysis attains almost a constant potential in few seconds as seen in Figure 6.7. At this stage, a hydrogen reaction takes place uninterruptedly on the electrode surface, where the current is invested completely in converting H^+ ions into H_2 gas. It is important to note that the steady-state potential of as-deposited Sn–Ni alloy coatings decreased with c.d., confirming the fact that H_2 evolution bears close relation with Ni content of the alloy.

6.3.5.2 Electrocatalysis for OER

a) Cyclic voltammetry

Sn–Ni alloy coatings, deposited at different c.d.'s was also tested for electrocatalytic activity for OER in the same 1.0 M KOH medium in the same line as HER. The CV experiments for OER on Sn–Ni alloy deposits were conducted in the potential range of 0.0 to 0.75 V at a scan rate of 50 mV s^{-1} , and corresponding voltammograms are recorded as shown in Figure 6.8.

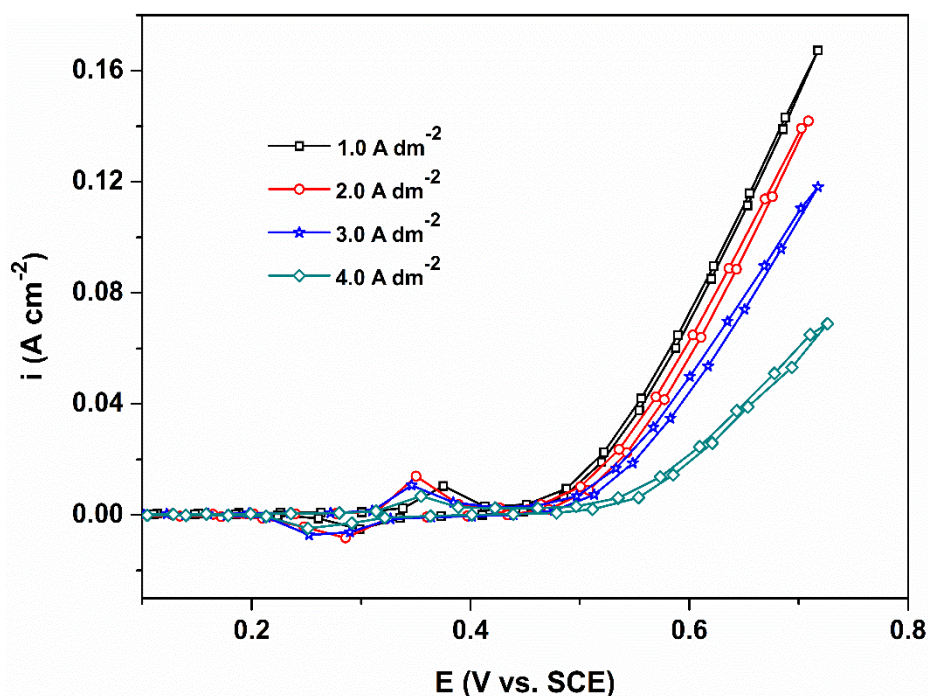


Figure 6.8 – CV curves for OER on as-deposited Sn–Ni alloy coatings deposited at different c.d.'s showing their anodic peak current densities (i_{pa})

The anodic peak current density (i_{pa}) and onset potentials for continuous evolution of O_2 gas on each coating are reported in Table 6.4. From the electrochemical data, it may be noted that the Sn–Ni alloy deposited at 1.0 A dm^{-2} gave good activity toward OER with maximum anodic peak potential (i_{pa}) of 0.167 A cm^{-2} , and the least onset potential (0.45 V), compared to the coatings developed at other c.d.'s.

Table 6.4 – Electrochemical parameters for OER on as-deposited Sn–Ni alloy coatings developed at different c.d.'s from the optimal bath

Deposition c.d. (A dm^{-2})	Anodic peak c.d. (i_{pa}) (A cm^{-2})	Onset potential OER (V vs. SCE)	Volume of O_2 evolved 300 s (cm^3)
1.0	0.167	0.45	13.3
2.0	0.141	0.47	12.8
3.0	0.118	0.49	12.3
4.0	0.069	0.50	11.1

b) Chronopotentiometry

Sn–Ni alloy coatings are tested for their OER efficiency also by CP technique in the same line as discussed earlier. Coatings deposited from 1.0 to 4.0 A dm^{-2} are subjected to CP study, and corresponding chronopotentiograms are shown in Figure 6.9. The inset in Figure 6.9 shows the relative amount of O_2 liberated in 300 s. It may be noted from the CP curves, initially, there exists a sharp increase in potential on each electrode surface, which later remains stable throughout with continuous evolution of oxygen. This increase in potential is attributed to the equilibrium state existing between the newly formed O_2 molecules and the ones that are escaping from the electrode surface. The volume of O_2 liberated corresponding to each test specimen is given in Table 6.4. As seen from the data, the Sn–Ni alloy coatings developed at 1.0 A dm^{-2} could liberate the highest quantity of O_2 compared to all coatings at higher c.d.'s. This behavior is attributed to a specific composition of the alloy, showing a synergistic effect toward OH^- adsorption and, hence, for OER. Furthermore, it may be noted that the steady-state

potential of Sn–Ni alloy coatings increased with deposition c.d. confirming the fact that O_2 evolution bears close relation with Sn content of the alloy.

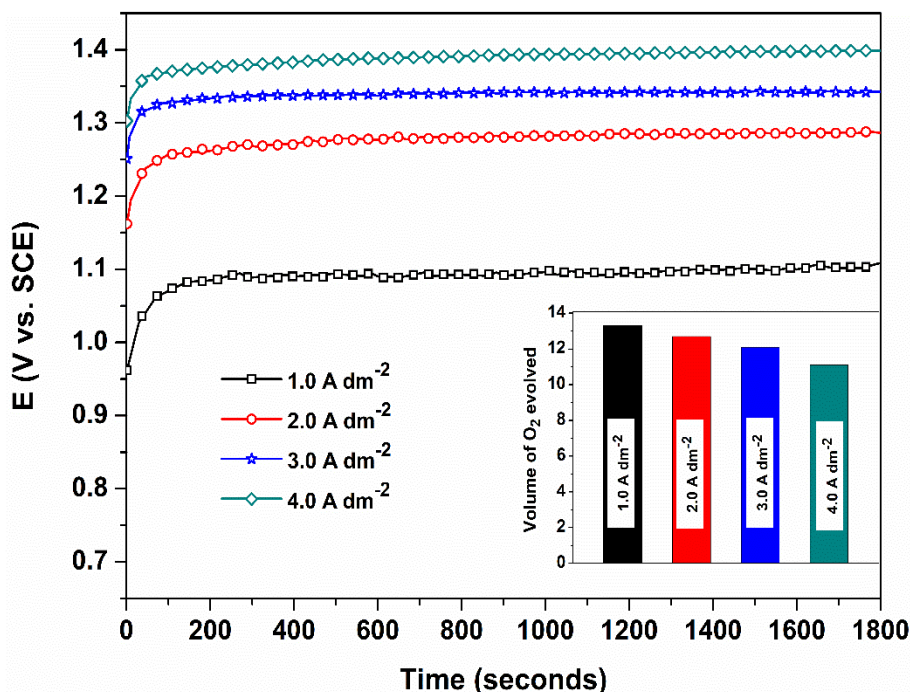


Figure 6.9 – Chronopotentiograms of as-deposited Sn–Ni alloys for OER, at different deposition c.d.'s under impressed anodic current of $+300 \text{ mA cm}^{-2}$. The volume of O_2 evolved in 300 s on each test electrode is shown in the inset

6.3.6 Electrochemical Dissolution Treatment

The electrocatalytic activity of as-deposited Sn–Ni alloy coating was tried to improve further by electrochemical dissolution method, by making it an anode. The process is also termed as anodic dissolution. The Sn–Ni alloy deposited at 4.0 A dm^{-2} (optimal c.d. for HER) was selected for anodic dissolution test. The anodic c.d. of 4.0 A dm^{-2} arrived on the basis of a well-defined structural matrix of the alloy coating obtained when observed under SEM. The surface of as-deposited Sn–Ni alloy coating appeared to be bright, and after electrochemical treatment (anodic dissolution), the surface lost its lustrous appearance and turned rough powdery. Figure 6.10 displays the SEM micrographs of the surface morphology of Sn–Ni alloy coating (deposited at 4.0 A dm^{-2}) before and after the anodic dissolution. A well-defined micro-porous structure,

responsible for increased surface area of Sn–Ni alloy coating can be seen in Figure 6.10 (b) compared to as-deposited alloy (Figure 6.10 (a)).

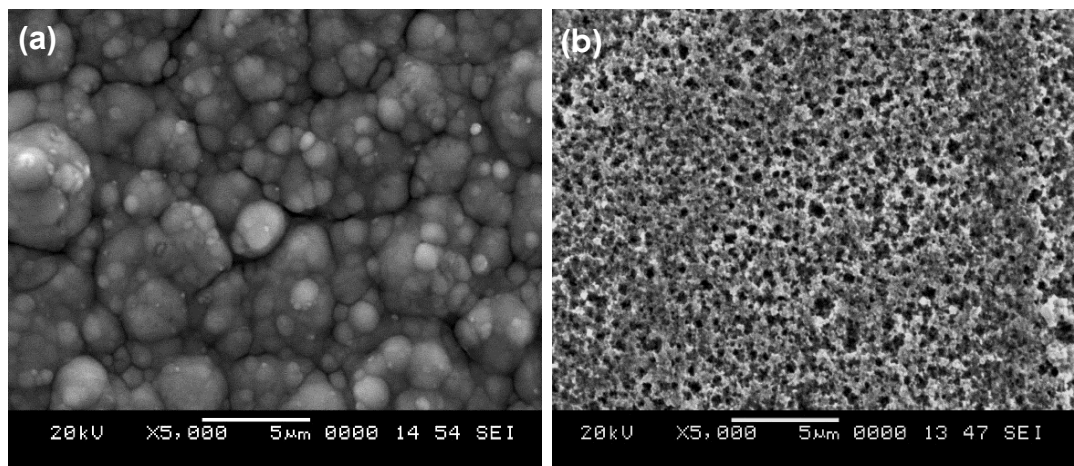


Figure 6.10 – SEM images of Sn–Ni alloy coatings deposited at optimal *c.d.* of 4.0 A dm^{-2} : a) as-deposited surface, and b) after anodic dissolution showing micro-porous structure

The 3D Atomic Force Microscopy (AFM) image, showing the surface roughness of Sn–Ni alloy coating (deposited at 4.0 A dm^{-2}) before and after the anodic dissolution is given in Figure 6.11. It is evident from the AFM image, shown in Figure 6.11 (b) that after the dissolution treatment roughness of the coating increased with micro-pores extended deep into the surface. The formation of these pores is vital for higher HER efficiency, because of cracks, being filled with the electrolyte, renders a greater part of the internal surface of Sn–Ni alloy, accessible to electrochemical gas evolution, than would be possible in as-deposited Sn–Ni alloy. Numerous pores, as generated by leaching lead to sufficiently short diffusion paths of dissolved hydrogen, for the fastest release of the gas and for avoiding excessive gas accumulation and concentration polarization in the micropores (Sheela et al. 2002). This increase in the surface area results in lower overvoltage for HER which is reflected in the parameters derived from the CV and CP study, given in Figure 6.12 and Table 6.6.

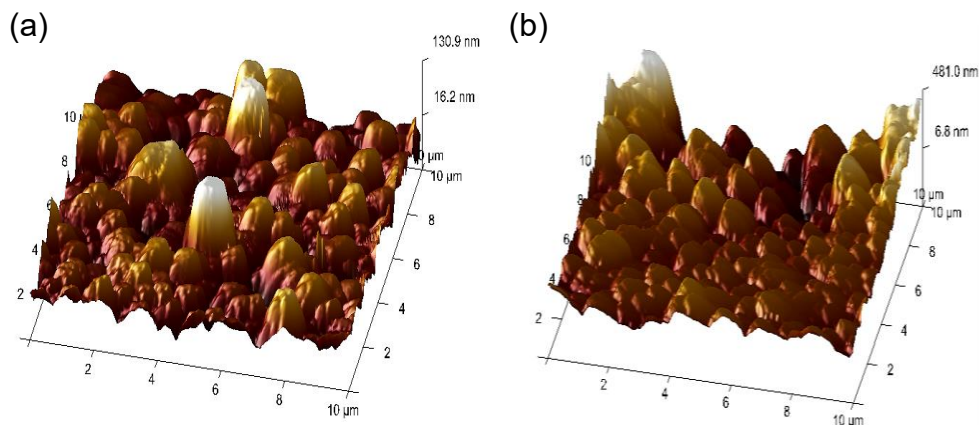


Figure 6.11 – AFM images of Sn–Ni alloy coatings at optimal c.d. of 4.0 A dm^{-2} : a) as-deposited surface, and b) after anodic dissolution

The light and dark regions correspond to areas above and below the mean elevation, respectively. Some parameters extracted from AFM image have been used for characterizing Sn–Ni alloy surface topography. Among all parameters, the mean roughness (R_a) is the most universally used one, which is defined as the average absolute deviation of the roughness irregularities from the mean line over one sampling length. In addition, root mean square roughness (R_q) represents the standard deviation of the distribution of surface heights (Gadelmawla et al. 2002). The difference in the morphology of as-deposited and anodically treated Sn–Ni alloy, responsible for the improved electrocatalytic property are given through two parameters, like R_a and R_q in Table 6.5.

Table 6.5 – AFM parameters of Sn–Ni alloy coatings deposited at 4.0 A dm^{-2} before and after electrochemical dissolution

Coating condition ($10 \mu\text{m}$)	Surface roughness parameters	
	R_a (nm)	R_q (nm)
as-deposited Sn–Ni alloy	22.5	29.5
anodically treated Sn–Ni alloy	77.8	112

From the data shown Table 6.5, it is evident that the surface roughness of Sn–Ni alloy coated at 4.0 A dm^{-2} has increased after the anodic dissolution treatment. The porous structure of Sn–Ni alloy coating, seen in Figure 6.10 (b) may be attributed to the leaching of Sn and Ni during electrochemical dissolution, and is responsible for increased surface area, hence better electrocatalytic behavior. The electrocatalytic character of anodically treated Sn–Ni alloy coatings was studied by same CV and CP methods as described earlier. The CV and CP curves of anodically dissolved Sn–Ni alloy coatings, in comparison with that of as-deposited Sn–Ni alloy are shown in Figure 6.12 (a) and (b), respectively. Electrocatalytic parameters, like i_{pc} , onset potential, and volume H_2 liberated from CV and CP study respectively is reported in Table 6.6.

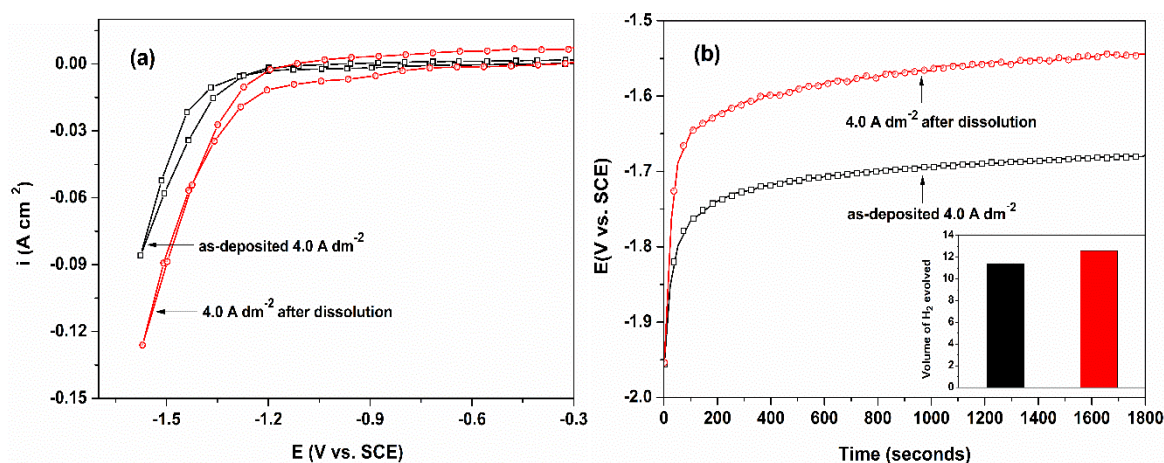


Figure 6.12 – Electrocatalytic response of as-deposited and anodically treated Sn–Ni alloy coatings, deposited at optimal c.d. (4.0 A dm^{-2}), through a) CV study, and b) CP study (with volume of H_2 liberated in the inset)

The increased electrocatalytic property of Sn–Ni alloy coatings due to anodic dissolution may be credited to the increased porosity, affected due to selective leaching. Due to an increase of porosity, the metal particles residing in a pore of similar size are more, and hence, a considerable part of its surface will be in intimate contact with the pore walls and, therefore, favors hydrogen production (Wieckowski et al. 2003). Thus, improved electrocatalytic activity after anodic treatment is due to increase in the porosity of the coatings; which leads to an increase in the surface area of the coating, thereby making more active metal atoms to come in intimate contact with the electrolyte

(1.0 M KOH). The increased porosity is ascertained from the SEM image, shown in Figure 6.10 (b).

Table 6.6 – Electrocatalytic parameters of CV and CP study for HER in 1.0 M KOH on Sn–Ni alloy, deposited at 4.0 A dm^{-2} under different conditions

Coating condition	i_{pc} at 1.6 V (A cm^{-2})	Onset potential for H_2 evolution (V vs. SCE)	Volume of H_2 evolved 300s (cm^3)
as-deposited Sn–Ni alloy	–0.085	–1.26	11.4
anodically treated Sn–Ni alloy	–0.127	–1.18	12.1

6.3.7 Effect of Electrode Composition on Electrocatalytic Activity

The experimental results after an investigation on the electrocatalytic behavior of Sn–Ni alloy coatings revealed that Sn–Ni alloys having 37.6 wt.% Ni (deposited at 4.0 A dm^{-2}) and 19.6 wt.% Ni (deposited at 1.0 A dm^{-2}) are more favorable for HER and OER, respectively. It may be further noted that electrocatalytic activity of Sn–Ni alloy coatings for HER and OER increased linearly with Ni and Sn content of the deposit, respectively (Tables 6.3 and 6.4). It was also reported that the HER efficiency bears a close relationship with adsorption strength of hydrogen on the metal surface (Nørskov et al. 2005). If the M–H_{ads} bond strength is too weak, activation of the hydrogen to the metal surface is difficult. On the other hand, strong M–H_{ads} bond blocks the available reaction sites on the metal surface (Jaksic 2000). This suggests that an optimal M–H_{ads} bond strength is required for maximum HER to occur (Jaksic 2000, Nørskov et al. 2005). Based on this, many reports stated Ni as the best non-precious metal with suitable H–adsorption energy and can be enhanced through proper alloying with other metals or non-metals (Jaksic 2000, Ahn et al. 2012). Thus, the better electrocatalytic activity of Sn–Ni alloy coatings at high c.d. is due to the highest Ni content of the alloy. Also, electrocatalytic activity of Ni for HER among the non-noble metals is highest,

which on alloying with Sn in definite proportion imparts minimum hydrogen adsorption energy, leading to the maximum evolution of H₂. (Gómez et al. 1997, Ahn et al. 2012).

6.3.8 Mechanism of HER and OER

The electrocatalytic evolution of H₂ (HER) on the surface of Ni–M electrodes can also be explained by the mechanism shown in Figure 6.13 (a). The HER in an alkaline solution is considered as an amalgamation of three basic steps, two electrochemical (Eqn. (6.1) and (6.2)) and one chemical (Eqn. (6.3)).



It can be observed that the initial step is an electrochemical reduction of the water molecule, to give hydrogen adsorbed on the electrode surface by Volmer reaction (Eqn. (6.1)), followed by Heyrovsky reaction (Eqn. (6.2)), an electrochemical step for adsorbed hydrogen to produce H₂, and/or by chemical reaction i.e. Tafel reaction (Eqn. (6.3)). Choquette et al. (1990) have reported the HER mechanism based on the value of cathodic Tafel slope, β_c . It has been described that Tafel slope in range -66 mV dec^{-1} corresponds to the Heyrovsky-Volmer mechanism, and in the neighborhood of -118 mV dec^{-1} follows Volmer-Tafel mechanism, and finally above -200 mV dec^{-1} exhibit the Tafel mechanism.

Tafel slope is an inherent property of a catalyst determined by the rate-limiting step of HER. Hence, a lower β_c means that a catalyst requires a lower applied overpotential to generate a required current (Jiang 2015). Tafel slope (β_c) values are determined from the linear part of Tafel plots (Figure 6.5) of the coatings, and corresponding β_c values are reported in Table 6.2. In the present study, it can be seen that β_c values of Sn–Ni alloy coatings deposited at increasing c.d. fall in the range of about -118 mV dec^{-1} . Hence, it may be inferred that Sn–Ni alloy coatings follow Volmer-Tafel type of mechanism for HER, and is shown schematically in Figure 6.13 (a).

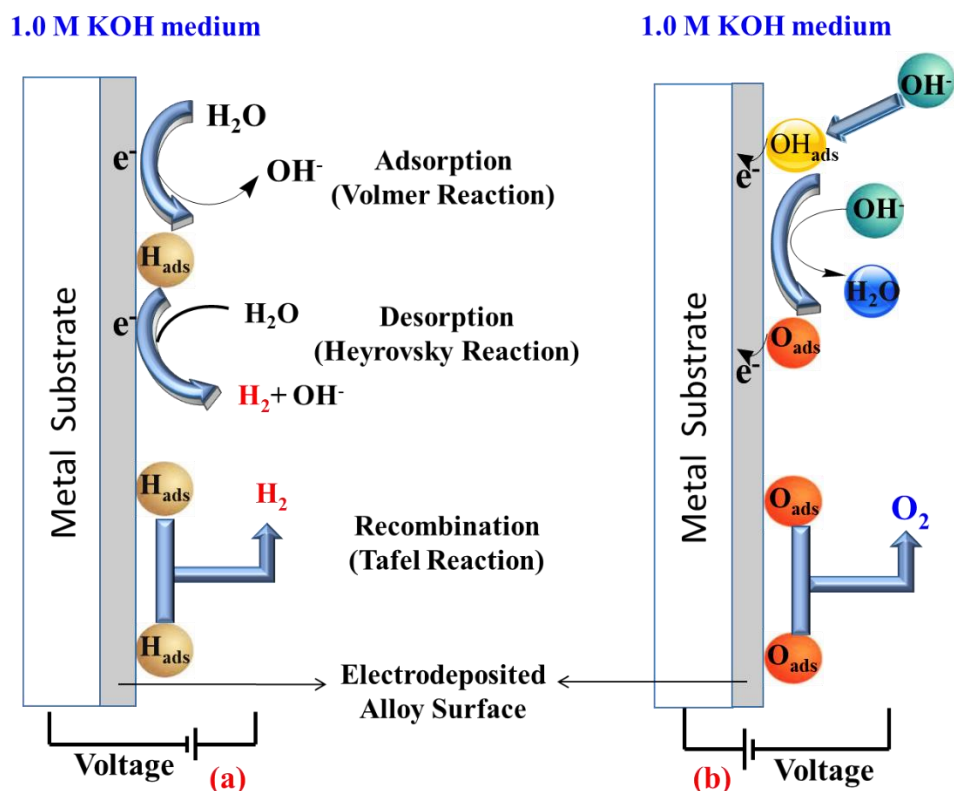


Figure 6.13 – Schematic diagram showing the mechanism of HER (a) and OER (b) on the surface of Sn–Ni alloy coatings having definite composition, used as cathode and anode respectively in 1.0 M KOH solution

Similarly, the OER proceeds in alkaline media via the steps sequentially shown below (Chekin et al. 2014) and is shown schematically in Figure 6.13 (b)



This behavior could be described by the adsorption of relatively large OH^- ions on the surface of an electrode, and at the same time, it overlaps with other processes like oxygen reduction reaction. Therefore, improved OER activity of Sn–Ni coating, developed at 1.0 A dm^{-2} can be ascribed to the increased adsorption of OH^- ions

through the formation of a semiconducting layer in the range of applied potential (Elias et al. 2015).

6.4 CONCLUSIONS

Bright Sn–Ni alloy coatings has been developed on the copper substrate to use as an effective electrode material for alkaline water-splitting applications. Electrocatalytic study of as-deposited Sn–Ni alloy has been studied and is improved further by anodic dissolution. The experimental results established the following conclusions.

- 1) The Sn–Ni alloy coatings deposited at 4.0 A dm^{-2} (having 37.6 wt.% Ni) and 1.0 A dm^{-2} (having 19.6 wt.% Ni) was found to be the good electrocatalyst for HER and OER, respectively in 1.0 M KOH medium, evident from CV and CP studies.
- 2) Under working conditions of electrolysis, as-deposited Sn–Ni alloy coatings deposited at 1.0 A dm^{-2} found to be least susceptible to corrosion compared to coatings developed at higher c.d.'s confirmed by electrochemical corrosion tests.
- 3) The high electrocatalytic activity of Sn–Ni alloy coatings for both HER and OER are specific of their composition, surface morphology, and active surface area.
- 4) A drastic improvement in the electrocatalytic activity of anodically treated Sn–Ni alloy was found, compared to its as-deposited alloy.
- 5) Improved electrocatalytic activity of anodically treated Sn–Ni alloy coatings is attributed to the increased number of pores, making the more active metal atoms to come in intimate contact with the electrolyte.

CHAPTER 7

CHAPTER 7**ELECTRODEPOSITION OF Ni–Mo ALLOY COATINGS
AND ITS ELECTROCATALYTIC ACTIVITY FOR WATER
SPLITTING REACTION**

This chapter details the optimization of a new citrate bath for the production of bright and uniform Ni–Mo alloy coating on copper by conventional electrodeposition (ED) method (using DC). The performance of the coatings was evaluated in terms of its ability to catalyze the hydrogen evolution reaction (HER) and oxygen evolution reaction (OER) in 1.0 M KOH. Experimental results are discussed in terms of surface micrograph, composition, and phase structure of the coatings, using SEM, EDX and XRD analyses.

7.1 INTRODUCTION

From the literature, it is well known that though molybdenum (Mo) is quite electroactive metal, it cannot be deposited by itself from its electrolytic bath (Brenner 1963). However, it can be deposited in the presence of another metal, through induced co-deposition. Accordingly, in electrodeposition of Ni–Mo alloy, Ni stimulates the deposition process, and is called the inducing metal; and Mo is called the reluctant metal. Generally, it has been observed that in induced codeposition there is no consistent trend in the reluctant metal content in the deposit with c.d. i.e., variations in properties of electrodeposited Ni–Mo alloy coatings with c.d. is quite vagarious, and hence the scope for studying the structure-property relationship of Ni–Mo alloy is quite interesting. Studies on Ni oxides and hydroxides, when combined with Co, Mo, and Fe, produced by several chemical, thermal and electrochemical routes (Lian et al. 1992, Chi et al. 2005, Li et al. 2006) and high-energy ball mill method (Kedzierzawski et al. 2001), have been carried out in order to develop an efficient electrocatalyst. Arul Raj and Venkatesan (1988) exhibited an improved electrocatalytic effect of electrodeposited Ni–Mo alloys for HER than that of Ni and other Ni-based binary alloys such as Ni–Co, Ni–W, Ni–Fe, and Ni–Cr. It was also reported that electrodeposited

Ni–Mo alloy coatings exhibit good anticorrosive behavior, mechanical and thermal stability (Chassaing et al. 1995). Non-toxic citric acid and its salts belong to the most promising complexing compounds used in galvanic baths, which allow a variety of electrodeposited coatings to be produced. Moreover, citrate aqueous solutions are characterized by buffering, leveling and brightening properties, which allows in obtaining galvanic coatings of good quality (Beltowska-Lehman and Indyka 2012). Hence in the present study, the benefit of the electrolytic bath having mixed sulphate solutions complexed with citrate ions is used to formulate a new Ni–Mo alloy bath. The experimental conditions of bath composition and c.d. have been optimized for best electrocatalytic activity for water splitting. The first part deals the conventional electrodeposition (ED) and characterization of Ni–Mo alloy coating using DC, and the second part details its electrocatalytic study for water splitting applications.

7.2 ELECTRODEPOSITION OF Ni–Mo ALLOY COATINGS

ED Ni–Mo alloy coating is accomplished by using DC, where mass transport of metal ions towards cathode is accomplished through only natural convection i.e. due to applied c.d. To begin with, a new citrate bath of Ni–Mo alloy has been optimized through conventional Hull cell method, explained elsewhere (Pardhasaradhy 1987). Limiting conditions of bath composition and operating parameters have been arrived, based on both quality and performance of alloy coatings. The composition and operating parameters of the bath, arrived after optimization is given in Table 7.1.

Table 7.1 – Composition and deposition conditions of the optimized Ni–Mo bath

Bath constituents	Amount (g L ⁻¹)	Operating parameters
NiSO ₄ ·6H ₂ O	18	Anode: Pure Ni plate
Na ₂ MoO ₄	48	Cathode: Copper
Na ₃ C ₆ H ₅ O ₇	105	pH: 9.5
		Temperature: 298 K
		Deposition time: 10 min
		Current density: 1.0 – 4.0 Adm ⁻²

Electrodeposition of Ni–Mo alloy coatings was carried out on copper substrate at different c.d. (from 1.0 to 4.0 A dm⁻²) using optimal bath with the setup as seen in Figure 6.1, they are subjected to various analyses, and the results are reported below.

7.3 RESULTS AND DISCUSSION

7.3.1 SEM Analysis

The surface morphology of ED Ni–Mo alloy coatings, developed at different c.d.'s is shown in Figure 7.1. It can be observed that the coatings deposited at 1.0 A dm⁻² and 2.0 A dm⁻² exhibit a nodular structure, as shown in Figure 7.1 (a) and (b), respectively. Then, as the c.d. increased the size of nodules increased, but fewer in numbers making the surface smoother and uniform as seen in Figure 7.1 (c) and (d).

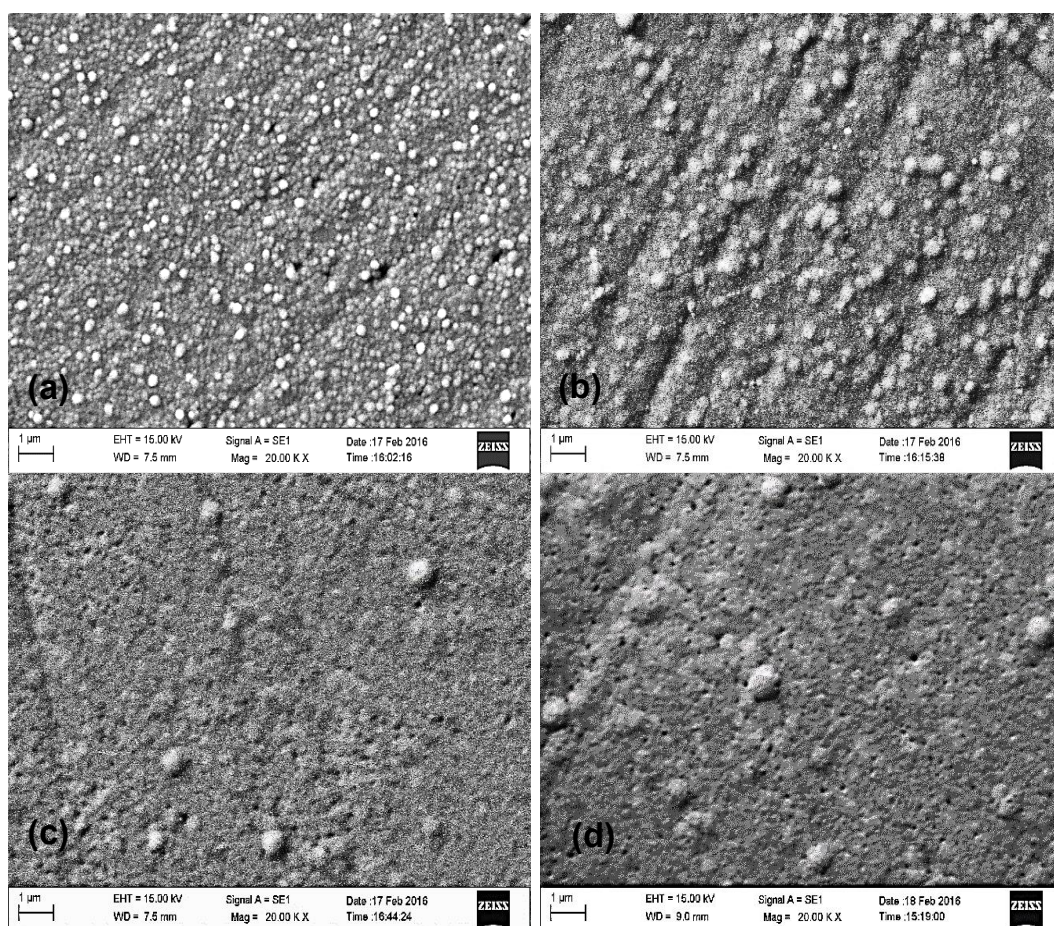


Figure 7.1 – SEM images of Ni–Mo alloy deposited from optimal bath at a) 1.0 A dm⁻², b) 2.0 A dm⁻², c) 3.0 A dm⁻² and d) 4.0 A dm⁻²

Further, Ni–Mo alloy coatings deposited at high c.d. were characterized by some pin holes, attributed to the evolution of hydrogen during codeposition (Aaboubi 2011). Thus, from SEM micrographs of Ni–Mo alloy coatings, it may be inferred that surface morphology of the coatings bears a close relationship to applied c.d. From the data shown in Table 7.2, it is evident that applied c.d. has a strong influence on the composition of coatings as well. Further, it is evident that towards lower c.d. the wt.% of Mo is high, which is characterized by a nodular coarse-grained structure. As the c.d. increased, the wt.% of Ni also increased, which is responsible for the increased electrocatalytic activity of the coatings for OER, as will be discussed.

7.3.2 AFM Study

The AFM is a powerful means to characterize the microstructure of the coatings, in terms of their porosity and surface roughness. Accordingly, a 3D AFM image of the Ni–Mo alloy coatings at 1.0 A dm^{-2} and 4.0 A dm^{-2} (only representative) have been taken, and are shown in Figure 7.2 (a) and (b), respectively.

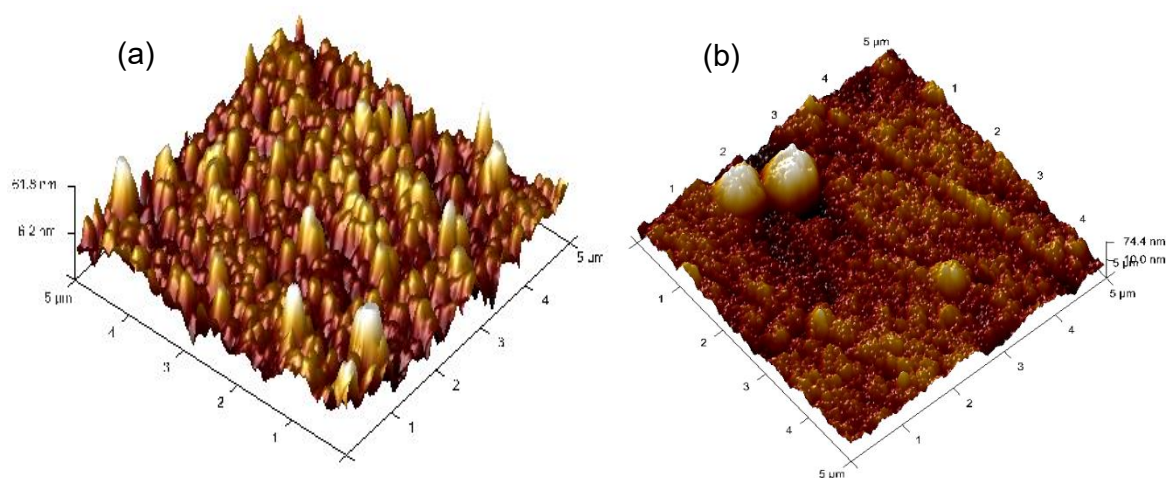


Figure 7.2 – 3D AFM images of Ni–Mo alloy coatings deposited at a) 1.0 A dm^{-2} , and b) 4.0 A dm^{-2}

A clear difference in the surface roughness of the coatings was found when the c.d. is increased from 1.0 A dm^{-2} to 4.0 A dm^{-2} . Experimental data revealed that the average roughness of coatings at 1.0 A dm^{-2} and 4.0 A dm^{-2} are 17.0 and 9.11 nm, respectively. It is further supported by the visual observation, shown in Figure 7.2 (a) and Figure 7.2

(b). Further, the high surface roughness of Ni–Mo alloy coatings, deposited at 1.0 A dm^{-2} is in compliance with SEM micrograph, shown in Figure 7.1 (a).

7.3.3 EDX Analysis

The compositional analysis of Ni–Mo alloys deposited at various applied c.d.'s was carried out by EDX method, and experimental data are reported in Table 7.2. The EDX spectrum of Ni–Mo alloy corresponding to 1.0 A dm^{-2} (only representative) is shown in Figure 7.3 and their wt.% is reported in Table 7.2. A strong influence of the c.d. on Mo content of the coating may be observed. It may be noted that Mo content of the alloy is maximum, for the coating developed at 1.0 A dm^{-2} (38.3%), and it decreased with an increase in c.d.

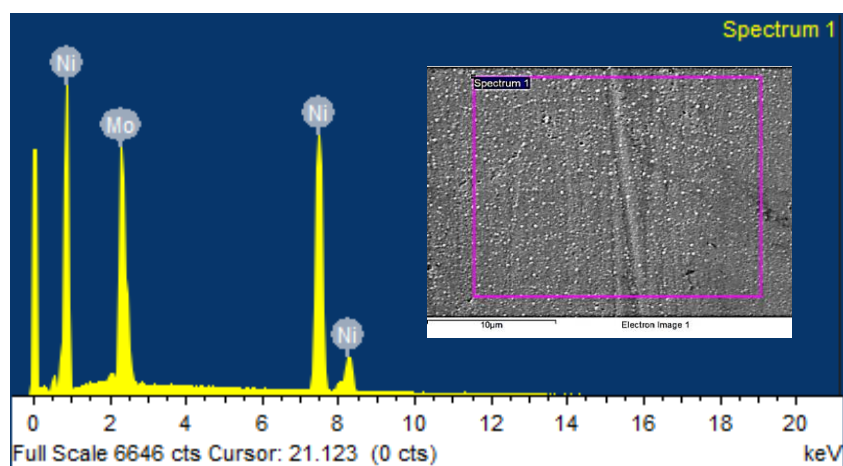


Figure 7.3 – EDX spectrum of Ni–Mo alloy coating, deposited at 1.0 A dm^{-2} showing the relative peaks corresponding to its Ni and Mo content

When compared to very high Mo content in the bath, the maximum Mo content of the ED Ni–Mo alloy coating is only 38.3 wt.%. Further, it may be noted that an increase of c.d. from 1.0 to 4.0 A dm^{-2} resulted in the decrease of the Mo content to only about 5 wt.%. This unusual small variation of Mo content with c.d. may be attributed to the complexation of metal ions which affects the static potentials of the parent metals remarkably (Halim et al. 2012). In other words, the bath exhibits very low partial c.d. for deposition of Mo (compared to its calculated i_L), due to a low rate of mass transport of electroactive species (Mo^{+2} ions) from a pH dependent molybdate-citrate complex. Hence, an unusual decrease of Mo content with c.d. is more due to change in pH (due

to the evolution of H_2 gas), responsible for shifting the equilibrium of its citrate complex, than due to change in its i_L (Vayenas et al. 2008). This unusual change of composition with the c.d. is a distinctive nature of induced co-deposition of Ni–Mo alloy as observed by Bratoeva et al. (2000).

7.3.4 XRD Study

XRD technique was used to determine the phase and crystallite size of the Ni–Mo alloy coatings at different c.d.'s. The characteristic XRD peaks of Ni–Mo alloys deposited at 1.0 A dm^{-2} to 4.0 A dm^{-2} is presented in Figure 7.4. The XRD peaks at $2\theta = 22.3^\circ$, 43.3° , 50.4° , 74.03° and 89.8° represent tetragonal $MoNi_4$ phase (Jaksic et al. 2000), corresponding to the planes (110), (211), (130), (420) and (501), respectively, which is in good agreement with standard pattern of $MoNi_4$ (JCPDS No. 03-065-1533).

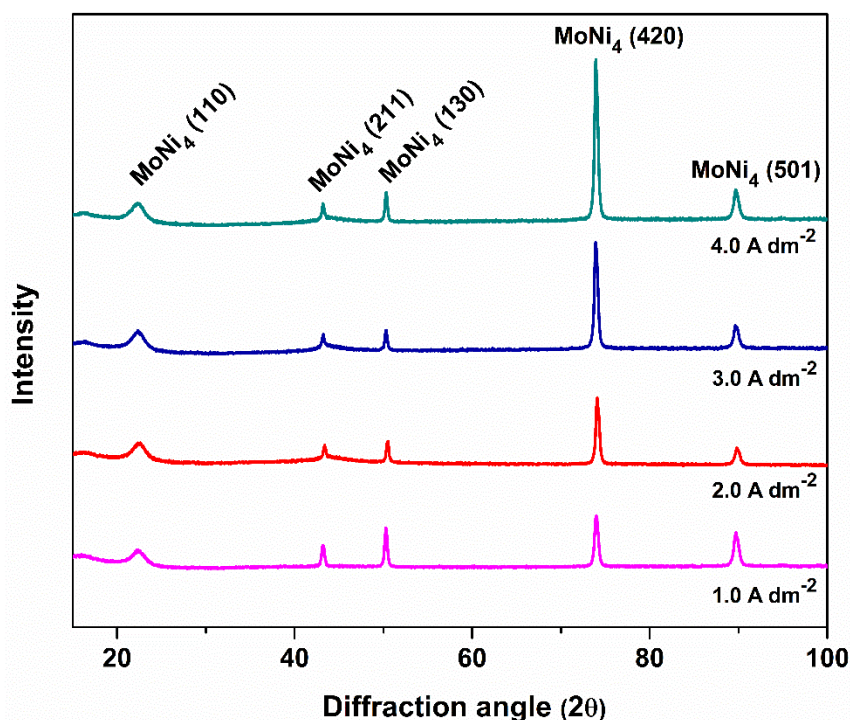


Figure 7.4 – XRD patterns of Ni–Mo alloy coatings deposited at different c.d.'s from the optimal bath

A gradual increase in the intensity of peaks with c.d. clearly, indicates that deposition c.d. plays a significant role in structural property and composition of coatings (Ullal and Hegde 2014). The grain size of the electroplated Ni–Mo alloy

coatings, at different c.d., has been calculated using Scherrer equation (Eqn. (3.4)). The calculated average crystallite size of the coatings, deposited over the wide range of c.d., was found to be 22 nm.

7.3.5 Potentiodynamic Polarization Study

To assess the ability of Ni–Mo alloy coatings as an effective material for water splitting applications, they are subjected to corrosion test in 1.0 M KOH (same medium in which water electrolysis is to be studied) by potentiodynamic polarization method to determine their stability in the said alkaline medium. The polarization behavior of the coatings, corresponding to different c.d. is shown in Figure 7.5.

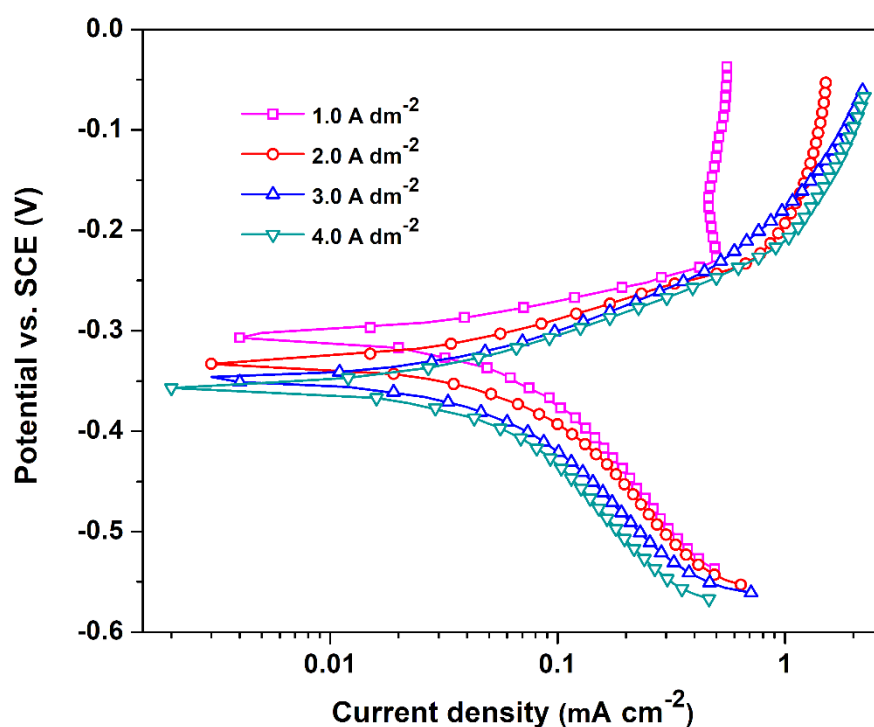


Figure 7.5 – Potentiodynamic polarization curves of Ni–Mo deposits, developed at different c.d. using optimal bath

The corrosion rates (CR's) of Ni–Mo alloy coatings at different c.d. were calculated by Tafel extrapolation method, and corresponding data are reported in Table 7.2. From the corrosion data, like E_{corr} , i_{corr} , β_c and CR's reported in Table 7.2, it may be noted that the Ni–Mo alloy deposited at 4.0 A dm^{-2} (having about 66.8 % Ni) shows the least CR, i.e. $19.94 \times 10^{-2} \text{ mm y}^{-1}$, while coatings at lower c.d.'s are more

susceptible to corrosion. Further, the decrease of CR towards high c.d. is attributed to the increased smoothness and higher Ni content of the alloy coating (Table 7.2), supported by SEM and AFM study as discussed earlier.

Table 7.2 – Corrosion data, like E_{corr} , i_{corr} and CR of Ni–Mo alloy, electrodeposited at different c.d., from the optimal bath

c.d. (A dm ⁻²)	wt.% Ni	wt.% Mo	$-E_{\text{corr}}$ (V vs. SCE)	i_{corr} ($\mu\text{A cm}^{-2}$)	CR ($\times 10^{-2}$) mm y ⁻¹)
1.0	61.7	38.3	0.306	26.90	25.27
2.0	64.3	35.7	0.323	25.08	23.76
3.0	65.6	34.4	0.340	22.12	21.06
4.0	66.8	33.2	0.345	20.85	19.94

The exchange current density (i_o) is generally accepted as one of the most important parameter describing the kinetics of the electrochemical charge transfer reaction at the particular metal-solution interface and is a measure of electrocatalytic activity of the cathode (Yüce et al. 2013). The electrocatalytic kinetic parameters, like i_o and β_c , were deduced from the linear part of semi-logarithmic polarization plots. Apparent i_o values were derived by extrapolation of Tafel plots to zero current potential. Accordingly, i_o , β_c , and overpotentials (both cathodic (η_c) and anodic (η_a)) for water splitting reactions of both HER and OER corresponding to the coating at each c.d. have also been determined from their potentiodynamic polarization curves, and are reported in Table 7.3. From the data in Table 7.3, it can be noted that Ni–Mo alloy deposited at 1.0 A dm⁻² shows lowest values for β_c and η_c , highest value for i_o proving that it is electrocatalytically more active for HER than rest of the coatings developed at higher c.d.'s.

Table 7.3 – Kinetic parameters for HER and OER on Ni–Mo electrode in 1.0 M KOH solution, obtained from the potentiodynamic polarization curves

c.d. (A dm ⁻²)	i_o (μ A cm ⁻²)	$-\beta_c$ (mV dec ⁻¹)	$-\eta_c$ (mV vs. SCE)	η_a (mV vs. SCE)
1.0	3.18	115	438.7	234.8
2.0	2.89	116	441.6	233.7
3.0	2.64	118	444.1	226.4
4.0	2.49	120	451.2	217.2

7.3.6 Electrocatalytic Study

The electrocatalytic behavior of any materials can be assessed on the basis of their ability to catalyze the HER and OER since they are the fundamental process involved in water electrolysis and fuel cell applications (Kubiszta et al. 2008). CV and CP techniques are considered to deliver a wealth of information, required to understand the suitability of test electrode for water electrolysis. Hence, Ni–Mo alloy coatings, deposited at different c.d.'s from the proposed bath have been subjected to electrocatalytic activity test for HER and OER in 1.0 M KOH medium. The experimental results are presented in the following sections.

7.3.6.1 Electrocatalytic behavior for HER

a) Cyclic voltammetry study

CV is a powerful tool to explore substantial information about the thermodynamics of redox processes, the kinetics of heterogeneous electron-transfer reactions and of coupled chemical reactions or adsorption processes. Hence, CV study on Ni–Mo deposits developed at 1.0 to 4.0 A dm⁻² for HER was carried out in the potential range of 0.0 V to –1.6 V, at a scan rate of 50 mVs⁻¹ for 50 cycles. The cyclic voltammograms for HER of Ni–Mo alloy deposits, developed at different c.d.'s are shown collectively in Figure 7.6, and corresponding electrochemical parameters drawn are given in Table 7.4.

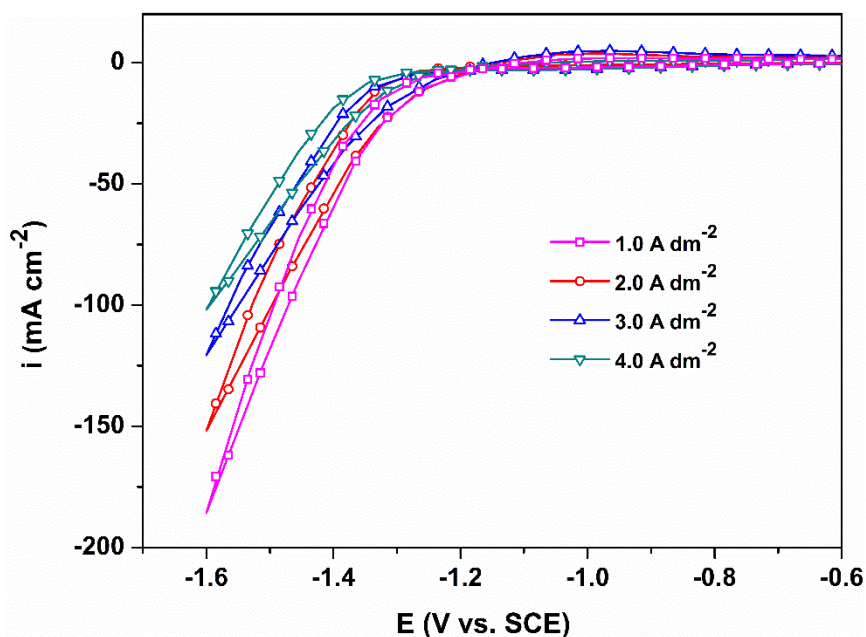


Figure 7.6 – Cyclic voltammograms of Ni–Mo alloy deposits developed at different c.d.'s with their cathodic peak current density, i_{pc} for HER

Table 7.4 – HER parameters of Ni–Mo alloy deposits, developed at different c.d.'s from the optimal bath

c.d. (A dm ⁻²)	Cathodic peak c.d. (i_{pc}) (A cm ⁻²)	Onset potential for HER (V vs. SCE)	Volume of H ₂ evolved 300 s (cm ³)
1.0	-0.186	-1.28	12.0
2.0	-0.152	-1.30	11.5
3.0	-0.121	-1.31	10.8
4.0	-0.102	-1.33	10.2

From CV curves shown in Figure 7.6, it can be concluded that Ni–Mo alloy deposited at 1.0 A dm⁻² exhibits highest i_{pc} value (-0.186 A cm⁻²), compared to all other coatings. The highest i_{pc} value recorded by the coating at 1.0 A dm⁻² may be ascribed to its highest Mo content (38.3 wt.%) when compared to other coatings. As the wt.% of Mo in the alloy is increased, the onset potential for HER has shifted in the

positive direction, favoring hydrogen generation with lower overpotential (Refer Table 7.3), as reported by Manazoğlu et al. (2016). Therefore, this particular coating deposited at 1.0 A dm^{-2} showed the least onset potential as reported in Table 7.4. Further, it is important to note that the observed onset potential for HER on Ni–Mo alloy, deposited at 1.0 A dm^{-2} is -1.28 V , which is on par with the values already reported in the literature (Elias and Hegde 2016, Yu et al. 2016). The enhanced HER activity of Ni–Mo alloy coatings is due to the combination of both increased surface area and catalytic activity of Ni, in the alloy matrix (McKone et al. 2013).

b) Chronopotentiometry study

The CP study on Ni–Mo alloy coatings, deposited at different c.d. ($1.0 - 4.0 \text{ A dm}^{-2}$) to analyze their efficiency towards HER was made by applying a constant current of -300 mA cm^{-2} for the duration of 1800 s. The electrocatalytic activity of each Ni–Mo alloy deposits was assessed by measuring the volume of H_2 liberated for initial 300 s. The chronopotentiograms obtained for each sample are shown in Figure 7.7, with the volume of hydrogen gases collected (in the inset), reported in Table 7.4.

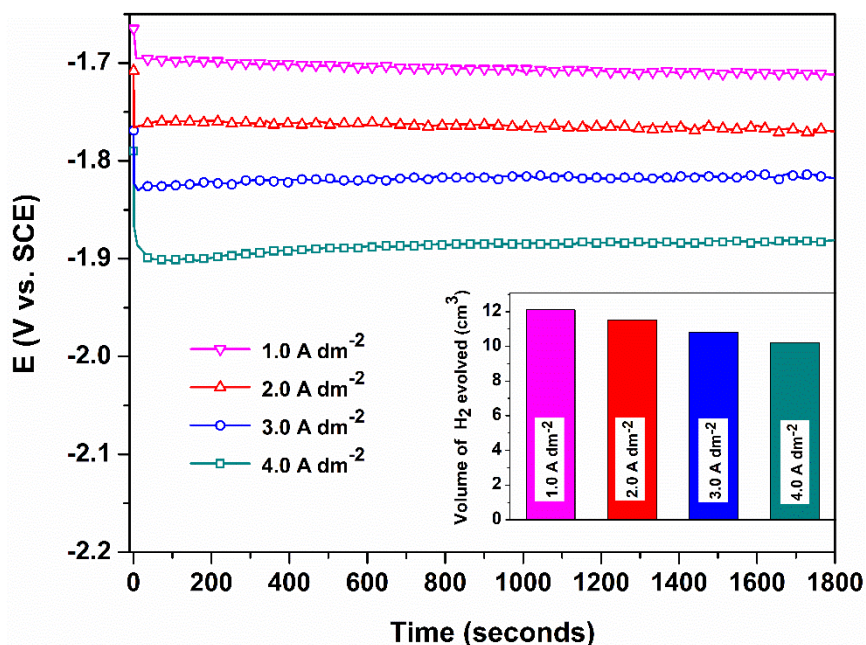


Figure 7.7 – Chronopotentiograms of Ni–Mo deposits, developed at different c.d.'s under impressed cathodic current of -300 mA cm^{-2} (volume of H_2 evolved in 300 s on each test electrodes are shown in the inset)

Experimental results showed that alloy deposited at 1.0 A dm^{-2} produces a maximum amount of H_2 , compared to the coatings deposited at higher c.d., pointing the fact that it is electro-catalytically more active for HER. Further, an initial change of potential was observed in all samples, soon after the initiation of electrolysis followed by a steady-state potential response. This may be due to sudden exhaustion of the electrolyte components at the electrode surface, where H^+ ions from the solution undergo reduction to release H_2 gas, and ultimately a state of equilibrium is established between H^+ ions and H_2 during the process (Ahn et al. 2012, Ullal and Hegde 2014). However, as the electrolysis further proceeds, almost a constant potential is achieved as observed in Figure 7.7. At this stage, the evolution of hydrogen gas takes place uninterruptedly on the surface of an electrode, where the current applied is spent completely for conversion of H^+ ions into H_2 gas.

7.3.6.2 Electrocatalytic behavior for OER

a) Cyclic voltammetry study

Figure 7.8 shows the cyclic voltammograms recorded for Ni–Mo alloy coatings at 1.0, 2.0, 3.0 and 4.0 A dm^{-2} in the potential range of 0.0 to 0.75 V at a scan of 50 mV s^{-1} . The OER is believed to catalyze by the redox transitions of interfacial oxy-cations between higher and lower oxidation states (Lee et al. 1996, Kim et al. 2012). Therefore, OER of Ni–Mo alloy coatings is attributed to electrochemical properties of redox pair just before the onset of oxygen evolution (Hu et al. 1997). The onset potential of oxygen evolution is defined as the decomposition potential of water under the anodic polarization because the OER is an irreversible reaction with a high activation overpotential (Hu and Wu 2003). The values for i_{pa} and onset potentials derived from the graphs for OER are reported in Table 7.5.

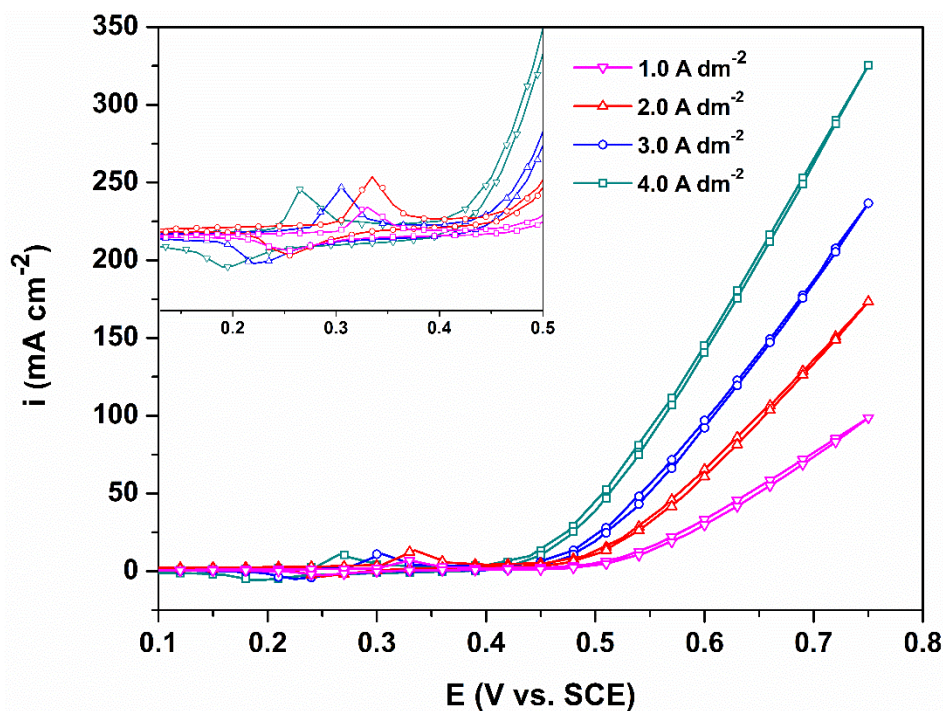


Figure 7.8 – CV curves of Ni–Mo alloy coatings deposited at different c.d.'s demonstrating their anodic peak current density i_{pa} for OER, and their redox couples are shown in the inset

From the recorded electrochemical parameters (Table 7.5), it may be noted that the Ni–Mo alloy coating deposited at 4.0 A dm^{-2} shows maximum i_{pa} of 0.325 A cm^{-2} , and least onset potential of 0.44 V , compared to the coatings deposited at lower c.d.'s. Here, it is important to note, from the nature of CV curves both i_{pa} and onset potentials of Ni–Mo alloy coatings has a strong dependency on the c.d. used. In other words, it depends directly on the Mo content of the alloy. Oxygen evolution on the Ni–Mo coating deposited at 4.0 A dm^{-2} occurs at a less positive potential than on the alloy deposited at lower c.d. (0.44 V) which is in agreement with the value reported in the literature (Ullal and Hegde 2014, Elizabeth et al. 2017). This further confirms that alloy coating at 4.0 A dm^{-2} shows improved OER activity than the rest of the coatings. The positive shift in redox potentials leads to the fact that oxygen evolution commences immediately when the electrode potentials just reach the redox potential of this redox couple, probably indicating a better catalytic activity for the OER (Hu and Wu 2003).

Table 7.5 – Electrode kinetic parameters of OER on the surface of Ni–Mo alloy coatings electrodeposited at different c.d.’s from the optimal bath

c.d. (A dm ⁻²)	Anodic peak c.d. (<i>i</i> _{pa}) (A cm ⁻²)	Onset potential for OER (V vs. SCE)	Volume of O ₂ evolved 300 s (cm ³)
1.0	0.098	0.51	8.1
2.0	0.173	0.49	8.7
3.0	0.237	0.47	9.5
4.0	0.325	0.44	10.3

b) Chronopotentiometry study

The CP technique has been employed to estimate the OER activity of Ni–Mo alloy coatings in the same medium, following CV study in a similar manner as HER analysis, with the quantity of O₂ liberated during the study was also measured. The chronopotentiograms for OER were recorded at a constant applied current of +300 mA cm⁻² (anodic) and the corresponding potential obtained were plotted against the time as shown in Figure 7.9, with the volume of O₂, collected shown in the inset. Initially, during the beginning of the analysis, a sharp increase in the potential was observed, later this potential attains a stability, i.e. until the potential for the formation of O₂ is reached (by the oxidation of OH⁻). This stability is an equilibrium state associated with the newly forming oxygen bubble and bubbles escaping from the surface of the electrode (Brown et al. 1982, Kim et al. 2012).

Thus, from data obtained from *i*_{pc} and *i*_{pa} values, onset potentials, the amount of gases liberated and their overpotentials (Tables 7.4 and 7.5), it can be concluded that ED Ni–Mo alloy developed at the lower c.d. (1.0 A dm⁻²) is more suitable for HER and those at higher c.d. (4.0 A dm⁻²) are best suitable for OER. Hence, from the experimental study for the electrocatalytic behavior of Ni–Mo alloy coatings deposited under natural convection (by using only DC), it is finally deduced that the coatings

deposited at lower and higher c.d.'s show good electrocatalytic activity towards HER and OER, respectively and vice versa.

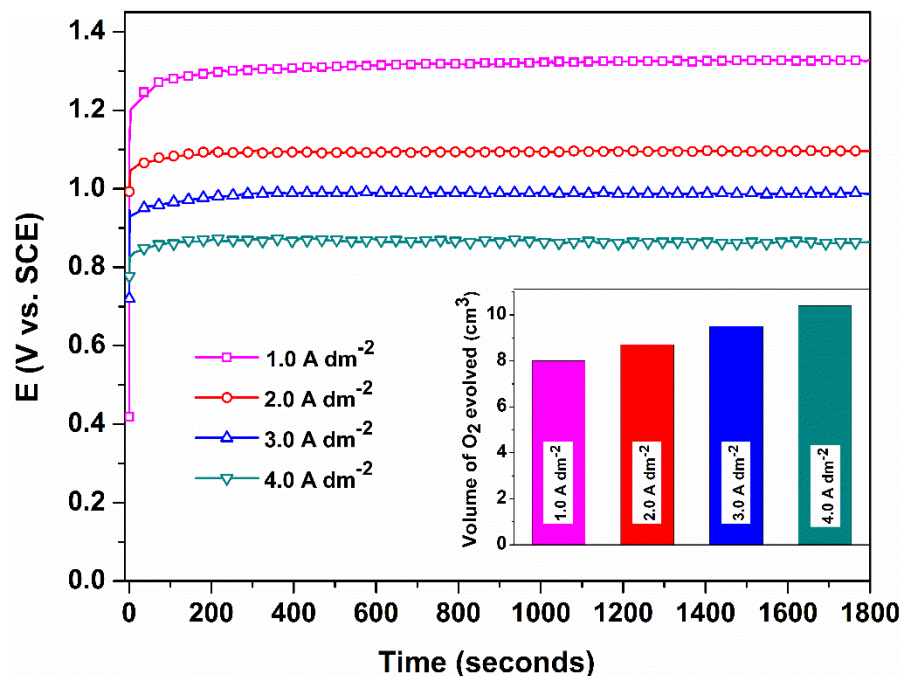


Figure 7.9 – Chronopotentiograms of Ni–Mo deposits developed at different c.d.'s under impressed anodic current of $+300 \text{ mA cm}^{-2}$ (volumes of O_2 evolved in 300 s on each test electrodes are shown in the inset)

7.4 MECHANISM OF WATER SPLITTING REACTION

To understand the mechanism of water electrolysis on the surface of ED Ni–Mo alloy coatings, and the factors responsible for favored HER and OER under different conditions of compositions, a well-known ‘*spillover*’ process of heterogeneous catalysis has been proposed. It generally considers the synergism of transition metal-based alloys for water electrolysis. Hence, it can be extended to Ni–Mo alloy coatings as well. According to this theory, a simple cooperative functioning of the alloy components is arbitrated via, rapid intra- and inter-particle surface diffusion of H ad-atoms. It is postulated that Ni sites on the Ni–Mo surface influence proton discharge, and serve as a hydrogen source for neighboring Mo sites which act as hydrogen ‘trap’ sites where the ion/atom recombination of adsorbed hydrogen atom to form hydrogen molecule and its desorption is promoted more efficiently. Highfield et al. (1999)

fundamentally ruled out any relationship between the electronic interactions among Ni–Mo alloy and observed synergy.

The electrocatalytic evolution of H₂ and O₂ (i.e. for HER and OER) on the surface of Ni–Mo alloy coatings having definite composition can also be explained by means of a mechanism, as shown in Figure 6.13 (Chapter 6, Section 6.3.8). In alkaline media, the HER pathway could follow through either the Volmer–Tafel process, or Volmer–Heyrovsky pathways, as seen in Figure 6.13 (a). Analysis of the HER mechanism for Ni–Mo coatings has also been made on the basis of its β_c values (Tasić et al. 2013). In the present study, it may be seen that β_c values of Ni–Mo alloy coatings deposited at increasing c.d. of Ni–Mo alloy (determined from the linear part of Tafel plots, see Figure 7.5) fall in the range of about -118 mV dec^{-1} , confirming that HER on these coatings follow the Volmer–Tafel mechanism (Choquette et al. 1990). The mechanism of OER (Kubiszta and Budniok 2008) on Ni–Mo alloy is shown schematically in Figure 6.13 (b). This behavior may be explained by the adsorption of comparatively large OH⁻ ions on the electrode surface. Since the adsorption characteristics of the OH⁻ can lead to the formation of NiOOH on the electrode surface, the highest Ni content in the coating (66.8%), electrodeposited at 4.0 A dm^{-2} mainly favors the OER.

7.5 CONCLUSIONS

The following conclusions are drawn on the basis of an experimental study carried out on optimization, deposition, characterization and electrocatalytic study of Ni–Mo alloy coatings, deposited by ED method.

1. A stable citrate bath of Ni–Mo alloy has been optimized for the best performance of the coatings for good corrosion resistance and water splitting applications (for both HER and OER) in 1.0 M KOH solution.
2. Experimental results revealed that Ni–Mo alloy electrodeposited at 1.0 A dm^{-2} (having 38.3 wt.% Mo) and 4.0 A dm^{-2} (having 33.2 wt.% Mo) shows better electrocatalytic property for both HER and OER, respectively.
3. Ni–Mo alloy coatings developed at 1.0 A dm^{-2} exhibit a maximum cathodic peak current density, $i_{pc} = -0.186 \text{ A cm}^{-2}$ at -1.6 V for HER and 4.0 A dm^{-2}

shows maximum anodic peak current density, $i_{pa} = 0.325 \text{ A cm}^{-2}$ at 0.75 V for OER.

4. The highest electrocatalytic activity of Ni–Mo alloy coatings for both HER and OER, depending on deposition c.d. were attributed to their composition (in terms of wt.% Ni and Mo), structure and surface morphology, supported by EDX, XRD, SEM and AFM analyses.
5. Ni–Mo alloy coated at 4.0 A dm^{-2} is said to be most corrosion resistant ($19.94 \times 10^{-2} \text{ mm y}^{-1}$) in 1.0 M KOH medium, compared to coatings deposited at lower c.d.
6. The experimental study demonstrated that Ni–Mo alloy deposit follows the Volmer-Tafel type of mechanism for HER, supported by Tafel slope analyses.

CHAPTER 8

CHAPTER 8

EFFECT OF INDUCED MAGNETIC FIELD ON ELECTRODEPOSITION OF Ni–Mo ALLOY COATINGS AND ITS ELECTROCATALYTIC ACTIVITY FOR HER

This chapter details the effect of induced magnetic field, during the process of electrodeposition of Ni–Mo alloy coatings, and its electrocatalytic activity for hydrogen evolution reaction (HER). The conditions of magneto-electrodeposition (MED) for best HER performance has been optimized. A significant increase in the electrocatalytic activity of MED Ni–Mo alloy was due to change in the crystallographic orientation of alloy coatings, explained by magneto-hydrodynamic (MHD) effect. The improved electrocatalytic activity of MED Ni–Mo alloy coatings are also compared with that of conventionally electrodeposited (ED) alloy coatings, discussed earlier in Chapter 7.

8.1 INTRODUCTION

During the past decades, the influence of a superimposed magnetic field on electrochemical processes was extensively investigated (Tacken and Janssen 1995). The most established impact on the electrochemical processes is the MHD effect (Aogaki et al. 1975). This is a macroscopic effect, which induces additional stirring of the electrolyte and as a result, mass transport is increased (Wassef and Fahidy 1976, Rabah et al. 2004, Krause et al. 2004, Uhlemann et al. 2005, Ipas et al. 2007, Koza et al. 2008, Koza et al. 2008). The resulting Lorentz force increases the convection of the electrolytic solution, thus decreasing the concentration polarization and the ohmic polarization, consequently increasing the limiting current density, i_L (Lin et al. 2012). It was found that convection could be also introduced on a microscopic level when a magnetic field is applied parallel to the electric field. This is due to fluctuations in the current distribution over the electrode surface, i.e. micro-MHD effect (Koza et al. 2008). Zabinski et al. (2009) considered that due to the MHD convection, the morphology of the deposit was affected causing the high activity of Co–P alloy for

HER. Fernandez et al. (2010) stated that the Lorentz force seems to be an important factor governing hydrogen bubble release and that the bubbles are swept off the electrode earlier than without magnetic field.

The experimental study made in Chapter 7, demonstrated that Ni–Mo alloy developed at c.d. = 1.0 A dm⁻² showed the highest electrocatalytic activity for HER, deposited from the electrolyte bath shown in Table 7.1. However, its activity decreased as the c.d. is increased. Hence, the electrocatalytic behavior of Ni–Mo alloy coating was tried to increase using the same bath at same c.d., by modulating the mass transfer process at cathode film by inducing external magnetic field, parallel to the process of deposition. In an effort to increase the electrocatalytic activity of HER, Ni–Mo alloy coating was developed under the condition of induced magnetic field, called magneto-electrodeposition (MED), using its optimized bath. It may be recalled that in MED process, the mass transport of metal ions towards cathode is accomplished by both applied c.d. and magnetic field intensity (B). Here, MED Ni–Mo alloy coating is abbreviated as (Ni–Mo)_{B=0.1 T/perp} (where 0.1 represents the applied magnetic field intensity in Tesla, and perp. stands for a magnetic field applied in the perpendicular direction). MED Ni–Mo alloy coatings were carried out at the different intensity of magnetic field at constant c.d., and change in their crystallographic orientations, responsible for the change in composition, surface morphology and phase structures have been identified using advanced analytical techniques.

8.2 MAGNETO–ELECTRODEPOSITION OF Ni–Mo ALLOY COATINGS

The MED of Ni–Mo alloy coatings has been accomplished by keeping the other parameters constant except the applied magnetic field intensity, i.e. under optimal conditions of deposition, like c.d. = 1.0 A dm⁻² and pH = 9.5. All depositions were carried out in a custom-made glass setup, using the pre-cleaned copper rod as cathode and Ni plate as an anode for the same duration (600 s) at room temperature (298 K) from the same electrolyte bath shown in Table 7.1. The experimental setup used for MED is shown schematically in Figure 8.1. The MED Ni–Mo alloy coating was carried out under induced magnetic field of varying intensity, applied perpendicular to the direction of metal ions (parallel to the plane of the cathode). The MED Ni–Mo alloy

coatings were rinsed several times with distilled water, dried and desiccated until further analysis.

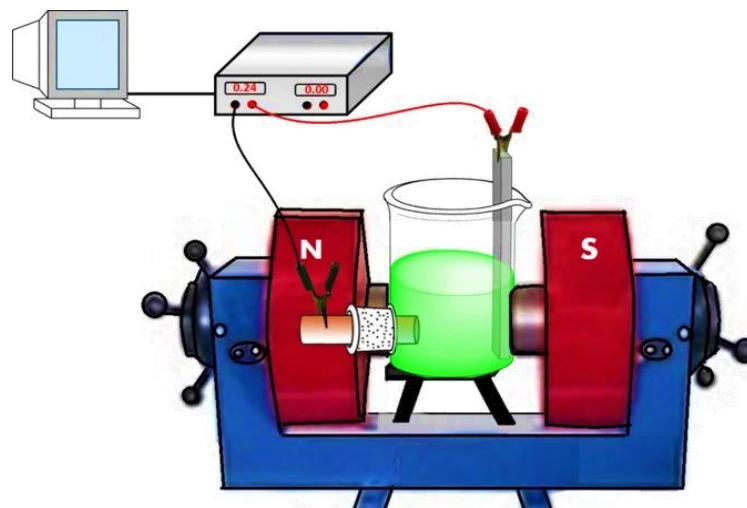


Figure 8.1 – Schematic of the experimental setup used for development of MED Ni–Mo alloy coatings

8.3 RESULTS AND DISCUSSION

8.3.1 Surface and Compositional Analysis

Change in the composition of Ni–Mo alloy coatings due to the effect of induced magnetic field is reported in Table 8.1. From the data, it can be inferred that the wt.% of Ni (more noble metal) in the coating increases gradually with the intensity of magnetic field (from 0.1 – 0.4 T). It is due to the fact that the applied magnetic field increases the rate of mass transport of Ni^{+2} ions, which leads to the decrease of diffusion layer thickness, as explained by Fick's law of diffusion (Bard and Faulkner 2001). This decrease of diffusion layer thickness eventually leads to an increase of i_L of Ni, as will be discussed in Section 8.4. Here, it is important to note that the i_L of only Ni increases, compared that Mo, even though both Ni^{+2} and Mo^{+2} ions are present in the bath. It may be ascribed to the fact that Ni is more readily deposit-able metal than Mo. Experimental results revealed that MED Ni–Mo alloy deposited at 0.4 T (at 1.0 A dm^{-2}) exhibits the maximum electrocatalytic activity for HER, with 65.4 wt.% Ni content.

SEM micrographs of MED Ni–Mo coatings at different magnetic field intensity are shown in Figure 8.2. From SEM micrograph, it is evident that Ni–Mo alloy,

deposited without the effect of magnetic field displays a rough surface (Figure 8.2 (a)), compared to the MED coatings. It can be also noted that degree of smoothness increases with the intensity of magnetic field, as seen in Figure 8.2 (b–e).

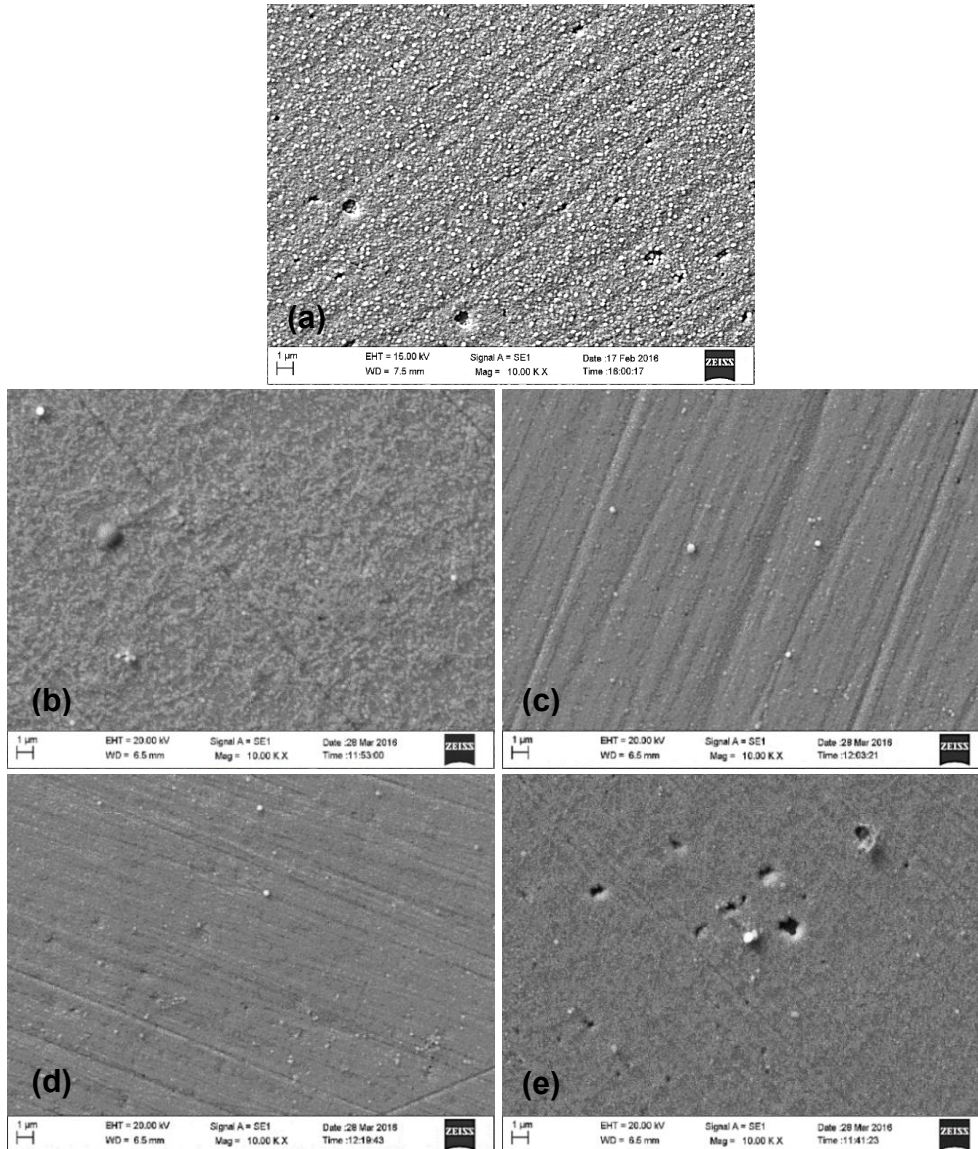


Figure 8.2 – SEM micrographs of MED Ni–Mo alloy deposited under different conditions of magnetic field intensity: a) $B = 0$ T, b) $B = 0.1$ T, c) $B = 0.2$ T, d) $B = 0.3$ T and e) $B = 0.4$ T (applied perpendicular to the flow of metal ions)

This is due to the decrease in EDL thickness affected by induced magnetic field, explained by earlier researchers (Fahidy 1983, Hinds et al. 2001). Another important

observation is the formation of holes of varying size on the surface of the coatings (Figure 8.2 (e)) which may be attributed to the bursting of hydrogen bubbles, formed during deposition due to MHD effect (Aaboubi 2011). The formation of such pores/holes increases with magnetic field intensity and is found to be maximum for the coating deposited at $B = 0.4$ T.

8.3.2 XRD Study

It is well known that magnetically induced co-deposition of metal ions obviously bring change in the mass transfer process at EDL, and hence responsible for the change in composition, surface morphology, and crystallographic orientation. Hence, XRD study of MED Ni–Mo alloy coatings, deposited at different magnetic field intensity, i.e. $B =$ from 0.1 T to 0.4 T is carried out, and are shown in Figure 8.3, along with one coating corresponding to no magnetic field effect ($B = 0$ T). The XRD patterns clearly show that the peak corresponding to MoNi_4 reflection is the prominent one in all coatings (Jakšić et al. 2000).

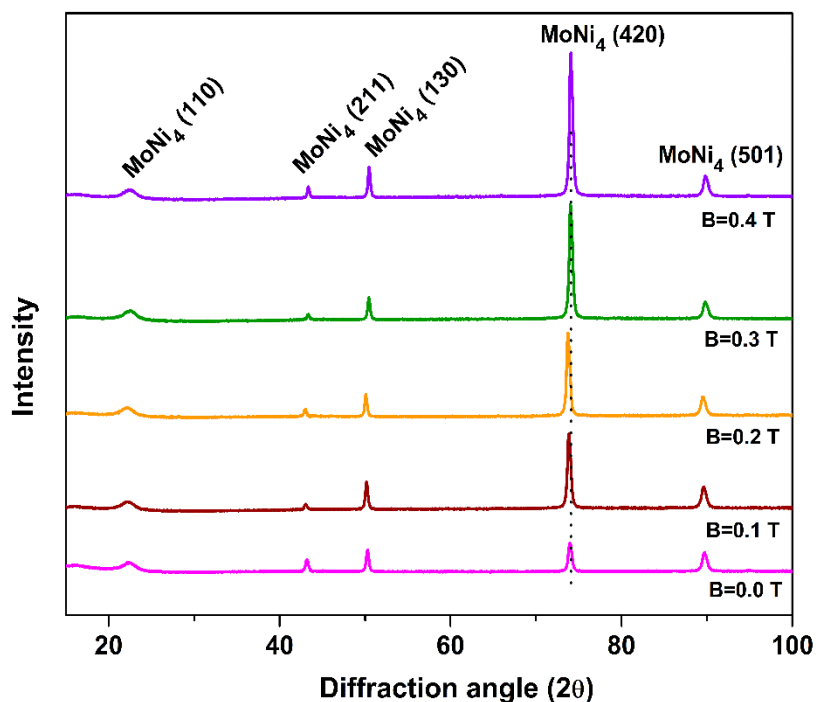


Figure 8.3 – XRD patterns of Ni–Mo alloy coatings deposited at different magnetic field intensity, in comparison with ED coating (deposited at $B = 0$ T)

Further, regardless of the condition/intensity of MED, the phase structure of alloy coatings remained almost same. In other words, no new peaks have formed when magnetic field strength was varied, except for the increase in peak intensity, as shown in Figure 8.3. This confirms the fact that the applied magnetic field was able to increase the wt.% of Ni in the deposit by increasing the i_L of Ni, affected by the MHD effect. Further, the grain size of MoNi₄ (420) plane was found to increase from 26 to 29 nm as the intensity of magnetic field increased (from 0 to 0.4 T), displaying an improved crystallinity of the coatings.

8.3.3 Potentiodynamic Polarization Study

The corrosion efficacy of MED Ni–Mo alloy coatings was studied in 1.0 M KOH (medium in which electrocatalytic study is carried out) through potentiodynamic polarization method. The corrosion rates (CRs) at different conditions of magnetic field intensity were evaluated by Tafel extrapolation method. The potentiodynamic polarization behavior of MED Ni–Mo alloy coatings is shown in Figure 8.4, and corresponding corrosion data are reported in Table 8.1.

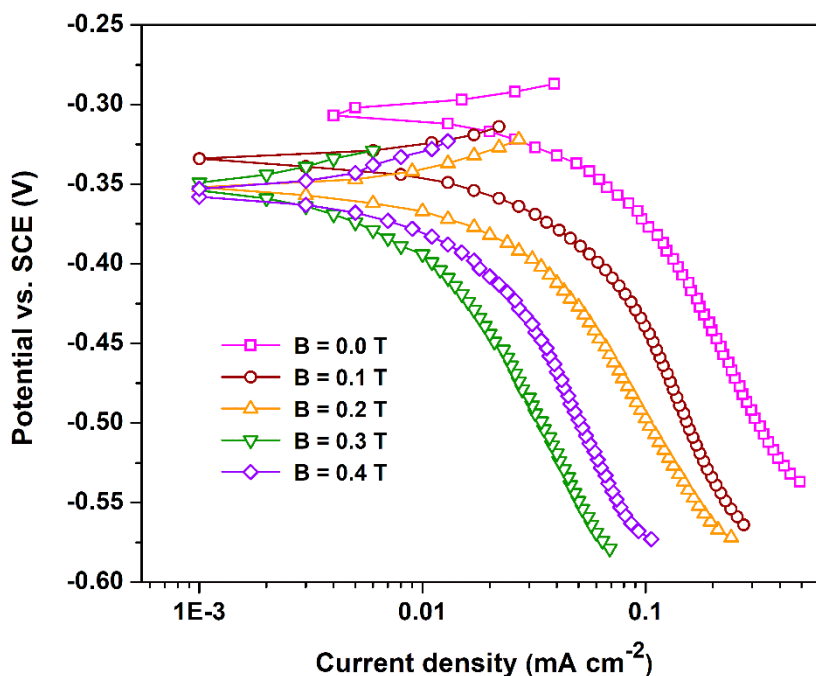


Figure 8.4 – Potentiodynamic polarization behavior of MED Ni–Mo alloy coatings, deposited under varying magnetic field intensity B , using the same bath at same $c.d.$

Experimental data showed that Ni–Mo alloy coating, deposited at $B = 0.3$ T having ~ 64.6 wt.% Ni, represented as $(\text{Ni–Mo})_{B=0.3 \text{ T/perp}}$ is proved to be the most immune to corrosion, compared to other coatings. It showed a CR of $3.49 \times 10^{-2} \text{ mm y}^{-1}$, with the least i_{corr} value ($3.68 \mu\text{A cm}^{-2}$). Further, CR's were found to decrease with increase in magnetic flux density, up to $B = 0.3$ T, and then increased. This less CR of Ni–Mo alloy is attributed to both surface morphology and composition of the coatings. However, at a very high magnetic field strength ($B = 0.4$ T), the increase of CR is due to increase of pores and pinhole on the surface of the coating.

Table 8.1 – Corrosion data of MED Ni–Mo alloy coatings deposited at the different intensity of applied magnetic field B , using the same bath at same c.d.

Coating Configuration	wt.% Ni	wt.% Mo	$-E_{\text{corr}}$ (V vs. SCE)	i_{corr} ($\mu\text{A cm}^{-2}$)	CR ($\times 10^{-2} \text{ mm y}^{-1}$)
$(\text{Ni–Mo})_{B=0 \text{ T/perp}}$	61.7	38.3	0.306	26.90	25.27
$(\text{Ni–Mo})_{B=0.1 \text{ T/perp}}$	62.4	38.6	0.333	15.62	14.71
$(\text{Ni–Mo})_{B=0.2 \text{ T/perp}}$	63.5	36.5	0.348	10.75	10.16
$(\text{Ni–Mo})_{B=0.3 \text{ T/perp}}$	64.6	35.4	0.351	3.68	3.49
$(\text{Ni–Mo})_{B=0.4 \text{ T/perp}}$	65.4	34.6	0.349	5.34	5.08

The cathodic Tafel slope (β_c), exchange current density (i_o), and cathodic overpotential (η_c) at $B = 0, 0.1, 0.2, 0.3,$ and 0.4 T were determined from the corresponding cathodic polarization curves, and values are listed in Table 8.2. The apparent i_o was estimated by extrapolating the Tafel lines to the corresponding zero current potentials. From the data given in Table 8.2, it is apparent that MED Ni–Mo alloy coatings with configuration $(\text{Ni–Mo})_{B=0.4 \text{ T/perp}}$ shows lower η_c (-408.3 mV), highest i_o ($3.60 \mu\text{A cm}^{-2}$), and least β_c (100 mV dec^{-1}) which points to the fact that this electrode composition is most active for the HER, supported by the earlier research (Merki and Hu 2011).

Table 8.2 – Electrocatalytic kinetic parameters for HER on MED Ni–Mo coatings, deposited at different magnetic field intensity B , using the same bath at same c.d.

Coating Configuration	i_o ($\mu\text{A cm}^{-2}$)	$-\beta_c$ (mV dec^{-1})	$-\eta_c$ (mV vs. SCE)
(Ni–Mo) $_{B=0}$ T/perp	2.39	115	438.7
(Ni–Mo) $_{B=0.1}$ T/perp	3.34	111	431.2
(Ni–Mo) $_{B=0.2}$ T/perp	3.52	108	418.3
(Ni–Mo) $_{B=0.3}$ T/perp	3.58	104	413.8
(Ni–Mo) $_{B=0.4}$ T/perp	3.60	100	408.3

8.3.4 Hydrogen Evolution Reaction on MED Ni–Mo Alloy

Alkaline water electrolysis, using electricity generated by renewable energy sources, is considered as an environmentally friendly route for the production of large volumes of hydrogen gas, required by a possible hydrogen economy (Lyons and Brandon 2010). In this direction, to evaluate the electrocatalytic activity of Ni–Mo alloy coatings deposited at different conditions of superimposed magnetic field, they are further subjected to the cathodic polarization of HER as discussed below.

8.3.4.1 Cyclic voltammetry study

CV tests have been considered as the best method to establish the discharge potentials for the liberation of hydrogen gas onto the surface of different alloys. The electrocatalytic activity of MED Ni–Mo alloy coatings was evaluated by CV method in 1.0 M KOH, using the same experimental procedure as given in Section 7.3.6.1. CV curves of MED Ni–Mo coatings with varying magnetic field intensity are shown in Figure 8.5 and corresponding electrochemical data are given in Table 8.3. As shown by data, given in Table 8.3, the cathodic peak current density (i_{pc}) for MED Ni–Mo alloy coating was found to increase with intensity of the magnetic field applied, and it reaches its maximum for (Ni–Mo) $_{B=0.4}$ T/perp (-0.274 A cm^{-2}) with least onset potential of -1.24 V , indicating that it is the most effective coating for HER activity. Thus, the highest i_{pc}

value exhibited by $(\text{Ni-Mo})_{B=0.4 \text{ T/perp}}$ may be attributed to high Ni content (65.4 wt.%) of the alloy, and its increased surface area due to the pores/pinholes, formed as a result of hydrogen liberation during MED.

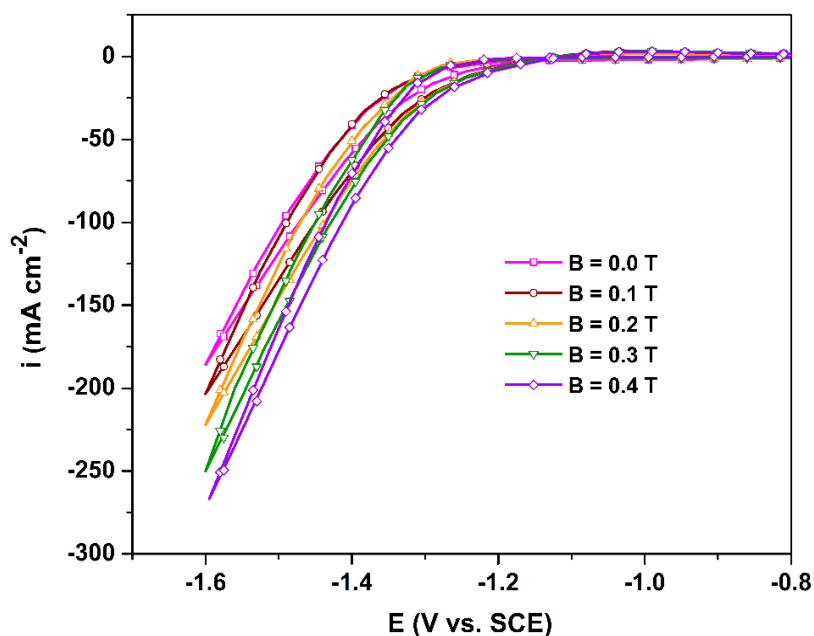


Figure 8.5 – CV curves of MED Ni–Mo alloy coatings, showing the increase in cathodic peak current density (i_{pc}) with magnetic field intensity for HER

Table 8.3 – Electrocatalytic parameters for HER on MED Ni–Mo coatings developed at different magnetic field strength B , from the same optimal bath at same c.d.

Coating Configuration	Cathodic peak c.d. (i_{pc}) (A cm^{-2})	Onset potential for HER (V vs. SCE)	Volume of H_2 evolved 300 s (cm^3)
$(\text{Ni-Mo})_{B=0 \text{ T/perp}}$	-0.186	-1.28	12.0
$(\text{Ni-Mo})_{B=0.1 \text{ T/perp}}$	-0.204	-1.27	12.4
$(\text{Ni-Mo})_{B=0.2 \text{ T/perp}}$	-0.222	-1.26	12.9
$(\text{Ni-Mo})_{B=0.3 \text{ T/perp}}$	-0.250	-1.25	13.5
$(\text{Ni-Mo})_{B=0.4 \text{ T/perp}}$	-0.274	-1.24	14.0

8.3.4.2 Chronopotentiometry study

CP involves the study of voltage transients at an electrode upon which a constant current is imposed. When a constant current is applied to an electrode, then its voltage response is a measure of changes in the electrode processes occurring on its surface. Therefore, CP study of the MED Ni–Mo alloy coatings was carried out at definite c.d. of -300 mA cm^{-2} (ideal c.d. used in industrial operations), and their resulting potentials were measured vs. SCE, as a function of time for a period of 1800 s. The electrocatalytic activity of MED Ni–Mo alloy coatings developed with different magnetic field strength was evaluated by measuring the amount of H_2 liberated. The volume of hydrogen gas evolved as a product of electrolysis was measured quantitatively using glass setup shown in Figure 6.2, and are reported in Table 8.3. The nature of chronopotentiograms corresponding to each coating is shown in Figure 8.6, with the relative volume of hydrogen gas liberated for initial 300 s shown in the inset.

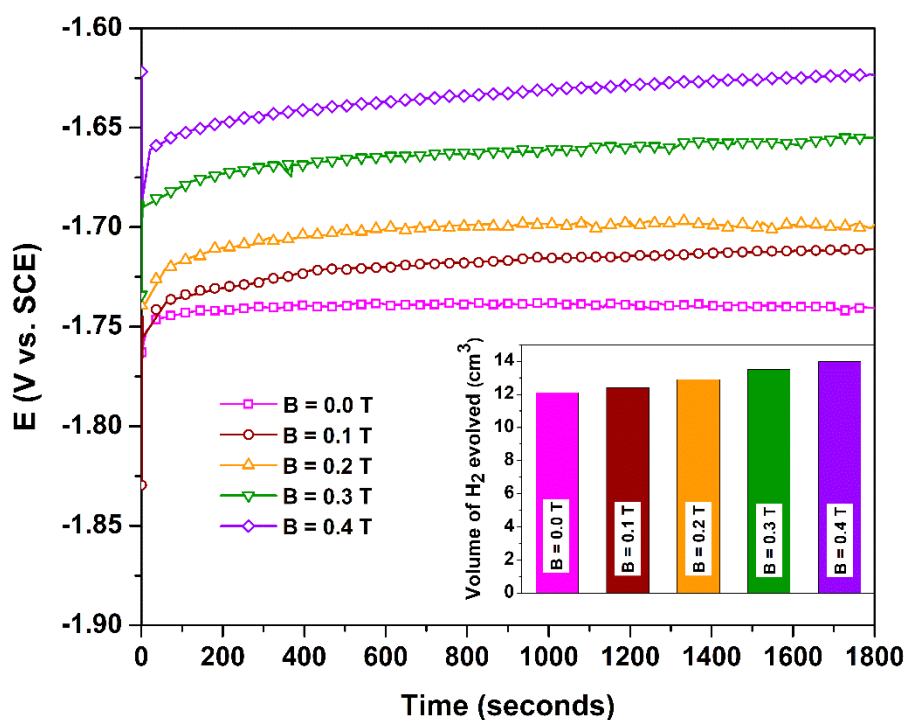


Figure 8.6 – CP curves of MED Ni–Mo alloy coatings in comparison with ED Ni–Mo alloy coating under impressed cathode c.d. of -300 mA cm^{-2} with the volume of H_2 evolved in 300 s on each test electrodes shown in the inset

From the nature of CP curves, it may be noted that MED Ni–Mo alloy, deposited at $B = 0.4$ T is found to liberate a maximum amount of H_2 gas (14.0 mL in first 300 s) at least operating cathodic potential (around -1.65 V). Hence, Ni–Mo alloy deposited at $(Ni-Mo)_{B=0.4\text{ T/perp}}$ is the most electroactive for HER, compared to all other coatings.

8.4 DISCUSSION

The observed increase of Ni content in the presence of magnetic field may be attributed to increased i_L for deposition of Ni (more noble metal). This is explained as follows: Generally, effects of plating variables on the composition of the electrodeposit are determined by simple diffusion theory. In the region of the limiting current, when electrode process is mass-transfer controlled, the value of the i_L is given by Eqn. (4.1). Thus, increase of i_L for deposition of Ni, due to induced magnetic field can be best explained through MHD effect. According to which, the induced magnetic field causes the concentration gradient of Ni^{+2} ions to increase drastically at cathode film by the combined effect of both hydrodynamics and Lorentz force (Fahidy 1983). Hence, induced magnetic field can increase the i_L by decreasing the diffusion layer thickness (or EDL) as shown in Figure 8.7.

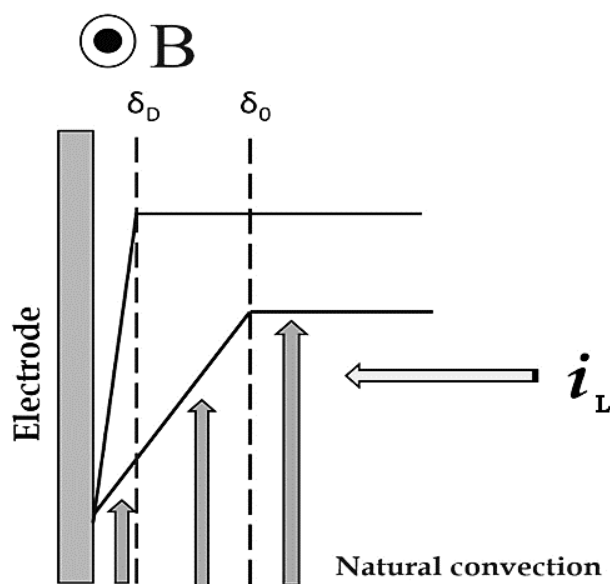


Figure 8.7 – Diagrammatic representation showing decrease in the thickness of EDL from δ_0 to δ_D , due to the effect of induced magnetic field (Ebadi et al. 2010)

Generally, the practical relevance of the application of a magnetic field in electrochemical processes is potentially large; improved mass transfer in cells, better deposit quality, and control of corrosion are just a few of many processes which can be promoted. In addition, a magnetic field is a powerful scientific tool in reaction kinetics and metal deposition or dissolution studies (Fahidy 1983). It may be noted that the H₂ evolution activity of MED Ni–Mo alloy coatings has increased gradually with magnetic field strength, used during deposition (Table 8.8). This increased activity is attributed to two factors: (1) a gradual increase in the wt.% Ni (electro-catalytically more active than Mo) in the deposit (Table 8.1), affected due to its increased i_L as discussed earlier; and (2) increased porosity due to cathodically formed hydrogen bubbles on the surface at higher limits of magnetic field intensity which creates pores or pinholes on the surface. As porosity increased, the metal particles residing in the pores will be exposed more, and hence, a number of active sites will be increased (Wieckowski et al. 2003). In other words, increased porosity leads to increase in the surface area, and thereby making the most active metal (Ni) to come in intimate contact with the electrolyte (Elias and Hegde 2016). Thus, it may be concluded that increased electrocatalytic activity of H₂ evolution reaction onto the surface of MED Ni–Mo alloy coatings is due to the combined effect of both increased porosity and wt.% of Ni, affected due to cathodically formed hydrogen bubbles on the surface (during MED) and increased i_L of Ni, respectively. Further, the better corrosion protection of MED Ni–Mo coatings compared to ED alloy coatings is also attributed to its more homogeneous and smooth surface. The smooth surface provides fewer sites for localized corrosion attack. However, coating developed at highest intensity of magnetic field ($B = 0.4$ T) shows the presence of some pores/holes caused due to excessive hydrogen evolution (Shinohara et al. 2002, Rao et al. 2013), making the surface more irregular and thereby increasing the active sites for the hydrogen adsorption. Hence, coating developed at $B = 0.4$ T has enhanced the electrocatalytic property, and increased corrosion resistance compared to coatings developed in the absence of induced magnetic field.

8.5 MECHANISM OF HER

The electrocatalytic evolution of H₂ on the surface of MED Ni–Mo alloy coatings having definite composition can also be explained by the same mechanism, as shown in Figure 6.13, with the same explanation detailed in Section 6.3.8. (Chapter 6) The Tafel plots are shown in Figure 8.4 and the corresponding β_c values are reported in Table 8.2. It may be noted that all the slope values are in the range of -118 mV dec^{-1} confirming that the HER on these coatings follows Volmer-Tafel mechanism.

8.6 CONCLUSIONS

The electrocatalytic activity of Ni–Mo alloy coatings has been improved by superimposing the magnetic field, parallel to the process of ED, and the following conclusions are made:

1. The electrocatalytic property and corrosion performance of Ni–Mo alloy coatings can be increased by many folds by taking the advent of induced magnetic field, applied in the direction perpendicular to the deposition process.
2. The increased electrocatalytic activity of H₂ evolution reaction onto the surface of Ni–Mo alloy coatings, deposited at higher limits of the magnetic field is attributed to the cathodically formed hydrogen bubbles on the surface (during deposition) and increased i_L of Ni, respectively.
3. The coating with (Ni–Mo)_{B=0.4 T/perp} configuration (developed at optimal c.d. = 1.0 A dm⁻² and B = 0.4 T) is found to exhibit the highest electrocatalytic activity for HER (with highest i_{pc} of -0.274 A cm^{-2} , least onset potential of -1.24 V , and highest volume of H₂ liberated = 14.0 mL), demonstrated by CV and CP experiments.
4. Ni–Mo alloy electrodeposited at B = 0.3 T shows nearly 7 times ($3.49 \times 10^{-2} \text{ mm y}^{-1}$) more corrosion resistance than the alloy deposited without B ($25.27 \times 10^{-2} \text{ mm y}^{-1}$).
5. Tafel slope analysis confirmed that HER on to the surface of MED Ni–Mo alloy coatings follows Volmer-Tafel mechanism.

CHAPTER 9

CHAPTER 9

EFFECT OF rGO ON ELECTROCATALYTIC ACTIVITY OF HYDROGEN EVOLUTION REACTION ON Ni–Mo ALLOY COATINGS

In this chapter, the effect of the addition of reduced graphene oxide (rGO) into Ni–Mo bath, in terms of its ability to enhance the electrocatalytic property of Ni–Mo alloy for HER in 1.0 M KOH solution is studied. The kinetics of electrocatalytic activity for HER on Ni–Mo–rGO composite electrodes were investigated by CV, CP, and potentiodynamic polarization techniques. The effect of integrating rGO into the alloy matrix on surface morphology and phase structure of Ni–Mo alloy has also been investigated.

9.1 INTRODUCTION

Nowadays, graphene, an emerging two-dimensional structure of free-standing carbon atoms which are packed into a honeycomb-like crystal structure, are being predicted to have numerous potential applications because of its unusual electron transport properties and other distinct characters. Also, graphene based materials possess large specific surface area, excellent conductivity, and availability for surface functionalization, which are important characteristics in the electrochemical applications (Kumar et al. 2013). The high conductivity of graphene makes it an inexpensive alternative to carbon nanotubes (CNTs) (Cheng et al. 2011). Because of the plane structure of graphene, both sides of graphene sheets could be utilized as a support for catalysts (Luo et al. 2012). These properties make graphene a promising and favorable catalyst support (Ojani et al. 2014).

In the present work, electrodeposition of Ni–Mo alloys along with reduced graphene oxide (rGO) is carried out on a copper substrate of a known surface area. The rGO can facilitate charge transfer and ionic interchange to enhance electrocatalysis (Li et al. 2011, Zheng et al. 2014). The enhancement of its electrocatalytic efficiency is studied using electrochemical techniques like CV and CP in 1.0 M KOH medium. Further, the stability of the electrocatalysts in the same alkaline medium is tested by

potentiodynamic polarization technique, from the parameters derived via Tafel curves, corrosion rates and HER mechanism pathway are determined as well.

9.2 MATERIALS AND METHODS

9.2.1 Synthesis of Reduced Graphene Oxide (rGO)

Graphene oxide is synthesized by modified Hummers method. In brief, natural graphite flasks (1.0 g) and NaNO_3 (0.5 g) was mixed homogeneously in a 250 mL beaker, with simultaneous addition of concentrated H_2SO_4 (50 mL) under constant mechanical stirring. KMnO_4 (3.0 g) was then added slowly to the above mixture and stirred at a constant room temperature (25 °C) for 1 hour. Later, distilled water (75 mL) was added into the mixture and continuously stirred for 30 minutes at 95 °C. Finally, the mixture of distilled water (100 mL) and H_2O_2 (1.0 mL) was consequently added to terminate the reaction, at this stage the colour of the reaction suspension turned from brown to yellow. Then obtained graphite oxide suspension was separated by centrifugation, washed with distilled water and further sonicated to get graphene oxide solution. The rGO is finally synthesized by microwave irradiation method. The resultant graphene oxide solution was then irradiated with microwave radiation at 350 W for 10 minutes, here the color of the reaction suspension turned black. The obtained black precipitate of rGO was separated by filtration, washed several times with distilled water and dried at 80 °C for 12 hours in vacuum to get rGO powder.

9.2.2 Electrodeposition of Ni–Mo–rGO Composite Coatings

The electrodeposition of Ni–Mo–rGO electrocatalyst was accomplished on a copper substrate from an alkaline sulphate bath with composition and operating parameters as given in Table 9.1. The electrolytic bath was prepared from analytical grade reagents (Merck, India) and double distilled water. Then synthesized rGO (0.5 g L^{-1}) was added into the Ni–Mo alloy electrolyte bath. The rGO loaded bath was agitated ultrasonically for 2 hours to ensure uniform dispersion. The copper rod was sealed with a Teflon tape, leaving an exposed area of 1.0 cm^2 for electrodeposition. Further, the obtained composite coating was subjected to electrochemical analysis in 1.0 M KOH solution. The total time for electrodeposition was fixed at 600 s in all the cases for optimal comparison.

Table 9.1 – Composition and deposition conditions of the optimized Ni–Mo–rGO bath

Bath constituents	Amount (g L ⁻¹)	Operating parameters
NiSO ₄ ·6H ₂ O	18	Anode: Ni plate
Na ₂ MoO ₄	48	Cathode: Copper
Na ₃ C ₆ H ₅ O ₇	105	pH: 9.5
rGO	0.5	Temperature: 298 K
		Deposition time: 10 min
		Current density: 1.0 – 4.0 A dm ⁻²

9.3 RESULTS AND DISCUSSION

9.3.1 SEM Analysis

With the addition of graphene to the deposition bath, as expected a change in surface morphology of the coatings was observed. As shown in Figure 9.1, an apparent hybrid structure is successfully produced. Nanoparticles are well dispersed on or covered under the rGO sheets. It can be observed that the size of the nodules increases with increase in c.d. but becomes few in numbers. Due to the high specific surface area of graphene, the adsorption of the electrolytes onto the surface is expected to be very high. On applying current, the electrolyte adsorbed graphene gets dragged towards the cathode and gets incorporated into it along with the growing alloy layer. The adsorbed metal ions on the graphene get reduced into metal atoms and deposit as an encapsulated bundle of alloy particles within the graphene network (Figure 9.1). Such structural changes due to the addition of graphene increase the surface roughness and hence increases the electroactive surface area of the composite coating, which in turn enhances the electrocatalytic activity of the binary alloy coating. The observation of such structural changes due to the addition of graphene is of great importance in understanding its significance in enhancing the electrocatalytic activity of the binary alloy coatings (Subramanya et al. 2015).

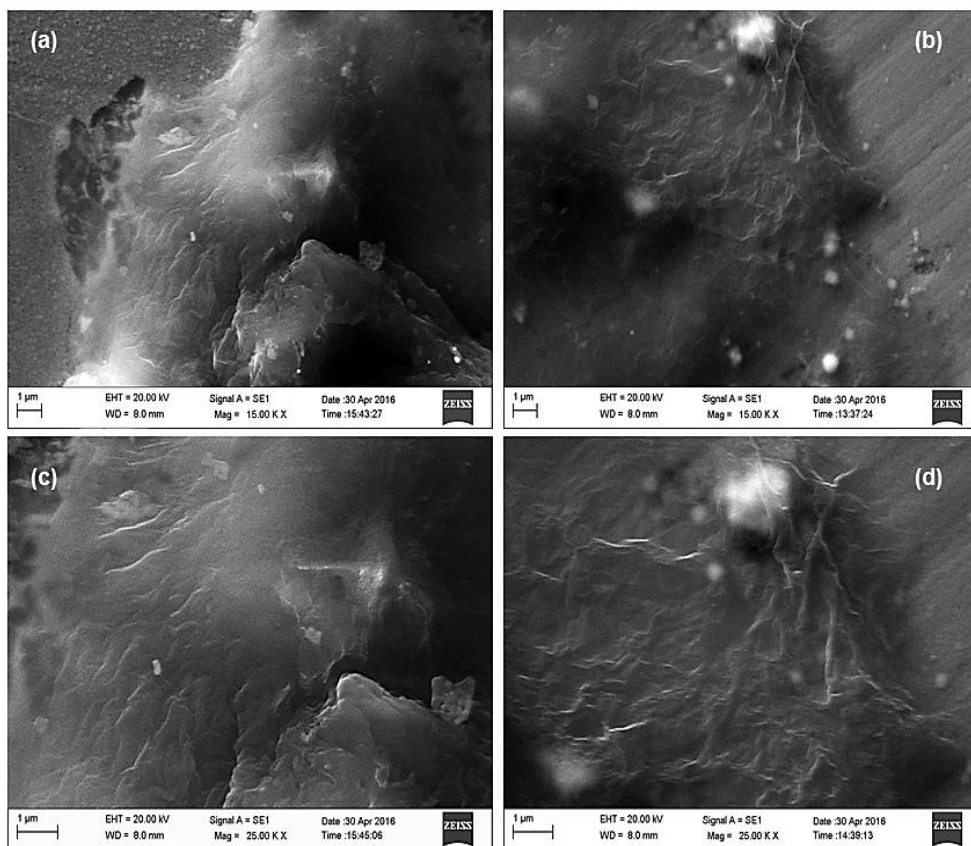


Figure 9.1 – SEM images of Ni–Mo–rGO composite coatings deposited from optimal bath at (a) 1.0 A dm^{-2} (b) 4.0 A dm^{-2} displaying irregularly shaped graphene layers embedded in Ni–Mo alloy matrix; (c) and (d) are magnified images showing layers of graphene and encapsulated alloy nodules on the graphene network

9.3.2 EDX Analysis

EDX analysis was carried out to determine the presence of different elements in the coatings. The EDX spectrum for Ni–Mo–rGO coatings (Figure 9.2) shows the presence of Ni, Mo, O and C confirming the incorporation of rGO into the Ni–Mo alloy matrix during electrodeposition. The composition of the Ni–Mo–rGO coatings is shown in Table 9.2. From the data reported in Table 9.2, it is clear that c.d. has a great influence on the composition of the coatings. Also, Ni–Mo–rGO electrodes prepared at 4.0 A dm^{-2} contain the maximum carbon content 16.14% when compared to the coatings deposited at lower c.d.'s.

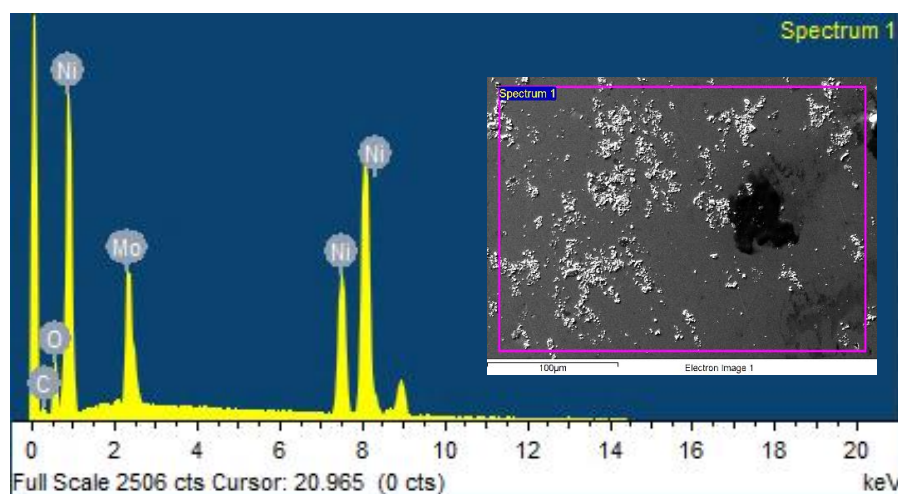


Figure 9.2 – EDX spectrum of the composite coating developed at 1.0 A dm^{-2} showing the peaks for Ni, Mo, and C

Table 9.2 – Elemental composition of Ni–Mo–rGO coatings deposited at different c.d.'s from the optimal bath

Coating configuration	wt.% Ni	wt.% Mo	wt.% C
(Ni–Mo–rGO) $_{1.0 \text{ A dm}^{-2}}$	49.36	42.08	8.56
(Ni–Mo–rGO) $_{2.0 \text{ A dm}^{-2}}$	50.10	38.05	11.85
(Ni–Mo–rGO) $_{3.0 \text{ A dm}^{-2}}$	54.54	32.03	13.43
(Ni–Mo–rGO) $_{4.0 \text{ A dm}^{-2}}$	57.55	26.31	16.14

It is well known that molybdenum in the metallic state cannot be electrodeposited separately from an aqueous solution (Marlot et al. 2002), but it can be co-deposited with ferrous metals forming an alloy. This phenomenon is so-called induced co-deposition (Brenner 1963). In the induced co-deposition, the behavior of individual metal is irregular and difficult to predict, which reflects the complicated mechanism of the alloy formation. During this process, the discharge of Ni (II) and Mo (VI) complex ions and hydrogen evolution occur on the cathode at the same time. However, besides the induced co-deposition of metallic molybdenum, low valence state oxides of molybdenum reduced from Mo (VI) may exist in the deposited films (Chassing et al.

2004, Jović et al. 2008). Hence, the element O found in the EDX spectrum probably comes from the oxides of molybdenum in the film.

9.3.3 XPS Analysis

XPS analysis was also performed to determine the chemical states of the elements in Ni–Mo–rGO and Ni–Mo alloy deposits which are very important for the electrochemical and catalysis behavior. Figure 9.3 (a–d) displays the chemical composition and states of Ni–Mo–rGO and Ni–Mo coating. From the survey spectrum (Figure 9.3 (a)) the presence of C, Ni and Mo peaks were observed.

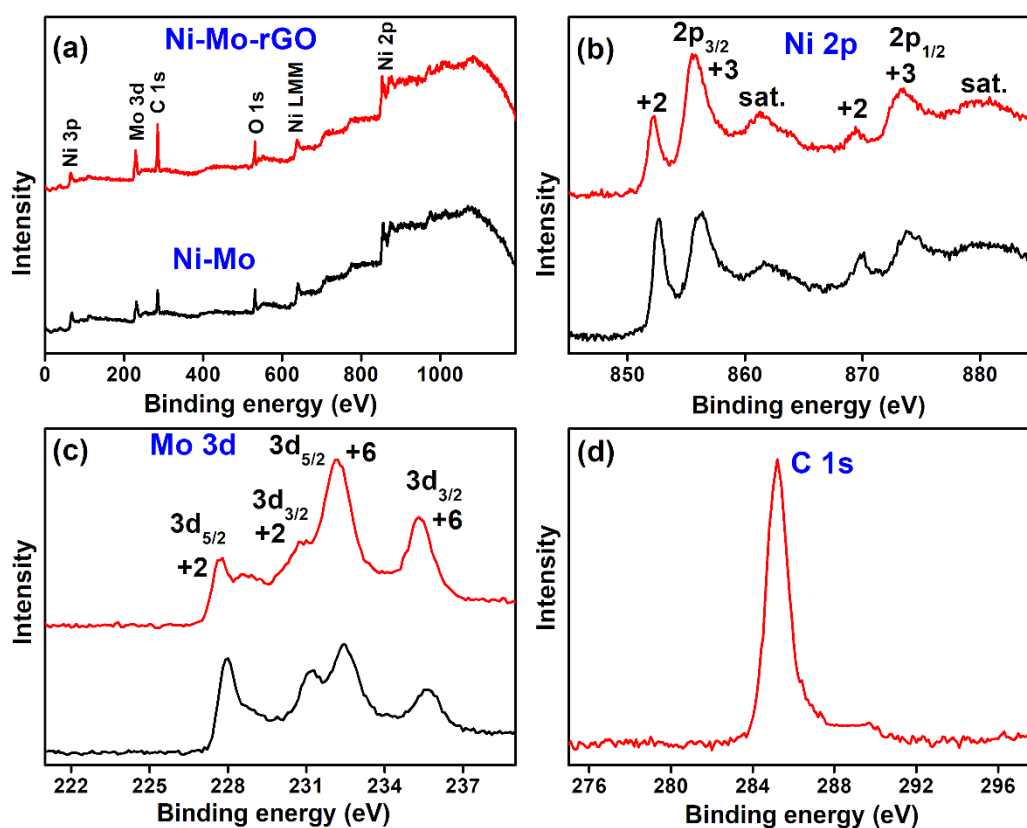


Figure 9.3 – Survey spectrum (a) and high-resolution spectrum of Ni 2p (b), Mo 3d (c) and C 1s (d) of Ni–Mo–rGO and Ni–Mo coatings

The high-resolution Ni (Figure 9.3 (b)) XPS spectra shows that the binding energies of Ni 2p_{3/2} (+2 = 852.2, +3 = 855.6) and Ni 2p_{1/2} (+2 = 869.4, +3 = 873.3) for Ni–Mo–rGO and Ni 2p_{3/2} (+2 = 852.6, +3 = 855.9) and Ni 2p_{1/2} (+2 = 869.8, +3 = 873.7) for Ni–Mo and its satellite, respectively. The high-resolution Mo (Figure 9.3 (c)) XPS spectra shows that the binding energies of Mo 3d_{3/2} (+6 = 235.2, +2 = 230.7)

and Mo 3d_{5/2} (+6 = 232.1, +2 = 227.7) for Ni–Mo–rGO and Mo 3d_{3/2} (+6 = 235.6, +2 = 231.1) and Mo 3d_{5/2} (+6 = 232.4, +2 = 228) Ni–Mo, respectively. However, from the peak positions it is observed that the Ni and Mo binding energy peak in Ni–Mo–rGO is negatively shifted as compared to Ni–Mo sample ($\Delta E = 0.3\text{--}0.4$ eV) (Figure 9.3 (b) and 9.3 (c)) indicating the existence of electron transfer process between Ni–Mo and rGO network, which is beneficial for increasing the catalytic activity and also favourable for stabilizing the electronic and ionic conductivity. High resolution spectrum of C 1s shows the peak located at 284.7 eV, which corresponds to the carbon of the rGO (Figure 9.3 (d)).

9.3.4 XRD Study

XRD was used for the structural characterization of the Ni–Mo–rGO composite coating. The obtained diffraction patterns are shown in Figure 9.4.

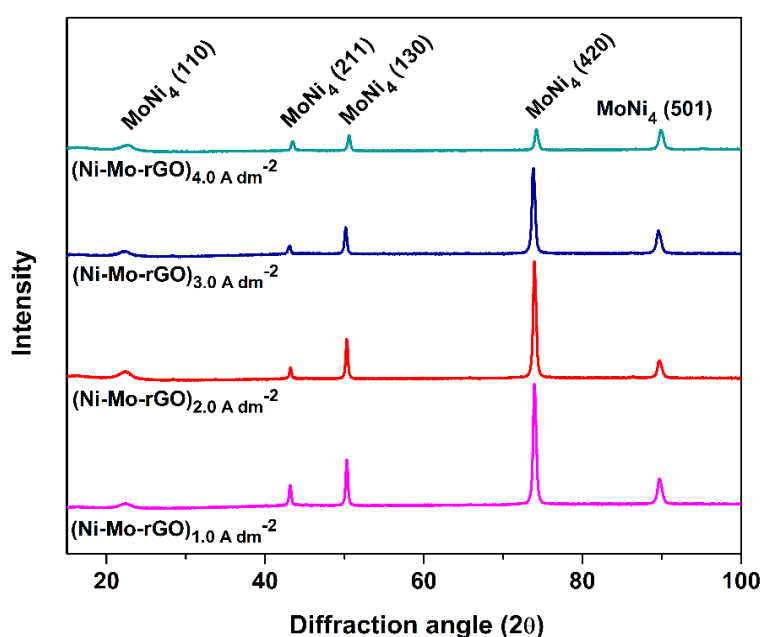


Figure 9.4 – XRD patterns of Ni–Mo–rGO composite coatings deposited at different c.d.'s

As observed in Figure 9.4, the peaks at 22.3°, 43.3°, 50.4°, 74.03° and 89.8° are the characteristic peaks of tetragonal MoNi₄ phase (JCPDS no. 03-065-1533), corresponds to (110), (211), (130), (420) and (501) planes (Jakšić et al. 2000). As seen from the XRD patterns, there was no apparent reflections of rGO, this could be ascribed

to the lower percentage of rGO in the coatings. The grain size was obtained from the XRD line broadening analysis of the peaks using Scherrer equation (Eqn. (3.4), chapter 3). On calculating, the average crystallite size of the coatings was found to be 25 nm.

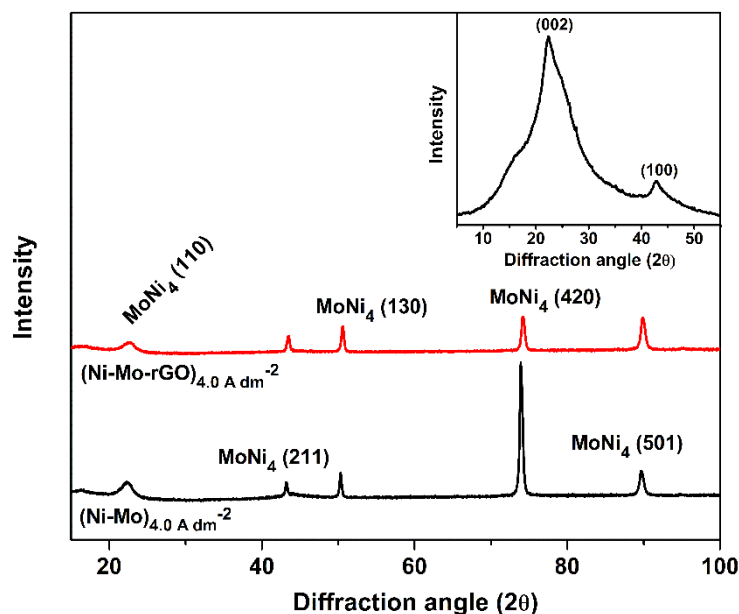


Figure 9.5 – XRD patterns of Ni–Mo alloy and Ni–Mo–rGO composite coatings deposited at 4.0 A dm^{-2} , along with the XRD pattern of rGO shown in the inset

Figure 9.5 shows the comparison of diffraction patterns of Ni–Mo alloy coating and Ni–Mo–rGO composite coating deposited at 4.0 A dm^{-2} . From the graph, it is evident that there are no significant changes in the crystallographic orientation after the addition of rGO, however, the intensity of (420) plane is reduced substantially indicating the reduction in its crystallinity. The values of Scherrer parameters for (420) plane of Ni–Mo and Ni–Mo–rGO composite coatings are given in Table 9.3. The crystallite size of (420) plane of the composite coating was 24.1 nm against the 29.6 nm of Ni–Mo alloy coating. This reduction in the crystallite size of the composite coating was further supported by higher peak width in their diffractograms. This increase in peak width of composite coating exhibited the influence of graphene on the Ni–Mo coating. During the deposition of the composite coating, the incorporation of graphene into the matrix enhances the nucleation by creating disorder. The diffusion of graphene towards the growth centers on the surface caused a detrimental effect on the

crystal growth. This increase in the nucleation growth and retardation in the crystal growth is responsible for the reduction of the crystal size (Kumar et al. 2013).

Table 9.3 – Scherrer's equation parameters of Ni–Mo and Ni–Mo–rGO composite coatings

Coating Configuration	θ	hkl plane	FWHM	d (nm)
(Ni–Mo) _{4.0 A dm⁻²}	73.90	420	0.3361	29.6
(Ni–Mo–rGO) _{4.0 A dm⁻²}	74.13	420	0.4137	24.1

9.3.5 Potentiodynamic Polarization Study

In order to evaluate the suitability of Ni–Mo–rGO composite electrode for the possible industrial application, the electrochemical stability of electrode was investigated by potentiodynamic polarization study. The corrosion behavior of the Ni–Mo–rGO coatings was evaluated by Tafel plots. Figure 9.6 shows the Tafel curves of the Ni–Mo–rGO composite coatings, and the CR's of the coatings, deposited at different c.d.'s is reported in Table 9.4.

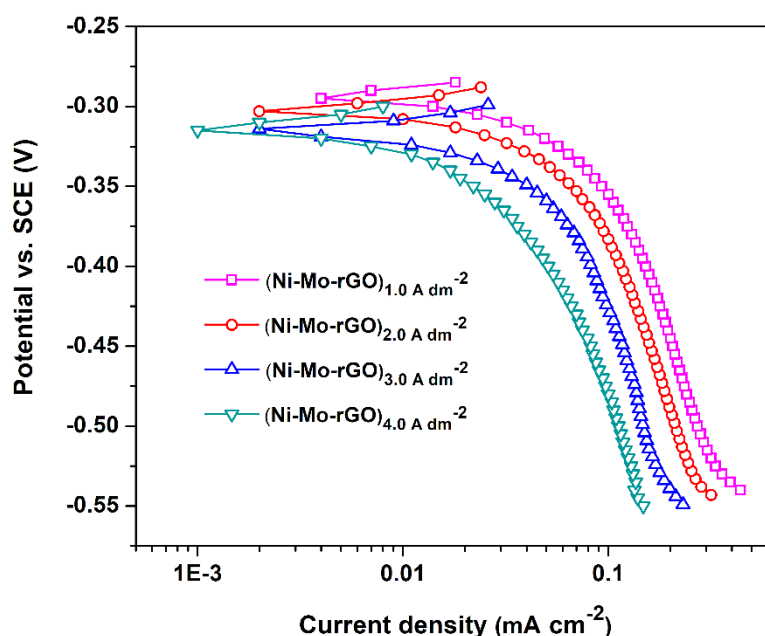


Figure 9.6 – Potentiodynamic polarization curves of Ni–Mo–rGO composite coatings deposited at different c.d.'s

Table 9.4 – Corrosion parameters like E_{corr} , i_{corr} and CR's of Ni–Mo–rGO composite coatings deposited at different c.d.'s, using same optimal bath

Coating configuration	$-E_{\text{corr}}$ (V vs SCE)	i_{corr} ($\mu\text{A cm}^{-2}$)	CR $\times 10^{-2}$ (mm y^{-1})
(Ni–Mo–rGO) $_{1.0 \text{ A dm}^{-2}}$	0.290	21.50	12.56
(Ni–Mo–rGO) $_{2.0 \text{ A dm}^{-2}}$	0.298	19.61	10.28
(Ni–Mo–rGO) $_{3.0 \text{ A dm}^{-2}}$	0.311	15.36	7.80
(Ni–Mo–rGO) $_{4.0 \text{ A dm}^{-2}}$	0.315	9.91	4.69

From the corrosion data, it can be inferred that the Ni–Mo–rGO composite coating deposited at 4.0 A dm^{-2} (having about 57.6% Ni) shows the least CR, i.e. $4.69 \times 10^{-2} \text{ mm y}^{-1}$, while the coatings deposited at lower c.d.'s are more susceptible to corrosion.

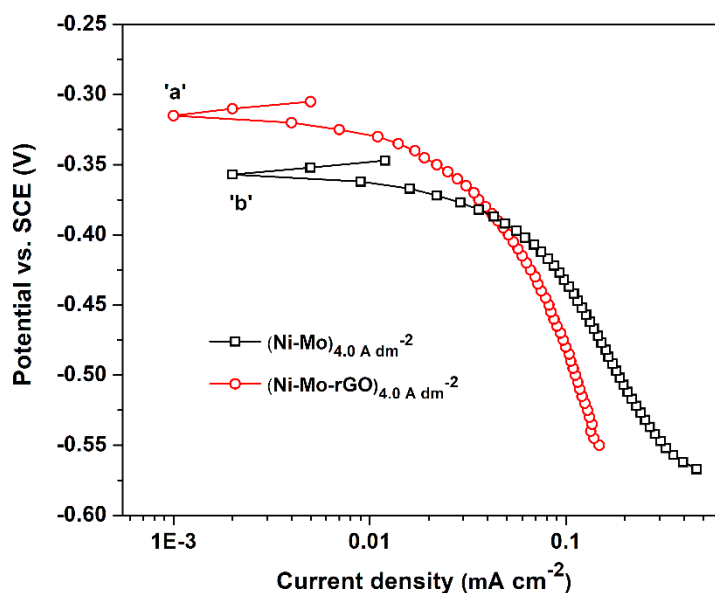


Figure 9.7 – Comparison of Tafel curves of Ni–Mo alloy and Ni–Mo–rGO composite coatings developed at same c.d.

Figure 9.7 compares the Tafel curves of Ni–Mo alloy and Ni–Mo–rGO composite coatings recorded under electrocatalytic working conditions. It can be observed from the Figure 9.7 that curve 'a' is shifted to more positive potential compared to the curve 'b' indicating the more noble character of Ni–Mo–rGO composite coating and also its i_{corr} value decreased significantly relative to the Ni–Mo alloy deposit. This shift of E_{corr} ,

and a decrease in i_{corr} indicates the higher corrosion resistance property of the composite coatings.

In order to decouple the chemical composition related intrinsic activity of the Ni–Mo–rGO composites towards hydrogen evolution, the effective exchange current density, i_o for Ni–Mo–rGO electrodes were calculated. The i_o is derived directly from the intercept by the extrapolation of Tafel slope to equilibrium potential. The optimal HER electrocatalyst is the material that gives the highest current at the least overpotential and this particular electrocatalyst shows a low β_c and a large i_o values. The kinetic parameters of the Tafel curves are given in Table 9.5.

Table 9.5 – Kinetic parameters obtained from the cathodic polarization curves for HER on Ni–Mo–rGO composite coatings developed at different c.d.'s

Coating configuration	$-\eta_c$ (mV vs. SCE)	$-\beta_c$ (mV dec ⁻¹)	i_o ($\mu\text{A cm}^{-2}$)
(Ni–Mo–rGO) _{1.0 A dm⁻²}	401.6	89	4.31
(Ni–Mo–rGO) _{2.0 A dm⁻²}	409.9	95	4.11
(Ni–Mo–rGO) _{3.0 A dm⁻²}	419.5	98	3.92
(Ni–Mo–rGO) _{4.0 A dm⁻²}	426.6	103	3.78

As it seen from the data given in Table 9.5, i_o values decreases with the c.d. and found to be maximum for the composite coated at 1.0 A dm⁻² indicating the better efficiency of that electrode for highest HER activity. Furthermore, values of β_c that were directly obtained from slopes of Tafel curves, which increases with the increase in c.d. This signifies to a better electrocatalytic behavior for HER by the coatings developed at lower c.d. (1.0 A dm⁻²) as it was found to have least β_c and highest i_o value. A lower Tafel slope means that a catalyst requires a low applied overpotential to generate a required current. Since i_o is the measure of electron transfer rate of a catalyst (Jiang et al. 2015), a higher amount of i_o means the higher electrocatalytic activity (Ojani et al. 2013), further proving the point.

From Table 9.6, it can be seen that the i_0 for HER on the Ni–Mo–rGO electrodes are obviously higher than that on Ni–Mo electrodes, showing that the intrinsic activity of the Ni–Mo–rGO composite coating toward HER is remarkably higher than that of Ni–Mo alloy coating. This suggests that the introduction of rGO into Ni–Mo alloy coating enhances its intrinsic electrocatalytic activity for HER in addition to an increase in surface area (Xia et al. 2014).

Table 9.6 – Comparison of Tafel slope (β_c) exchange current density (i_0) and cathodic overpotential (η_c) of Ni–Mo alloy and Ni–Mo–rGO composite coatings deposited at 1.0 A dm⁻² and 4.0 A dm⁻²

Coating Configuration	$-\beta_c$ (mV dec ⁻¹)	i_0 ($\mu\text{A cm}^{-2}$)	$-\eta_c$ (mV vs. SCE)
(Ni–Mo) _{1.0 A dm⁻²}	115	3.18	438.8
(Ni–Mo) _{4.0 A dm⁻²}	120	2.49	451.2
(Ni–Mo–rGO) _{1.0 A dm⁻²}	89	4.31	401.6
(Ni–Mo–rGO) _{4.0 A dm⁻²}	103	3.78	426.6

9.3.6 Cyclic Voltammetry

The electrocatalytic activity of Ni–Mo–rGO composite coating deposited at the c.d. range of 1.0 A dm⁻² to 4.0 A dm⁻² for HER has been evaluated by CV method in the potential range of 0.0 V to –1.6 V at a scan rate for 50 mV s⁻¹ for 50 cycles. The CV curves for HER of Ni–Mo–rGO composite coatings are shown collectively in Figure 9.8, and corresponding electrochemical parameters are listed in Table 9.7. From the data in Table 9.7, it is evident that i_{pc} decreases with the increase in c.d. It can be observed that Ni–Mo–rGO composite coatings developed at the lowest c.d. (1.0 A dm⁻²) shows maximum i_{pc} value (–0.517 A cm⁻²), with the least onset potential (–1.06 V), proving that it is the most effective coating for HER activity, compared to other coatings.

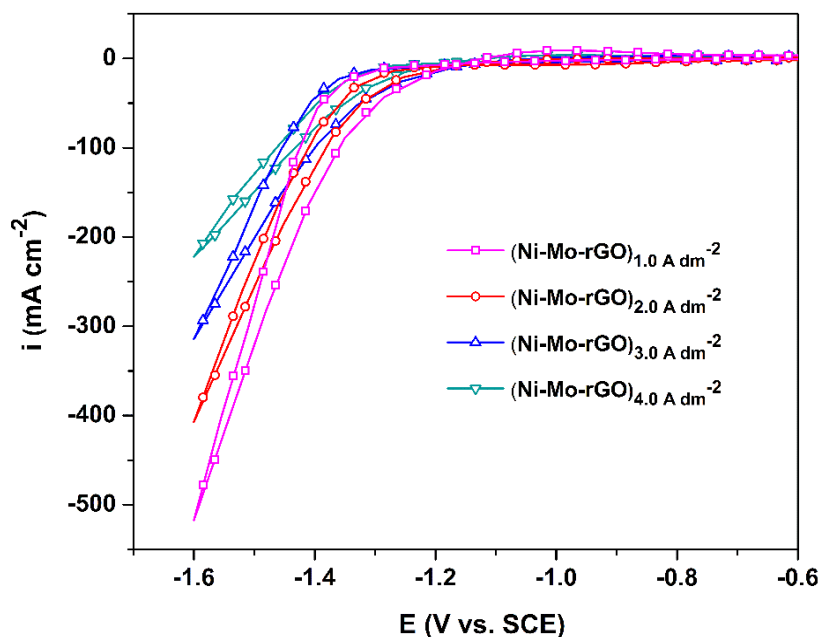


Figure 9.8 – Cyclic voltammograms of Ni–Mo–rGO coatings deposited at different c.d.'s showing their cathodic peak current density, i_{pc} for HER

Table 9.7 – HER parameters of Ni–Mo–rGO coatings developed at different c.d.'s from the optimal bath

Coating configuration	Cathodic peak c.d. (i_{pc}) (A cm ⁻²)	Onset potential for HER (V vs. SCE)	Volume of H ₂ evolved 300 s (cm ³)
(Ni–Mo–rGO) _{1.0} A dm ⁻²	-0.517	-1.06	15.7
(Ni–Mo–rGO) _{2.0} A dm ⁻²	-0.407	-1.09	14.4
(Ni–Mo–rGO) _{3.0} A dm ⁻²	-0.314	-1.11	13.2
(Ni–Mo–rGO) _{4.0} A dm ⁻²	-0.222	-1.14	12.3

The onset potential is defined as the potential at which hydrogen evolution reaction commences. For this study, the onset potential of HER is obtained by the intersection of the extrapolated baseline current and the prolonged tangent of the cathodic linear curve. Moreover, the measured onset potential of the Ni–Mo–rGO electrode for HER was significantly more positive than that of the Ni–Mo electrode as shown in the

comparison graph of Figure 9.9. It may be observed that at -1.6 V, i_{pc} for HER decreases as the deposition c.d. increases and is approximately 3 times better than that of binary Ni–Mo alloy coating (Figure 9.9). This increase in the i_{pc} can be attributed to the increased electrochemically active surface area of the electrode, which is supported by the increased area covered under the CV plot. Therefore, it can be concluded the Ni–Mo–rGO composite electrode displayed considerably higher electrochemical activity for hydrogen evolution and better electrocatalytic performance by reducing the overpotential of HER. Apparently, the enhanced performance of Ni–Mo–rGO electrode toward electrocatalytic activity of HER is strongly credited to its chemical composition and the microstructure (Xia et al. 2014).

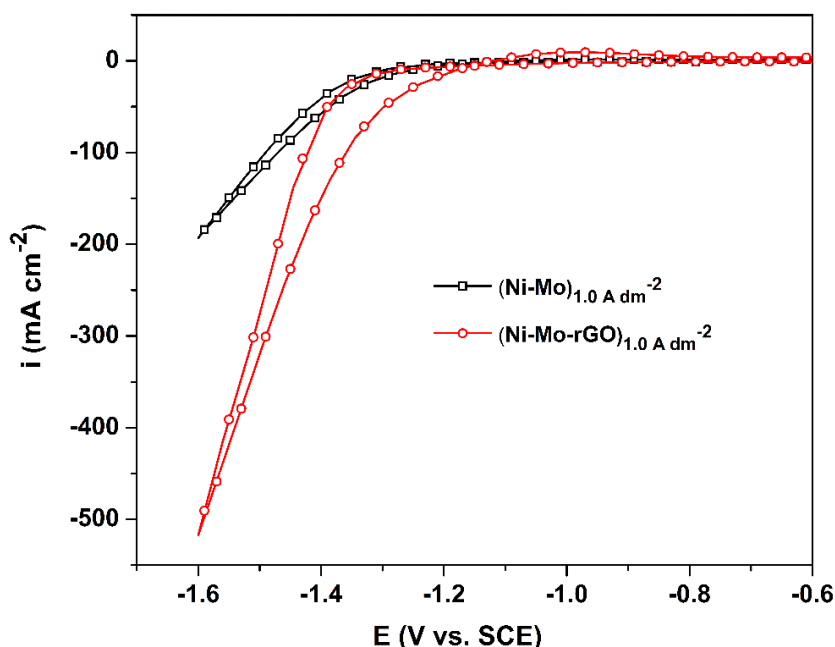


Figure 9.9 – Comparison of CV curves for HER on the surface of Ni–Mo alloy and Ni–Mo–rGO composite coatings deposited at same c.d. (1.0 A dm^{-2})

9.3.7 Chronopotentiometry

To test the electrocatalytic activity and stability of a catalyst, CP was employed as a suitable technique. An electrochemical technique in which a controlled current, usually a constant current, is caused to flow between two electrodes; the potential of one electrode is monitored as a function of time with respect to a suitable reference electrode. The solution is usually, but not necessarily, unstirred and contains an excess

of a supporting electrolyte so that diffusion is the principal mechanism of mass transport. Conventional industrial low-pressure alkaline electrolyzers operate usually at c.d.'s from -100 mA cm^{-2} to -300 mA cm^{-2} (Tasić et al. 2013). Figure 9.10 shows chronopotentiograms of Ni–Mo–rGO composite coatings deposited at different c.d.'s and the volume of H_2 gas liberated is shown in the inset, for initial 300 s. As observed, for all of the modified electrodes, the electrode potential reached a constant value after some time.

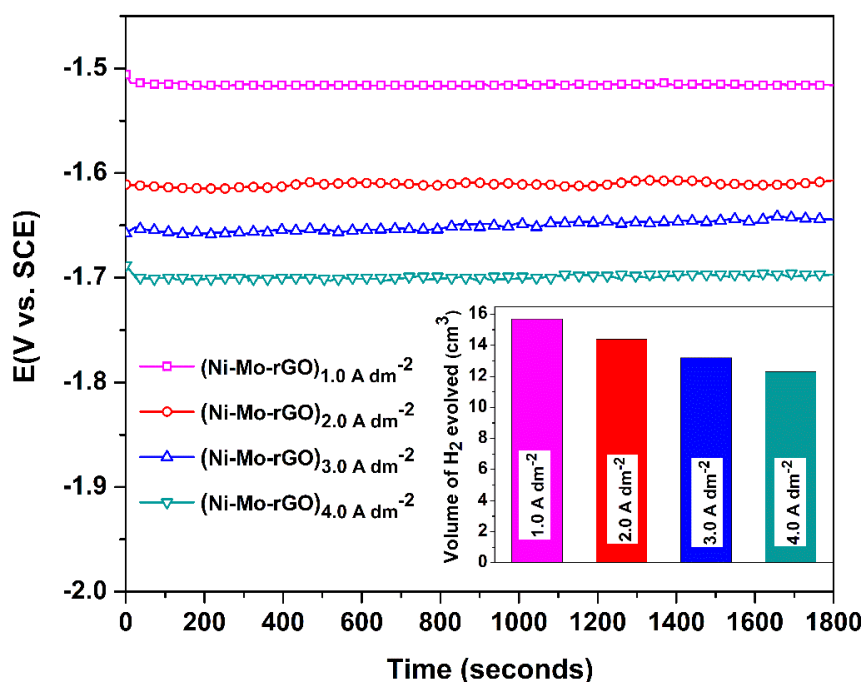


Figure 9.10 – Chronopotentiograms of Ni–Mo–rGO composite coatings, deposited at different c.d.'s under impressed cathodic current of -300 mA cm^{-2} with the volume of H_2 evolved in 300 s on each test electrodes are shown in the inset

It can be seen that coating corresponding to 1.0 A dm^{-2} shows maximum liberation of H_2 , due to excess reduction of H^+ ions as there are plenty of active site for their adsorption, provided by the graphene incorporated binary alloy matrix. This is further proved by the substantial reduction in the operating cathodic potential (-1.51 V) of Ni–Mo–rGO composite coating as compared to its binary alloy coating (-1.74 V). Also, the volume of hydrogen gas liberated in first 300 s was found to be much higher in the case of composite coatings, as shown graphically in the inset of Figure 9.11.

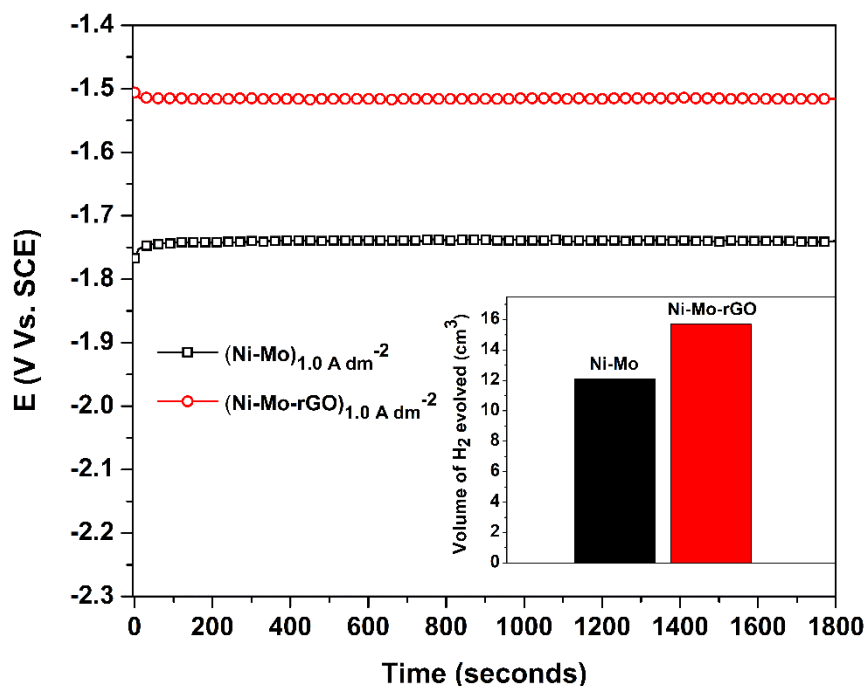


Figure 9.11 – CP curves at -300 mA cm^{-2} recorded for Ni–Mo alloy and Ni–Mo–rGO composite coatings developed at 1.0 A dm^{-2} . The inset chart shows the volume of H_2 liberated in 300 s on each of the electrodes

9.3.8 Mechanism for HER

Tafel slope has often been used to identify the mechanism and rate-limiting step of HER. These characterization techniques revealed that the HER mechanism in high alkaline media consisted of the three following steps (Safizadeh et al. 2015): *i*) electro-reduction of water molecules with hydrogen adsorption; Volmer reaction (Eqn. (6.1)) *ii*) electrochemical hydrogen desorption; Heyrovsky reaction (Eqn. (6.2)) *iii*) chemical desorption; Tafel reaction (Eqn. (6.3)). The electrocatalytic HER on Ni–Mo–rGO composite coatings can also be explained by means of a mechanism, shown in Figure 6.13 (Chapter 6, Section 6.3.8). For a complete HER, the combinations of Volmer–Heyrovsky or Volmer–Tafel mechanism should be involved to produce molecular hydrogen. The Tafel plots are shown in Figure 9.6 and the corresponding β_c values are reported in Table 9.5. The Tafel slope for Ni–Mo–rGO was found to be around the theoretically obtained value of -118 mV dec^{-1} indicating that the rate-limiting step was the Volmer–Tafel mechanism (Eqn. (6.1) and (6.3)) of the HER (Choquette et al. 1990).

When compared with the binary alloy coating rGO induced Ni–Mo alloy shows better catalytic activity towards hydrogen production, this is because graphene acted as a communicating platform in facilitating the electron transfer and transport during the HER. As a result, the ohmic loss of the whole system was reduced and the c.d. of the HER was enhanced. Therefore, the improved HER performances of Ni–Mo–rGO could be also attributed to the high specific surface area and excellent electrical conductivity of graphene present in the alloy matrix (Huang et al. 2016).

9.4 CONCLUSIONS

In this study, a simple electrochemical method was used to synthesize an electrocatalyst consisting of graphene. Ni–Mo–rGO composite coatings were electrochemically deposited on a copper electrode and characterized by different techniques in view of their possible applications as an electrocatalyst for the HER in alkaline solution. Based on the above experiments following conclusions are drawn.

- 1 The introduction of rGO into Ni–Mo alloy matrix provided an abundance of available edge sites for HER.
- 2 With the highly-exposed edge sites, Ni–Mo–rGO film achieved an excellent electrocatalytic activity towards HER with a low η_c (–401.6 mV) and large i_o (up to $4.31 \mu\text{A cm}^{-2}$).
- 3 The best coating exhibits a maximum i_{pc} of -0.517 A cm^{-2} at -1.6 V , which is approximately 3 times better than that of binary Ni–Mo alloy indicating higher activity for hydrogen production.
- 4 Tafel slope analysis revealed that HER on the surface of composite coatings follows Volmer–Tafel mechanism.
5. The prepared Ni–Mo–rGO composite coating shows 4 times better corrosion stability in the alkaline medium than Ni–Mo alloy electrodes.
6. The highest electrocatalytic activity for Ni–Mo–rGO composite coating is attributed to a synergistic effect between binary alloy and rGO, in terms of composition and increased surface area.

CHAPTER 10

CHAPTER 10

SUMMARY AND CONCLUSIONS

This chapter summarizes the experimental results of investigation embodied in the whole thesis on electrodeposition of Sn–Ni and Ni–Mo alloy coatings for peak protection of their coatings against corrosion, and optimal electrocatalytic performance. The peak performance of the coatings is seen in the light of changed composition, morphology, and phase structure, affected by the forced convection of metal ions (mass transport) towards cathode film, due to the effect of magnetic field/ultrasound field. The conclusions are made to figure out the most suitable mode of electrodeposition, among magneto-electrodeposition (MED), sono-electrodeposition (SED), and Ni–Mo–rGO composite coating in terms of their corrosion stability, and electrocatalytic activity towards HER and OER, through Tables and Figures.

10.1 SUMMARY

A systematic study on the development of monolayer coatings of Sn–Ni and Ni–Mo alloys have been developed by conventional electrodeposition (ED) method, using only DC. All depositions were carried out galvanostatically on copper/MS substrate from their respective optimized baths for the same duration for comparison purpose. The corrosion protection ability of binary alloy coatings was increased drastically either by forced convection or by multilayer coating approach. i.e. by either modulating the mass transfer process at cathode film by applying magnetic field/ultrasound field during deposition (for monolayer coating) or by pulsing the current density (c.d.)/magnetic field intensity (B)/ultrasound power density (p.d.) during deposition (for multilayer coating). In this regard, the effort has been made to improve the property of monolayer Sn–Ni and Ni–Mo alloy coatings by making use of modern approach of electrodeposition, namely through *magneto-electrodeposition (MED)* and *sono-electrodeposition (SED)*.

Table 10.1 – Composition and operating parameters of binary alloy baths for deposition of uniform alloy coating

<i>Bath constituents</i>	<i>Sn–Ni Bath</i>	<i>Ni–Mo Bath</i>
SnCl ₂ . 2H ₂ O	22.6 g L ⁻¹	–
NiCl ₂ . 6H ₂ O	33.7 g L ⁻¹	–
NiSO ₄ . 6H ₂ O	–	18 g L ⁻¹
Na ₂ MoO ₄	–	48 g L ⁻¹
K ₄ P ₂ O ₇	119 g L ⁻¹	–
Na ₃ C ₆ H ₅ O ₇	–	105 g L ⁻¹
Gelatin	5.0 g L ⁻¹	–
<i>Operating parameters</i>		
c.d. range	1.0 – 4.0 A dm ⁻²	1.0 – 4.0 A dm ⁻²
pH	8.6	9.5
Temperature (K)	298	298
Anode	Tin	Nickel
Cathode	Mild steel	Copper

10.1.1 Corrosion Performance of Binary Alloys

To start with, two new alkaline baths, namely Sn–Ni and Ni–Mo have been optimized for development of their most corrosion resistant coatings. CR and other properties of each monolayer Ni–M (where M = Sn or Mo) alloy coatings developed from those optimized baths using DC (Table 10.1) are summarized in in Table 10.2.

The benefit of MED, working on the principle of MHD effect has been tried to further increase the corrosion resistance behavior of monolayer Sn–Ni and Ni–Mo

alloy coatings. MED has been carried out under the different intensity of magnetic field (B), applied both parallel and perpendicular to the plane of cathode and results are reported. Experimental investigation proved that corrosion resistance of both Sn–Ni and Ni–Mo coatings can be increased by many folds by inducing the magnetic field, during deposition.

Table 10.2 – Comparative account of CR's and other deposit characters of conventional electrodeposited monolayer Ni–M alloy coatings, developed from their optimal baths (given in Table 10.1)

Monolayer alloy coating	Sn–Ni	Ni–Mo
Optimal c.d.	1.0 A dm ⁻²	4.0 A dm ⁻²
pH	8.6	9.5
Temperature (K)	298	298
Corrosion medium	NaCl	KOH
Nature of the deposit	Bright silvery	Metallic
CR (mm y ⁻¹)	18.60	19.94
i_{corr} ($\mu\text{A cm}^{-2}$)	9.76	20.85
wt.% of Ni in the deposit	19.6	61.7

Accordingly, the corrosion resistance of monolayer alloy coatings was tried to improve further by applying ultrasound field, parallel to the process of deposition. A drastic change in surface morphology and phase structure of both the coatings were caused due to superimposition of external force (magnetic field or ultrasound field). The effect of these two forces on composition and CR's of Sn–Ni and Ni–Mo alloy coatings were studied and results are reported. Furthermore, the corrosion protection of

Ni–M alloys was tried to enhance by increasing the surface area of the coatings, which is achieved by layered coating. The multilayer alloy coating was developed electrolytically by modulating the ultrasound field, keeping the c.d. constant (optimal). Multilayer coatings, having nano/micrometric layers of alloys (with alternately different compositions) were developed by turning the ultrasound generator ON and OFF periodically, during deposition. The periodic pulsing of the sonicator probe (between ON and OFF) allowed the deposition to take place in multilayers. This technique proved to be efficient, as it protected the substrate from corrosion attack by many folds.

Experimentally determined CR's of different coatings (Sn–Ni and Ni–Mo), deposited under different conditions of mass transfer towards the cathode, controlled by the applied magnetic field, ultrasound field and by composite coating is shown in the form of a histogram in Figure 10.1.

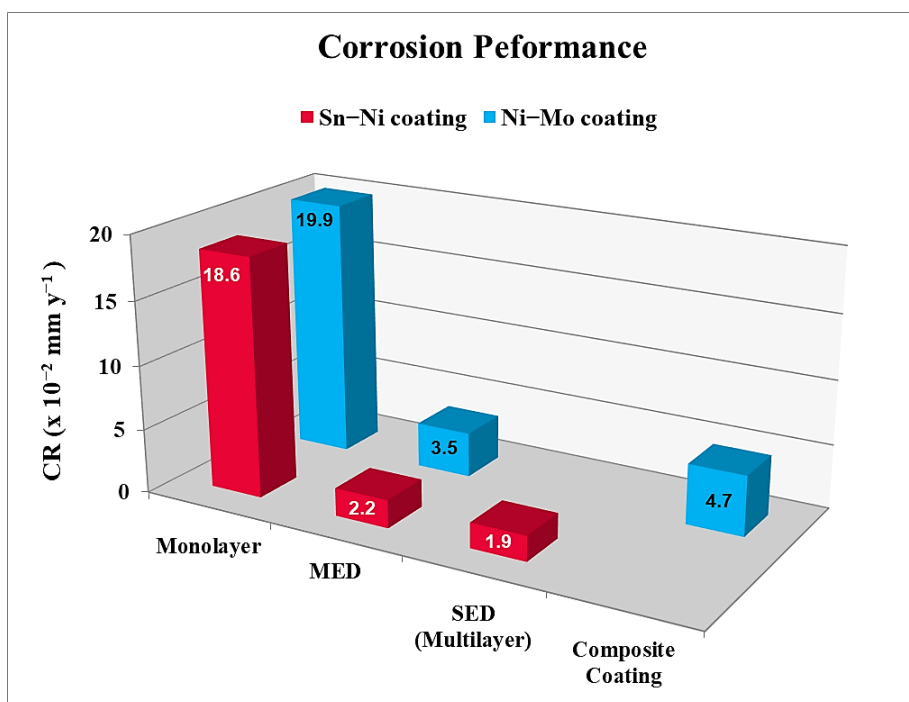


Figure 10.1 – Histogram showing the corrosion rates of Sn–Ni and Ni–Mo alloy coatings, deposited under different conditions of electrodeposition (from the respective baths given in Table 10.1)

10.1.2 Electrocatalytic Performance of Binary Alloys

Alkaline water electrolysis is one of the easiest and simplest methods for production of hydrogen and oxygen for industrial applications. Though the technique seems to be very simple, reducing the energy consumption, maintaining the durability and the safety of these systems are the main challenges. In this regard, the second part of the thesis outlines the proficiency of these electrodeposited binary alloys, as an active electrocatalytic material for water splitting applications. It has been shown that electrodeposited Sn–Ni and Ni–Mo alloy coatings can be used as the most cost-effective electrode materials for water electrolysis of HER and OER when tested in 1.0 M KOH solution using the same setup shown in Figure 6.2. Electrochemical kinetic parameters, like onset potential, peak current density (i_{pc} and i_{pa}), overpotential (η_c and η_a) and volume of gas (H_2 and O_2) evolved at steady state potentials were obtained from CV and CP experiments. Experiments conducted on these coatings revealed that Sn–Ni alloy coated at high c.d. and Ni–Mo alloy coated at low c.d. are most suitable for HER, and the reverse trend is true for the OER activity when tested under same conditions.

Optimizing the conditions for the development of advanced electrode materials is a crucial issue for improving the efficiency of water electrolysis and to reduce the power consumption. Therefore, considerable efforts have been devoted in enhancing the electrocatalytic activity of electrodes to reduce the overpotentials for the HER. In this regard, a new approach like MED technique has been used to bring improvement in their electrocatalytic activity. The effect of MHD effect has been used effectively to bring change in their surface morphology, composition and phase structure. The electrocatalytic activity of Sn–Ni alloy coatings for HER has been further enhanced by anodic dissolution treatment. This is attributed to a profound increase in the surface area of the coatings evident from the SEM images (Figure 6.10 and Figure 8.2). After the dissolution treatment, a large number of pores were created on the surface, which increases the adsorption site for hydrogen atoms, thereby accelerating the rate of hydrogen gas reduction. Similarly, the effect of the addition of rGO into Ni–Mo bath, in terms of its ability to enhance the electrocatalytic property of Ni–Mo alloy for HER

has been examined by CV, CP, and potentiodynamic polarization techniques. The effect of integrating rGO into the alloy matrix, on surface morphology, phase structure, and finally on the electrocatalytic property of Ni–Mo alloy has been studied, and results are discussed. MED, anodic dissolution treatment, and the addition of rGO have proved to be an effective route for increasing the electrocatalytic activity for HER, compared to its conventional alloy coatings. The electrocatalytic activity of different Ni-based alloy coatings, developed under different conditions (using either different mode of mass transport/or with different additive) are evaluated on the basis of their cathodic peak c.d. (i_{pc}) values, and are shown diagrammatically in Figure 10.2. The comparison of i_{pc} values verified that the coating, represented as Ni–Mo–rGO is electro-catalytically more active for HER than its conventional alloy coatings.

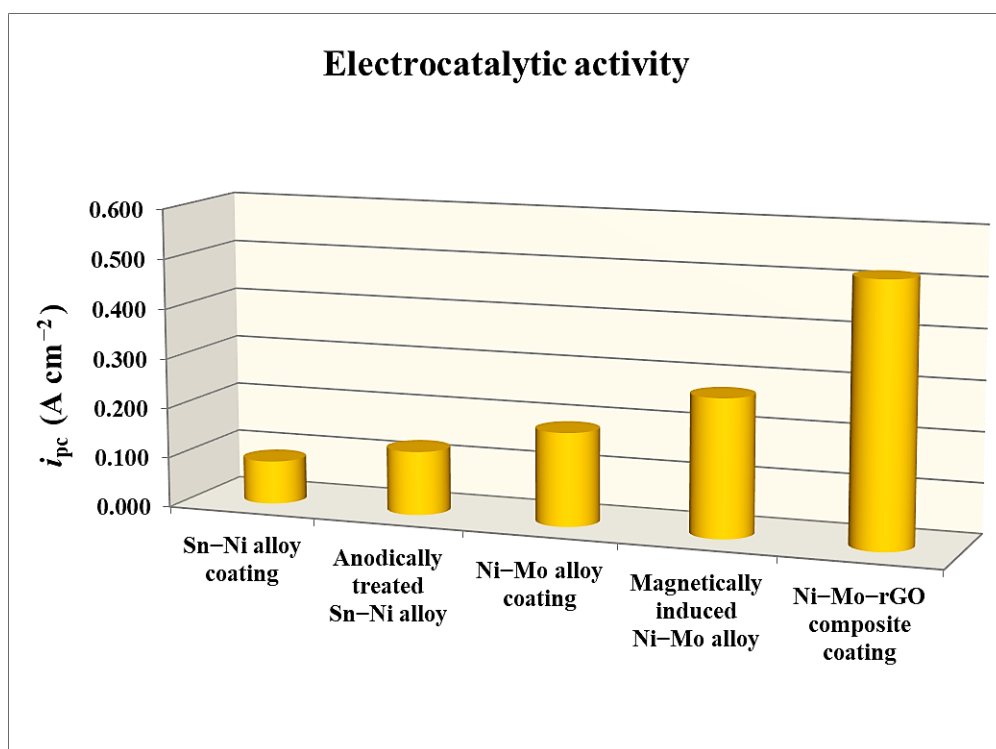


Figure 10.2 – Histogram showing the electrocatalytic activity of Sn–Ni and Ni–Mo alloy coatings, expressed in terms of their cathodic peak current density (i_{pc}) developed through different mode of electrodeposition, from their respective bath for the same duration of time

10.2 CONCLUSIONS

Based on the experimental research carried out on electrodeposition of Sn–Ni and Ni–Mo alloy coatings through a different mode of electrodeposition, optimization of their deposition conditions for better corrosion resistance and electrocatalytic performance of the coatings, following conclusions are drawn in compliance with the proposed objectives:

1. Two new electrolytic baths, namely Sn–Ni and Ni–Mo alloy have been formulated, and conditions of electrodeposition have been optimized. Under all conditions of c.d.'s and bath composition, Sn–Ni alloy bath followed the anomalous type of co-deposition and Ni–Mo bath followed induced a type of co-deposition.
2. The corrosion protection efficacy of monolayer ED alloy coating has been increased to many folds, by MED approach. The improved corrosion resistance was reasoned by the changed crystallographic orientation of alloy coatings, affected due to MHD effect.
3. The corrosion resistance property of monolayer ED Sn–Ni alloy coating is further increased to a great extent, by multilayer technique, accomplished by modulating the ultrasound power density (p.d.), parallel to the process of deposition.
4. The corrosion resistance of multilayer Sn–Ni alloy coating is found to increase with a number of layers, due to increase in the interfacial surface area.
5. The electrocatalytic activity of ED Ni–Mo alloy coatings for HER is increased substantially by modulating mass transfer process at the EDL, during deposition. This is accomplished by inducing the artificial convection at the interface, using a magnetic field.
6. The enhancement in the property of alloy coatings is attributed to the increase of noble metal content in the alloy, due to an increase of its i_L , affected by the changed mass transfer process due to induced magnetic field.

7. The electrocatalytic activity of binary alloys is further enhanced by modifying the structural properties of the electrode materials, using the techniques, like anodic dissolution treatment and composite coating.
8. The highest electrocatalytic activity recorded by Ni–Mo–rGO composite coating is attributed to the synergistic effect of Ni-based alloy and rGO, in terms of their composition and increased surface area, respectively.
9. The experimental results demonstrated that between two binary alloys, ultrasound induced multilayer Sn–Ni alloy coating, abbreviated as (Sn–Ni)_{2/2/150} showed the least corrosion rate among all other coatings. Further, Ni–Mo–rGO composite coating exhibited the highest electrocatalytic activity for HER.

10.3 SCOPE FOR THE FUTURE WORK

Based on the success of having achieved better corrosion performance of multilayer Sn–Ni coatings on MS, it is planned to develop high-performance multilayer Ni–Mo alloy coatings by modulating the ultrasound power density (p.d.). The coating characteristics, like corrosion resistance and electrocatalytic properties of different binary/ternary alloy coatings can also be improved further by developing them in either monolayer or multilayer, by changing the mass transfer process at cathode interface (a place where electrons are transferred from/to cathode to/electrolyte) by modulating/pulsing the external fields (like electrical, magnetic and ultrasound field). The advent of MED and SED can also be tried to explore for the development of some new electrode materials, using certain non-precious metals, and their structure-property relationship can also be studied. Additionally, the effect of different nanoparticles, like TiO_2 , RuO_2 , Ce_2O_3 , and AgO on the electrocatalytic property of Ni-based alloys can be studied, as it is one of the promising approaches for developing highly active electrocatalytic materials. Thus, a variety of materials can be synthesized and characterized using the subject of electrochemistry as a definite tool for the indefinite possibility, by knowing the fundamental aspects of electrochemistry and governing the principles of electrodeposition.

REFERENCES

- Aaboubi, O. (2011). "Hydrogen evolution activity of Ni–Mo coating electrodeposited under magnetic field control." *Int. J. Hydrogen Energy*, 36(8), 4702-4709.
- Aaboubi, O. and Msellak, K. (2017). "Magnetic field effects on the electrodeposition of CoNiMo alloys." *Appl. Surf. Sci.*, 396, 375-383.
- Aaboubi, O., Hadjaj, A. and Omar, A.A. (2015). "Application of Adomian Method for the Magnetic field effects on mass transport at vertical cylindrical electrode." *Electrochim. Acta*, 184, 276-284.
- Abbas, S.A., Iqbal, M.I., Kim, S.H. and Jung, K.D. (2017). "Catalytic Activity of Urchin-like Ni nanoparticles Prepared by Solvothermal Method for Hydrogen Evolution Reaction in Alkaline Solution." *Electrochim. Acta*, 227, 382-390.
- Aguilar, A., Sagüés, A.A. and Powers, R.G. (1990). "Corrosion measurements of reinforcing steel in partially submerged concrete slabs." In *Corrosion Rates of Steel in Concrete*. ASTM International.
- Ahmad, Z. (2006). *Principles of corrosion engineering and corrosion control*. Butterworth-Heinemann, Great Britain.
- Ahn, S.H., Hwang, S.J., Yoo, S.J., Choi, I., Kim, H.J., Jang, J.H., Nam, S.W., Lim, T.H., Lim, T., Kim, S.K. and Kim, J.J. (2012). "Electrodeposited Ni dendrites with high activity and durability for hydrogen evolution reaction in alkaline water electrolysis." *J. Mater. Chem.*, 22(30), 15153-15159.
- Anicaia, L., Peticab, A. Costovicic, S. Prioteasab, P. and Visand, T. (2013). "Electrodeposition of Sn and NiSn alloys coatings using choline chloride based ionic liquids—Evaluation of corrosion behaviour." *Electrochim. Acta*, 114, 868–877.
- Aogaki, R., Fueki, K. and Mukaibo, T. (1975). "Application of magnetohydrodynamic effect to the analysis of electrochemical reactions. 2. diffusion process in mhd forced flow of electrolyte solution." *Denki Kagaku*, 43(9), 509-514.

-
- Badea, G.E., Caraban, A., Sebesan, M., Dzitac, S., Cret, P. and Setel, A. (2010). "Polarisation Measurements Used for Corrosion Rates Determination." *J. Sust. Energy*, 1.
- Bakhit, B. and Akbari, A. (2013). "Nanocrystalline Ni–Co alloy coatings: electrodeposition using horizontal electrodes and corrosion resistance." *J. Coating. Tech. Res*, 10(2), 285-295.
- Banks, C.E. and Compton, R.G. (2003). "Ultrasonically Enhanced Voltammetric Analysis and Applications: An Overview." *Electroanal.*, 15 (5-6), 329–346.
- Banks, C.E. and Compton, R.G. (2003). "Ultrasonically Enhanced Voltammetric Analysis and Applications: An Overview." *Electroanalysis*, 15 (5-6), 329–346.
- Bard, A.J and Faulkner, L.R. (2001). *Electrochemical methods: fundamentals and applications*, second ed, John Wiley & Sons, New York.
- Barsoukov, E. and Macdonald, J.R. (2005). *Impedance spectroscopy: theory, experiment, and applications*. John Wiley & Sons, New Jersey.
- Beltowska-Lehman, E. and Indyka, P., (2012). "Kinetics of Ni–Mo electrodeposition from Ni-rich citrate baths." *Thin Solid Films*, 520(6), 2046-2051.
- Birss, V. I., Damjanovic, A. and Hudson, P. G. (1986). "oxygen evolution at platinum electrodes in alkaline solutions II. mechanism of the reaction." *J. Electrochem. Soc.*, 133(8), 1621-1625.
- Bonin, L., Bains, N., Vitry, V. and Cobley, A.J. (2017). "Electroless deposition of nickel-boron coatings using low frequency ultrasonic agitation: Effect of ultrasonic frequency on the coatings." *Ultrasonics*, 77, 61-68.
- Bratoeva, M. and Atanasov, N. (2000). "Effect of sulfamate-citrate electrolyte pH on the Ni-W alloy electrodeposition." *Russ. J. Electrochem.*, 36(1), 60-63.
- Brenner, A. (1963). *Electrodeposition of alloys-principles and practice*. Vol. 1 & 2. Academic Press, New York.

- Brett C. M. and Brett, A. M. O. (1993). *Electrochemistry: principles, methods, and applications*, Oxford university press, United Kingdom.
- Brewer, L. and Beck, P. (1963). *Electronic structure and alloy chemistry of the transition elements*. ed., Wiley-Interscience, New York.
- Brillas, E., Rambla, J. and Casado, J. (1999). "Nickel electrowinning using a Pt catalysed hydrogen-diffusion anode. Part I: Effect of chloride and sulfate ions and a magnetic field." *J. Appl. Electrochem.*, 29(12), 1367-1376.
- Brooman, E.W. (2000). "Corrosion performance of environmentally acceptable alternatives to cadmium and chromium coatings: Chromium-Part II." *Met Finish*, 98(8), 39-45.
- Brown, A.P., Krumpelt, M., Loutfy, R.O. and Yao, N.P. (1982). "The effect of surface roughness on the hydrogen evolution reaction kinetics with mild steel and nickel cathodes." *Electrochim. Acta*, 27(5), 557-560.
- Camargo, M.K., Tudela, I., Schmidt, U., Cobley, A.J. and Bund, A. (2016). "Ultrasound assisted electrodeposition of Zn and Zn-TiO₂ coatings." *Electrochim. Acta*, 198, 287-295.
- Campillo, B., Sebastian, P.J., Gamboa, S.A., Albarran, J.L. and Caballero, L.X. (2002). "Electrodeposited Ni-Co-B alloy: application in water electrolysis." *Mater Sci Eng C*, 19(1), 115-118.
- Cesiulis, H., Tsyntaru, N., Ramanavicius, A. and Ragoisha, G. (2016). *The Study of Thin Films by Electrochemical Impedance Spectroscopy*. Nanostructures and Thin Films for Multifunctional Applications, Springer International Publishing.
- Chade, D., Berlouis, L., Infield, D., Cruden, A., Nielsen, P.T. and Mathiesen, T. (2013). "Evaluation of Raney nickel electrodes prepared by atmospheric plasma spraying for alkaline water electrolyzers." *Int. J. Hydrogen Energy*, 38(34), 14380-14390.
- Chassaing, E., Portail, N., Levy, A.F. and Wang, G. (2004). "Characterisation of electrodeposited nanocrystalline Ni-Mo alloys." *J Appl. Electrochem.*, 34(11), 1085-1091.

- Chassaing, E., Roumegas, M.P. and Trichet, M.F. (1995). "Electrodeposition of Ni-Mo alloys with pulse reverse potentials." *J. Appl. Electrochem.*, 25(7), 667-670.
- Cheh, H.Y. (1971). "Electrodeposition of gold by pulsed current." *J. Electrochem. Soc.*, 118(4), 551-557.
- Chekin, F., Tahermansouri, H. and Besharat, M.R. (2014). "Nickel oxide nanoparticles prepared by gelatin and their application toward the oxygen evolution reaction." *J. Electrochem. Soc.*, 18(3), 747-753.
- Chen, L. and Lasia, A. (1991). "Study of the Kinetics of Hydrogen Evolution Reaction on Nickel-Zinc Alloy Electrodes." *J. Electrochem. Soc.*, 138(11), 3321-3328.
- Chen, S., Duan, J., Ran, J. and Qiao, S.Z. (2015). "Paper-Based N-Doped Carbon Films for Enhanced Oxygen Evolution Electrocatalysis." *Adv. Sci.*, 2(1-2).
- Cheng, Q., Tang, J., Ma, J., Zhang, H., Shinya, N. and Qin, L.C. (2011). "Graphene and nanostructured MnO₂ composite electrodes for supercapacitors." *Carbon*, 49(9), 2917-2925.
- Chi, B., Li, J., Yang, X., Gong, Y. and Wang, N. (2005). "Deposition of Ni-Co by cyclic voltammetry method and its electrocatalytic properties for oxygen evolution reaction." *Int J Hydrogen Energy*, 30(1), 29-34.
- Chiba, A., Kitamura, K. and Ogawa, T. (1986). "Magnetic field effects on the electrodeposition of nickel from a high pH water bath." *Surf. Coat. Technol.*, 27(1), 83-88.
- Chin, D.T. (1983). "Mass Transfer and Current-Potential Relation in Pulse Electrolysis." *J. Electrochem. Soc.*, 130(8), 1657-1667.
- Choquette, Y., Brossard, L., Lasia, A. and Menard, H. (1990). "Study of the kinetics of hydrogen evolution reaction on raney nickel composite-coated electrode by ac impedance technique." *J. Electrochem. Soc.*, 137(6), 1723-1730.
- Clark, D., Wood, D. and Erb, U. (1997). "Industrial applications of electrodeposited nanocrystals." *Nanostruct. Mater.*, 9(1), 755-758.

- Clarke, M. and Elbourne, R.G. (1971). "The peculiarly low passivation potentials of some intermetallic tin compounds." *Electrochim. Acta.*, 16 (11), 1949-1954.
- Coey, J.M.D. and Hinds, G. (2001). "Magnetic electrodeposition." *J. Alloys Compd.*, 326(1), 238-245.
- Cohen, U., Koch, F.B. and Sard, R. (1983). "Electroplating of cyclic multilayered alloy (CMA) coatings." *J. Electrochem. Soc.*, 130(10), 1987-1995.
- Cohen, U., Koch, F.B. and Sard, R. (1983). "Electroplating of cyclic multilayered alloy (CMA) coatings." *J. Electrochem. Soc.*, 130(10), 1987-1995.
- Compton, R. G., Eklund, J. C., Marken, F., Rebbitt, T. O., Akkermans, R. P. and Waller, D. N. (1997). "Dual activation: coupling ultrasound to electrochemistry—an overview." *Electrochim. Acta*, 42(19), 2919-2927.
- Conway, B. E. and Liu, T. C. (1990). "Characterization of electrocatalysis in the oxygen evolution reaction at platinum by evaluation of behavior of surface intermediate states at the oxide film." *Langmuir*, 6(1), 268-276.
- Dabo, P., Brossard, L., Me, H. and Tremblay, P. (1998). "Hydrogen activation of spectroscopic graphite surface by argon plasma etching." *J. Appl. Electrochem.*, 28(6), 601-606.
- De la Torre, S.D., Oleszak, D., Kakitsuji, A., Miyamoto, K., Miyamoto, H., Martínez-S, R., Almeraya-C, F., Martínez-V, A. and Rios-J, D. (2000). "Nickel-molybdenum catalysts fabricated by mechanical alloying and spark plasma sintering." *Mater. Sci. Eng. A*, 276(1), 226-235.
- Del Campo, F.J., Coles, B.A., Marken, F., Compton, R.G. and Cordemans, E. (1999). "High-frequency sonoelectrochemical processes: mass transport, thermal and surface effects induced by cavitation in a 500-kHz reactor." *Ultrason. Sonochem.*, 6(4), 189-197.
- Devos, O., Olivier, A., Chopart, J., Aaboubi, O. and Maurin, G. (1998). "Magnetic field effects on nickel electrodeposition." *J. Electrochem. Soc.*, 145(2), 401-405.

Dhanapal, K., Narayanan, V. and Stephen, A. (2016). "Influence of Sn on the magnetic ordering of Ni–Sn alloy synthesized using chemical reduction method." *J. Magn. Mater.*, 406, 103-109.

Dinodi, N. and Shetty, A.N. (2014). "Alkyl carboxylates as efficient and green inhibitors of magnesium alloy ZE41 corrosion in aqueous salt solution." *Corr. Sci.*, 85, 411-427.

Dobrzański, L.A., Lukaszewicz, K., Pakuła, D. and Mikuła, J. (2007). "Corrosion resistance of multilayer and gradient coatings deposited by PVD and CVD techniques." *Arch. Mater. Sci. Eng.*, 28(1), 12-18.

Dobrzański, L.A., Lukaszewicz, K., Zarychta, A. and Cunha, L. (2005). "Corrosion resistance of multilayer coatings deposited by PVD techniques onto the brass substrate." *J. Mater. Process. Technol.*, 164, 816-821.

Donten, M., Cesiulis, H. and Stojek, Z. (2005). "Electrodeposition of amorphous/nanocrystalline and polycrystalline Ni–Mo alloys from pyrophosphate baths." *Electrochim. Acta*, 50(6), 1405-1412.

Ebadi, M., Basirun, W.J., Alias, Y. and Mahmoudian, M. (2010). "Electrodeposition of quaternary alloys in the presence of magnetic field." *Chem. Cent. J.*, 4(1), 14.

Eklund, J.C., Marken, F., Waller, D.N. and Compton, R.G. (1996). "Voltammetry in the presence of ultrasound: a novel sono-electrode geometry." *Electrochim. Acta*, 41(9), 1541-1547.

Elias, L. and Hegde, A.C. (2015). "Electrodeposition of laminar coatings of Ni–W alloy and their corrosion behaviour." *Surf. Coat. Technol.*, 283, 61-69.

Elias, L. and Hegde, A.C. (2016). "Modification of Ni–P alloy coatings for better hydrogen production by electrochemical dissolution and TiO₂ nanoparticles." *RSC Adv.*, 6, 66204-66214.

Elias, L., Bhat, K.U. and Hegde, A.C. (2016). "Development of nanolaminated multilayer Ni–P alloy coatings for better corrosion protection." *RSC Adv.*, 6(40), 34005-34013.

- Elias, L., Scott, K. and Hegde, A.C. (2015). "Electrolytic synthesis and characterization of electrocatalytic Ni-W alloy." *J. Mater. Eng. Perform.*, 24 (11), 4182-4191.
- Elizabeth, I., Nair, A.K., Singh, B.P. and Gopukumar, S. (2017). "Multifunctional Ni-NiO-CNT Composite as High Performing Free Standing Anode for Li Ion Batteries and Advanced Electro Catalyst for Oxygen Evolution Reaction." *Electrochim. Acta*, 230, 98-105.
- Erb, U., El-Sherik, A.M., Palumbo, G. and Aust, K.T. (1993). "Synthesis, structure and properties of electroplated nanocrystalline materials." *Nanostruct. Mater.*, 2(4), 383-390.
- Ezaki, H., Morinaga, M. and Watanabe, S. (1993). "Hydrogen overpotential for transition metals and alloys, and its interpretation using an electronic model." *Electrochim. Acta*, 38(4), 557-564.
- Fahidy, T. Z. (1983). "Magnetoelectrolysis." *J. Appl. Electrochem.*, 13, 553-563.
- Fernández, D., Diao, Z., Dunne, P. and Coey, J.M.D. (2010). "Influence of magnetic field on hydrogen reduction and co-reduction in the Cu/CuSO₄ system." *Electrochim. Acta*, 55(28), 8664-8672.
- Fontana, M. G. (1987). *Corrosion engineering*. Third Edition. Mc Graw Hill Book Co., New York.
- Gabe, D.R., Sheir, L.L., Jarman, R.A. and Burstein, G.T., (1994). *Corrosion vol. 2*.
- Gadelmawla, E.S., Koura, M.M., Maksoud, T.M.A., Elewa, I.M. and Soliman, H.H. (2002). "Roughness parameters." *J. Mater. Process. Technol.*, 123(1), 133-145.
- Ganesan, P., Kumaraguru, S.P. and Popov, B.N. (2007). "Development of compositionally modulated multilayer Zn-Ni deposits as replacement for cadmium." *Surf. Coat. Technol.*, 201(18), 7896-7904.
- Ganesh, V., Vijayaraghavan, D. and Lakshminarayanan, V. (2005). "Fine grain growth of nickel electrodeposit: effect of applied magnetic field during deposition." *Appl. Surf. Sci.*, 240(1), 286-295.

- Gao, M.Y., Yang, C., Zhang, Q.B., Zeng, J.R., Li, X.T., Hua, Y.X., Xu, C.Y. and Dong, P. (2017). “Facile electrochemical preparation of self-supported porous Ni–Mo alloy microsphere films as efficient bifunctional electrocatalysts for water splitting.” *J Mater. Chem. A*, 5(12), 5797-5805.
- Georgiou, E.P., Dosta, S., Fernández, J., Matteazzi, P., Kowalski, K., Kusinski, J., Piticescu, R.R. and Celis, J.P. (2016). “Structural and Tribological Properties of Nanostructured Supersonic Cold Sprayed Ni-20 wt.% Sn Coatings.” *J. Therm. Spray Technol.*, 25(5), 1029-1039.
- Gómez, R., Feliu, J.M. and Aldaz, A. (1997). “Effects of irreversibly adsorbed bismuth on hydrogen adsorption and evolution on Pt (111).” *Electrochim. Acta*, 42(11), 1675-1683.
- Goswami, G.L., Kumar, S., Galun, R. and Mordike, B.L. (2003). “Laser cladding of Ni-Mo alloys for hardfacing applications.” *Lasers Eng.*, 13(1), 1-12.
- Gray, H.B. (2009). “Powering the planet with solar fuel.” *Nat. Chem.*, 1(1), 7-7.
- Gu, Y., Liu, J., Qu, S., Deng, Y., Han, X., Hu, W. and Zhong, C. (2017). “Electrodeposition of alloys and compounds from high-temperature molten salts.” *J. Alloys Compd.*, 690, 228-238.
- Halim, J., Abdel-Karim, R., El-Raghy, S., Nabil, M. and Waheed, A. (2012). “Electrodeposition and characterization of nanocrystalline Ni-Mo catalysts for hydrogen production.” *J. Nanomater.*, 2012, 18.
- Haseeb, A.S.M.A., Celis, J.P. and Roos, J.R. (1994). “Dual-Bath electrodeposition of Cu/Ni compositionally modulated multilayers.” *J. Electrochem. Soc.*, 141(1), 230-237.
- Herraz-Cardona, I., Ortega, E., Antón, J.G. and Pérez-Herranz, V. (2011). “Assessment of the roughness factor effect and the intrinsic catalytic activity for hydrogen evolution reaction on Ni-based electrodeposits.” *Int. J. Hydrogen Energy*, 36(16), 9428-9438.

- Highfield, J.G., Claude, E. and Oguro, K. (1999). "Electrocatalytic synergism in Ni/Mo cathodes for hydrogen evolution in acid medium: a new model." *Electrochim. Acta*, 44(16), 2805-2814.
- Hinds, G., Coey, J.M.D. and Lyons, M.E.G. (1998). "Magnetoelectrolysis of copper." *J. Appl. Phys.*, 83(11), 6447-6449.
- Hinds, G., Spada, F., Coey, J., Ní Mhíocháin, T. and Lyons, M. (2001). "Magnetic field effects on copper electrolysis." *J. Phys. Chem. B.*, 105(39), 9487-9502.
- Hoffman, L.R., Breene, C., Diallo, A., Chowdhury, R.R. and Mukaibo, H. (2016). "Competitive Current Modes for Tunable Ni-Sn Electrodeposition and Their Lithiation/Delithiation Properties." *JOM*, 68(10), 2646-2652.
- Hu, C.C. and Weng, C.Y. (2000). "Hydrogen evolving activity on nickel–molybdenum deposits using experimental strategies. *J. Appl. Electrochem.*, 30(4), 499-506.
- Hu, C.C. and Wu, Y.R. (2003). "Bipolar performance of the electroplated iron–nickel deposits for water electrolysis." *Mater. Chem. Phys.*, 82588–82596.
- Hu, C.C., Lee, Y.S. and Wen, T.C. (1997). "The physicochemical/electrochemical properties of binary Ni–Co oxides." *Mater. Chem. Phys.*, 48(3), 246-254.
- Huang, Y. G., Fan, H. L., Chen, Z. K., Gu, C. B., Sun, M. X., Wang, H. Q. and Li, Q. Y. (2016). "The effect of graphene for the hydrogen evolution reaction in alkaline medium." *Int. J. Hydrogen Energy*, 41(6), 3786-3793.
- Huttunen-Saarivirta, E. and Tiainen, T. (2005). "Autocatalytic tin plating in the fabrication of tin-coated copper tube." *J. Mater. Process. Technol.*, 170(1), 211-219.
- Hwang, S. J., Yoo, S. J., Jang, S., Lim, T.-H., Hong, S. A. and Kim, S.-K. (2011). "Ternary Pt-Fe-Co alloy electrocatalysts prepared by electrodeposition: elucidating the roles of Fe and Co in the oxygen reduction reaction." *J. Phys. Chem. C*, 115, 2483-2488.

Ispas, A., Matsushima, H., Plieth, W. and Bund, A. (2007). "Influence of a magnetic field on the electrodeposition of nickel–iron alloys." *Electrochim. Acta*, 52(8), 2785-2795.

Jakšić, J.M., Vojnović, M.V. and Krstajić, N.V. (2000). "Kinetic analysis of hydrogen evolution at Ni–Mo alloy electrodes." *Electrochim. Acta*, 45(25), 4151-4158.

Jaksic, M. M. and Jaksic, J. M. (1994). "Fermi dynamics and some structural bonding aspects of electrocatalysis for hydrogen evolution." *Electrochim. Acta*, 39(11), 1695-1714.

Jaksic, M.M. (2000). "Interionic nature of synergism in catalysis and electrocatalysis." *Solid State Ionics*, 136, 733-746.

Jiang, Y., Li, X., Yu, S., Jia, L., Zhao, X. and Wang, C. (2015). "Reduced Graphene Oxide-Modified Carbon Nanotube/Polyimide Film Supported MoS₂ Nanoparticles for Electrocatalytic Hydrogen Evolution." *Adv. Funct. Mater.*, 25(18), 2693-2700.

Jiménez, H., Gil, L., Staia, M.H. and Puchi-Cabrera, E.S. (2008). "Effect of deposition parameters on adhesion, hardness and wear resistance of Sn–Ni electrolytic coatings". *Surf. Coat. Technol.*, 202(10), 2072-2079.

Jones, D.A. (1996). *Principles and Prevention of Corrosion*, Prentice Hall, New Jersey.

Jović, B.M., Jović, V.D., Maksimović, V.M. and Pavlović, M.G. (2008). "Characterization of electrodeposited powders of the system Ni–Mo–O." *Electrochim. Acta*, 53(14), 4796-4804.

Jović, B.M., Lačnjevac, U.Č., Krstajić, N.V. and Jović, V.D. (2013). "Ni–Sn coatings as cathodes for hydrogen evolution in alkaline solutions." *Electrochim. Acta*, 114, 813-818.

Jović, V.D., Lačnjevac, U., Jović, B.M., Karanović, L. and Krstajić, N.V. (2012). "Ni–Sn coatings as cathodes for hydrogen evolution in alkaline solution. Chemical composition, phase composition and morphology effects." *Int J. Hydrogen Energy*, 37(23), 17882-17891.

- Kanan, M. W. and Nocera, D. G. (2008). "In situ formation of an oxygen-evolving catalyst in neutral water containing phosphate and Co^{2+} ." *Science*, 321(5892), 1072-1075.
- Kanani, N. (2006). *Electroplating: basic principles, processes and practice*. Elsevier Ltd, Berlin, Germany.
- Kedzierzawski, P., Oleszak, D. and Janik-Czachor, M. (2001). "Hydrogen evolution on hot and cold consolidated Ni–Mo alloys produced by mechanical alloying." *Mater Sci Eng A*, 300(1), 105-112.
- Kelly, J.J., Cantoni, M. and Landolt, D. (2001). "Three-dimensional structuring of electrodeposited Cu-Co multilayer alloys." *J. Electrochem. Soc.*, 148(9), C620-C626.
- Kelly, R.G., Scully, J.R., Shoesmith, D. and Buchheit, R.G. (2002). *Electrochemical techniques in corrosion science and engineering*. CRC Press.
- Kim, K.H., Zheng, J.Y., Shin, W. and Kang, Y.S. (2012). "Preparation of dendritic NiFe films by electrodeposition for oxygen evolution." *RSC Adv.*, 2(11), 4759-4767.
- Kobayashi, K., Chiba, A. and Minami, N. (2000). "Effects of ultrasound on both electrolytic and electroless nickel depositions." *Ultrasonics*, 38(1), 676-681.
- Kong, Y., Shao, J., Wang, W., Liu, Q. and Chen, Z. (2009). "Electroless Sn–Ni alloy plating with high Sn content free of activation pretreatment." *J. Alloys Compd.*, 477(1), 328-332.
- Koper, M. T. (2011). "Thermodynamic theory of multi-electron transfer reactions: Implications for electrocatalysis." *J. Electroanal.*, 660(2), 254-260.
- Koza, J. A., Uhlemann, M., Gebert, A. and Schultz, L. (2008). "The effect of magnetic fields on the electrodeposition of CoFe alloys." *Electrochim. Acta*, 53(16), 5344-5353.
- Koza, J., Uhlemann, M., Gebert, A. and Schultz, L. (2008). "The effect of magnetic fields on the electrodeposition of iron." *J. Solid State Electrochem.*, 12(2), 181-192.
- Krause, A., Uhlemann, M., Gebert, A. and Schultz, L. (2004). "The effect of magnetic fields on the electrodeposition of cobalt." *Electrochim. Acta*, 49(24), 4127-4134.

- Krause, A., Uhlemann, M., Gebert, A. and Schultz, L. (2006). "A study of nucleation, growth, texture and phase formation of electrodeposited cobalt layers and the influence of magnetic fields." *Thin Solid Films*, 515(4), 1694-1700.
- Kubisztal, J. and Budniok, A. (2008). "Study of the oxygen evolution reaction on nickel-based composite coatings in alkaline media." *Int J. Hydrogen Energy*, 33(17), 4488-4494.
- Kumar, C.P., Venkatesha, T.V. and Shabadi, R. (2013). "Preparation and corrosion behavior of Ni and Ni-graphene composite coatings." *Mater. Res. Bull.*, 48(4), 1477-1483.
- Landolt, D. (2002). "Electrodeposition science and technology in the last quarter of the twentieth century." *J. Electrochem. Soc.*, 149(3), S9-S20.
- Lasia, A. (1998). "Hydrogen evolution/oxidation reactions on porous electrodes." *J. Electroanal. Chem.*, 454(1), 115-121.
- Lasia, A. (2014). *Electrochemical impedance spectroscopy and its applications*. Springer, New York.
- Lee, Y., Suntivich, J., May, K.J., Perry, E.E. and Shao-Horn, Y. (2012). "Synthesis and activities of rutile IrO₂ and RuO₂ nanoparticles for oxygen evolution in acid and alkaline solutions." *J. Phys. Chem. Lett.*, 3(3), 399-404.
- Lee, Y.S., Hu, C.C. and Wen, T.C. (1996). "Oxygen Evolution on Co-Cu-Zn Ternary Spinel Oxide-Coated Electrodes in Alkaline Solution Integration of Statistical, Electrochemical, and Textural Approaches." *J. Electrochem. Soc.*, 143(4), 1218-1225.
- Leisner, P., Nielsen, C.B., Tang, P.T., Dörge, T.C. and Møller, P. (1996). "Methods for electrodepositing composition-modulated alloys." *J. Mater. Process Tech.*, 58(1), 39-44.
- Li, Y., Wang, H., Xie, L., Liang, Y., Hong, G. and Dai, H. (2011). MoS₂ nanoparticles grown on graphene: an advanced catalyst for the hydrogen evolution reaction. *J. Amer. Chem. Soc.*, 133(19), 7296-7299.

- Lian, K., Thorpe, S.J. and Kirk, D.W. (1992). "The electrocatalytic activity of amorphous and crystalline Ni-Co alloys on the oxygen evolution reaction." *Electrochim. Acta*, 37(1), 169-175.
- Lin, M.Y., Hourng, L.W. and Kuo, C.W. (2012). "The effect of magnetic force on hydrogen production efficiency in water electrolysis." *Int. J. Hydrogen Energy*, 37(2), 1311-1320.
- Liu, H., Xia, G., Zhang, R., Jiang, P., Chen, J. and Chen, Q. (2017). "MOF-derived RuO₂/Co₃O₄ heterojunctions as highly efficient bifunctional electrocatalysts for HER and OER in alkaline solutions." *RSC Adv.*, 7(7), 3686-3694.
- Los, P., Rami, A. and Lasia, A. (1993). "Hydrogen evolution reaction on Ni-Al electrodes." *J. Appl. Electrochem.*, 23(2), 135-140.
- Łosiewicz, B., Budniok, A., Rówiński, E., Łągiewka, E. and Lasia, A. (2004). "The structure, morphology and electrochemical impedance study of the hydrogen evolution reaction on the modified nickel electrodes" *Int. J. Hydrogen Energy*, 29(2), 145-157.
- Lowenheim F. A. (1974). *Modern Electroplating*, 3rd Edition, Wiley-Interscience, New Jersey.
- Luo, J., Jiang, S., Zhang, H., Jiang, J. and Liu, X. (2012). "A novel non-enzymatic glucose sensor based on Cu nanoparticle modified graphene sheets electrode." *Anal. Chim. Acta*, 709, 47-53.
- Lupi, C., Dell'Era, A. and Pasquali, M. (2009). "Nickel-cobalt electrodeposited alloys for hydrogen evolution in alkaline media." *Int. J. Hydrogen Energy*, 34(5), 2101-2106.
- Lyons, M. E. and Brandon, M. P. (2008). "The oxygen evolution reaction on passive oxide covered transition metal electrodes in aqueous alkaline solution. Part 1-Nickel." *Int. J. Electrochem. Sci.*, 3, 1386-1424.
- Lyons, M.E. and Brandon, M.P. (2010). "A comparative study of the oxygen evolution reaction on oxidised nickel, cobalt and iron electrodes in base." *J. Electroanal. Chem.*, 641(1), 119-130.

- Mahale, N.K. and Ingle, S.T. (2017). "Electrocatalytic hydrogen evolution reaction on nano-nickel decorated graphene electrode." *Energy*, 119, 872-878.
- Manazoğlu, M., Hapçı, G. and Orhan, G. (2016). "Effect of electrolysis parameters of Ni–Mo alloy on the electrocatalytic activity for hydrogen evaluation and their stability in alkali medium." *J. Appl. Electrochem.*, 46(2), 191-204.
- Marbán, G. and Valdés-Solís, T. (2007). "Towards the hydrogen economy?" *Int. J. Hydrogen Energy*, 32(12), 1625-1637.
- Marlot, A., Kern, P. and Landolt, D. (2002). "Pulse plating of Ni–Mo alloys from Ni-rich electrolytes." *Electrochim. Acta*, 48(1), 29-36.
- Marozzi, C.A. and Chialvo, A.C. (2001). "Development of electrode morphologies of interest in electrocatalysis: part 2: hydrogen evolution reaction on macroporous nickel electrodes." *Electrochim. Acta*, 46(6), 861-866.
- Maslovara, S.L., Kaninski, M.P.M., Perovic, I.M., Lausevic, P.Z., Tasic, G.S., Radak, B.B. and Nikolic, V.M. (2013). "Novel ternary Ni–Co–Mo based ionic activator for efficient alkaline water electrolysis." *Int. J. Hydrogen Energy*, 38(36), 15928-15933.
- Mason T. J. and Cordemans, E. D. (1996). "Ultrasonic intensification of chemical processing and related operations: a review." *Chem. Eng. Res. Des.*, 74, 511–516.
- Matsushima, H., Ispas, A., Bund, A. and Bozzini, B. (2008). "Magnetic field effects on the initial stages of electrodeposition processes." *J. Electroanal. Chem.*, 615(2), 191-196.
- McCafferty, E. (2010). *Introduction to corrosion science*. Springer Science & Business Media.
- McKone, J.R., Sadtler, B.F., Werlang, C.A., Lewis, N.S. and Gray, H.B. (2013). "Ni–Mo nanopowders for efficient electrochemical hydrogen evolution." *ACS Catalysis*, 3(2), 166-169.
- Merki, D. and Hu, X. (2011). "Recent developments of molybdenum and tungsten sulfides as hydrogen evolution catalysts." *Energy Environ. Sci.*, 4(10), 3878-3888.

- Montemor, M.F., Simoes, A.M.P. and Ferreira, M.G.S. (2003). "Chloride-induced corrosion on reinforcing steel: from the fundamentals to the monitoring techniques." *Cem. Concr. Compos.*, 25(4), 491-502.
- Monzon, L.M. and Coey, J.M.D. (2014). "Magnetic fields in electrochemistry: The Lorentz force. A mini-review." *Electrochem. commun.*, 42, 38-41.
- Monzon, L.M. and Coey, J.M.D. (2014). "Magnetic fields in electrochemistry: The Lorentz force. A mini-review." *Electrochem. Comm.*, 42, 38-41.
- Nakanishi, T., Ozaki, M., Nam, H.S., Yokoshima, T. and Osaka, T. (2001). "Pulsed electrodeposition of nanocrystalline CoNiFe soft magnetic thin films." *J. Electrochem. Soc.*, 148(9), C627-C631.
- Narayanan, T. S. and Seshadri, S. (2004). "Formation and characterization of borohydride reduced electroless nickel deposits." *J. Alloys Compd.*, 365(1), 197-205.
- Navarro-Flores, E., Chong, Z. and Omanovic, S. (2005). "Characterization of Ni, NiMo, NiW and NiFe electroactive coatings as electrocatalysts for hydrogen evolution in an acidic medium." *J. Mol. Catal. A: Chem.*, 226, 179-197.
- Nevers, A., Hallez, L., Touyeras, F. and Hihn, J.Y. (2017). "Effect of ultrasound on silver electrodeposition: Crystalline structure modification." *Ultrason. Sonochem.*,
- Nørskov, J.K., Bligaard, T., Logadottir, A., Kitchin, J.R., Chen, J.G., Pandelov, S. and Stimming, U. (2005). "Trends in the exchange current for hydrogen evolution." *J. Electrochem. Soc.*, 152(3), J23-J26.
- O'reilly, C., Hinds, G. and Coey, J. (2001). "Effect of a magnetic field on electrodeposition: Chronoamperometry of Ag, Cu, Zn, and Bi." *J. Electrochem. Soc.*, 148(10), C674-C678.
- Ojani, R., Raoof, J.B. and Hasheminejad, E. (2013). "One-step electroless deposition of Pd/Pt bimetallic microstructures by galvanic replacement on copper substrate and investigation of its performance for the hydrogen evolution reaction." *Int. J. Hydrogen Energy*, 38(1), 92-99.

- Ojani, R., Valiollahi, R. and Raoof, J.B. (2014). "Comparison between graphene supported Pt hollow nanospheres and graphene supported Pt solid nanoparticles for hydrogen evolution reaction." *Energy*, 74, 871-876.
- Okido, M., Depo, J. K. and Capuano, G. A. (1993). "The Mechanism of hydrogen evolution reaction on a modified raney nickel composite-coated electrode by ac impedance." *J. Electrochem. Soc.*, 140(1), 127-133.
- Oleszak, D., Portnoy, V.K. and Matyja, H. (1999). "Structure of mechanically alloyed Ni-Mo powders." *J. Metastable Nanocryst. Mater.*, 2, 345-350
- Pardhasaradhy N. V. (1987). *Practical electroplating hand book*. Prentice Hall Incl. Pub., New Jersey.
- Parsons, R. (1958). "The rate of electrolytic hydrogen evolution and the heat of adsorption of hydrogen". *Trans. Faraday Soc.*, 54, 1053-1063.
- Paunovic, M. and Schlesinger, M. (2006). *Fundamentals of electrochemical deposition* (Vol. 45). John Wiley & Sons, New Jersey.
- Pavithra, G.P. and Hegde, A.C. (2012). "Magnetic property and corrosion resistance of electrodeposited nanocrystalline iron–nickel alloys." *Appl. Surf. Sci.*, 258(18), 6884-6890.
- Pérez-Alonso, F.J., Adan, C., Rojas, S., Pena, M.A. and Fierro, J.L.G. (2014). "Ni/Fe electrodes prepared by electrodeposition method over different substrates for oxygen evolution reaction in alkaline medium." *Int. J. Hydrogen Energy*, 39(10), 5204-5212.
- Peters, D. (1996). "Ultrasound in materials chemistry." *J. Mater. Chem.*, 6 (10), 1605–1618.
- Peters, D. (1996). "Ultrasound in materials chemistry." *J. Mater. Chem.*, 6(10), 1605-1618.
- Podlaha, E.J. and Landolt, D. (1996). "Induced Codeposition I. An Experimental Investigation of Ni-Mo Alloys." *J. Electrochem. Soc.*, 143(3), 885-892.

- Prasad, P.B.S.N.V., Vasudevan, R., Seshadri, S.K. and Ahila, S. (1993). "The effect of ultrasonic vibration on nickel electrodeposition." *Mater. Lett.*, 17(6), 357-359.
- Rabah, K.L. Chopart, J.P. Schloerb, H. Saulnier, S. Aaboubi, O. Uhlemann, M. Elmi, D. and Amblard, J. (2004). "Analysis of the magnetic force effect on paramagnetic species." *Electroanal. Chem.* 571, 85.
- Ragsdale, S. R. and White, H. S. (1999). "Imaging microscopic magnetohydrodynamic flows." *Anal. Chem.*, 71(10), 1923-1927.
- Ragsdale, S. R., Grant, K. M. and White, H. S. (1998). "Electrochemically generated magnetic forces. Enhanced transport of a paramagnetic redox species in large, nonuniform magnetic fields." *J. Amer. Chem. Soc.*, 120(51), 13461-13468.
- Raj, I. A. and Vasu, K. I. (1990). "Transition metal-based hydrogen electrodes in alkaline solution—electrocatalysis on nickel based binary alloy coatings." *J. Appl. Electrochem.*, 20(1), 32-38.
- Raj, I.A. (1993). "Nickel-based, binary-composite electrocatalysts for the cathodes in the energy-efficient industrial production of hydrogen from alkaline-water electrolytic cells." *J. Mater. Sci.*, 28(16), 4375-4382.
- Raj, I.A. and Venkatesan, V.K. (1988). "Characterization of nickel-molybdenum and nickel-molybdenum-iron alloy coatings as cathodes for alkaline water electrolyzers." *Int. J. Hydrogen Energy*, 13(4), 215-223.
- Ramalho, A. and Miranda, J. C. (2005). "Friction and wear of electroless NiP and NiP⁺ PTFE coatings." *Wear*, 259(7), 828-834.
- Rao, V. R., Bangera, K. V. and Hegde, A. C. (2013). "Magnetically induced electrodeposition of Zn–Ni alloy coatings and their corrosion behaviors." *J. Magn. Magn. Mater.*, 345, 48-54.
- Rao, V.R. and Hegde, A.C. (2013). "Nanofabricated multilayer coatings of Zn-Ni alloy for better corrosion protection." *Prot. Met. Phys. Chem. Surf.*, 6(49), 693-698.

Rao, V.R. and Hegde, A.C. (2014). "Magnetically Induced Codeposition of Ni–Cd Alloy Coatings for Better Corrosion Protection." *Ind. Eng. Chem. Res.*, 53(13), 5490-5497.

Rao, V.R., Hegde, C.A. and Bhat, K.U. (2013). "Effect of heat treatment on structure and properties of multilayer Zn-Ni alloy coatings." *J. Electrochem. Sci. Eng.*, 3(4), 137-149.

Ray, A. (2015). "Electrodeposition of Thin Films for Low-cost Solar Cells." *InTech*, 145-172.

Refaey, S.A.M., Taha, F. and Hasanin, T.H.A. (2006). "Passivation and pitting corrosion of nanostructured Sn–Ni alloy in NaCl solutions." *Electrochim. Acta*, 51(14), 2942-2948.

Ribeiro, D.V. and Abrantes, J.C.C. (2016). "Application of electrochemical impedance spectroscopy (EIS) to monitor the corrosion of reinforced concrete: A new approach." *Constr. Build. Mater.*, 111, 98-104.

Rosalbino, F., Delsante, S., Borzone, G. and Angelini, E. (2007). "Correlation of microstructure and catalytic activity of crystalline Ni–Co–Y alloy electrode for the hydrogen evolution reaction in alkaline solution." *J. Alloys Compd.*, 429(1), 270-275.

Sáez, V. and Mason, T.J. (2009). "Sonochemical synthesis of nanoparticles." *Molecules*, 14(10), 4284-4299.

Safizadeh, F., Ghali, E. and Houlachi, G. (2015). "Electrocatalysis developments for hydrogen evolution reaction in alkaline solutions—a review." *Int. J. Hydrogen Energy*, 40(1), 256-274.

Sanches, L.S., Domingues, S.H., Marino, C.E. and Mascaro, L.H. (2004). "Characterisation of electrochemically deposited Ni–Mo alloy coatings." *Electrochem. Comm.*, 6(6), 543-548.

Santos, M.B.F., Da Silva, E.P., Andrade, R. and Dias, J.A.F. (1992). "NiSn and porous NiZn coatings for water electrolysis." *Electrochim. Acta*, 37(1), 29-32.

- Schlesinger, M. and Paunovic, M. (2000). *Modern Electroplating*. Fourth edition, John Wiley and Sons Publication, New Jersey.
- Schwarzacher, W. (2006). "Electrodeposition: a technology for the future." *Interface*, 15(1), 32-35.
- Sen, D., Isaac, K. M., Leventis, N. and Fritsch, I. (2011). "Investigation of transient redox electrochemical MHD using numerical simulations." *Int. J. Heat Mass Transfer*, 54 5368–5378.
- Serek, A. and Budniok, A. (2003). "Electrodeposition and thermal treatment of nickel layers containing titanium." *J. Alloys Compd.*, 352(1), 290-295.
- Shannon, J., Gu, Z. and Fahidy, T. (1997). "Surface morphology of cathodic nickel deposits produced via magnetoelectrolysis." *J. Electrochem. Soc.*, 144(12), L314-L316.
- Shannon, J., Gu, Z. and Fahidy, T. (1999). "A statistical analysis of the electrodeposition of nickel in the presence of a magnetic field." *J. Appl. Electrochem.*, 29(5), 577-584.
- Sheela, G., Pushpavanam, M. and Pushpavanam, S. (2002). "Zinc–nickel alloy electrodeposits for water electrolysis." *Int. J. Hydrogen Energy*, 27(6), 627-633.
- Shervedani, R. K. and Madram, A. R. (2008). "Electrocatalytic activities of nanocomposite Ni₈₁ P₁₆ C₃ electrode for hydrogen evolution reaction in alkaline solution by electrochemical impedance spectroscopy." *Int. J. Hydrogen Energy*, 33(10), 2468-2476.
- Shinohara, K., Hashimoto, K. and Aogaki, R. (2002). "Macroscopic fluid motion accompanying copper corrosion in nitric acid under a vertical magnetic field." *Electrochemistry*, 70(10), 772-778.
- Solmaz, R. and Kardaş, G. (2009). "Electrochemical deposition and characterization of NiFe coatings as electrocatalytic materials for alkaline water electrolysis." *Electrochim. Acta*, 54(14), 3726-3734.

- Song, L. J. and Meng, H. M. (2010). "Effect of carbon content on Ni–Fe–C electrodes for hydrogen evolution reaction in seawater." *Int. J. Hydrogen Energy*, 35, 10060-10066.
- Spriano, S., Baricco, M., Antonione, C., Angelini, E., Rosalbino, F. and Spinelli, P. (1994). "Electrocatalytic behaviour of Zr 64 Ni 36 and Zr 48 Ni 27 Al 25 amorphous alloys." *Electrochim. Acta*, 39(11), 1781-1786.
- Stansbury, E.E. and Buchanan, R.A. (2000). *Fundamentals of electrochemical corrosion*. ASM international.
- Stepanova, L.I., Purovskaya, O.G. and Sviridov, V.V. (2000). "Applied Electrochemistry and Corrosion Protection of Metals-Influence of Ammonium Ions on Chemical and Phase Composition of Ni-Mo Alloy Films Electrodeposited from Citrate Electrolytes." *Russ. J. Electrochem*, 73(1), 66-70.
- Subramanya, B., Ullal, Y., Shenoy, S. U., Bhat, D. K. and A. C. Hegde. "Novel Co–Ni–graphene composite electrodes for hydrogen production." *RSC Adv.*, 5(59), 47398-47407.
- Suryanarayana, C. (1995). "Nanocrystalline materials." *Int. Mat. Rev*, 40(2), 41-64.
- Tachibana, Y., Vayssieres, L. and Durrant, J.R. (2012). "Artificial photosynthesis for solar water-splitting." *Nat. Photonics*, 6(8), 511-518.
- Tacken, R.A. and Janssen, L.J.J. (1995). "Applications of magnetoelectrolysis." *J. Appl. Electrochem.*, 25(1), 1-5.
- Tan, C.H., Qi, G.W., Li, Y.P., Guo, J., Wang, X., Kong, D.L., Wang, H.J. and Zhang, S.Y. (2013). "The improved performance of porous Sn–Ni alloy as anode materials for lithium-ion battery prepared by electrochemical dissolution treatment." *Int. J. Electrochem. Sci.*, 8, 1966-1975.
- Tanaka, S. I., Hirose, N. and Tanaki, T. (1999). "Evaluation of raney-nickel cathodes prepared with aluminum powder and titanium hydride powder." *J. Electrochem. Soc.*, 146(7), 2477-2480.

- Tasić, G. S., Lačnjevac, U., Tasić, M. M., Kaninski, M. M., Nikolić, V. M., Žugić, D. L. and Jović, V. D. (2013). "Influence of electrodeposition parameters of Ni–W on Ni cathode for alkaline water electrolyser." *Int. J. Hydrogen Energy*, 38(11), 4291-4297.
- Thangaraj, V. and Hegde, A.C. (2006). "Electrodeposition and characterisation of Zinc-Nickel alloy." *Bull. Electrochem.*, 22, 49-53.
- Thangaraj, V., Eliaz, N. and Hegde, A.C. (2009). "Corrosion behavior of composition modulated multilayer Zn–Co electrodeposits produced using a single-bath technique." *J. Appl. Electrochem.*, 39(3), 339.
- Thomas F.G. and Henze G. (2001). *Introduction to Voltammetric Analysis, Theory and Practice*, CSIRO Publishing, Australia.
- Tian, G.L., Zhao, M.Q., Yu, D., Kong, X.Y., Huang, J.Q., Zhang, Q. and Wei, F. (2014). "Nitrogen-Doped Graphene/Carbon Nanotube Hybrids: In Situ Formation on Bifunctional Catalysts and Their Superior Electrocatalytic Activity for Oxygen Evolution/Reduction Reaction." *Small*, 10(11), 2251-2259.
- Touyeras, F., Hihn, J.Y., Bourgoïn, X., Jacques, B., Hallez, L. and Branger, V. (2005). "Effects of ultrasonic irradiation on the properties of coatings obtained by electroless plating and electro plating." *Ultrason. Sonochem.*, 12(1), 13-19.
- Trasatti, S. (1999) "1799–1999: Alessandro Volta's 'Electric pile': Two hundred years, but it doesn't seem like it." *J. Electroanal. Chem.*, 46(1), 1-4.
- Trzaska, M. (2012). *Studies of Resistance to Corrosion of Selected Metallic Materials Using Electrochemical Methods*. INTECH Open Access Publisher.
- Tudela, I., Zhang, Y., Pal, M., Kerr, I., Mason, T.J. and Cobley, A.J. (2015). "Ultrasound-assisted electrodeposition of nickel: Effect of ultrasonic power on the characteristics of thin coatings." *Surf. Coat. Technol.*, 264, 49-59.
- Turner, J.A. (2004). "Sustainable hydrogen production." *Science*, 305(5686), 972-974.

- Uhlemann, M., Krause, A., Chopart, J.P. and Gebert, A. (2005). "Electrochemical deposition of Co under the influence of high magnetic fields." *J. Electrochem. Soc.*, 152(12), C817-C826.
- Ullal, Y. and Hegde, A.C. (2014). "Electrodeposition and electro-catalytic study of nanocrystalline Ni-Fe alloy." *Int. J. Hydrogen Energy*, 39(20), 10485-10492.
- Ullal, Y. and Hegde, A.C. (2014). "Electrofabrication of multilayer Fe-Ni alloy coatings for better corrosion protection." *Appl. Phys. A*, 116(4), 1587-1594.
- Vayenas, C.G., White, R.E. and Gamboa-Aldeco, M.E. (2008). *Modern Aspects of Electrochemistry*, Number 42, Springer, New York.
- Venkatakrishna, K. and Hegde, A.C. (2010). "Electrolytic preparation of cyclic multilayer Zn-Ni alloy coating using switching cathode current densities." *J. Appl. Electrochem.*, 40(11), 2051-2059.
- Venkatakrishna, K. and Hegde, A.C. (2011). "Composition modulated multilayer Zn-Fe alloy coatings on mild steel for better corrosion resistance." *Mater. Manuf. Processes*, 26(1), 29-36.
- Vijayakumar, J., Mohan, S., Kumar, S.A., Suseendiran, S.R. and Pavithra, S. (2013). "Electrodeposition of Ni-Co-Sn alloy from choline chloride-based deep eutectic solvent and characterization as cathode for hydrogen evolution in alkaline solution." *Int. J. Hydrogen Energy*, 38(25), 10208-10214.
- Viswanathan, K., Epstein, M.F. and Cheh, H.Y. (1978). "The Application of Pulsed Current Electrolysis to a Rotating-Disk Electrode System I. Mass Transfer." *J. Electrochem. Soc.*, 125(11), 1772-1776.
- Walker, C.T. and Walker, R. (1973). "Effect of ultrasonic agitation on some properties of electrodeposits." *Electrodepos. Surface Treat.*, 1(6), 457-469.
- Walter, M.G., Warren, E.L., McKone, J.R., Boettcher, S.W., Mi, Q., Santori, E.A. and Lewis, N.S. (2010). "Solar water splitting cells." *Chem. Rev.*, 110(11), 6446-6473.

- Wang, J. (2000). *Analytical Electrochemistry*. Second edition, Wiley-VCH, New Jersey.
- Wang, L., Zhao, L., Zhang, B., Hu, W., Shu, X., Sheng, X. and Fang, Z. (1999). “Crystallization study of electroless Fe–Sn–B amorphous alloy deposits.” *J. Alloys Compd.*, 287(1), 234-238.
- Wassef, O. Fahidy, T.Z. (1976). “Magnetoelectrolysis in the presence of bubble formation at the cathode.” *Electrochim. Acta*, 21, 727.
- Watanabe, T. (2004). *Nano-plating, microstructure control theory of plated film and data base of plated film*. Elsevier Ltd, Japan.
- Wieckowski, A., Savinova, E.R. and Vayenas, C.G. (2003). *Catalysis and electrocatalysis at nanoparticle surfaces*. CRC Press.
- Wilcox, G.D., (2003). Surface modification with compositionally modulated multilayer coatings. *J. Corr. Sci. Eng.*, 6, 52.
- Wilson, G. (1972). “The use of tin when alloyed with nickel or lead as a printed circuit finish.” *Trans Inst Met Finish.*, 50(3), 109-113.
- Winter, M, and Ralph J. B. (2004). “What are batteries, fuel cells, and supercapacitors?” *Chem. Rev.*, 104 (10), 4245-4270.
- Wu, H., Zhao, G., Mu, J., Li, X. and He, Y. (2010). “Effects of ultrasonic dispersion on structure of electrodeposited Ni coating on AZ91D magnesium alloy.” *Trans. Nonferrous Met. Soc. China*, 20, Supplement 2. s703–s707.
- Xia, M., Lei, T., Lv, N. and Li, N. (2014). “Synthesis and electrocatalytic hydrogen evolution performance of Ni–Mo–Cu alloy coating electrode.” *Int. J. Hydrogen Energy* 39(10), 4794-4802.
- Xu, C., Zhou, J. B., Zeng, M., Fu, X. L., Liu, X. J. and Li, J. M. (2016). “Electrodeposition mechanism and characterization of Ni–Mo alloy and its electrocatalytic performance for hydrogen evolution.” *Int. J. Hydrogen Energy*, 41(31), 13341-13349.

- Yahalom, J. and Zadok, O. (1987). "Formation of composition-modulated alloys by electrodeposition." *J. Mater. Sci.*, 22(2), 499-503.
- Yamashita, H., Yamamura, T. and Yoshimoto, K. (1993). "The relation between catalytic ability for hydrogen evolution reaction and characteristics of nickel-tin alloys." *J. Electrochem. Soc.*, 140(8), 2238-2243.
- Yogesha, S. and Hegde, A.C. (2010). "Electrodeposition of high performance multilayer coatings of Zn–Co using triangular current pulses." *Trans. IMF*, 88(6), 317-323.
- Yogesha, S. and Hegde, A.C. (2011). "Development of Composition Modulated Multilayer Alloy Coatings and their Corrosion Behavior." *J. Met., Mater. Mine.*, 21(1), 83-92.
- Yogesha, S., Bhat, R.S., Venkatakrishna, K., Pavithra, G.P., Ullal, Y. and Hegde, A.C. (2011). "Development of Nano-structured Zn-Ni Multilayers and their Corrosion Behaviors." *Synth. React. Inorg. M.*, 41(1), 65-71.
- Yogesha, S., Kaje, V. and A. C. Hegde, (2011). "Development of anti-corrosive multi-layered coatings of zinc-nickel alloy." *Anti. Corros. Method M.*, 58(2), 84-89.
- Yu, L., Lei, T., Nan, B., Jiang, Y., He, Y. and Liu, C.T. (2016). "Characteristics of a sintered porous Ni–Cu alloy cathode for hydrogen production in a potassium hydroxide solution." *Energy*, 97, 498-505.
- Yuan, X.-Z. R. Song, C. Wang H. and Zhang, J. (2009). *Electrochemical impedance spectroscopy in PEM fuel cells: fundamentals and applications*, Springer Science & Business Media.
- Yüce, A.O., Döner, A. and Kardaş, G. (2013). "NiMn composite electrodes as cathode material for hydrogen evolution reaction in alkaline solution." *Int. J. Hydrogen Energy*, 38(11), 4466-4473.
- Zabinski, P.R., Jarek, A. and Kowalik, R. (2009). "Effect of applied external magnetic field on electrodeposition of cobalt alloys for hydrogen evolution in 8M NaOH." *Magnetohydrodynamics*, 45(2), 275-280.

- Zeng, K. and Zhang, D. (2010). "Recent progress in alkaline water electrolysis for hydrogen production and applications." *Prog. Energy Combust. Sci.*, 36(3), 307-326.
- Zeng, K. and Zhang, D. (2014). "Evaluating the effect of surface modifications on Ni based electrodes for alkaline water electrolysis." *Fuel*, 116, 692-698.
- Zhang, K., Xiao, W., Li, J., Liu, J. and Yan, C. (2017). "Two-step Preparation of Porous Nickel-sulfur Electrode for Hydrogen Evolution in Alkaline Water Electrolysis." *Electrochim. Acta*, 228, 422-427.
- Zhao, Y., Nakamura, R., Kamiya, K., Nakanishi, S. and Hashimoto, K. (2013). "Nitrogen-doped carbon nanomaterials as non-metal electrocatalysts for water oxidation." *Nat. Comm.*, 4.
- Zheng, Y., Jiao, Y., Zhu, Y., Li, L.H., Han, Y., Chen, Y., Du, A., Jaroniec, M. and Qiao, S.Z. (2014). Hydrogen evolution by a metal-free electrocatalyst. *Nat. Comm.*, 5.
- Zhu, L., Younes, O., Ashkenasy, N., Shacham-Diamand, Y. and Gileadi, E. (2002). "STM/AFM studies of the evolution of morphology of electroplated Ni/W alloys." *Appl. Surf. Sci.*, 200(1), 1-14.
- Zieliński, M., Miękoś, E., Szczukocki, D., Dałkowski, R., Leniart, A., Krawczyk, B. and Juszcak, R. (2015). "Effects of constant magnetic field on electrodeposition of Co-W-Cu alloy." *Int. J. Electrochem. Sci.*, 10, 4146-4154.
- Zou, X. and Zhang, Y. (2015). "Noble metal-free hydrogen evolution catalysts for water splitting." *Chem. Soc. Rev.*, 44(15), 5148-5180.

RESEARCH PUBLICATIONS

International Journals

1. **Shetty S.** and Hegde A. C. (2015). "Electrodeposition of Sn–Ni alloy coatings and their characterization." *Mater. Sci. Forum*, 830-831, 655-658.
2. **Shetty S.**, Rao, V.R. and Hegde A. C. (2016). "Magneto-electrodeposition of Sn–Ni alloy coating for better corrosion protection." *Int. J. chem. Eng. Process.*, 2(1), 29-42.
3. **Shetty S.**, Sadiq M.M.J., Bhat D.K and Hegde A. C. (2016). "Development of multilayer Sn–Ni alloy coating by pulsed sonoelectrolysis for enhanced corrosion protection." *RSC Adv.*, 6(81), 77465-77473.
4. **Shetty S.** and Hegde A. C. (2017). "Electrodeposition of Sn–Ni Alloy Coatings for Water-Splitting Application from Alkaline Medium." *Metall. Mater. Trans. B*, 48(1), 632-641.
5. **Shetty S.**, Sadiq M.M.J., Bhat D.K and Hegde A. C. (2017). "Electrodeposition and characterization of Ni–Mo alloy as an electrocatalyst for alkaline water electrolysis." *J. Electroanal. Chem.*, 796, 57-65.
6. **Shetty S.** and Hegde A. C. (2017). "Magnetically induced electrodeposition of Ni–Mo alloy for hydrogen evolution reaction." *Electrocatalysis*, 8(3), 179-188.
7. **Shetty, S.** and Hegde, A.C. (2017). "A Study on Composition Dependent Electrocatalytic Behaviour of Electrodeposited Ni–Mo Alloy." *Nano Hybrids and Composites*, 17, 113-120.
8. **Shetty S.**, Sadiq M.M.J., Bhat D.K. and Hegde A. C. (2017). "Electrodeposited Ni–Mo–rGO composites as an electrode material for efficient hydrogen production from alkaline water electrolysis." *New J. Chem.* (under review).

International Conferences

1. **Shetty S.** and Hegde A.C. (2014). "Effect of magnetic field on electrodeposition of Sn–Ni alloy coatings." International Conference on Electrochemical Science

- and Technology (ICONEST-2014), IISc, Bengaluru, Karnataka, August 7-9, 2014.
- 2. Shetty S. and Hegde A. C. (2015).** “Electrodeposition of Sn–Ni alloy coatings and their characterization.” International Conference on Advanced Materials and Manufacturing Processes for Strategic Sector (ICAMPS-2015), Thiruvananthapuram, Kerala, May 13-15, 2015.
 - 3. Shetty S. and Hegde A. C. (2015).** “Electrodeposition of Sn–Ni Alloy and its electrocatalytic Behaviour.” International Corrosion Prevention Symposium for Research Scholars, CORSYM-2015, IITM, Chennai, Tamil Nadu, July 31-August 1, 2015.
 - 4. Shetty S. and Hegde A. C. (2016).** “Electrofabrication of multilayer Sn–Ni alloy plating by sonoelectrolysis.” 17th Asian Pacific Corrosion Control Conference (APCCC), IITB, Mumbai, January 27-30, 2016.
 - 5. Shetty S. and Hegde A. C. (2016).** “A study on composition dependent electrocatalytic behaviour of electrodeposited Ni–Mo alloy.” International Conference on Nanoscience and Nanotechnology for Energy Application (EApp-2016), Sathyabama University, Chennai, June 27-29, 2016.
 - 6. Shetty S. and Hegde A. C. (2017).** “Magneto-electrodeposited Ni–Mo alloy as cathode material for better hydrogen evolution reaction” International Conference on Recent Trends in Chemical Sciences (ICRCS-2017), Government Engineering College, Bikaner, Rajasthan, January 12-13, 2017.
 - 7. Shetty S. and Hegde A. C. (2017).** “The Improved Performance of Sn–Ni Alloy for Better Hydrogen Production by Electrochemical Dissolution Treatment” International Conference on Green Chemistry & Nanotechnology Opportunities and Challenges (GCNOC-2017), St. Aloysius College, Mangalore, Karnataka, February 27-28, 2017.

BIODATA

Sandhya S

Phone: +91-9620949176

Email: sandhya19shetty@gmail.com

OBJECTIVES

To work in a professional environment with prospects of growth, where I can apply my academic skills and sharpen my skills and competence for the realization of goals entrusted to me efficiently and effectively.

RESEARCH AND TEACHING INTERESTS

Electroplating of metal/alloys/composites, surface coating technology, corrosion testing and evaluation, electrocatalysis, and water splitting reaction.

EXPERIENCE

Organization	Description	Year
Project assistant for Post Graduate	National Institute of Technology Karnataka, Surathkal	2014-2016
Lecturer in Chemistry for Pre-University	Vikas Pre-University College, Mangalore	2011-2013

EDUCATION

Degree	Institution	Year
Ph.D. Chemistry	National Institute of Technology Karnataka, Surathkal	2013-2018
M.Sc. (Analytical Chemistry)	St Aloysius College, Mangalore	2009-2011
B.Sc. (Biotechnology, Chemistry, Botany)	St Aloysius College, Mangalore	2006-2009

SKILLS

- Proficiency in MS Office (Word, Excel, PowerPoint), Origin, EndNote, ChemDraw, CorrView software and ZSimpWin 3.21.

- Hands-on experience in handling and usage of instruments like electrochemical workstations (Versastat-3, Ivium, Gill AC, Biologic SP-150).
- Familiar with XPS, FT-IR, XRD SEM and AFM techniques.
- Strong knowledge and research experience in electroplating of metal/alloys at different conditions, characterization, and evaluation of the materials for their corrosion protection and water splitting applications.
- Well versed in several electrochemical techniques (Electrochemical impedance spectroscopy, potentiodynamic polarization, cyclic voltammetry, linear sweep voltammetry, chronopotentiometry and chronoamperometry).
- Communicating effectively in verbal and written form on research results, issues, and plans.
- Good organization skills (time management and prioritization).
- Highly detail oriented, a strong commitment to the timely execution of tasks.

PUBLICATIONS

1. Shetty S. and Hegde A. C. (2015). "Electrodeposition of Sn-Ni alloy coatings and their characterization." *Mater. Sci. Forum*, 830-831, 655-658.
2. Shetty S. and Hegde A. C. (2016). "Magneto-electrodeposition of Sn-Ni alloy coating for better corrosion protection." *Int. J. chem. Eng. Process.*, 2(1), 29-42.
3. Shetty S., Sadiq M.M.J., Bhat D.K and Hegde A. C. (2016). "Development of multilayer Sn–Ni alloy coating by pulsed sonoelectrolysis for enhanced corrosion protection." *RSC Adv.*, 6(81), 77465-77473.
4. Shetty S. and Hegde A. C. (2017). "Electrodeposition of Sn-Ni Alloy Coatings for Water-Splitting Application from Alkaline Medium." *Metall. Mater. Trans. B*, 48(1), 632-641.
5. Shetty S., Sadiq M.M.J., Bhat D.K. and Hegde A. C. (2017). "Electrodeposition and characterization of Ni-Mo alloy as an electrocatalyst for alkaline water electrolysis." *J. Electroanal. Chem.*, 796, 57-65.
6. Shetty S. and Hegde A. C. (2017). "Magnetically induced electrodeposition of Ni-Mo alloy for hydrogen evolution reaction." *Electrocatalysis*, 8(3), 179-188.
7. Shetty, S. and Hegde, A.C. (2017). "A Study on Composition Dependent Electrocatalytic Behaviour of Electrodeposited Ni-Mo Alloy." *Nano Hybrids and Composites*, 17, 113-120.

8. Shetty S., Sadiq M.M.J., Bhat D.K. and Hegde A. C. (2017). “Electrodeposited Ni-Mo-rGO composites as an electrode material for efficient hydrogen production from alkaline water electrolysis.” *New J. Chem.* (under review).

CONFERENCES

ORAL

- **Shetty S.** and Hegde A.C. “Effect of magnetic field on electrodeposition of Sn-Ni alloy coatings.” International Conference on Electrochemical Science and Technology (ICONEST- 2014), IISc. Bengaluru, Karnataka, August 2014.
- **Shetty S.** and Hegde A. C. “Electrodeposition of Sn-Ni Alloy and its electrocatalytic Behaviour.” CORSYM-2015, IITM, Chennai, Tamil Nadu, July 2015.
- **Shetty S.**, and Hegde A. C. “Electrofabrication of multilayer Sn-Ni alloy plating by sonoelectrolysis.” 17th Asian Pacific Corrosion Control Conference (APCCC), IITB, Mumbai, Maharashtra, January 2016.
- **Shetty S.**, and Hegde A. C. “A study on composition dependent electrocatalytic behaviour of electrodeposited Ni-Mo alloy.” International Conference on Nanoscience and Nanotechnology for Energy Application (EApp-2016), Sathyabama University, Chennai, Tamil Nadu, June 2016.

POSTER

- **Shetty S.** and Hegde A. C. “Electrodeposition of Sn-Ni alloy coatings and their characterization.” International Conference on Advanced Materials and Manufacturing Processes for Strategic Sector (ICAMPS-2015), Thiruvananthapuram, Kerala, May 2015.
- **Shetty S.** and Hegde A. C. (2017). “Magneto-electrodeposited Ni-Mo alloy as cathode material for better hydrogen evolution reaction” International Conference on Recent Trends in Chemical Sciences (ICRCS-2017), Government Engineering College, Bikaner, Rajasthan, January 2017.
- **Shetty S.** and Hegde A. C. (2017). “The Improved Performance of Sn-Ni Alloy for Better Hydrogen Production by Electrochemical Dissolution Treatment” International Conference on Green Chemistry & Nanotechnology Opportunities and Challenges (GCNOC-2017), St. Aloysius College, Mangalore, Karnataka, February 2017.

AWARDS

Best paper awarded (poster presentation) at International Conference on Green Chemistry & Nanotechnology Opportunities and Challenges, St. Aloysius College, Mangalore, February 2017.

HOBBIES AND INTERESTS

Reading (literary fiction), music (Western and Indian), fitness, cycling, traveling, trekking, food, mentoring.

PERSONAL DETAILS

Address for correspondence	'Shree Sadan' 8-5-393/3 Kulur Ferry Road, Alake, Mangalore-575003, Karnataka, India.
Date of birth	19/10/1988
Sex	Female
Nationality	Indian
Languages known	English, Hindi, Kannada and Tulu

REFERENCES

Dr. A. Chitharanjan Hegde Professor & Former HOD Department of Chemistry National Institute of Technology Karnataka Mangalore-575 025, India Mobile: + 91-9980360242. E-mail: acrhegde@gmail.com	Dr. D. Krishna Bhat Head of the Department Department of Chemistry National Institute of Technology Karnataka Mangalore-575025, India Mobile: +919481271262 E-mail: denthajekb@gmail.com
---	---